Title

Investigating Nighttime Oxidation of Wildfire-Emitted VOCs: Implications for Oxidation Mechanisms, Secondary Organic Aerosol, and Brown Carbon Formation

Permalink

https://escholarship.org/uc/item/9wq189dx

Author

Mayorga, Raphael

Publication Date

2024

UNIVERSITY OF CALIFORNIA
RIVERSIDE

Investigating Nighttime Oxidation of Wildfire-Emitted VOCs: Implications for Oxidation Mechanisms, Secondary Organic Aerosol, and Brown Carbon Formation

A Dissertation submitted in partial satisfaction
of the requirements for the degree of

Doctor of Philosophy

in

Chemistry

by

Raphael Mayorga

September 2024

Dissertation Committee:
  Dr. Haofei Zhang, Chairperson
  Dr. James Davies
  Dr. Ryan Julian

The Dissertation of Raphael Mayorga is approved:

Committee Chairperson

University of California, Riverside

ACKNOWLEDGEMENTS

Over the past five years, the University of California, Riverside has provided so much for me, and I have created countless wonderful memories during my time here. At the center of all the positive experiences, opportunities, and relationships that I formed during my PhD has been Professor Haofei Zhang.

Professor Zhang, when I first joined your lab in 2019, I had no experience in the field of atmospheric chemistry. Upon joining the lab and beginning to read papers, I quickly developed a passion for the subject. Early on, you allowed me to get hands-on experience in the lab and provided the perfect balance of independence and support which allowed me to become familiar and confident with many new analytical instruments and experimental procedures. In our daily and weekly discussions, your unwavering support and willingness to answer all my questions has been crucial in enabling me to become the scientist that I am today. I cannot thank you enough for all that you have done to guide me through my PhD and develop me into who I am today.

In addition to my advisor, I would like to thank my qualifying exam and dissertation committee members: Professor James Davies, Professor Wenwan Zhong, Professor Jingsong Zhang, Professor Kelly Barsanti and Professor Ryan Julian. I would also like to thank Professor Ying-Hsuan Lin and Professor Roya Bahreini who regularly provided invaluable advice to improve my experiments, data analysis and scientific writing. I also wanted to thank Professor Roya Bahreini and Professor Ying-Hsuan Lin for providing

wonderful letters of recommendation over the years which have allowed me to be awarded several fellowships during my PhD.

I want to express my deep gratitude towards the Chemistry Department and Graduate Division at the University of California, Riverside for awarding me with several fellowships during my Ph.D. such as the Graduate Research Mentorship Program award, the Chemistry Advancing Faculty Diversity award, the Thomas H. Morton award and the Dissertation Completion Fellowship award. I will forever be grateful to have been awarded each one of these as they allowed me to fully focus on my research during the award period and will allow for countless more opportunities as I continue my career.

I am extremely thankful to all of my lab mates and collaborators: Dr. Zixu Zhao, Dr. Wen Zhang, Dr. Chuanyang Shen, Dr. Kunpeng Chen, Sean Murphy, Xiaoyan Yang, Dr. Linhui Tian, Michael Lum and Bradley Ries who all provided invaluable research discussions, were always available to help and enabled me to develop as a person and as a scientist. All of you made it a joy to come to the lab each day and have truly had a lifelong impact on me.

To my wife, Carlyn Mayorga, I am eternally grateful for all the love, support and patience that you have provided to me over the years. I truly would not have been able to pursue or obtain my PhD without you always being by my side. I love you with all my heart and I cannot wait to see what our next adventure in life will be together. To Carlyn's family, who have constantly supported me during my PhD, I am forever grateful to you.

To my parents, I will never be able to thank you enough for all that you have provided me. I could not have asked for better parents. You have instilled wonderful values in me and raised me to be the man that I am today. To my siblings and their spouses, I thank you for your constant love and support and I am forever grateful for the wonderful relationship that we have.

COPYRIGHT ACKNOWLEDGEMENTS

Figure 1.1 in Chapter 1 is reproduced with permission from Nature Reviews: Earth and Environment, **2022**, *3* (6), 363–379.

The text of this dissertation, in part or in full, is a reprint of the materials as they appear in the following publications:

Chapter 2: Mayorga, R. J**.**; Zhao, Z.; Zhang, H. Formation of secondary organic aerosol from nitrate radical oxidation of phenolic VOCs: Implications for nitration mechanisms and brown carbon formation, *Atmos. Environ.* **2021,** 224, 117910.

Chapter 3: Mayorga, R.; Xia, Y.; Zhao, Z.; Long, B.; Zhang, H. Peroxy Radical Autoxidation and Sequential Oxidation in Organic Nitrate Formation during Limonene Nighttime Oxidation. *Environ. Sci. Technol.* **2022**, *56* (22), 15337–15346.

Chapter 4: Mayorga, R.; Chen, K.; Raeofy, N.; Woods, M.; Lum, M.; Zhao, Z.; Zhang, W.; Bahreini, R.; Lin, Y.-H.; Zhang, H. Chemical Structure Regulates the Formation of Secondary Organic Aerosol and Brown Carbon in Nitrate Radical Oxidation of Pyrroles and Methylpyrroles. *Environ. Sci. Technol.* **2022**, *56* (12), 7761−7770.

ABSTRACT OF THE DISSERTATION

Investigating Nighttime Oxidation of Wildfire-Emitted VOCs: Implications for Oxidation Mechanisms, Secondary Organic Aerosol, and Brown Carbon Formation

by

Raphael Mayorga

Doctor of Philosophy, Graduate Program in Chemistry
University of California, Riverside, September 2024
Dr. Haofei Zhang, Chairperson

Wildfires have shown an increase in occurrence and severity in recent years. These biomass burning events release volatile organic compounds (VOCs) and particulate matter in the atmosphere which impact air quality, human health, and Earth's radiative balance. The oxidation of these wildfire-emitted VOCs at nighttime by the nitrate radical (NO_3) can lead to the formation of secondary organic aerosol (SOA) and light-absorbing brown carbon (BrC). Despite their significance, the understanding of NO_3-initiated oxidation mechanisms of wildfire-emitted VOCs leading to SOA and BrC in previous studies have been very limited. The major SOA constituents from these reactions have remained a challenge to uncover largely due to limitations in analytical techniques used to uncover the gas- and particle-phase chemical composition. In the following projects, we use a suite of analytical methods to elucidate the major reactions leading to the formation of SOA and BrC from representative wildfire-emitted VOCs. In Chapter 2, we studied the NO_3

oxidation of seven phenolic VOCs. From this study, we discovered many products that were previously undiscovered from this system and found nitrophenol products were very dominant adding to evidence that these are a major class of compounds responsible for significant light absorption in BrC. We also found evidence of diphenyl ether dimers forming from NO_3 oxidation of each of the studied phenolic VOCs. In Chapter 3, we investigated the NO_3 oxidation of limonene. From this project, we discovered that the primary nitrooxy peroxy radical formed from limonene can rapidly undergo autoxidation leading to highly oxidized organonitrates. We also identified the formation of several dinitrate compounds highlighting the importance of sequential oxidation for limonene. In Chapter 4, we investigated the NO_3 oxidation of selected N-containing heterocyclic VOCs: pyrrole, 1-methylpyrrole (1-MP) and 2-methylpyrrole (2-MP). From the observed product distribution in the SOA from these systems, we concluded that the presence of an easily abstractable hydrogen in precursor structure regulates the mechanism of initial NO_3 oxidation and has significant effect on light absorption of the SOA. Furthermore, we propose a novel gas-phase mechanism for the addition of three NO_2 groups to the backbone of pyrrole.

TABLE OF CONTENTS

LIST OF FIGURES

LIST OF TABLES

CHAPTER 1: Introduction

1.1 Background and Motivation

Volatile organic compounds (VOCs) are constantly emitted into the atmosphere from a variety of sources, such as biogenic and anthropogenic emissions and wildfires.[1,2] These VOCs undergo oxidation due to several major oxidants in the atmosphere and form secondary organic aerosol (SOA) which pose threats to air quality and the Earth's climate.[3] Oxidation of these VOCs at nighttime by nitrate radicals (NO_3) may represent a significant pathway of formation of SOA and light-absorbing brown carbon (BrC).[4] BrC is known by its characteristic brown color, visible in smog, and has been shown to have strong light-absorbing properties which ultimately lead to the warming of our planet.[5] Despite their significance, their formation pathways during nighttime oxidation have been understudied. To address this, the main objective of my research is to establish a detailed understanding of the nighttime oxidation mechanisms of key relevant VOCs leading to the formation of SOA and BrC.[6]

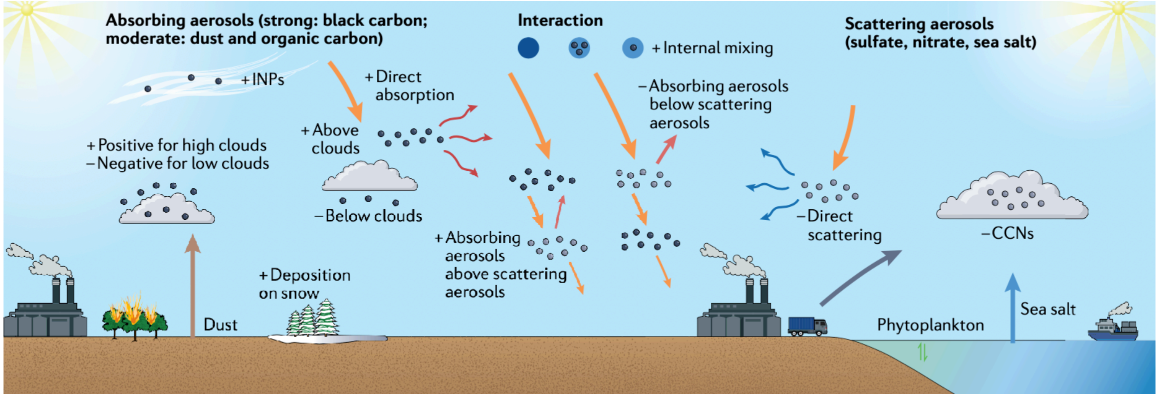

Figure 1.1 Schematic of radiative effects of absorbing (dark grey dots) and scattering aerosols (light grey dots), as well as their interactive effects. Scattering aerosols induce negative forcing (−) by directly reflecting sunlight and interacting with clouds; absorbing aerosols, in general, have a warming effect (+), although their interaction with clouds might produce slight cooling. The interaction between scattering and absorbing aerosols enhances the absorption and, thus, the warming effect. Light orange arrows represent incident sunlight; dark orange, scattered radiation by scattering aerosols; red, the radiation re-emitted by absorbing aerosols; and dark blue, scattered sunlight. CCN, cloud condensation nuclei; INPs, ice-nucleating particles. Reproduced with permission by Li, J. et al. (2022).[7] Copyright 2022 Li, J. et al.[7]

1.1.1 Light Absorption and Light Scattering of Aerosols

Based on the chemical and physical properties of aerosols, they can either scatter or absorb incoming sunlight which in turn can have cooling or warming effects on the earth's surface, respectively.[7–9] As shown in **Figure 1.1** from Li, J. et al, the effects of scattering and absorbing by aerosols on the climate are interactive and complex.[7] Aerosols can scatter incoming sunlight, leading to atmospheric cooling through negative radiative forcing. [8,10] Conversely, aerosols can also absorb incoming sunlight which induces positive radiative forcing and has a warming effect on the climate.[9,11,12] While absorption, like scattering, tends to reduce sunlight at the ground level, the enhanced atmospheric heating by absorbing aerosols eventually warms up the Earth's surface, and counteracts the cooling caused by scattering.

BrC is unique because it absorbs light strongly in the UV-visible range. Black carbon (BC) is emitted from high temperature combustion of inorganics and is highly light absorbing over wide range of wavelengths. The planetary radiative forcing of BrC is estimated to be 0.1-0.25 W m^{-2} and this is roughly 25% of the radiative forcing of BC.[13] Within the UV-visible range, BrC can be highly wavelength dependent with higher absorption typically observed at shorter wavelengths within the range.[14] The specific distribution of chromophores within BrC determines how the incoming sunlight is absorbed or scattered. Due to the strong effect of radiative forcing by BrC and the complex distribution of chromophores within BrC, it is critical to uncover the key mechanisms leading to the formation of BrC from wildfire-emitted VOCs.

1.1.2 Sources and Chemistry of Wildfire and Biogenic VOCs

Wildfires and prescribed burns occur regularly throughout the globe from a wide variety of fuels producing particulate matter, nitrogen oxides ($NO_x = NO + NO_2$) and VOCs.[15–17] In several studies performed during the last decade, the non-methane gas emissions from a variety of biomass burning sources were comprehensively identified and quantified.[1,2,18,19] From fuels native to the western united states, oxygenated aromatic compounds represent ~40-70% and heterocyclic VOCs represent ~10-20% of non-methane gas emissions.[2,20] Initial NO_3 oxidation of VOCs typically occurs through addition to the double bond or through hydrogen abstraction. The hydrogen abstraction mechanism has been proposed for many aromatic VOCs and may result in the formation of nitroaromatic compounds when NO_2 is present.[6,21–25] The nitroaromatics resulting from NO_3 oxidation of aromatic VOCs in the presence of NO_2 have been shown to be strongly light absorbing and major components of BrC.[21,23,24,26–29]

Biogenic VOCs (BVOCs), such as monoterpenes, are another major class of VOCs which are primarily emitted from plants. Monoterpenes ($C_{10}H_{16}$) are highly reactive with NO_3 mainly producing organic nitrates, which represent an important reservoir of atmospheric NO_x and are a key driver for SOA formation.[30–33] Initial NO_3 oxidation of monoterpenes occurs through addition to the double bond. Due to the formation of organic nitrates as well as highly oxidized molecules (HOMs) from NO_3 oxidation of limonene, substantial SOA yields have been reported.[34–37] Previous studies had observed the formation of HOMs from NO_3 oxidation of certain monoterpenes and proposed autoxidation reactions to be responsible for their formation.[38,39] However, the detailed autoxidation mechanisms and reaction rates remained unknown.

1.1.3 Initial Mechanism of Oxidation

During the daytime, the primary oxidant is the OH radical. The initial attack of OH to the backbone of a VOC is very similar to that of NO_3 proceeding either by addition to a double bond or by abstraction of a hydrogen. NO_x is also present during the daytime and nighttime at varying concentrations depending on how polluted the environment is. Nitroaromatics are well-known chromophores contributing significantly to BrC from aromatic precursors.[21,23,24,26–29] These compounds are strongly light absorbing due to the conjugation of double bonds within the aromatic ring and the presence of an electron-withdrawing group, NO_2, enhances this stability. Nitroaromatics can be formed through

OH or NO_3 oxidation, but typically require the first step of oxidation to be H-abstraction instead of addition to a double bond because the latter breaks the aromaticity.

1.1.4 Experimental Procedure and Analytical Instruments

In my research, I have used several types of atmospheric reactors which are each used to simulate chemical reactions occurring in the real atmosphere.[6,49] In the experiments, VOCs of interest are injected into the reactor at pre-calculated rates and NO_3 is formed by reacting O_3 with NO_2 inside the reactor or just before the reactor entrance. With our 1 L flowtube and 250 L continuous flow stirred tank reactor, we can carefully control oxidation conditions (VOC + O_3/NO_3) and peroxy radical pathways under steady state. A 10 m^3 smog chamber was used for the experiments in Chapter 4 and this reactor requires a single injection of VOC and oxidants as opposed to constant injection as is used in our continuous flow reactors.[50–54] During the experiments, a suite of online and offline analytical instruments were implemented to study the optical properties and chemical composition of the SOA.

Kinetic simulations were used throughout these projects to estimate VOC decay and NO_3 concentrations. iChamber in Igor Pro and the Framework for 0-D Atmospheric Modeling in MATLAB are Master Chemical Mechanism (MCM) based kinetic box models that we used. The MCM is a near-explicit library of gas-phase reactions (both organic and inorganic reactions) occurring in the troposphere including chemical structures, reaction rates and literature references. Direct measurements of NO_3 and VOC concentrations were unavailable for most of our experiments, so these kinetic box models were very useful. In our reactors we can monitor concentrations of NO_2 and O_3 using NO_x and O_3 analyzers.

Based on these initial concentrations and reactions rates of VOCs with various oxidants present in our reactors, the chemical box model allows for the estimation of oxidant and VOC concentrations in our reactors at any given time within the experiment. Comparison of our experimental results to model results can also allow for the proposal of new pathways in the mechanism if there is a significant gap observed between and model and experimental results.

The major SOA constituents of these reactions and the underlying mechanisms remain a challenge to uncover, largely due to the limitations in detection and identification of the particle-phase products. Most of the analytical instruments typically used are incapable of unambiguously characterizing the SOA constituents, especially on the isomer level. We use electrospray ionization coupled to an ion mobility spectrometry time-of-flight mass spectrometer (IMS-TOF) for offline analysis of the SOA from these experiments. Following ionization, the ions are introduced into a drift-tube and are met with a counterflow of nitrogen gas which serves to slow down some ions based on their size and conformation, and they are given a specific drift time. The IMS-TOF allows for separation, characterization, and sometimes, identification of structural isomers.

1.2 Aims and Scope of Dissertation

The primary aims of this dissertation are to: 1) elucidate NO_3 oxidation of the major wildfire-emitted VOCs including the phenolic and heterocyclic VOCs that lead to BrC formation and 2) examine the synergistic role of O_3 and NO_3 in the nighttime oxidation of limonene and investigate how sequential oxidation and fate of RO_2 affect the observed gas-and particle-phase product distributions. Our variety of custom-made atmospheric simulation reactors allow us to carefully control oxidant and VOC concentrations as well as environmental conditions. The suite of online and offline analytical instruments which we use allow us to characterize the optical properties and chemical composition of SOA and BrC and provide mechanistic insight into how the chemical composition changes through SOA formation and aging. With the combined investigation of optical properties and chemical composition, we can gain key insights into the specific chromophores which contribute significantly to BrC. Through this, we can fill the knowledge gaps and expand the mechanistic understandings of these systems and provide significant insight into the characteristics of chromophores that contribute to their light absorption.

In Chapter 2, we studied the NO_3 oxidation of seven phenolic VOCs. Phenolic VOCs are substantially emitted from wildfires, but the formation of SOA and BrC from the NO_3 oxidation of phenolic VOCs was understudied. In this study, our use of IMS-TOF was fundamental in the separation of isomers in observed products. From this study, we discovered many products that were previously undiscovered from this system: 1) nitrophenol products with additional hydroxyl groups, 2) non-aromatic ring-opening products, 3) the formation of C_7 products from C_6 precursors and 4) nitrated diphenyl ether dimers. These newly identified products may contribute significantly to SOA. We found nitrophenol products were very dominant adding to evidence that these are a major class of compounds responsible for significant light absorption in BrC. These new products were also identified in ambient samples collected during biomass burning events, underlining their atmospheric relevance.

In Chapter 3, we investigate the NO_3 oxidation of limonene. Limonene is a very significant monoterpene emitted from citrus plants and from wildfires, but the SOA formation and gas-phase NO_3 oxidation from limonene were largely understudied. In this project, we combined our experimental results with kinetic simulations and quantum chemical calculations from collaborators. From this project, we observed several different highly oxidized organonitrates forming within a short timescale. We discovered that the primary nitrooxy peroxy radical formed from limonene NO_3 oxidation can rapidly undergo autoxidation through two pathways leading to highly oxidized organonitrates. Limonene has two double bonds and can therefore undergo sequential NO_3 oxidation of each of the double bonds. We also observed highly oxidized dinitrates highlighting the importance of sequential oxidation in the nighttime oxidation of limonene. The same organonitrates were also observed in ambient samples collected during biomass burning and during the nighttime in the southeastern United States.

In Chapter 4, we investigated the NO_3 oxidation of a few N-containing heterocyclic VOCs: pyrrole, 1-methylpyrrole (1-MP) and 2-methylpyrrole (2-MP). These three compounds are close in chemical structure and the goal of this study was to determine the effects of VOC precursor structure on SOA and BrC formation. In the SOA from pyrrole and 2-MP, the most dominant products were dinitro- and trinitro-products. From 1-MP, dominant products were mostly organonitrates. Analysis of the optical properties from these systems revealed that the SOA from pyrrole and 2-MP were strongly light absorbing and the SOA from 1-MP were mostly light scattering. From the observed product distribution in the SOA from these systems, we concluded that the presence of an easily abstractable hydrogen controls the mechanism of initial NO_3 oxidation and has significant effect on light absorption of the SOA. We also proposed a mechanism involving hydrogen abstraction, followed by radical shift and addition of NO_2 for the formation of dinitropyrrole and trinitropyrrole from NO_3 oxidation. For 1-MP, we propose that with the absence of an easily abstractable hydrogen, NO_3 addition to the double bond leading to the formation of organonitrates dominates the initial NO_3 oxidation. Furthermore, we underscore the importance of including pyrrole and methylpyrroles in air quality models by estimating that the total SOA mass and light absorption from pyrrole and 2-MP are comparable to those from phenolic VOCs from NO_3 oxidation.

1.3 References

(1) Hatch, L. E.; Luo, W.; Pankow, J. F.; Yokelson, R. J.; Stockwell, C. E.; Barsanti, K. C. Identification and Quantification of Gaseous Organic Compounds Emitted from Biomass Burning Using Two-Dimensional Gas Chromatography–Time-of-Flight Mass Spectrometry. *Atmos. Chem. Phys.* **2015**, *15* (4), 1865–1899.

(2) Hatch, L. E.; Yokelson, R. J.; Stockwell, C. E.; Veres, P. R.; Simpson, I. J.; Blake, D. R.; Orlando, J. J.; Barsanti, K. C. Multi-Instrument Comparison and Compilation of Non-Methane Organic Gas Emissions from Biomass Burning and Implications for Smoke-Derived Secondary Organic Aerosol Precursors. *Atmos. Chem. Phys.* **2017**, *17* (2), 1471–1489.

(3) Hobbs, P. V. Direct Radiative Forcing by Smoke from Biomass Burning. *Science* **1997**, *275* (5307), 1777–1778.

(4) Rollins, A. W.; Browne, E. C.; Min, K.-E.; Pusede, S. E.; Wooldridge, P. J.; Gentner, D. R.; Goldstein, A. H.; Liu, S.; Day, D. A.; Russell, L. M.; Cohen, R. C. Evidence for NO_x Control over Nighttime SOA Formation. *Science* **2012**, *337* (6099), 1210–1212.

(5) Laskin, A.; Laskin, J.; Nizkorodov, S. A. Chemistry of Atmospheric Brown Carbon. *Chem. Rev.* **2015**, *115* (10), 4335–4382.

(6) Mayorga, R. J.; Zhao, Z.; Zhang, H. Formation of Secondary Organic Aerosol from Nitrate Radical Oxidation of Phenolic VOCs: Implications for Nitration Mechanisms and Brown Carbon Formation. *Atmos. Environ.* **2021**, *244*, 117910.

(7) Li, J.; Carlson, B. E.; Yung, Y. L.; Lv, D.; Hansen, J.; Penner, J. E.; Liao, H.; Ramaswamy, V.; Kahn, R. A.; Zhang, P.; Dubovik, O.; Ding, A.; Lacis, A. A.; Zhang, L.; Dong, Y. Scattering and Absorbing Aerosols in the Climate System. *Nat Rev Earth Environ* **2022**, *3* (6), 363–379.

(8) Li, Z.; Kou, L. The Direct Radiative Effect of Smoke Aerosols on Atmospheric Absorption of Visible Sunlight. *Tellus B: Chemical and Physical Meteorology* **1998**, *50* (5), 543.

(9) Lu, Z.; Streets, D. G.; Winijkul, E.; Yan, F.; Chen, Y.; Bond, T. C.; Feng, Y.; Dubey, M. K.; Liu, S.; Pinto, J. P.; Carmichael, G. R. Light Absorption Properties and Radiative Effects of Primary Organic Aerosol Emissions. *Environ. Sci. Technol.* **2015**, *49* (8), 4868–4877.

(10) Crisp, D. Absorption of Sunlight by Water Vapor in Cloudy Conditions: A Partial Explanation for the Cloud Absorption Anomaly. *Geophysical Research Letters* **1997**, *24* (5), 571–574.

(11) Lee, H. J.; Aiona, P. K.; Laskin, A.; Laskin, J.; Nizkorodov, S. A. Effect of Solar Radiation on the Optical Properties and Molecular Composition of Laboratory Proxies of Atmospheric Brown Carbon. *Environ. Sci. Technol.* **2014**, *48* (17), 10217–10226.

(12) Kasthuriarachchi, N. Y.; Rivellini, L.-H.; Adam, M. G.; Lee, A. K. Y. Light Absorbing Properties of Primary and Secondary Brown Carbon in a Tropical Urban Environment. *Environ. Sci. Technol.* **2020**, *54* (17), 10808–10819.

(13) Feng, S.; Fu, Q. Expansion of Global Drylands Under a Warming Climate. *Atmos. Chem. Phys.* **2013**, *13* (19), 10081-10094.

(14) Bahadur, R.; Praveen, P. S.; Xu, Y.; Ramanathan, V. Solar Absorption by Elemental and Brown Carbon Determined from Spectral Observations. *Proc. Natl. Acad. Sci.* **2012**, *109* (43), 17366-17371.

(15) Van Der Werf, G. R.; Randerson, J. T.; Giglio, L.; Collatz, G. J.; Mu, M.; Kasibhatla, P. S.; Morton, D. C.; DeFries, R. S.; Jin, Y.; Van Leeuwen, T. T. Global Fire Emissions and the Contribution of Deforestation, Savanna, Forest, Agricultural, and Peat Fires (1997–2009). *Atmos. Chem. Phys.* **2010**, *10* (23), 11707–11735.

(16) Andreae, M. O.; Merlet, P. Emission of Trace Gases and Aerosols from Biomass Burning. *Global Biogeochemical Cycles* **2001**, *15* (4), 955–966.

(17) Yokelson, R. J.; Burling, I. R.; Gilman, J. B.; Warneke, C.; Stockwell, C. E.; De Gouw, J.; Akagi, S. K.; Urbanski, S. P.; Veres, P.; Roberts, J. M.; Kuster, W. C.; Reardon, J.; Griffith, D. W. T.; Johnson, T. J.; Hosseini, S.; Miller, J. W.; Cocker Iii, D. R.; Jung, H.; Weise, D. R. Coupling Field and Laboratory Measurements to Estimate the Emission Factors of Identified and Unidentified Trace Gases for Prescribed Fires. *Atmos. Chem. Phys.* **2013**, *13* (1), 89–116.

(18) Oros, D. R.; Simoneit, B. R. T. Identification and Emission Factors of Molecular Tracers in Organic Aerosols from Biomass Burning Part 1. Temperate Climate Conifers. *Applied Geochemistry* **2001**, *16* (13), 1513–1544.

(19) Fine, P. M.; Cass, G. R.; Simoneit, B. R. T. Chemical Characterization of Fine Particle Emissions from the Fireplace Combustion of Wood Types Grown in the Midwestern and Western United States. *Environmental Engineering Science* **2004**, *21* (3), 387–409.

(20) Palm, B. B.; Peng, Q.; Fredrickson, C. D.; Lee, B. H.; Garofalo, L. A.; Pothier, M. A.; Kreidenweis, S. M.; Farmer, D. K.; Pokhrel, R. P.; Shen, Y.; Murphy, S. M.; Permar, W.; Hu, L.; Campos, T. L.; Hall, S. R.; Ullmann, K.; Zhang, X.; Flocke, F.; Fischer, E. V.; Thornton, J. A. Quantification of Organic Aerosol and Brown Carbon

Evolution in Fresh Wildfire Plumes. *Proc. Natl. Acad. Sci. U.S.A.* **2020**, *117* (47), 29469–29477.

(21) Finewax, Z.; de Gouw, J. A.; Ziemann, P. J. Identification and Quantification of 4-Nitrocatechol Formed from OH and NO3 Radical-Initiated Reactions of Catechol in Air in the Presence of NO_x: Implications for Secondary Organic Aerosol Formation from Biomass Burning. *Environ. Sci. Technol.* **2018**, *52* (4), 1981–1989.

(22) Finewax, Z.; de Gouw, J. A.; Ziemann, P. J. Products and Secondary Organic Aerosol Yields from the OH and NO_3 Radical-Initiated Oxidation of Resorcinol. *ACS Earth Space Chem.* **2019**, *3* (7), 1248–1259.

(23) Vidović, K.; Lašič Jurković, D.; Šala, M.; Kroflič, A.; Grgić, I. Nighttime Aqueous-Phase Formation of Nitrocatechols in the Atmospheric Condensed Phase. *Environ. Sci. Technol.* **2018**, *52* (17), 9722–9730.

(24) Bolzacchini, E.; Bruschi, M.; Hjorth, J.; Meinardi, S.; Orlandi, M.; Rindone, B.; Rosenbohm, E. Gas-Phase Reaction of Phenol with NO_3. *Environ. Sci. Technol.* **2001**, *35* (9), 1791–1797.

(25) Kroflič, A.; Grilc, M.; Grgić, I. Unraveling Pathways of Guaiacol Nitration in Atmospheric Waters: Nitrite, A Source of Reactive Nitronium Ion in the Atmosphere. *Environ. Sci. Technol.* **2015**, *49* (15), 9150–9158.

(26) Vidović, K.; Kroflič, A.; Šala, M.; Grgić, I. Aqueous-Phase Brown Carbon Formation from Aromatic Precursors under Sunlight Conditions. *Atmosphere* **2020**, *11* (2), 131.

(27) Frka, S.; Šala, M.; Kroflič, A.; Huš, M.; Čusak, A.; Grgić, I. Quantum Chemical Calculations Resolved Identification of Methylnitrocatechols in Atmospheric Aerosols. *Environ. Sci. Technol.* **2016**, *50* (11), 5526–5535.

(28) Kitanovski, Z.; Čusak, A.; Grgić, I.; Claeys, M. Chemical Characterization of the Main Products Formed through Aqueous-Phase Photonitration of Guaiacol. *Atmos. Meas. Tech.* **2014**, *7* (8), 2457–2470.

(29) Yuan, B.; Liggio, J.; Wentzell, J.; Li, S.-M.; Stark, H.; Roberts, J. M.; Gilman, J.; Lerner, B.; Warneke, C.; Li, R.; Leithead, A.; Osthoff, H. D.; Wild, R.; Brown, S. S.; de Gouw, J. A. Secondary Formation of Nitrated Phenols: Insights from Observations during the Uintah Basin Winter Ozone Study (UBWOS) 2014. *Atmos. Chem. Phys.* **2016**, *16* (4), 2139–2153.

(30) Brown, S. S.; Stutz, J. Nighttime Radical Observations and Chemistry. *Chem. Soc. Rev.* **2012**, *41* (19), 6405.

(31) Perring, A. E.; Pusede, S. E.; Cohen, R. C. An Observational Perspective on the Atmospheric Impacts of Alkyl and Multifunctional Nitrates on Ozone and Secondary Organic Aerosol. *Chem. Rev.* **2013**, *113* (8), 5848–5870.

(32) Kiendler-Scharr, A.; Mensah, A. A.; Friese, E.; Topping, D.; Nemitz, E.; Prevot, A. S. H.; Äijälä, M.; Allan, J.; Canonaco, F.; Canagaratna, M.; Carbone, S.; Crippa, M.; Dall Osto, M.; Day, D. A.; De Carlo, P.; Di Marco, C. F.; Elbern, H.; Eriksson, A.; Freney, E.; Hao, L.; Herrmann, H.; Hildebrandt, L.; Hillamo, R.; Jimenez, J. L.; Laaksonen, A.; McFiggans, G.; Mohr, C.; O'Dowd, C.; Otjes, R.; Ovadnevaite, J.; Pandis, S. N.; Poulain, L.; Schlag, P.; Sellegri, K.; Swietlicki, E.; Tiitta, P.; Vermeulen, A.; Wahner, A.; Worsnop, D.; Wu, H. -C. Ubiquity of Organic Nitrates from Nighttime Chemistry in the European Submicron Aerosol. *Geophys. Res. Lett.* **2016**, *43* (14), 7735–7744.

(33) Ng, N. L.; Brown, S. S.; Archibald, A. T.; Atlas, E.; Cohen, R. C.; Crowley, J. N.; Day, D. A.; Donahue, N. M.; Fry, J. L.; Fuchs, H.; Griffin, R. J.; Guzman, M. I.; Herrmann, H.; Hodzic, A.; Iinuma, Y.; Jimenez, J. L.; Kiendler-Scharr, A.; Lee, B. H.; Luecken, D. J.; Mao, J.; McLaren, R.; Mutzel, A.; Osthoff, H. D.; Ouyang, B.; Picquet-Varrault, B.; Platt, U.; Pye, H. O. T.; Rudich, Y.; Schwantes, R. H.; Shiraiwa, M.; Stutz, J.; Thornton, J. A.; Tilgner, A.; Williams, B. J.; Zaveri, R. A. Nitrate Radicals and Biogenic Volatile Organic Compounds: Oxidation, Mechanisms, and Organic Aerosol. *Atmos. Chem. Phys.* **2017**, *17* (3), 2103–2162.

(34) Fry, J. L.; Draper, D. C.; Barsanti, K. C.; Smith, J. N.; Ortega, J.; Winkler, P. M.; Lawler, M. J.; Brown, S. S.; Edwards, P. M.; Cohen, R. C.; Lee, L. Secondary Organic Aerosol Formation and Organic Nitrate Yield from NO_3 Oxidation of Biogenic Hydrocarbons. *Environ. Sci. Technol.* **2014**, *48* (20), 11944–11953.

(35) Fry, J. L.; Kiendler-Scharr, A.; Rollins, A. W.; Brauers, T.; Brown, S. S.; Dorn, H.-P.; Dubé, W. P.; Fuchs, H.; Mensah, A.; Rohrer, F.; Tillmann, R.; Wahner, A.; Wooldridge, P. J.; Cohen, R. C. SOA from Limonene: Role of NO_3 in Its Generation and Degradation. *Atmos. Chem. Phys.* **2011**, *11* (8), 3879–3894.

(36) Spittler, M.; Barnes, I.; Bejan, I.; Brockmann, K. J.; Benter, Th.; Wirtz, K. Reactions of NO_3 Radicals with Limonene and α-Pinene: Product and SOA Formation. *Atmospheric Environment* **2006**, *40*, 116–127.

(37) Hallquist, M.; Wängberg, I.; Ljungström, E.; Barnes, I.; Becker, K.-H. Aerosol and Product Yields from NO_3 Radical-Initiated Oxidation of Selected Monoterpenes. *Environ. Sci. Technol.* **1999**, *33* (4), 553–559.

(38) Guo, Y.; Shen, H.; Pullinen, I.; Luo, H.; Kang, S.; Vereecken, L.; Fuchs, H.; Hallquist, M.; Acir, I.-H.; Tillmann, R.; Rohrer, F.; Wildt, J.; Kiendler-Scharr, A.; Wahner, A.; Zhao, D.; Mentel, T. F. Identification of Highly Oxygenated Organic Molecules and

Their Role in Aerosol Formation in the Reaction of Limonene with Nitrate Radical. *Atmos. Chem. Phys.* **2022**, *22*, 11323–11346.

(39) Draper, D. C.; Myllys, N.; Hyttinen, N.; Møller, K. H.; Kjaergaard, H. G.; Fry, J. L.; Smith, J. N.; Kurtén, T. Formation of Highly Oxidized Molecules from NO_3 Radical Initiated Oxidation of Δ-3-Carene: A Mechanistic Study. *ACS Earth Space Chem.* **2019**, *3* (8), 1460–1470.

(40) Decker, Z. C. J.; Robinson, M. A.; Barsanti, K. C.; Bourgeois, I.; Coggon, M. M.; DiGangi, J. P.; Diskin, G. S.; Flocke, F. M.; Franchin, A.; Fredrickson, C. D.; Gkatzelis, G. I.; Hall, S. R.; Halliday, H.; Holmes, C. D.; Huey, L. G.; Lee, Y. R.; Lindaas, J.; Middlebrook, A. M.; Montzka, D. D.; Moore, R.; Neuman, J. A.; Nowak, J. B.; Palm, B. B.; Peischl, J.; Piel, F.; Rickly, P. S.; Rollins, A. W.; Ryerson, T. B.; Schwantes, R. H.; Sekimoto, K.; Thornhill, L.; Thornton, J. A.; Tyndall, G. S.; Ullmann, K.; Van Rooy, P.; Veres, P. R.; Warneke, C.; Washenfelder, R. A.; Weinheimer, A. J.; Wiggins, E.; Winstead, E.; Wisthaler, A.; Womack, C.; Brown, S. S. Nighttime and Daytime Dark Oxidation Chemistry in Wildfire Plumes: An Observation and Model Analysis of FIREX-AQ Aircraft Data. *Atmos. Chem. Phys.* **2021**, *21* (21), 16293–16317.

(41) Bluvshtein, N.; Lin, P.; Flores, J. M.; Segev, L.; Mazar, Y.; Tas, E.; Snider, G.; Weagle, C.; Brown, S. S.; Laskin, A.; Rudich, Y. Broadband Optical Properties of Biomass-Burning Aerosol and Identification of Brown Carbon Chromophores: OPTICAL AND CHEMICAL PROPERTIES OF BROWN CARBON AEROSOLS. *J. Geophys. Res. Atmos.* **2017**, *122* (10), 5441–5456.

(42) Selimovic, V.; Yokelson, R. J.; McMeeking, G. R.; Coefield, S. In Situ Measurements of Trace Gases, PM, and Aerosol Optical Properties during the 2017 NW US Wildfire Smoke Event. *Atmos. Chem. Phys.* **2019**, *19* (6), 3905–3926.

(43) Sumlin, B. J.; Pandey, A.; Walker, M. J.; Pattison, R. S.; Williams, B. J.; Chakrabarty, R. K. Atmospheric Photooxidation Diminishes Light Absorption by Primary Brown Carbon Aerosol from Biomass Burning. *Environ. Sci. Technol. Lett.* **2017**, *4* (12), 540–545.

(44) Forrister, H.; Liu, J.; Scheuer, E.; Dibb, J.; Ziemba, L.; Thornhill, K. L.; Anderson, B.; Diskin, G.; Perring, A. E.; Schwarz, J. P.; Campuzano-Jost, P.; Day, D. A.; Palm, B. B.; Jimenez, J. L.; Nenes, A.; Weber, R. J. Evolution of Brown Carbon in Wildfire Plumes. *Geophysical Research Letters* **2015**, *42* (11), 4623–4630.

(45) Schnitzler, E. G.; Liu, T.; Hems, R. F.; Abbatt, J. P. D. Emerging Investigator Series: Heterogeneous OH Oxidation of Primary Brown Carbon Aerosol: Effects of Relative Humidity and Volatility. *Environ. Sci.: Processes Impacts* **2020**, 10.1039.D0EM00311E.

(46) Li, C.; He, Q.; Schade, J.; Passig, J.; Zimmermann, R.; Meidan, D.; Laskin, A.; Rudich, Y. Dynamic Changes in Optical and Chemical Properties of Tar Ball Aerosols by Atmospheric Photochemical Aging. *Atmos. Chem. Phys.* **2019**, *19* (1), 139–163.

(47) Li, C.; He, Q.; Hettiyadura, A. P. S.; Käfer, U.; Shmul, G.; Meidan, D.; Zimmermann, R.; Brown, S. S.; George, C.; Laskin, A.; Rudich, Y. Formation of Secondary Brown Carbon in Biomass Burning Aerosol Proxies through NO_3 Radical Reactions. *Environ. Sci. Technol.* **2020**, *54* (3), 1395–1405.

(48) Lin, P.; Bluvshtein, N.; Rudich, Y.; Nizkorodov, S. A.; Laskin, J.; Laskin, A. Molecular Chemistry of Atmospheric Brown Carbon Inferred from a Nationwide Biomass Burning Event. *Environ. Sci. Technol.* **2017**, *51* (20), 11561–11570.

(49) Mayorga, R.; Xia, Y.; Zhao, Z.; Long, B.; Zhang, H. Peroxy Radical Autoxidation and Sequential Oxidation in Organic Nitrate Formation during Limonene Nighttime Oxidation. *Environ. Sci. Technol.* **2022**, *56* (22), 15337–15346.

(50) Chu, B.; Chen, T.; Liu, Y.; Ma, Q.; Mu, Y.; Wang, Y.; Ma, J.; Zhang, P.; Liu, J.; Liu, C.; Gui, H.; Hu, R.; Hu, B.; Wang, X.; Wang, Y.; Liu, J.; Xie, P.; Chen, J.; Liu, Q.; Jiang, J.; Li, J.; He, K.; Liu, W.; Jiang, G.; Hao, J.; He, H. Application of Smog Chambers in Atmospheric Process Studies. *National Science Review* **2022**, *9* (2), nwab103.

(51) Chen, K.; Raeofy, N.; Lum, M.; Mayorga, R.; Woods, M.; Bahreini, R.; Zhang, H.; Lin, Y.-H. Solvent Effects on Chemical Composition and Optical Properties of Extracted Secondary Brown Carbon Constituents. *Aerosol Science and Technology* **2022**, *56* (10), 917–930.

(52) Chen, K.; Mayorga, R.; Raeofy, N.; Lum, M.; Woods, M.; Bahreini, R.; Zhang, H.; Lin, Y.-H. Effects of Nitrate Radical Levels and Pre-Existing Particles on Secondary Brown Carbon Formation from Nighttime Oxidation of Furan. *ACS Earth Space Chem.* **2022**, *6* (11), 2709–2721.

(53) Chen, K.; Mayorga, R.; Hamilton, C.; Bahreini, R.; Zhang, H.; Lin, Y.-H. Contribution of Carbonyl Chromophores in Secondary Brown Carbon from Nighttime Oxidation of Unsaturated Heterocyclic Volatile Organic Compounds. *Environ. Sci. Technol.* **2023**, *57* (48), 20085–20096.

(54) Chen, K.; Hamilton, C.; Ries, B.; Lum, M.; Mayorga, R.; Tian, L.; Bahreini, R.; Zhang, H.; Lin, Y.-H. Relative Humidity Modulates the Physicochemical Processing of Secondary Brown Carbon Formation from Nighttime Oxidation of Furan and Pyrrole. *ACS EST Air* **2024**, *1* (5), 426–437.

CHAPTER 2: Formation of Secondary Organic Aerosol from Nitrate Radical Oxidation of Phenolic VOCs: Implications for Nitration Mechanisms and Brown Carbon Formation

2.1 Introduction

Wildfires are becoming increasingly severe globally and biomass burning events have been shown to strongly influence tropospheric chemistry, the climate, and human health.[1,2] Namely, volatile organic compounds (VOCs) and nitrogen oxides (NO_x) emitted from biomass burning undergo various oxidation reactions in the troposphere, substantially impacting the tropospheric ozone (O_3) budget.[3] Further, secondary organic aerosols (SOA) from these oxidation reactions can affect the Earth's radiative balance by scattering and absorbing solar radiation in the troposphere.[4] Phenolic derivatives have been shown to make up an important portion of the VOC emissions during biomass burning events.[5] They are also key intermediates from photooxidation of aromatic hydrocarbons (also abundant from biomass burning emissions) in the atmosphere.[6] The major phenolic VOCs have total emission factors ranging from 0.10 to 0.64 g kg^{-1} from the combustion of fuels native to the western United States.[5,7,8] Moreover, their SOA formation potential is among the highest due to their relatively large SOA yields.[9] These SOA are often found to be light absorbing (i.e., forming brown carbon, BrC), which further enhance their climate impacts.[10–12]

There have been extensive studies on the oxidation of phenolic VOCs and most of them have focused on hydroxyl radical (OH) oxidation [13–21]. In these studies, phenolic VOCs such as phenol, catechol, 3-methylcatechol (3MC), 4-methylcatechol (4MC), and guaiacol have been shown to produce SOA in high yields ranging from 25-145% from OH-initiated chemistry.[14,17,19–24] The OH-oxidation of phenolic VOCs in the presence of nitrogen oxides (NO_x) were also found to produce large amounts of BrC, due to the substantial formation of nitrophenol products.[10–12,25,26] These products, such as nitrophenols and nitrocatechols, have been reported from laboratory studies and field measurements.[10–12,14,25,26] The phenolic VOCs could also be oxidized by nitrate radicals ($NO_3\cdot$) which, however, has been understudied. The $NO_3\cdot$ oxidation could be an important reaction pathway of phenolic VOCs during nighttime, relevant to both biomass burning events and urban atmosphere.[27] BrC formation has also been recently reported during $NO_3\cdot$ oxidation of tar aerosols from wood pyrolysis which largely contain phenolic compounds.[28] Despite their significance, the understanding of $NO_3\cdot$ oxidation mechanisms of individual phenolic VOCs and the SOA formation in prior studies have been very limited. Often, nitro-phenolic compounds were the only major products reported in the SOA composition.[14,21,29–33] Other products such as those with additional functional groups and oligomers have not been systematically examined, despite that such low-volatility compounds could be important SOA constituents under ambient conditions. It is unclear whether and to what extent these types of products form during $NO_3\cdot$ oxidation of phenolic VOCs.

The major SOA constituents of these reactions and the underlying mechanisms remain a challenge to uncover, largely due to the limitations in detection and identification of the particle-phase products. Previously, a variety of analytical techniques have been implemented to characterize the phenolic VOC-derived SOA such as gas chromatography mass spectrometry (GC-MS), liquid chromatography mass spectrometry (LC-MS), chemical ionization mass spectrometry (CIMS), Fourier transform infrared spectroscopy (FTIR), and UV-Vis diode array detectors.[14,15,28–34] However, most of the instruments listed are incapable of unambiguously characterizing the SOA constituents, especially on the isomer level. In this study, we performed $NO_3\cdot$ oxidation experiments in a continuous flow stirred tank reactor (CFSTR) of five phenolic VOCs, including phenol, catechol, 3MC, 4MC, and guaiacol (structures shown in **Figure 2.1**). We use electrospray ionization (ESI) coupled to an ion mobility spectrometry time-of-flight mass spectrometer (IMS-TOF) for offline analysis of the SOA from these experiments. The IMS-TOF allows for separation, characterization, and sometimes, identification of structural isomers. Additionally, a UV-Vis spectrometer is utilized for analysis of the light absorption of the SOA materials. With these analytical instruments, we comprehensively identify the major products from these reactions and the underlying mechanisms as well as characterize their optical properties.

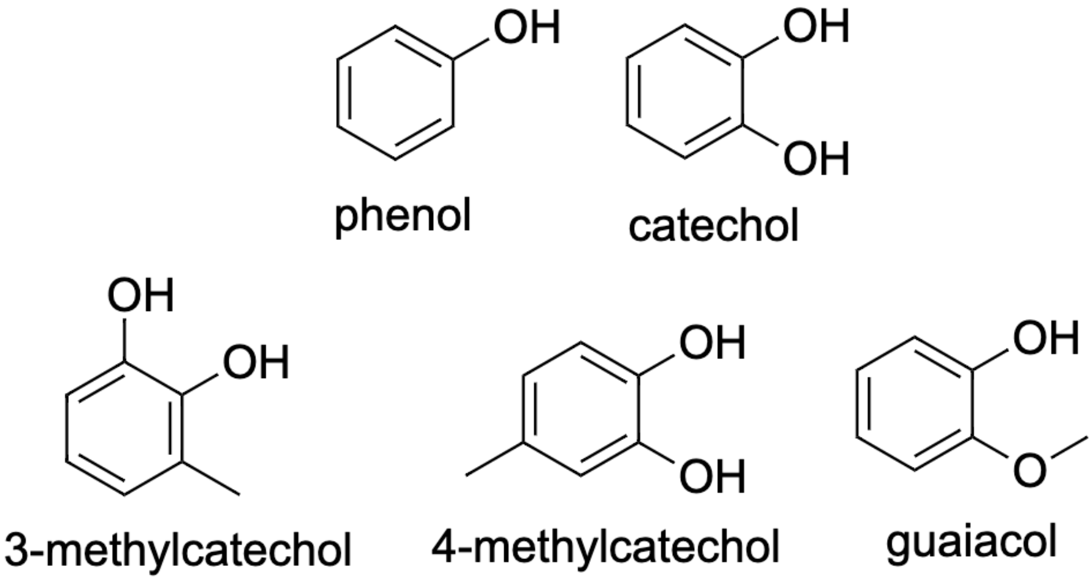

Figure 2.1 Chemical structures of the phenolic derivatives under study.

2.2 Experimental methods

2.2.1 Chemicals and reagents

The chemicals and reagents used in the present study and their purities and suppliers are as follows: phenol (99.5%, Sigma-Aldrich), guaiacol (≥98%, Aldon Corporation), catechol (>99%, Tokyo Chemical Industry), 3-methylcatechol (3MC, 95%, Combi Blocks), 4-methylcatechol (4MC, 98%, Frontier Scientific), 2-nitrophenol (2NP, 98%, Tokyo Chemical Industry), 3-nitrophenol (3NP, >98%, Tokyo Chemical Industry), 4-nitrophenol (4NP, >99%, Tokyo Chemical Industry), 4-nitrocatechol (4NC, 97%, Fischer Scientific), sodium chloride (99.5%, Sigma-Aldrich), methanol (HPLC Grade Fischer Chemical), acetonitrile (HPLC Grade Fischer Chemical), and deionized (DI) water (18MΩ , purified using a Milli-Q water system). All reagents and solvents were used without further purification.

2.2.2 Laboratory experiments

SOA was generated from oxidation of the five above-mentioned phenolic VOCs with NO_3· in a custom-made CFSTR (effective volume of 250 L, stainless steel enclosure with interior coating by Teflon PFA). The CFSTR setup is illustrated in **Figure 2.2**. The total flow rate of the CFSTR was approximately 4.1 L min^{-1} and the residence time in the CFSTR was approximately one hour. A clean air generator (Aadco Instruments, Inc., 747-30) was used to provide a constant flow of clean dry air at 2.5 L min^{-1} and humidified air at 1.0 L min^{-1} by bubbling dry air through DI water. The RH in the CFSTR stabilized at 35-40% for all experiments. This RH level is relevant to that observed at nighttime in the western US during summer seasons when biomass burning has a high frequency.[33] NaCl seed aerosols were generated by a constant output atomizer (TSI) and introduced into the CFSTR at ~ 0.6 L min^{-1} without upstream drying. Nevertheless, the RH in the CFSTR is maintained below the efflorescence RH of NaCl (45 – 55%) and thus the seed aerosols were dry throughout the experiments,[35] to minimize reactive uptakes of NO_3· and N_2O_5 and avoid aqueous-phase chemistry.[36–40] The size distribution and number concentration of SOA in the CFSTR were measured using a scanning electric mobility scanner (SEMS, Brechtel Inc., 2100) and a mixing condensation particle counter (MCPC, Brechtel Inc., 1720), respectively. The background particle concentrations in the CFSTR were very low (< 0.1 μm^3 cm^{-3}) before the experiments started. Once seed aerosol was injected, particle volume concentration was allowed to equilibrate to approximately 30 – 40 μm^3 cm^{-3} before oxidation started. The seed aerosols were used to enhance the partitioning of gas-phase semi-volatile products to the particle phase rather than loss to the walls. Each phenolic

VOC of interest was injected into the CFSTR a few hours before the experiments using a syringe pump (Chemyx Inc.) at pre-calculated rates to allow the concentration of the VOC in the reactor to stabilize at approximately 100 ppb, estimated based on the law of mass conservation. Most of the VOCs (except for guaiacol) investigated are solid at room temperature and hence were dissolved in methanol before being added into the syringe. The methanol concentrations in the CFSTR were estimated to be ~ 4 ppm. It was not expected to be involved in the oxidation chemistry, except to scavenge the negligible amount of produced OH. $NO_3\cdot$ was produced by reacting O_3 with nitrogen dioxide (NO_2) in the CFSTR. O_3 was generated by passing O_2 gas through an ozone generator (Ozone solution Inc.) at ~500 – 620 ppb. NO_2 was supplied directly from a gas cylinder of NO_2 (20 ppm in N_2, Airgas Inc.) at 50 cm^3 min^{-1}, indicative of an injection concentration of ~250 ppb. The concentrations of O_3 and NO_2 were measured using a 49C O_3 (Thermo Environmental Instruments) and a 42C NO-NO_2-NO_x analyzer (Thermo Environmental Instruments), respectively.[41] We apply the injection rates of VOCs, O_3, and NO_2, as well as the measured steady-state concentrations of O_3 and NO_x in a MCM-based kinetic model to estimate the concentrations of VOCs and $NO_3\cdot$ under steady state.[6] Once the formed SOA, O_3 and NO_x concentrations approximately reached steady state, sample collection was commenced using a sequential spot sampler (Aerosol Devices Inc.) at 1.6 L min^{-1} for 2 hours. After collection, the sample was immediately extracted into 60 µL acetonitrile with 0.1 mM NaCl for analysis by the IMS-TOF. At this time, another sample collection was begun using the spot sampler again at 1.6 L min^{-1} for another 2 hours. This sample was immediately extracted into 500 μL methanol for analysis with a UV-Vis spectrophotometer.

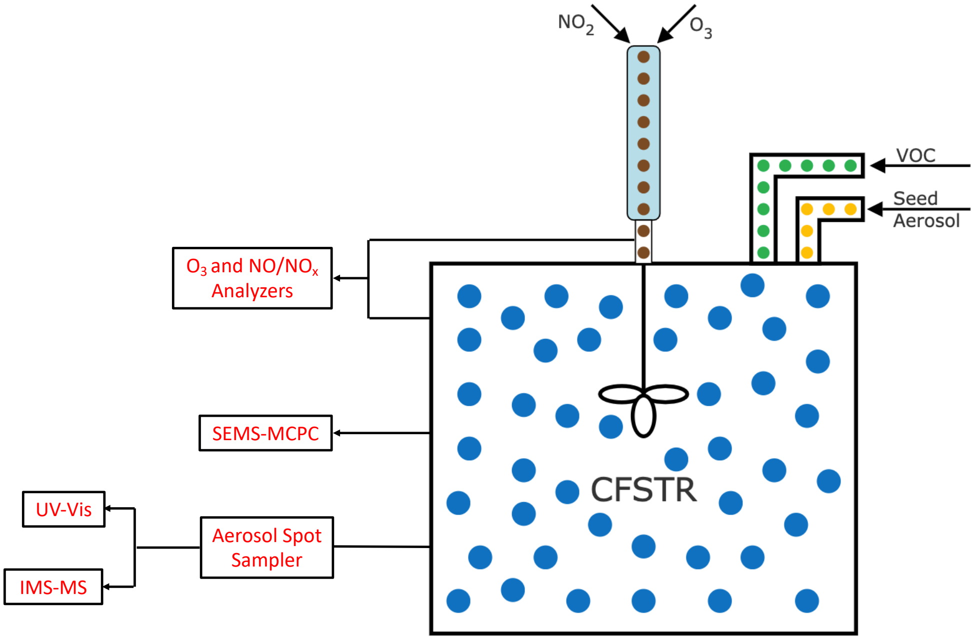

Figure 2.2 A diagram of the experimental setup is shown on the right which includes the CFSTR, VOC, O_3, NO_2, and seed aerosol injection lines. On the left, corresponding arrows are drawn to the analytical tools which were implemented in this study.

2.2.3 IMS-TOF

Following extraction of the samples into 60 μL acetonitrile with 0.1 mM NaCl, the samples were immediately analyzed using the IMS-TOF instrument (Tofwerk Inc. and Aerodyne Research Inc.) with ESI in the negative ion mode. The ACN-NaCl combined solvent was tested to lead to the best ionization efficiency using various chemical standards.[41–43] A detailed description of the instrument has been provided in our recent publications.[41–43] The organic concentration in the extracts ranged from ~50 ng μL^{-1} (phenol SOA) to ~200 ng μL^{-1} (catechol SOA). To further validate the atmospheric relevance of the products characterized from the laboratory experiments, a PM_1 aerosol sample collected from Centreville, AL, during the 2013 Southern Oxidant and Aerosol Study (SOAS) field campaign was analyzed using the IMS-TOF. This ambient sample was collected during the major biomass burning event on June 4th, 2013 from ~4 am to ~4 pm.[44] Thus, the composition in this aerosol sample could represent a combination of nighttime and daytime processing of the biomass burning emissions. This ambient aerosol sample was extracted following the procedure published previously before analysis.[45–47] Each sample extract was introduced into the instrument using a 250 μL syringe (Hamilton) mounted on a syringe pump (KD Scientific Inc.) with a flow rate of 1 μL min^{-1}. The samples were ionized by negative-mode ESI (-1650 V) before introduction into the drift tube. In our prior studies we reported nitrate and nitro species clustering with Cl^- in (-)ESI-IMS-TOF.[48] But for nitro-phenolic species that are slightly acidic the dominant ionization scheme turned out to be $[M-H]^-$. The flow of ions was aided by a flow of N_2 gas at 0.8 L min^{-1}. The drift tube was held at a constant pressure of 1000 mbar and a constant temperature of 60.0°C. The ions were met with a counterflow of N_2 gas at 1.2 L min^{-1} which served to separate the ions based on their size and geometry, termed as their collisional cross-section (CCS). Based on their extent of interaction with N_2 gas, each ion exits the drift tube with a specific drift time.[41] Next, the ions are focused into a pressure-vacuum interface composed of two segmented quadrupoles. Collision-induced dissociation (CID) can occur between the two segmented quadrupoles by adjusting the voltages on the ion optical elements.[48] Thus, the IMS-TOF allows for isomer-resolved characterization of the collected SOA constituents. In an effort to unambiguously identify the single nitro-products of phenol and catechol, chemical standards were run in the IMS-TOF for 2-nitrophenol (2NP), 3-nitrophenol (3NP), 4-nitrophenol (4NP), and 4-nitrocatechol (4NC). The IMS-TOF instrument was operated over an *m/Q* range of 20-1500 Th. The average resolution of the IMS is (t/Δt) ~ 100 and for the TOFMS (m/Δm) ~ 4000.[48] All post processing was done using Tofware (version 3.2.0, Tofwerk) running with Igor Pro (WaveMetrics, OR, USA).[41]

2.2.4 UV-visible spectroscopy

All UV-Vis spectroscopy measurements (Agilent Inc. 8453) were operated under 293 K and 1 atm. A 500 μL cuvette with a path length of 1.0 cm was used and all samples were run using methanol as the solvent. Three trials were run for each sample and the averaged results were reported. The data from this analysis was used to calculate the mass absorption coefficient (MAC) in $m^2\ g^{-1}$ and averaged <MAC> for each sample. The equations for these MAC are shown here:

$$MAC(\lambda) = \frac{A(\lambda) \times \ln(10)}{b \times C_m}$$

where A(λ) is the absorbance at the wavelength of interest, b is path length of cuvette (0.01 m) and C_m is the concentration of SOA in $g\ m^{-3}$.[49]

$$< MAC > = \frac{\sum_{i=1}^{n} MAC(\lambda_i)}{n}$$

The averaged MAC was calculated over the range of 290 – 700 nm and 400 – 550 nm so that our results can be compared with prior relevant studies.

2.3 Results and discussion

2.3.1 SOA formation from NO3· oxidation of phenolic VOCs and general mechanisms

The experimental setup used in this study leads to SOA formation from $NO_3\cdot$ oxidation of phenolic VOCs under approximate steady state. **Table 2.1** summarizes the experimental conditions. The timeseries for total aerosol mass and oxidant concentrations (O_3 and NO_x) are shown in the **Supporting Information** (**SI**), **Figure S.2.1**. Because a direct $NO_3\cdot$ measurement was not available in this work, we used the MCM mechanism to provide approximate estimates of $NO_3\cdot$ concentrations based on the injected and measured O_3 and NO_x.[6] In the MCM box model simulations, the injection concentrations were either measured directly (O_3 in the injection line) or estimated based on the law of mass conservation (for the phenolic VOCs and NO_2). The MCM mechanism includes detailed gas-phase reactions for phenol, catechol, and 3MC, but not for 4MC and guaiacol. Thus, the initial $NO_3\cdot$ oxidation reactions are added for 4MC (1.47×10^{-10} cm^3 molecules^{-1} s^{-1}) and guaiacol (2.69×10^{-11} cm^3 molecules^{-1} s^{-1}), using the rate constants reported in previous research. The products for 4MC oxidation are assumed to be the same as those for 3MC oxidation, while further reactions for guaiacol are not included due to limited information available. In addition, the loss of gas-phase $NO_3\cdot$ and N_2O_5 onto the Teflon wall and the dry NaCl seed aerosols are specifically represented in the simulations, using rates reported in previous studies.[36,39,51] The simulated O_3 concentrations at approximate steady state for the five experiments are generally consistent with the measurements, while the NO_x concentrations were under predicted (shown in **Figure S.2.1**, **SI**). This is likely due to the interference in NO_x measurements by other inorganic and organic nitrogen. The kinetic models suggest that the $NO_3\cdot$ concentrations in the experiments were on the order of 0.4 – 15 ppt under steady state, as shown in **Table 2.1**. The much higher steady-state $NO_3\cdot$ concentration for the phenol experiment is due to the slower reaction rate (3.8×10^{-12} cm^3 molecules^{-1} s^{-1}), compared to those of the other phenolic VOCs. Under the experimental conditions, the box model simulations suggest that the produced OH concentrations are very low ($< 5 \times 10^5$ molecules cm^{-3}) and the majority (> 90%) of the phenolic VOCs reacted with $NO_3\cdot$, rather than O_3 or OH. We should note that the MCM $NO_3\cdot$ oxidation mechanisms for the phenolic VOCs used here are not necessarily comprehensive and accurate; certain concentrations and rate constants were estimated because key gas-phase measurements were unavailable. Nevertheless, the goals of using these simulations were not to accurately describe the oxidation reactions, but rather to (1) demonstrate that $NO_3\cdot$ oxidation is the main loss pathway for the phenolic VOCs; and (2) develop a basic understanding of the oxidation regimes (e.g., concentrations of $NO_3\cdot$, reacted amounts of VOCs, etc.). The formed SOA mass concentrations from the steady-state experiments should be interpreted differently from the typical batch-mode chamber experiments and hence are not directly comparable. This is likely due to the short reaction time (~1 hr) in the present experimental setup and we expect that the observed SOA yields are likely lower than from other chamber experiments. Further, despite of the usage of seed aerosols, the relatively small reactor volume could have caused some wall loss of the gas-phase oxidation products. In addition, the parent phenolic VOCs might also have significant wall losses due their functionality that could more substantially lead to lower SOA formation.[52]

The vapor wall loss, however, should have little influence on the molecular characterization and optical properties of the SOA constituents.

Table 2.1 Experimental conditions.

VOC	Injected/steady-state[a] [VOC] (ppb)	Injected[b]/steady-state [O_3] (ppb)	Injected[b]/steady-state [NO_x] (ppb)[c]	Estimated steady-state[a] [$NO_3\cdot$] (ppt)	SOA mass concentration (μg m^{-3})[d]	<MAC> values (m^2 g^{-1}) (365 nm/400-500 nm/290-700 nm)[e]
Phenol	100/15.9	580/420	250/190	13.7	16.5	1.307/0.413/0.896
Catechol	100/17.6	450/325	250/110	0.4	65.6	3.121/0.799/1.389
3MC	100/8.5	600/415	250/125	0.6	56.8	1.981/0.553/0.974
4MC	100/8.7	600/400	250/130	0.6	40.5	1.990/0.973/1.298
Guaiacol	100/25.0	500/330	250/120	1.0	46.5	0.618/0.171/0.304

[a]Steady-state VOCs are estimated by the kinetic model; [b]injected concentrations of O_3 and NO_x are based on injection rates; [c]the steady-state NO_x was measured by the NO_x analyzer and could include some interference from other inorganic and organic nitrogen; [d]a density of 1.4 g cm^{-3} was assumed for the average density of SOA; [e]the 400-500 nm and 290-700 nm results are averaged values within the specific wavelength ranges.

The generalized initial gas-phase reaction scheme of $NO_3\cdot$ oxidation of phenolic VOCs that leads to the addition of one nitro group ($–NO_2$) to the phenolic backbone is shown in **Figure 2.3A**. It can likely be applied to the other phenolic VOCs studied here with slight adjustments.[15,29,32] Presented in **Figure 2.3B** is a more comprehensive mechanism showing the gas-phase formation pathways of the main products from the $NO_3\cdot$ oxidation of phenol including the nitro- and dinitro-phenols as well as a variety of their dimer products, which likely undergo gas-particle partitioning and were measured in the particle phase. The other studied phenolic VOCs all likely undergo similar mechanisms to form monomeric and dimeric products with 1 – 3 nitro groups. Some possible exceptions are discussed in later sections. The mechanism shown here, however, only presents the formation of nitro-phenolic products. Whether and how other types of products (e.g., additional functional groups on the aromatic ring) could be formed remains unclear. In

Figure 2.3A, the highlighted portion in green represents a phenyl radical intermediate whose stability determines the likelihood of isomeric ratios of the products. It should be noted that the type and number of substitution groups occupied on the initial aromatic ring likely govern the intermediate's stability, and hence the isomer preference and diversity. For example, prior studies suggest that 2NP and 4NC are the dominant products from $NO_3\cdot$ oxidation of phenol and catechol, respectively, in the absence of O_3.[14,29] However, Bolzacchini et al. reported that the presence of O_3 could affect the intermediate's stability during the phenol $NO_3\cdot$ oxidation and change the nitrophenol isomers' distribution (i.e., leading to the formation of 4NP). How the relevant isomers are distributed in the real atmosphere where O_3 is usually present in comparison to laboratory studies have not been demonstrated.

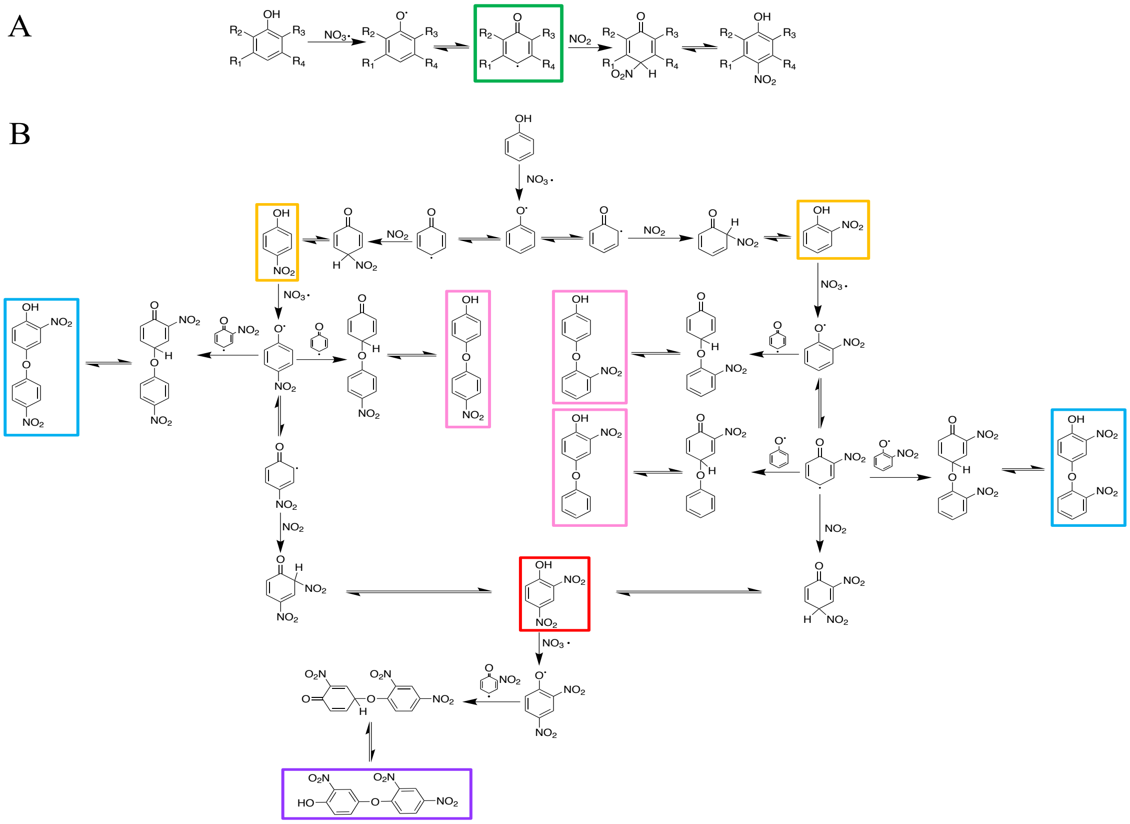

Figure 2.3 (A) General mechanism for the $NO_3\cdot$ oxidation of phenolic VOCs leading to the nitrophenol type of products. The various R groups represent a variety of functional groups including -H, -OH, $-OCH_3$, $-CH_3$. The structure highlighted in green represents a key phenyl radical intermediate in the mechanism. (B) General mechanism for the $NO_3\cdot$ oxidation of phenol to form single-nitro phenols (orange), dinitrophenol (red), single-nitro dimers (pink), dinitro dimers (blue) and a tri-nitro dimer (purple).

2.3.2 Characterization of the SOA constituents from $NO_3\cdot$ oxidation of the phenolic VOCs

The IMS is capable of separating isomers based on their CCS and the TOF allows for accurate molecular formula characterization of the products. The capability of the instrument to provide fragment mass spectra further facilitates identification of functional groups in the products and investigation of fragmentation patterns. Therefore, detailed analysis of molecular and structural information of the phenolic VOCs $NO_3\cdot$ oxidation products under study are possible. **Figure 2.4A** presents a two-dimensional plot of the drift time vs. *m/Q* for all of the products observed from the $NO_3\cdot$ oxidation of phenol and catechol; **Figure 2.4B** presents the same type of plot for the products of the $NO_3\cdot$ oxidation of 3MC, 4MC, and guaiacol. The two-dimensional drift times vs. *m/Q* diagrams enable visualization of the number of isomers formed at each *m/Q*.

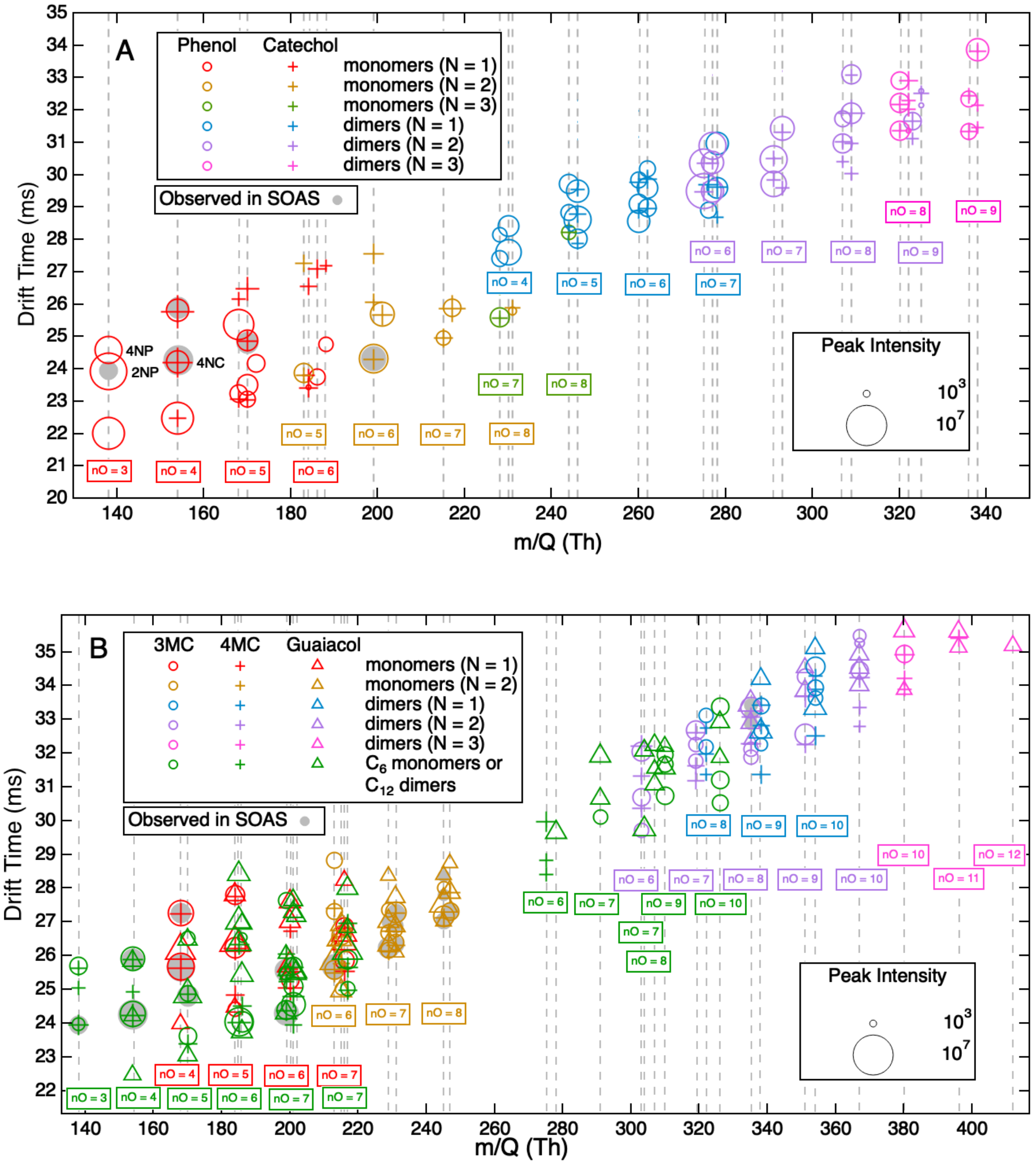

Figure 2.4 (A) 2D drift time vs. *m/Q* plot for the $NO_3\cdot$ oxidation experiments of phenol and catechol. (B) 2D drift time vs. *m/Q* plot for the $NO_3\cdot$ oxidation experiments of 3MC, 4MC and guaiacol. These products represent monomer and dimer products described in the text. The symbol sizes represent the relative peak intensities in the IMS-TOF. In (A), the drift times of the chemical standards, 2NP, 4NP, and 4NC are labelled. Also shown are the identical compounds identified from the SOAS biomass burning aerosol sample. The vertical dashed lines at the specific *m/Q*s are for guidance.

2.3.2.1 Formation of nitrophenol products with additional alcohol groups

The chemical formulas of the major SOA products from the five studied phenolic VOCs shown in **Figure 2.4** are usually featured by the additions of $x\mathrm{NO_2} + y\mathrm{O} - x\mathrm{H}$ (x = 1–3, y = 0–3) onto the initial chemical formulas. These formulas could represent addition of $-NO_2$ groups to the aromatic backbone, forming nitro-phenolic products as widely known. However, the additional oxygens are unexpected for $NO_3\cdot$ oxidation in which OH radicals are predicted to be very low. They could be due to the alcohol groups (–OH) in addition to the $-NO_2$ groups or formation of – $NO_3\cdot$ functional groups instead of $-NO_2$. It is also unlikely that these products are formed from peroxy radical cross reactions, as the phenol-derived peroxy radicals (with the $O_2\cdot$ on an aromatic carbon) do not undergo the Russell mechanism and produce ketones and alcohols as peroxy radicals on aliphatic carbons do.[53] It is apparent that many identical products (i.e., same *m/Q* and drift time) are observed in the $NO_3\cdot$ oxidation of phenol and catechol (**Figure 2.4A**). These results suggest that although catechol is functionalized with one more alcohol group than phenol, the $NO_3\cdot$ oxidation of phenol produces a number of identical products, evident for the addition of alcohol groups to the aromatic ring. A representative example for this observation is at *m/Q* 154 ($C_6H_4NO_4^-$) in the $NO_3\cdot$ oxidation of phenol and catechol. Shown in **Figure 2.5** are the driftgrams for *m/Q* 154 from the $NO_3\cdot$ oxidation of (A) phenol, (B) catechol, and (C) the SOAS aerosol sample. Three prominent drift time peaks are present in these samples, at 22.4 ms, 24.2 ms and 25.8 ms. The peak at 24.2 ms was confirmed to be 4NC by the authentic chemical standard. In the $NO_3\cdot$ oxidation of catechol (**Figure 2.5B**), only two major drift time peaks were present at *m/Q* 154, as expected, which would represent 3-

nitrocatechol (3NC) and 4NC. This suggests that the peak at 25.8 ms is likely 3NC, but it cannot be definitively assigned due to the lack of a standard for 3NC. With our tentative assignment, the substantial presence of 3NC in the $NO_3\cdot$ oxidation of catechol is in contrast to previous studies, where only 4NC was detected as a major product.[14] One likely explanation is that the presence of O_3 in our study has strongly affected the stability of the intermediate which modifies the products' isomer distribution,[29] while the study by Finewax et al., (2018) used N_2O_5 as the $NO_3\cdot$ precursor and O_3 was not present. Nonetheless, the perfect drift time peak matching clearly suggests that the $NO_3\cdot$ oxidation of phenol could produce nitrocatechols. Two possibilities for the additional peak at 22.4 ms are N-nitroresorcinol or N-nitrohydroquinone, which contain their alcohol groups in the 1,3-position and 1,4-positions respectively. Since the alcohol groups are not in the 1,2-positions in these structures, they could only be formed from the $NO_3\cdot$ oxidation of phenol which is evident at 22.4 ms in **Figure 2.5A**. We also note that both the nitrocatechol isomers were largely observed from the ambient aerosol sample (**Figure 2.5C**). These comparisons together suggest that the oxidation of phenolic VOCs produces dynamic and complex isomer distributions, likely mediated by O_3. Further investigation is warranted to elucidate the mechanistic pathways behind the formation of 3NC and 4NC from the $NO_3\cdot$ oxidation of phenol.

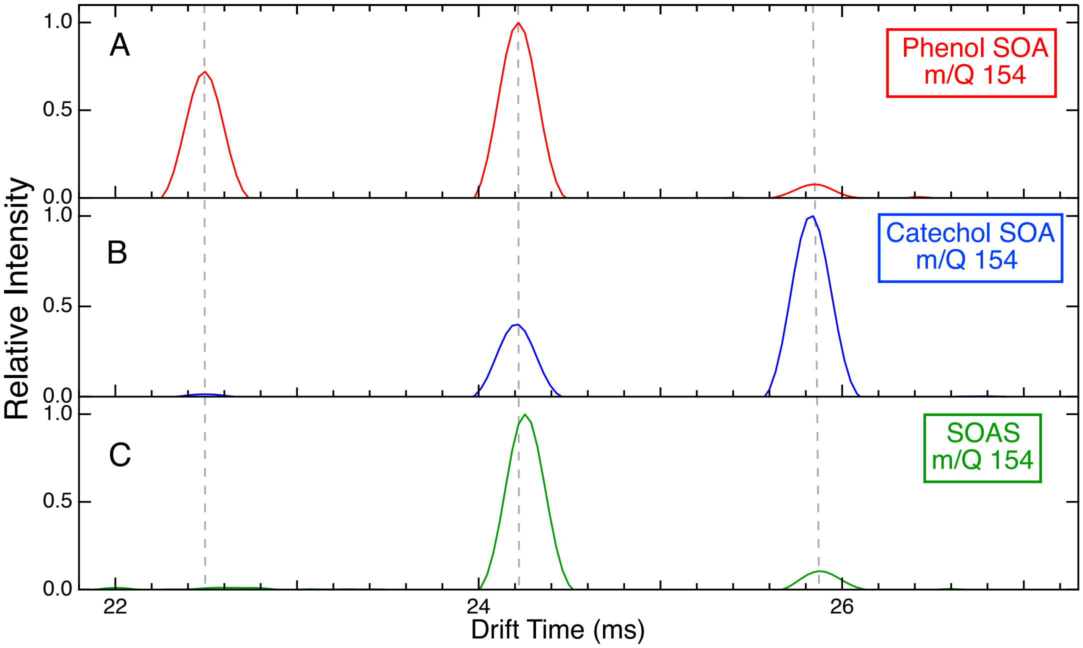

Figure 2.5 Driftgrams of *m/Q* 154 ($C_6H_4NO_4^-$) from (A) phenol + $NO_3\cdot$ SOA, (B) catechol + $NO_3\cdot$ SOA, and (C) the SOAS aerosol sample.

2.3.2.2 Oxidation products of the C_7 phenolic VOCs

In **Figure 2.4B**, a number of products with identical chemical formulas were observed in the $NO_3\cdot$ oxidation of 3MC, 4MC and guaiacol likely because these three phenolic VOCs have the same chemical formula. However, these products are expected to have different structures and thus should be separated by different drift times in the IMS-TOF. This is indeed the case, as evident in **Figure 2.4B**. Regardless, the major monomer products in all three systems appear to be highly consistent with the mechanisms shown in **Figure 2.3B**. In addition, a variety of six-carbon (C_6) monomers and twelve-carbon (C_{12}) dimers were observed. Many of these products have the same chemical formulas and drift times to the products identified in the $NO_3\cdot$ oxidation of phenol and catechol, indicating that they may exhibit identical structures. The observation of C_6 phenolic products in the

$NO_3\cdot$ oxidation of the three C_7 substituted phenolic VOCs suggests that the carbon-containing substitutes could be replaced by a –OH or by a $–NO_2$ group. Despite the fact that a methoxy group (in guaiacol) is typically a much better leaving group than a methyl group (in 3MC and 4MC), the observation of C_6 monomers in the $NO_3\cdot$ oxidation of 3MC and 4MC implies that some scission mechanism of the substituted groups must have occurred. However, the scope and techniques in the present study did not allow us to propose a mechanism for the observation that requires further studies. Moreover, the presence of C_{12} dimers in the $NO_3\cdot$ oxidation of C_7 phenolic VOCs demonstrate that the C_6 monomers were formed in amounts significant enough to undergo further chemistry including dimerization. The C_{14} dimer products, however, have some notable differences than the mechanism shown in **Figure 2.3B**. Specifically, dimers with one $–NO_2$ group are only observed with oxidation number (n_O) greater than or equal to 8. This observation suggests that simple dimers such as those from a nitromethylcatechol with a methylcatechol ($n_O = 6$) are not present, in contrast to **Figure 2.3B**. This difference is further discussed later.

There are some exceptions where the products share similar drift times between two or all three of these systems in **Figure 2.4B**. When the drift times of two products from 3MC and 4MC overlap, the only difference between the products is the position of a methyl group which may explain the identical drift times. However, when the products of guaiacol overlap with either 3MC or 4MC, this drift time overlap is not as easily explained because in one case the methyl group is part of a methoxy group and in the other case, it is attached to the ring. To verify the differences between such “identical” peaks, comparisons were made between the fragmentation mass spectra. For example, similar drift times were observed in the $NO_3\cdot$ oxidation of 3MC and 4MC at *m/Q* 168 ($C_7H_6NO_4^-$) with drift time ~ 25.6 ms, as well as in the $NO_3\cdot$ oxidation of 3MC, 4MC and guaiacol at *m/Q* 184 ($C_7H_6NO_5^-$) with drift time ~ 27.8 ms. **Figures S2.2** and **S2.3** compare the fragmentation mass spectra at CID 20V of these products. In both cases, although the peaks have similar drift times in the IMS, it is apparent that the fragmentation mass spectra are distinct, suggesting that they do not have the same chemical structures, as expected. Further research needs to be conducted to explain this observation, but it is possible that the resonance of the aromatic ring largely constrains the CCS of the products and hence the observed drift times.

2.3.2.3 Non-aromatic products

In the analysis of the SOA constituents from $NO_3\cdot$ oxidation of the phenolic VOCs, products with two additional hydrogens than the above-discussed compounds were observed. These products include: *m/Q* 185 ($C_6H_5N_2O_5^-$), and *m/Q* 201 ($C_6H_5N_2O_6^-$) in phenol; *m/Q* 201 ($C_6H_5N_2O_6^-$) and *m/Q* 217 ($C_6H_5N_2O_7^-$) in catechol; and *m/Q* 215 ($C_7H_7N_2O_6^-$), *m/Q* 231 ($C_7H_7N_2O_7^-$), and *m/Q* 247 ($C_7H_7N_2O_8^-$), in 3MC, 4MC and guaiacol oxidation. These peaks were not expected based on the known gas-phase reaction mechanisms (**Figure 2.3**) but were observed in substantial abundances as shown in **Figure 2.4**. The addition of two hydrogens in each of these phenolic VOCs effectively reduces the double bond equivalence (DBE) by one and removes its aromaticity or suggests a possible ring-opening. The fragment mass spectra (**Figures S2.4 – S2.8**) of these products at CID 20V revealed similar fragmentation patterns across each *m/Q* for each of the phenolic

VOCs studied. In these fragmentation mass spectra, neutral losses of *m/Q* 31 (NO + H), *m/Q* 47 (NO_2 + H), *m/Q* 63 (NO_2 + OH) are consistently observed to be dominant fragments from the parent compounds. These fragmentation patterns are in contrast to the products with the nitrophenol type of structures (e.g., *m/Q* 213 and *m/Q* 229), which will mainly lose NO_2 (*m/Q* 46) at high CID voltage due to their aromaticity. Unfortunately, the interpretation of these fragments does not help to uncover the exact structures of these products. Thus, it is still unclear how this class of products are produced through $NO_3\cdot$ oxidation of the phenolic VOCs. Nevertheless, the results suggest that these products are common across different phenolic VOCs and may comprise substantial fractions. It should also be mentioned that despite this loss of aromaticity or possible ring-opening, these products were stable enough to be observed in the presence of $NO_3\cdot$ and O_3. This suggests that the products might not contain C=C double bonds which could be quickly oxidized by $NO_3\cdot$ and O_3, but rather carbonyls (C=O) on the cyclohexane ring. Further studies are warranted to elucidate the chemical structures and formation mechanisms of these non-aromatic/ring-opening products because such products have not been previously reported in $NO_3\cdot$ oxidation of the phenolic VOC systems.

2.3.2.4 Dimers in the $NO_3\cdot$ oxidation products of the phenolic VOCs

All of the phenolic VOCs under study showed the capability to form a wide variety of dimers upon $NO_3\cdot$ oxidation with up to three nitrogen atoms per dimer molecule. Structural analysis of these dimers was carried out by investigating the mass spectra at the same drift times of the parent ions under high CID 20V. **Figure 2.6** presents the fragmentation mass spectra of five major dimers in phenol SOA (as shown in the reaction scheme in **Figure 2.3B**). These dimers are all characterized by the diphenyl ether structures. In the fragmentation mass spectra shown in **Figure 2.6**, bond scission at the ether linkages are evident, consistent with the proposed structures. In panels A and B are fragment mass spectra of two single nitro- dimers and both of these show strong peaks indicating the fragmentation of *m/Q* 92 (phenol). In the case of *m/Q* 246 in panel B, this loss of phenol indicates that the nitro and alcohol groups are located on the same ring. In panels C and D are fragment mass spectra of two dinitro- dimers and both of these show strong peaks indicating the loss of *m/Q* 169 ($C_6H_3NO_5$), possibly suggesting nitrophenol with two alcohol groups as the monomeric building block. Lastly, for *m/Q* 320, a trinitro- dimer in panel E, a large peak at *m/Q* 138 (nitrophenol) shows the loss of *m/Q* 182 (dinitrophenol). Since there are no additional oxygens in this molecule, the two monomer building blocks can be deduced as nitrophenol and dinitrophenol. Thus, the dimers' monomer building blocks are revealed. From the mechanism shown in **Figure 2.3B**, it was assumed that many of the dimers in these systems are formed in the gas phase via phenoxy radical pathways, followed by gas-particle partitioning. This is supported by the observation that volatile building blocks such as phenol and catechol are present in the dimers; they are unlikely to be present in the particle phase in substantial amount and participate in condensed-phase dimerization. Similar gas-phase phenoxy radical chemistry has been proposed previously from both experimental and computational studies [54,55]. Nevertheless, it is unclear whether all the dimers were formed via this pathway due to the lack of gas-phase measurements. Specifically, the volatile monomeric building blocks were not observed in the C_{14} dimers. The simplest single nitro dimer formed in the $NO_3\cdot$

oxidation of 3MC, 4MC and guaiacol was expected as $C_{14}H_{13}NO_6$, which would be composed of the building blocks $C_7H_8O_2$ and $C_7H_6NO_4$. However, the smallest single nitro dimer ions observed were $C_{14}H_{12}NO_8^-$ in 3MC and 4MC and $C_{14}H_{12}NO_9^-$ in guaiacol. The reason for such difference is unclear, but the fact that volatile monomer building blocks are not present might indicate that the major C_{14} dimers were formed via particle-phase reactions. Regardless, similar types of dimers are observed in all the studied phenolic VOC systems, suggesting that they are important constituents in the phenolic SOA from $NO_3\cdot$ oxidation.

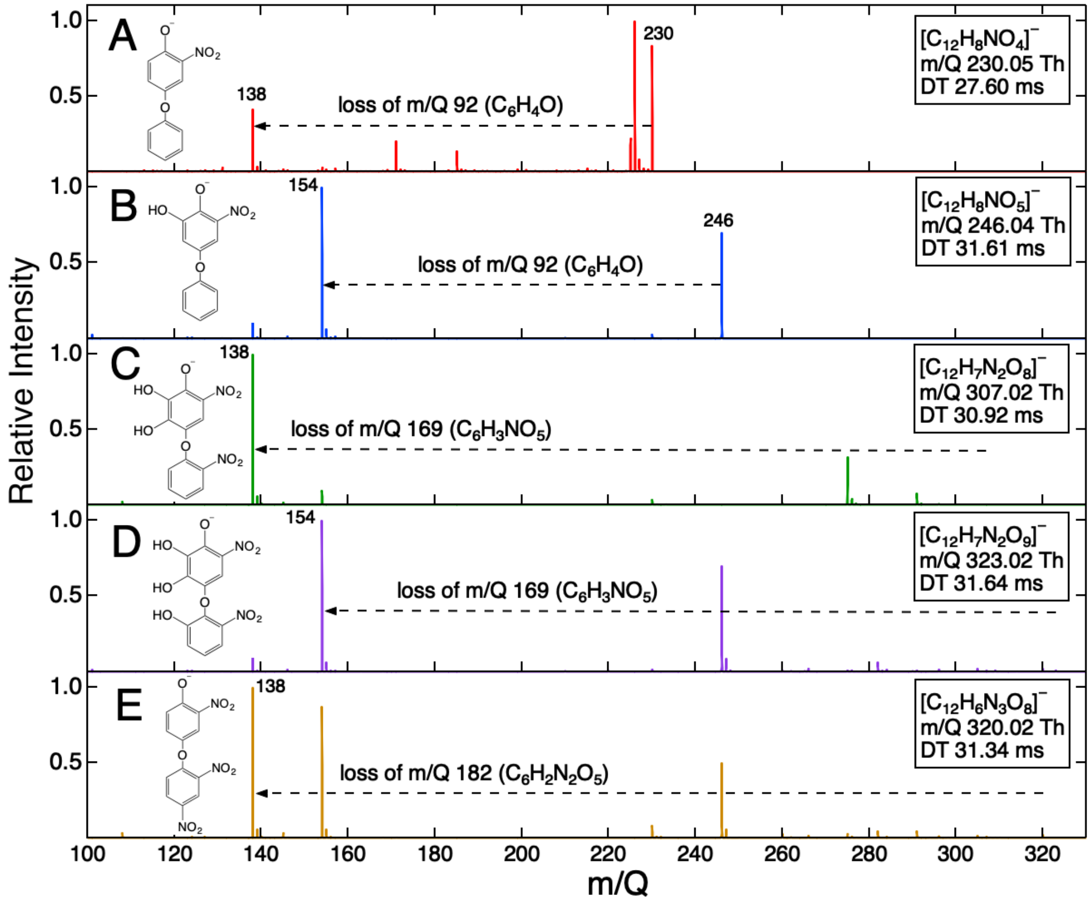

Figure 2.6 Fragment mass spectra of five dimers from the $NO_3\cdot$ oxidation of phenol performed at CID 20 V with their proposed structures shown on the left. From top to bottom the dimers' formulas are A ($C_{12}H_8NO_4^-$), B ($C_{12}H_8NO_5^-$), C ($C_{12}H_7N_2O_8^-$), D ($C_{12}H_7N_2O_9^-$), E ($C_{12}H_6N_3O_8^-$).

2.3.2.5 Phenolic VOC products in ambient biomass burning aerosols

In the analysis of the SOAS aerosol sample, some identical products to those characterized in the $NO_3\cdot$ oxidation of the five phenolic VOCs in this study were observed and displayed in **Figure 2.4**. Namely, a variety of C_6 and C_7 monomers as well as several C_{14} dimers were identified in the SOAS biomass burning sample with identical drift times to those observed in our study. Additionally, some products containing additional alcohol groups, such as *m/Q* 170 ($C_6H_4NO_5^-$) in phenol and catechol, *m/Q* 229 ($C_7H_5N_2O_7^-$) and

245 ($C_7H_5N_2O_8^-$) in 3MC, 4MC and guaiacol, and non-aromatic compounds, such as *m/Q* 215 ($C_7H_7N_2O_6^-$), 231 ($C_7H_7N_2O_7^-$) and 247 ($C_7H_7N_2O_8^-$) in 3MC, 4MC and guaiacol, identified in this study were also present in the SOAS aerosol sample, indicating that these new chemical processes discussed here are relevant to that observed in ambient biomass burning events. Furthermore, we should note that these compounds were only observed in the sample that was collected during a major wildfire event but not in the other 12 non-biomass burning samples, suggesting their relevance to biomass burning aerosol processing. Although it is the only sample relevant to a large biomass burning event at the beginning of the field campaign and its representativeness warrants further examination, the identical products from different pathways are worthwhile to mention. It is also notable that the particular SOAS biomass burning event started before sunrise, but the sample collection was during the morning hours. Therefore, interference from daytime OH-oxidation chemistry and primary emissions cannot be ruled out.[56,57] More distinct ambient aerosol samples with higher time resolution are needed to further confirm how the observed products are formed.

2.3.3 Optical properties of products from $NO_3\cdot$ oxidation of phenolic VOCs

The MAC values averaged at the various wavelength ranges for each of the phenolic derivatives are tabulated in **Table 2.1**. The UV-Vis absorption spectra for each of these compounds can be found in **Figure S2.9**. The MAC values were calculated for the SOA derived from each phenolic VOC at 365 nm, average of 400 – 550 nm, and average of the entire UV-Vis range (290 – 700 nm). The $\langle MAC \rangle_{400\text{-}500nm}$ values had standard deviations of ± 0.200 $m^2\ g^{-1}$ or less. The $\langle MAC \rangle_{290\text{-}700nm}$ values had standard deviations of ± 1.182 m^2 g^{-1} or less. Prior studies have suggested that 365 nm is a characteristic wavelength of peak absorption for BrC;[58,59] $\langle MAC \rangle_{400\text{–}550nm}$ were shown for consistent comparisons with previous measurements.[60] Among the five studied phenolic VOC systems, guaiacol SOA exhibit somewhat lower light absorption than the other four systems which all absorb light strongly. To our knowledge, this is the first report of optical properties (i.e., MAC values) of phenolic VOC + $NO_3\cdot$ SOA. Thus, we compared our measurements with laboratory aromatic SOA and ambient organic aerosols relevant to urban atmosphere or biomass burning. Despite that there are some variations between MAC values from different phenolic systems, our results suggest that the measured MAC values from the SOA derived from phenolic VOC + $NO_3\cdot$ oxidation are generally 3 – 10 times higher than the laboratory-generated aromatic SOA (e.g., from photooxidation of toluene and the xylenes).[61–64] These comparisons suggest that the SOA from photooxidation of aromatic VOCs are mostly less absorbing compounds than formed from $NO_3\cdot$ oxidation in the present work. In addition, prior studies suggest that the guaiacol OH oxidation SOA are much more light absorbing when NO_x was present (i.e., $\langle MAC \rangle_{400\text{–}550nm}$ of ~ 0.19 m^2 g^{-1} for SOA in the presence of NO_x; in contrast to that of ~ 0.02 – 0.03 m^2 g^{-1} in the absence of NO_x).[65,66] Note that the MAC values reported for guaiacol + OH/NO_x are very consistent with our measurements for guaiacol + $NO_3\cdot$ (i.e., $\langle MAC \rangle_{400\text{–}550nm}$ of ~ 0.17 m^2 g^{-1}). These comparisons could be explained by the fact that both OH/NO_x and $NO_3\cdot$ oxidation of guaiacol (or other phenolic VOCs) produce substantial nitrophenol-like products, but this is not the case for other aromatic VOCs such as toluene and the xylenes, which largely form non-absorbing oxygenated products.[67–70] We should also mention that almost all the phenolic SOA constituents observed here contain at least one nitro group on the aromatic rings, which is highly light absorbing. However, when comparing with ambient organic aerosols, especially those relevant to biomass burning events, our results are similar or lower than the ambient OA's MAC values: MAC_{365nm} = 1.52 ± 2.10 $m^2 g^{-1}$ and $\langle MAC \rangle_{400\text{-}500nm}$ = 1.76 ± 2.46 $m^2 g^{-1}$ (both values are represented as mean ± standard deviation).[71–82] The closer MAC values with ambient organic aerosols imply that nitro- or nitrophenol type of products are substantial, especially from biomass burning aerosols.

2.4 Conclusions and atmospheric implications.

In this work, the SOA constituents from the $NO_3\cdot$ oxidation of five major phenolic VOCs relevant in ambient biomass burning emissions were analyzed using IMS-TOF. In addition to the nitrophenolic products which have been demonstrated in prior research, our analysis suggested observations of new products indicative of previously unrecognized oxidation mechanisms. These new products and pathways include: (1) formation of multifunctional products containing both $-NO_2$ and –OH groups; (2) formation of non-aromatic/ring-opening products; (3) formation of diphenyl ether dimers; and (4) formation of fragmentation products when carbon-containing substitutes are present in the phenolic VOCs. These products may form a substantial portion of the total SOA mass. Additionally, the identification of these same products in the SOAS biomass burning sample shows the relevance of these new product pathways in the ambient biomass burning emissions. Although detailed mechanisms that are responsible for these products have not been elucidated, we suggest that they could be important focuses in future work to improve our understanding of the oxidation and evolution of phenolic VOCs in the atmosphere during nighttime. In particular, how the presence of O_3 influences the isomeric distribution of the oxidation products and how the additional alcohol functional groups are formed are critical to understand as biomass burning is becoming increasingly important globally. Finally, the optical analysis of the SOA from the $NO_3\cdot$ oxidation of these phenolic VOCs has shown that phenolic VOCs with additional functionalization form products with larger SOA mass and these products tend to absorb light strongly in the UV and visible ranges. This increased functionalization and dimerization both lead to lower SOA volatility and ultimately lead to an increase in light-absorbing brown carbon under atmospheric conditions. The observations reported in this work strengthen the assumption that nighttime $NO_3\cdot$ oxidation of phenolic VOCs can lead to a significant portion of light-absorbing brown carbon in the atmosphere.

2.5 Supporting Information

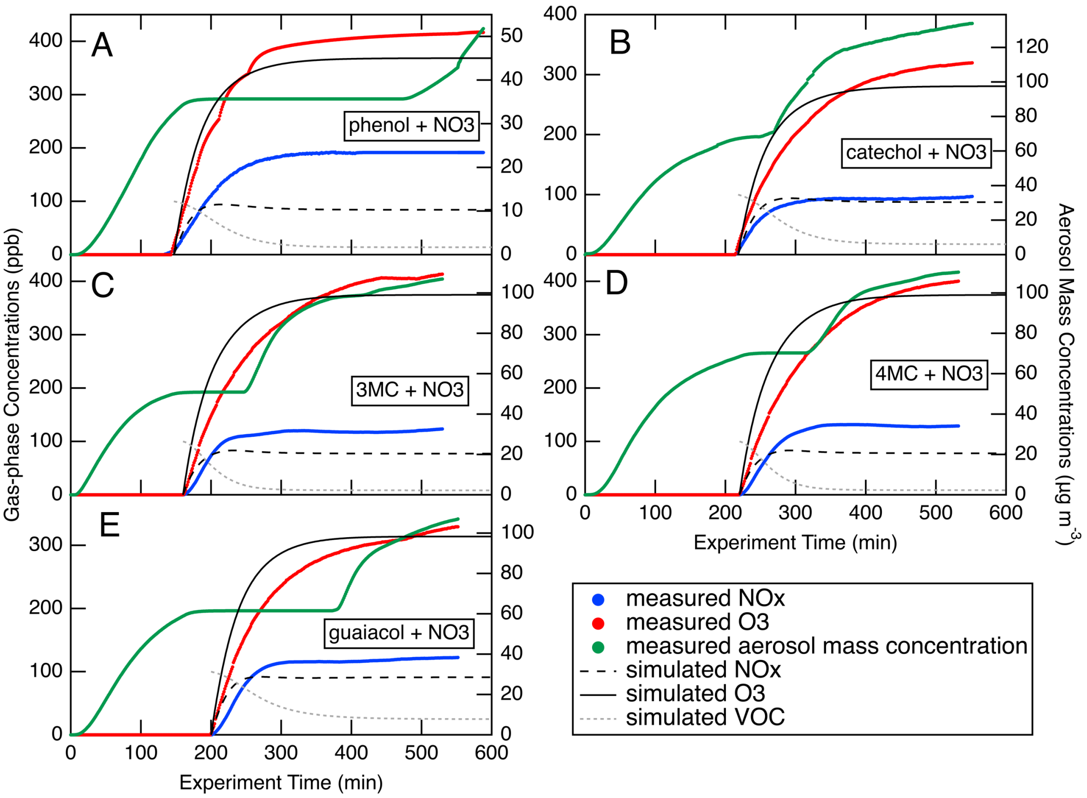

Figure S2.1 Time series of mass concentrations for NO_3 oxidation of each phenolic VOC plotted with the right y axis. Time series of O_3 and NO_x concentrations plotted with the left y axis.

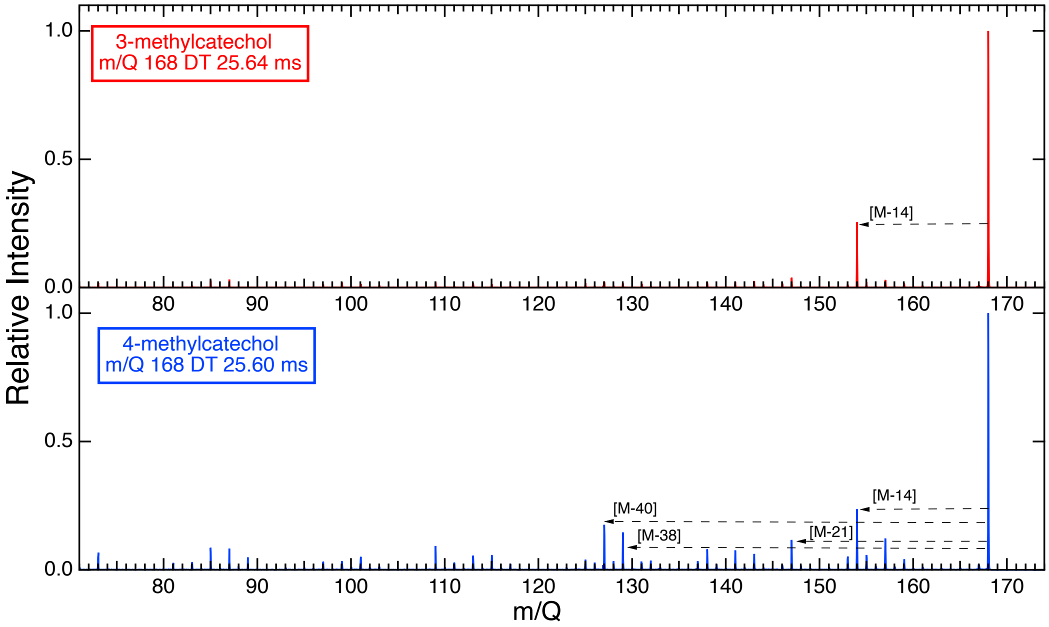

Figure S2.2 Fragment mass spectra of *m/Q* 168 ($C_7H_6NO_4^-$) with overlapping drift times from the NO_3 oxidation of 3MC and 4MC with significant fragments labeled.

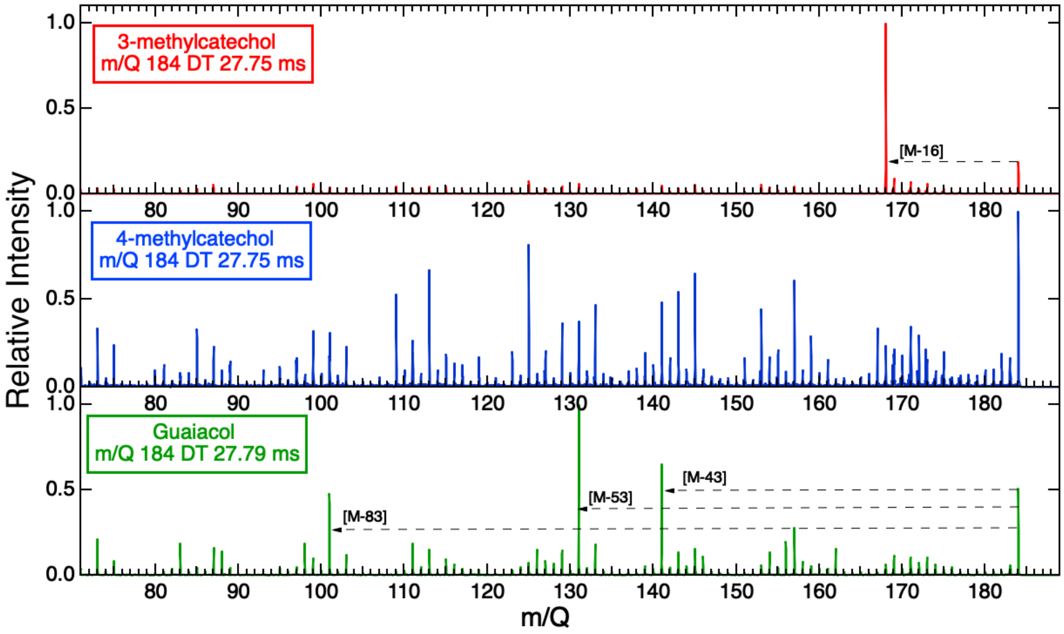

Figure S2.3 Fragment mass spectra of *m/Q* 184 ($C_7H_6NO_5^-$) with overlapping drift times from the NO_3 oxidation of 3MC, 4MC and guaiacol with significant fragments labeled.

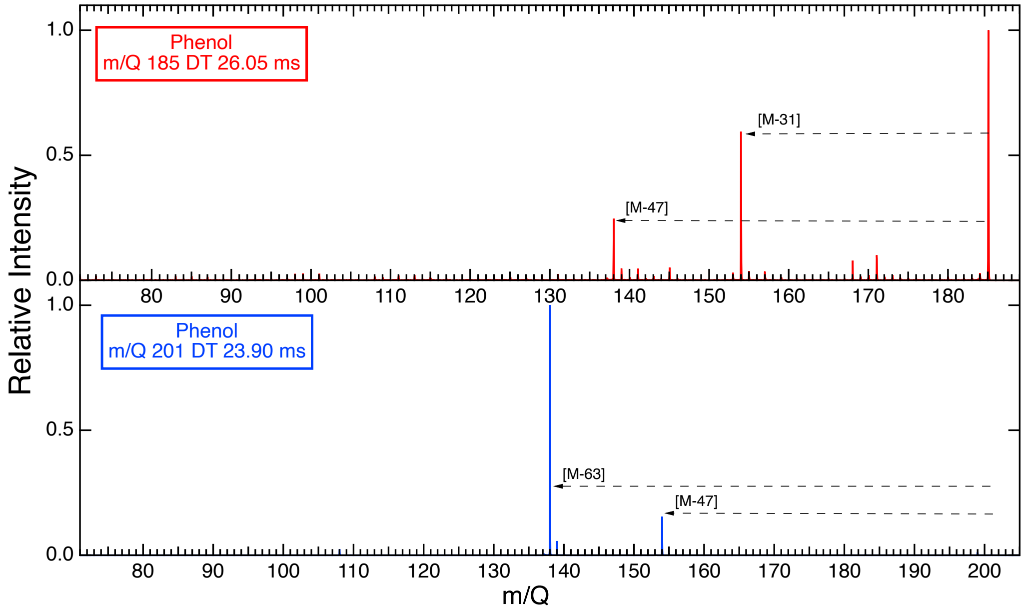

Figure S2.4 Fragment mass spectra of *m/Q* 185 ($C_6H_5N_2O_5^-$) and *m/Q* 201 ($C_6H_5N_2O_6^-$) from the NO_3 oxidation of phenol with significant fragments labeled.

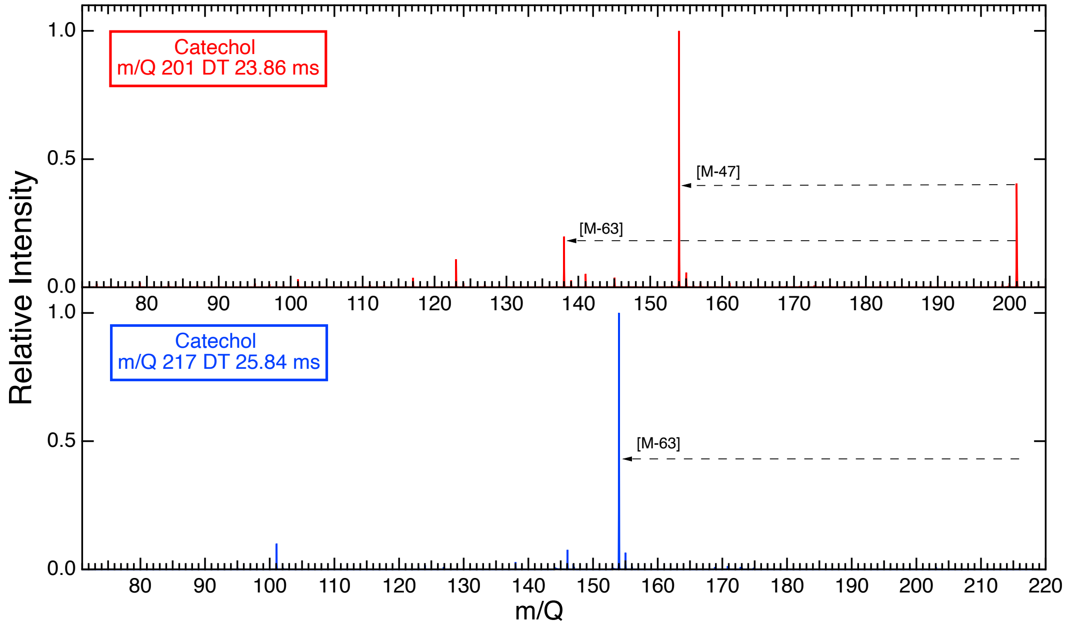

Figure S2.5 Fragment mass spectra of *m/Q* 201 ($C_6H_5N_2O_6^-$) and *m/Q* 217 ($C_6H_5N_2O_7^-$) from the NO_3 oxidation of catechol with significant fragments labeled.

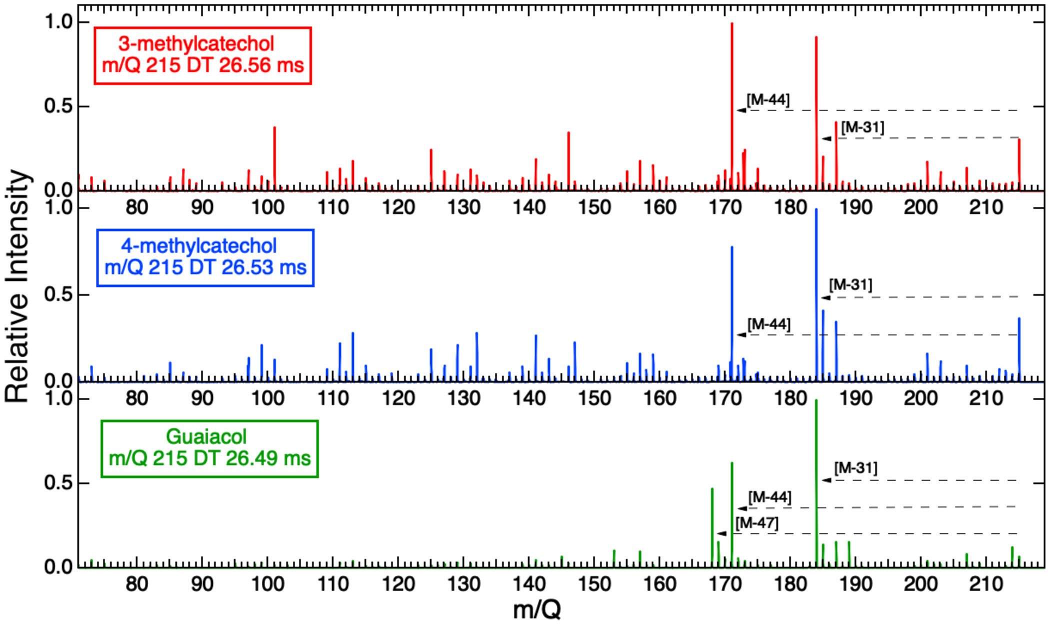

Figure S2.6 Fragment mass spectra of m/Q 215 ($C_7H_7N_2O_6^-$) from the NO_3 oxidation of 3MC, 4MC and guaiacol with significant fragments labeled.

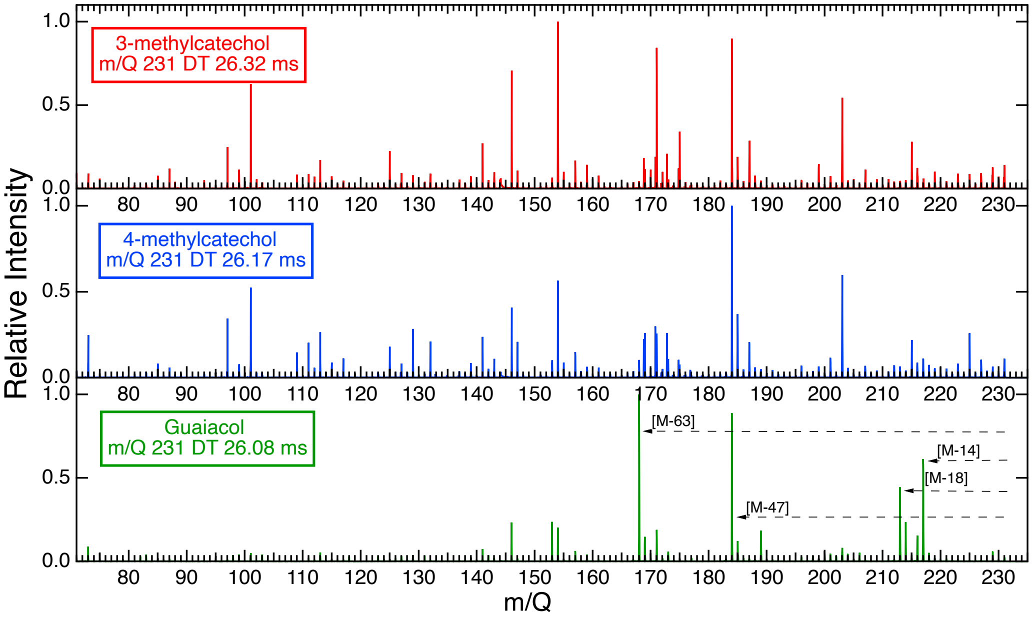

Figure S2.7 Fragment mass spectra of *m/Q* 231 ($C_7H_7N_2O_7^-$) from the NO_3 oxidation of 3MC, 4MC and guaiacol with significant fragments labeled.

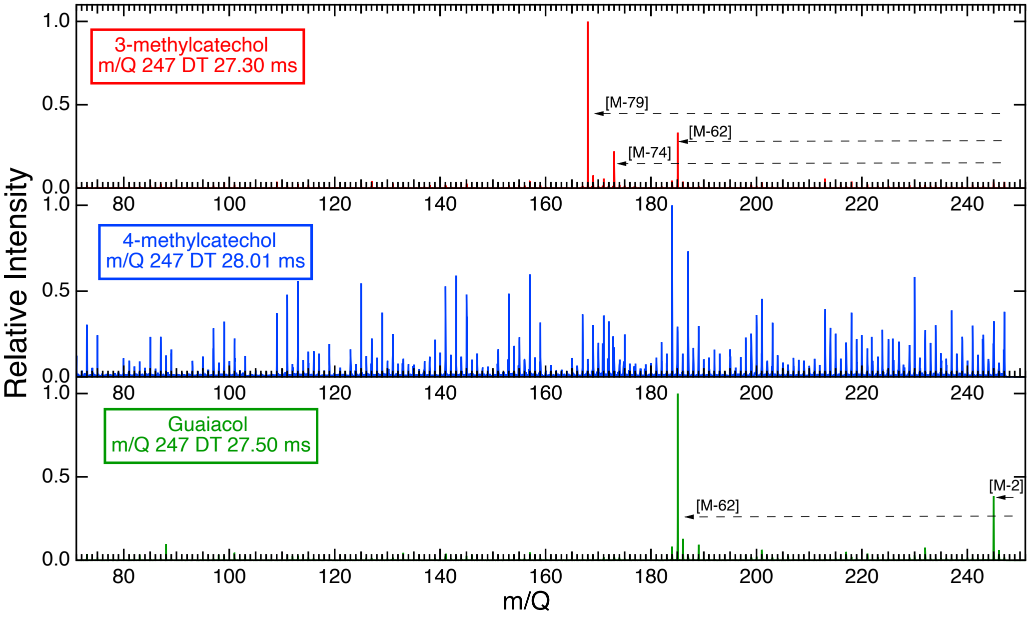

Figure S2.8 Fragment mass spectra of *m/Q* 247 ($C_7H_7N_2O_8^-$) from the NO_3 oxidation of 3MC, 4MC and guaiacol with significant fragments labeled.

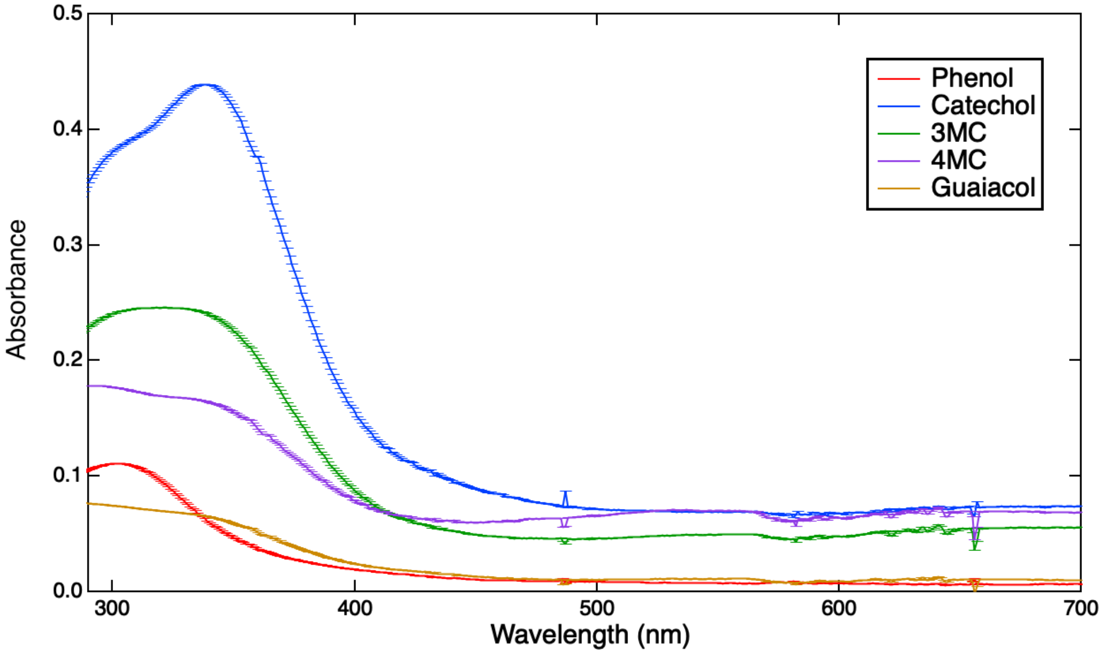

Figure S2.9 UV/Vis absorption spectra for phenol (red), catechol (blue), 3-methylcatechol (green), 4-methylcatechol (purple), and guaiacol (orange) from 290 nm to 700 nm.

2.6 References

(1) Crutzen, P. J.; Andreae, M. O. Biomass Burning in the Tropics: Impact on Atmospheric Chemistry and Biogeochemical Cycles. *Science* **1990**, *250* (4988), 1669–1678.

(2) Pope, C. A.; Dockery, D. W. Health Effects of Fine Particulate Air Pollution: Lines That Connect. *J. Air Waste Manag. Assoc.* **2006**, *56* (6), 709–742.

(3) Arnold, S. R.; Emmons, L. K.; Monks, S. A.; Law, K. S.; Ridley, D. A.; Turquety, S.; Tilmes, S.; Thomas, J. L.; Bouarar, I.; Flemming, J.; Huijnen, V.; Mao, J.; Duncan, B. N.; Steenrod, S.; Yoshida, Y.; Langner, J.; Long, Y. Biomass Burning Influence on High-Latitude Tropospheric Ozone and Reactive Nitrogen in Summer 2008: A Multi-Model Analysis Based on POLMIP Simulations. *Atmospheric Chem. Phys.* **2015**, *15* (11), 6047–6068.

(4) Hobbs, P. V. Direct Radiative Forcing by Smoke from Biomass Burning. *Science* **1997**, *275* (5307), 1777–1778.

(5) Hatch, L. E.; Luo, W.; Pankow, J. F.; Yokelson, R. J.; Stockwell, C. E.; Barsanti, K. C. Identification and Quantification of Gaseous Organic Compounds Emitted from Biomass Burning Using Two-Dimensional Gas Chromatography–Time-of-Flight Mass Spectrometry. *Atmospheric Chem. Phys.* **2015**, *15* (4), 1865–1899.

(6) Bloss, C.; Wagner, V.; Jenkin, M. E.; Volkamer, R.; Bloss, W. J.; Lee, J. D.; Heard, D. E.; Wirtz, K.; Martin-Reviejo, M.; Rea, G.; Wenger, J. C.; Pilling, M. J. Development of a Detailed Chemical Mechanism (MCMv3.1) for the Atmospheric Oxidation of Aromatic Hydrocarbons. *Atmospheric Chem. Phys.* **2005**, *5* (3), 641–664.

(7) Fine, P. M.; Cass, G. R.; Simoneit, B. R. T. Chemical Characterization of Fine Particle Emissions from the Fireplace Combustion of Wood Types Grown in the Midwestern and Western United States. *Environ. Eng. Sci.* **2004**, *21* (3), 387–409.

(8) Oros, D. R.; Simoneit, B. R. T. Identification and Emission Factors of Molecular Tracers in Organic Aerosols from Biomass Burning Part 1. Temperate Climate Conifers. *Appl. Geochem.* **2001**, *16* (13), 1513–1544.

(9) Hatch, L. E.; Yokelson, R. J.; Stockwell, C. E.; Veres, P. R.; Simpson, I. J.; Blake, D. R.; Orlando, J. J.; Barsanti, K. C. Multi-Instrument Comparison and Compilation of Non-Methane Organic Gas Emissions from Biomass Burning and Implications for Smoke-Derived Secondary Organic Aerosol Precursors. *Atmospheric Chem. Phys.* **2017**, *17* (2), 1471–1489.

(10) Lin, P.; Bluvshtein, N.; Rudich, Y.; Nizkorodov, S. A.; Laskin, J.; Laskin, A. Molecular Chemistry of Atmospheric Brown Carbon Inferred from a Nationwide Biomass Burning Event. *Environ. Sci. Technol.* **2017**, *51* (20), 11561–11570.

(11) Lin, P.; Fleming, L. T.; Nizkorodov, S. A.; Laskin, J.; Laskin, A. Comprehensive Molecular Characterization of Atmospheric Brown Carbon by High Resolution Mass Spectrometry with Electrospray and Atmospheric Pressure Photoionization. *Anal. Chem.* **2018**, *90* (21), 12493–12502.

(12) Lin, P.; Liu, J.; Shilling, J. E.; Kathmann, S. M.; Laskin, J.; Laskin, A. Molecular Characterization of Brown Carbon (BrC) Chromophores in Secondary Organic Aerosol Generated from Photo-Oxidation of Toluene. *Phys. Chem. Chem. Phys.* **2015**, *17* (36), 23312–23325.

(13) Finewax, Z.; de Gouw, J. A.; Ziemann, P. J. Products and Secondary Organic Aerosol Yields from the OH and NO_3 Radical-Initiated Oxidation of Resorcinol. *ACS Earth Space Chem.* **2019**, *3* (7), 1248–1259.

(14) Finewax, Z.; de Gouw, J. A.; Ziemann, P. J. Identification and Quantification of 4-Nitrocatechol Formed from OH and NO3 Radical-Initiated Reactions of Catechol in Air in the Presence of NO_x: Implications for Secondary Organic Aerosol Formation from Biomass Burning. *Environ. Sci. Technol.* **2018**, *52* (4), 1981–1989.

(15) Kroflič, A.; Grilc, M.; Grgić, I. Unraveling Pathways of Guaiacol Nitration in Atmospheric Waters: Nitrite, A Source of Reactive Nitronium Ion in the Atmosphere. *Environ. Sci. Technol.* **2015**, *49* (15), 9150–9158.

(16) Lauraguais, A.; El Zein, A.; Coeur, C.; Obeid, E.; Cassez, A.; Rayez, M.-T.; Rayez, J.-C. Kinetic Study of the Gas-Phase Reactions of Nitrate Radicals with Methoxyphenol Compounds: Experimental and Theoretical Approaches. *J. Phys. Chem. A* **2016**, *120* (17), 2691–2699.

(17) Nakao, S.; Clark, C.; Tang, P.; Sato, K.; Cocker III, D. Secondary Organic Aerosol Formation from Phenolic Compounds in the Absence of NO_x. *Atmospheric Chem. Phys.* **2011**, *11* (20), 10649–10660.

(18) Pang, H.; Zhang, Q.; Lu, X.; Li, K.; Chen, H.; Chen, J.; Yang, X.; Ma, Y.; Ma, J.; Huang, C. Nitrite-Mediated Photooxidation of Vanillin in the Atmospheric Aqueous Phase. *Environ. Sci. Technol.* **2019**, *53* (24), 14253–14263.

(19) Pereira, K. L.; Hamilton, J. F.; Rickard, A. R.; Bloss, W. J.; Alam, M. S.; Camredon, M.; Ward, M. W.; Wyche, K. P.; Muñoz, A.; Vera, T.; Vázquez, M.; Borrás, E.; Ródenas, M. Insights into the Formation and Evolution of Individual Compounds in the Particulate Phase during Aromatic Photo-Oxidation. *Environ. Sci. Technol.* **2015**, *49* (22), 13168–13178.

(20) Schwantes, R. H.; Schilling, K. A.; McVay, R. C.; Lignell, H.; Coggon, M. M.; Zhang, X.; Wennberg, P. O.; Seinfeld, J. H. Formation of Highly Oxygenated Low-

Volatility Products from Cresol Oxidation. *Atmospheric Chem. Phys.* **2017**, *17* (5), 3453–3474.

(21) Vidović, K.; Kroflič, A.; Šala, M.; Grgić, I. Aqueous-Phase Brown Carbon Formation from Aromatic Precursors under Sunlight Conditions. *Atmosphere* **2020**, *11* (2), 131.

(22) Lauraguais, A.; Coeur-Tourneur, C.; Cassez, A.; Deboudt, K.; Fourmentin, M.; Choël, M. Atmospheric Reactivity of Hydroxyl Radicals with Guaiacol (2-Methoxyphenol), a Biomass Burning Emitted Compound: Secondary Organic Aerosol Formation and Gas-Phase Oxidation Products. *Atmos. Environ.* **2014**, *86*, 155–163.

(23) Yee, L. D.; Kautzman, K. E.; Loza, C. L.; Schilling, K. A.; Coggon, M. M.; Chhabra, P. S.; Chan, M. N.; Chan, A. W. H.; Hersey, S. P.; Crounse, J. D.; Wennberg, P. O.; Flagan, R. C.; Seinfeld, J. H. Secondary Organic Aerosol Formation from Biomass Burning Intermediates: Phenol and Methoxyphenols. *Atmospheric Chem. Phys.* **2013**, *13* (16), 8019–8043.

(24) Coeur-Tourneur, C.; Foulon, V.; Laréal, M. Determination of Aerosol Yields from 3-Methylcatechol and 4-Methylcatechol Ozonolysis in a Simulation Chamber. *Atmos. Environ.* **2010**, *44* (6), 852–857.

(25) Bluvshtein, N.; Lin, P.; Flores, J. M.; Segev, L.; Mazar, Y.; Tas, E.; Snider, G.; Weagle, C.; Brown, S. S.; Laskin, A.; Rudich, Y. Broadband Optical Properties of Biomass-Burning Aerosol and Identification of Brown Carbon Chromophores: OPTICAL AND CHEMICAL PROPERTIES OF BROWN CARBON AEROSOLS. *J. Geophys. Res. Atmospheres* **2017**, *122* (10), 5441–5456.

(26) Fleming, L. T.; Lin, P.; Roberts, J. M.; Selimovic, V.; Yokelson, R.; Laskin, J.; Laskin, A.; Nizkorodov, S. A. Molecular Composition and Photochemical Lifetimes of Brown Carbon Chromophores in Biomass Burning Organic Aerosol. *Atmospheric Chem. Phys.* **2020**, *20* (2), 1105–1129.

(27) Rollins, A. W.; Browne, E. C.; Min, K.-E.; Pusede, S. E.; Wooldridge, P. J.; Gentner, D. R.; Goldstein, A. H.; Liu, S.; Day, D. A.; Russell, L. M.; Cohen, R. C. Evidence for NO_x Control over Nighttime SOA Formation. *Science* **2012**, *337* (6099), 1210–1212.

(28) Li, C.; He, Q.; Hettiyadura, A. P. S.; Käfer, U.; Shmul, G.; Meidan, D.; Zimmermann, R.; Brown, S. S.; George, C.; Laskin, A.; Rudich, Y. Formation of Secondary Brown Carbon in Biomass Burning Aerosol Proxies through NO_3 Radical Reactions. *Environ. Sci. Technol.* **2020**, *54* (3), 1395–1405.

(29) Bolzacchini, E.; Bruschi, M.; Hjorth, J.; Meinardi, S.; Orlandi, M.; Rindone, B.; Rosenbohm, E. Gas-Phase Reaction of Phenol with NO_3. *Environ. Sci. Technol.* **2001**, *35* (9), 1791–1797.

(30) Frka, S.; Šala, M.; Kroflič, A.; Huš, M.; Čusak, A.; Grgić, I. Quantum Chemical Calculations Resolved Identification of Methylnitrocatechols in Atmospheric Aerosols. *Environ. Sci. Technol.* **2016**, *50* (11), 5526–5535.

(31) Kitanovski, Z.; Čusak, A.; Grgić, I.; Claeys, M. Chemical Characterization of the Main Products Formed through Aqueous-Phase Photonitration of Guaiacol. *Atmospheric Meas. Tech.* **2014**, *7* (8), 2457–2470.

(32) Vidović, K.; Lašič Jurković, D.; Šala, M.; Kroflič, A.; Grgić, I. Nighttime Aqueous-Phase Formation of Nitrocatechols in the Atmospheric Condensed Phase. *Environ. Sci. Technol.* **2018**, *52* (17), 9722–9730.

(33) Yuan, B.; Liggio, J.; Wentzell, J.; Li, S.-M.; Stark, H.; Roberts, J. M.; Gilman, J.; Lerner, B.; Warneke, C.; Li, R.; Leithead, A.; Osthoff, H. D.; Wild, R.; Brown, S. S.; de Gouw, J. A. Secondary Formation of Nitrated Phenols: Insights from Observations during the Uintah Basin Winter Ozone Study (UBWOS) 2014. *Atmospheric Chem. Phys.* **2016**, *16* (4), 2139–2153.

(34) Zaytsev, A.; Koss, A. R.; Breitenlechner, M.; Krechmer, J. E.; Nihill, K. J.; Lim, C. Y.; Rowe, J. C.; Cox, J. L.; Moss, J.; Roscioli, J. R.; Canagaratna, M. R.; Worsnop, D. R.; Kroll, J. H.; Keutsch, F. N. Mechanistic Study of the Formation of Ring-Retaining and Ring-Opening Products from the Oxidation of Aromatic Compounds under Urban Atmospheric Conditions. *Atmospheric Chem. Phys.* **2019**, *19* (23), 15117–15129.

(35) Gao, Y.; Chen, S. B.; Yu, L. E. Efflorescence Relative Humidity of Airborne Sodium Chloride Particles: A Theoretical Investigation. *Atmos. Environ.* **2007**, *41* (9), 2019–2023.

(36) Gershenzon, M. Yu.; Il'in, Sergeid.; Fedotov, N. G.; Gershenzon, Y. M.; Aparina, E. V.; Zelenov, V. V. The Mechanism of Reactive NO_3 Uptake on Dry NaX (X=Cl, Br). *J. Atmospheric Chem.* **1999**, *34* (1), 119–135.

(37) Phillips, G. J.; Thieser, J.; Tang, M.; Sobanski, N.; Schuster, G.; Fachinger, J.; Drewnick, F.; Borrmann, S.; Bingemer, H.; Lelieveld, J.; Crowley, J. N. Estimating N_2O_5 Uptake Coefficients Using Ambient Measurements of NO_3, N_2O_5, $ClNO_2$ and Particle-Phase Nitrate. *Atmospheric Chem. Phys.* **2016**, *16* (20), 13231–13249.

(38) Seisel, S.; Caloz, F.; Fenter, F. F.; van den Bergh, H.; Rossi, M. J. The Heterogeneous Reaction of NO_3 with NaCl and KBr: A Nonphotolytic Source of Halogen Atoms. *Geophys. Res. Lett.* **1997**, *24* (22), 2757–2760.

(39) Stewart, D. J.; Griffiths, P. T.; Cox, R. A. Reactive Uptake Coefficients for Heterogeneous Reaction of N_2O_5 with Submicron Aerosols of NaCl and Natural Sea Salt. *Atmospheric Chem. Phys.* **2004**, *4* (5), 1381–1388.

(40) Thornton, J. A.; Kercher, J. P.; Riedel, T. P.; Wagner, N. L.; Cozic, J.; Holloway, J. S.; Dubé, W. P.; Wolfe, G. M.; Quinn, P. K.; Middlebrook, A. M.; Alexander, B.; Brown, S. S. A Large Atomic Chlorine Source Inferred from Mid-Continental Reactive Nitrogen Chemistry. *Nature* **2010**, *464* (7286), 271–274.

(41) Zhao, Z.; Le, C.; Xu, Q.; Peng, W.; Jiang, H.; Lin, Y.-H.; Cocker, D. R.; Zhang, H. Compositional Evolution of Secondary Organic Aerosol as Temperature and Relative Humidity Cycle in Atmospherically Relevant Ranges. *ACS Earth Space Chem.* **2019**, *3* (11), 2549–2558.

(42) Zhao, Z.; Yang, X.; Lee, J.; Tolentino, R.; Mayorga, R.; Zhang, W.; Zhang, H. Diverse Reactions in Highly Functionalized Organic Aerosols during Thermal Desorption. *ACS Earth Space Chem.* **2020**, *4* (2), 283–296.

(43) Zhao, Z.; Tolentino, R.; Lee, J.; Vuong, A.; Yang, X.; Zhang, H. Interfacial Dimerization by Organic Radical Reactions during Heterogeneous Oxidative Aging of Oxygenated Organic Aerosols. *J. Phys. Chem. A* **2019**, *123* (50), 10782–10792.

(44) Zhang, H.; Yee, L. D.; Lee, B. H.; Curtis, M. P.; Worton, D. R.; Isaacman-VanWertz, G.; Offenberg, J. H.; Lewandowski, M.; Kleindienst, T. E.; Beaver, M. R.; Holder, A. L.; Lonneman, W. A.; Docherty, K. S.; Jaoui, M.; Pye, H. O. T.; Hu, W.; Day, D. A.; Campuzano-Jost, P.; Jimenez, J. L.; Guo, H.; Weber, R. J.; de Gouw, J.; Koss, A. R.; Edgerton, E. S.; Brune, W.; Mohr, C.; Lopez-Hilfiker, F. D.; Lutz, A.; Kreisberg, N. M.; Spielman, S. R.; Hering, S. V.; Wilson, K. R.; Thornton, J. A.; Goldstein, A. H. Monoterpenes Are the Largest Source of Summertime Organic Aerosol in the Southeastern United States. *Proc. Natl. Acad. Sci.* **2018**, *115* (9), 2038–2043.

(45) Zhang, H.; Lin, Y.-H.; Zhang, Z.; Zhang, X.; Shaw, S. L.; Knipping, E. M.; Weber, R. J.; Gold, A.; Kamens, R. M.; Surratt, J. D. Secondary Organic Aerosol Formation from Methacrolein Photooxidation: Roles of NO_x Level, Relative Humidity and Aerosol Acidity. *Environ. Chem.* **2012**, *9* (3), 247.

(46) Zhang, H.; Worton, D. R.; Lewandowski, M.; Ortega, J.; Rubitschun, C. L.; Park, J.-H.; Kristensen, K.; Campuzano-Jost, P.; Day, D. A.; Jimenez, J. L.; Jaoui, M.; Offenberg, J. H.; Kleindienst, T. E.; Gilman, J.; Kuster, W. C.; de Gouw, J.; Park, C.; Schade, G. W.; Frossard, A. A.; Russell, L.; Kaser, L.; Jud, W.; Hansel, A.; Cappellin, L.; Karl, T.; Glasius, M.; Guenther, A.; Goldstein, A. H.; Seinfeld, J. H.; Gold, A.; Kamens, R. M.; Surratt, J. D. Organosulfates as Tracers for Secondary Organic Aerosol (SOA) Formation from 2-Methyl-3-Buten-2-Ol (MBO) in the Atmosphere. *Environ. Sci. Technol.* **2012**, *46* (17), 9437–9446.

(47) Zhang, H.; Surratt, J. D.; Lin, Y. H.; Bapat, J.; Kamens, R. M. Effect of Relative Humidity on SOA Formation from Isoprene/NO Photooxidation: Enhancement of 2-Methylglyceric Acid and Its Corresponding Oligoesters under Dry Conditions. *Atmospheric Chem. Phys.* **2011**, *11* (13), 6411–6424.

(48) Zhang, X.; Zhang, H.; Xu, W.; Wu, X.; Tyndall, G. S.; Orlando, J. J.; Jayne, J. T.; Worsnop, D. R.; Canagaratna, M. R. Molecular Characterization of Alkyl Nitrates in Atmospheric Aerosols by Ion Mobility Mass Spectrometry. *Atmospheric Meas. Tech.* **2019**, *12* (10), 5535–5545.

(49) Jiang, H.; Frie, A. L.; Lavi, A.; Chen, J. Y.; Zhang, H.; Bahreini, R.; Lin, Y.-H. Brown Carbon Formation from Nighttime Chemistry of Unsaturated Heterocyclic Volatile Organic Compounds. *Environ. Sci. Technol. Lett.* **2019**, *6* (3), 184–190.

(50) Olariu, R. I.; Bejan, I.; Barnes, I.; Klotz, B.; Becker, K. H.; Wirtz, K. Rate Coefficients for the Gas-Phase Reaction of NO_3 Radicals with Selected Dihydroxybenzenes. *Int. J. Chem. Kinet.* **2004**, *36* (11), 577–583.

(51) Fry, J. L.; Draper, D. C.; Barsanti, K. C.; Smith, J. N.; Ortega, J.; Winkler, P. M.; Lawler, M. J.; Brown, S. S.; Edwards, P. M.; Cohen, R. C.; Lee, L. Secondary Organic Aerosol Formation and Organic Nitrate Yield from NO_3 Oxidation of Biogenic Hydrocarbons. *Environ. Sci. Technol.* **2014**, *48* (20), 11944–11953.

(52) Matsunaga, A.; Ziemann, P. J. Gas-Wall Partitioning of Organic Compounds in a Teflon Film Chamber and Potential Effects on Reaction Product and Aerosol Yield Measurements. *Aerosol Sci. Technol.* **2010**, *44* (10), 881–892.

(53) Russell, G. A. Deuterium-Isotope Effects in the Autoxidation of Aralkyl Hydrocarbons. Mechanism of the Interaction of Peroxy Radicals [1]. *J. Am. Chem. Soc.* **1957**, *79* (14), 3871–3877.

(54) Strollo, C. M.; Ziemann, P. J. Investigation of the Formation of Benzoyl Peroxide, Benzoic Anhydride, and Other Potential Aerosol Products from Gas–Phase Reactions of Benzoylperoxy Radicals. *Atmos. Environ.* **2016**, *130*, 202–210.

(55) Xu, F.; Yu, W.; Gao, R.; Zhou, Q.; Zhang, Q.; Wang, W. Dioxin Formations from the Radical/Radical Cross-Condensation of Phenoxy Radicals with 2-Chlorophenoxy Radicals and 2,4,6-Trichlorophenoxy Radicals. *Environ. Sci. Technol.* **2010**, *44* (17), 6745–6751.

(56) Chow, K. S.; Huang, X. H. H.; Yu, J. Z. Quantification of Nitroaromatic Compounds in Atmospheric Fine Particulate Matter in Hong Kong over 3 Years: Field Measurement Evidence for Secondary Formation Derived from Biomass Burning Emissions. *Environ. Chem.* **2016**, *13* (4), 665.

(57) Li, J.; Li, J.; Wang, G.; Zhang, T.; Dai, W.; Ho, K. F.; Wang, Q.; Shao, Y.; Wu, C.; Li, L. Molecular Characteristics of Organic Compositions in Fresh and Aged Biomass Burning Aerosols. *Sci. Total Environ.* **2020**, *741*, 140247.

(58) Zhang, X.; Liu, Z.; Hecobian, A.; Zheng, M.; Frank, N. H.; Edgerton, E. S.; Weber, R. J. Spatial and Seasonal Variations of Fine Particle Water-Soluble Organic Carbon (WSOC) over the Southeastern United States: Implications for Secondary Organic Aerosol Formation. *Atmospheric Chem. Phys.* **2012**, *12* (14), 6593–6607.

(59) Lin, Y.-H.; Budisulistiorini, S. H.; Chu, K.; Siejack, R. A.; Zhang, H.; Riva, M.; Zhang, Z.; Gold, A.; Kautzman, K. E.; Surratt, J. D. Light-Absorbing Oligomer Formation in Secondary Organic Aerosol from Reactive Uptake of Isoprene Epoxydiols. *Environ. Sci. Technol.* **2014**, *48* (20), 12012–12021.

(60) Moise, T.; Flores, J. M.; Rudich, Y. Optical Properties of Secondary Organic Aerosols and Their Changes by Chemical Processes. *Chem. Rev.* **2015**, *115* (10), 4400–4439.

(61) Zhong, M.; Jang, M. Light Absorption Coefficient Measurement of SOA Using a UV–Visible Spectrometer Connected with an Integrating Sphere. *Atmos. Environ.* **2011**, *45* (25), 4263–4271.

(62) Nakayama, T.; Sato, K.; Matsumi, Y.; Imamura, T.; Yamazaki, A.; Uchiyama, A. Wavelength and NO_x Dependent Complex Refractive Index of SOAs Generated from the Photooxidation of Toluene. *Atmospheric Chem. Phys.* **2013**, *13* (2), 531–545.

(63) Nakayama, T.; Matsumi, Y.; Sato, K.; Imamura, T.; Yamazaki, A.; Uchiyama, A. Laboratory Studies on Optical Properties of Secondary Organic Aerosols Generated during the Photooxidation of Toluene and the Ozonolysis of α -Pinene: OPTICAL PROPERTIES OF SOAS. *J. Geophys. Res. Atmospheres* **2010**, *115* (D24).

(64) Liu, P. F.; Abdelmalki, N.; Hung, H.-M.; Wang, Y.; Brune, W. H.; Martin, S. T. Ultraviolet and Visible Complex Refractive Indices of Secondary Organic Material Produced by Photooxidation of the Aromatic Compounds Toluene and *m*-Xylene. *Atmospheric Chem. Phys.* **2015**, *15* (3), 1435–1446.

(65) Lambe, A. T.; Cappa, C. D.; Massoli, P.; Onasch, T. B.; Forestieri, S. D.; Martin, A. T.; Cummings, M. J.; Croasdale, D. R.; Brune, W. H.; Worsnop, D. R.; Davidovits, P. Relationship between Oxidation Level and Optical Properties of Secondary Organic Aerosol. *Environ. Sci. Technol.* **2013**, *47* (12), 6349–6357.

(66) Romonosky, D. E.; Ali, N. N.; Saiduddin, M. N.; Wu, M.; Lee, H. J. (Julie); Aiona, P. K.; Nizkorodov, S. A. Effective Absorption Cross Sections and Photolysis Rates of Anthropogenic and Biogenic Secondary Organic Aerosols. *Atmos. Environ.* **2016**, *130*, 172–179.

(67) Ji, Y.; Zhao, J.; Terazono, H.; Misawa, K.; Levitt, N. P.; Li, Y.; Lin, Y.; Peng, J.; Wang, Y.; Duan, L.; Pan, B.; Zhang, F.; Feng, X.; An, T.; Marrero-Ortiz, W.; Secrest, J.; Zhang, A. L.; Shibuya, K.; Molina, M. J.; Zhang, R. Reassessing the Atmospheric Oxidation Mechanism of Toluene. *Proc. Natl. Acad. Sci.* **2017**, *114* (31), 8169–8174.

(68) Kamens, R. M.; Zhang, H.; Chen, E. H.; Zhou, Y.; Parikh, H. M.; Wilson, R. L.; Galloway, K. E.; Rosen, E. P. Secondary Organic Aerosol Formation from Toluene in an Atmospheric Hydrocarbon Mixture: Water and Particle Seed Effects. *Atmos. Environ.* **2011**, *45* (13), 2324–2334.

(69) Wagner, V.; Jenkin, M. E.; Saunders, S. M.; Stanton, J.; Wirtz, K.; Pilling, M. J. Modelling of the Photooxidation of Toluene: Conceptual Ideas for Validating Detailed Mechanisms. *Atmospheric Chem. Phys.* **2003**, *3* (1), 89–106.

(70) Zhou, Y.; Zhang, H.; Parikh, H. M.; Chen, E. H.; Rattanavaraha, W.; Rosen, E. P.; Wang, W.; Kamens, R. M. Secondary Organic Aerosol Formation from Xylenes and Mixtures of Toluene and Xylenes in an Atmospheric Urban Hydrocarbon Mixture: Water and Particle Seed Effects (II). *Atmos. Environ.* **2011**, *45* (23), 3882–3890.

(71) Lack, D. A.; Langridge, J. M.; Bahreini, R.; Cappa, C. D.; Middlebrook, A. M.; Schwarz, J. P. Brown Carbon and Internal Mixing in Biomass Burning Particles. *Proc. Natl. Acad. Sci.* **2012**, *109* (37), 14802–14807.

(72) Chen, Y.; Bond, T. C. Light Absorption by Organic Carbon from Wood Combustion. *Atmospheric Chem. Phys.* **2010**, *10* (4), 1773–1787.

(73) Hoffer, A.; Gelencsér, A.; Guyon, P.; Kiss, G.; Schmid, O.; Frank, G. P.; Artaxo, P.; Andreae, M. O. Optical Properties of Humic-like Substances (HULIS) in Biomass-Burning Aerosols. *Atmospheric Chem. Phys.* **2006**, *6* (11), 3563–3570.

(74) Utry, N.; Ajtai, T.; Filep, Á.; Dániel Pintér, M.; Hoffer, A.; Bozoki, Z.; Szabó, G. Mass Specific Optical Absorption Coefficient of HULIS Aerosol Measured by a Four-Wavelength Photoacoustic Spectrometer at NIR, VIS and UV Wavelengths. *Atmos. Environ.* **2013**, *69*, 321–324.

(75) Kirchstetter, T. W.; Novakov, T.; Hobbs, P. V. Evidence That the Spectral Dependence of Light Absorption by Aerosols Is Affected by Organic Carbon: SPECTRAL LIGHT ABSORPTION BY AEROSOLS. *J. Geophys. Res. Atmospheres* **2004**, *109* (D21), n/a-n/a.

(76) Magi, B. I. Corrigendum to "Chemical Apportionment of Southern African Aerosol Mass and Optical Depth" Published in Atmos. Chem. Phys., 9, 7643–7655, 2009. *Atmospheric Chem. Phys.* **2011**, *11* (10), 4777–4778.

(77) Magi, B. I. Chemical Apportionment of Southern African Aerosol Mass and Optical Depth. *Atmospheric Chem. Phys.* **2009**, *9* (19), 7643–7655.

(78) Zhang, X.; Lin, Y.-H.; Surratt, J. D.; Weber, R. J. Sources, Composition and Absorption Ångström Exponent of Light-Absorbing Organic Components in Aerosol Extracts from the Los Angeles Basin. *Environ. Sci. Technol.* **2013**, *47* (8), 3685–3693.

(79) Zhang, X.; Lin, Y.-H.; Surratt, J. D.; Zotter, P.; Prévôt, A. S. H.; Weber, R. J. Light-Absorbing Soluble Organic Aerosol in Los Angeles and Atlanta: A Contrast in Secondary Organic Aerosol: SOLUBLE BROWN CARBON IN LA AND ATLANTA. *Geophys. Res. Lett.* **2011**, *38* (21), n/a-n/a.

(80) Hecobian, A.; Zhang, X.; Zheng, M.; Frank, N.; Edgerton, E. S.; Weber, R. J. Water-Soluble Organic Aerosol Material and the Light-Absorption Characteristics of Aqueous Extracts Measured over the Southeastern United States. *Atmospheric Chem. Phys.* **2010**, *10* (13), 5965–5977.

(81) Cheng, Y.; He, K.-B.; Zheng, M.; Duan, F.-K.; Du, Z.-Y.; Ma, Y.-L.; Tan, J.-H.; Yang, F.-M.; Liu, J.-M.; Zhang, X.-L.; Weber, R. J.; Bergin, M. H.; Russell, A. G. Mass Absorption Efficiency of Elemental Carbon and Water-Soluble Organic Carbon in Beijing, China. *Atmospheric Chem. Phys.* **2011**, *11* (22), 11497–11510.

(82) Flowers, B. A.; Dubey, M. K.; Mazzoleni, C.; Stone, E. A.; Schauer, J. J.; Kim, S.-W.; Yoon, S. C. Optical-Chemical-Microphysical Relationships and Closure Studies for Mixed Carbonaceous Aerosols Observed at Jeju Island; 3-Laser Photoacoustic Spectrometer, Particle Sizing, and Filter Analysis. *Atmospheric Chem. Phys.* **2010**, *10* (21), 10387–10398.

CHAPTER 3: Peroxy Radical Autoxidation and Sequential Oxidation in Organic Nitrate Formation during Limonene Nighttime Oxidation

3.1 Introduction

Monoterpenes are a class of biogenic volatile organic compounds (BVOCs) that are known as a significant driver of atmospheric chemistry and precursors for secondary organic aerosol (SOA).[1,2] As one of the major monoterpenes, limonene is mostly emitted from citrus plants and coniferous trees with a total emission rate of 11 Tg yr^{-1} in the atmosphere.[3] Typical ambient concentrations of limonene range from 0.1 – 2.0 ppb.[4] Limonene is also found in wildfires with emission factors up to 0.23 g kg^{-1} from fuels native to North America.[5] Limonene is readily oxidized by oxidants such as hydroxyl radicals (OH), ozone (O_3), and nitrate radicals (NO_3). Nighttime concentrations of O_3 in the atmosphere range from 5-50 ppb and NO_3 are formed from O_3 + NO_2 and can reach up to ~1 ppt.[6,7] Hence, NO_3 often co-exist with O_3 at nighttime in the atmosphere and can be the dominant limonene oxidants in polluted areas with high NO_x (= NO + NO_2) levels.[2,8–10] The formation of organic nitrates from NO_3 oxidation of BVOCs represents an important reservoir of atmospheric NO_x and a key pathway for SOA formation.[11–14] Recently, improved analytical methods have allowed for detailed qualitative and quantitative information about the organic nitrates found in the gas and particle phases from NO_3 oxidation of BVOCs.[10,15–19] In previous laboratory experiments, substantial yields (30–72%) of organic nitrates from NO_3 oxidation of limonene have been reported,[15,20–22] suggesting their crucial role in limonene nighttime oxidation.

In the southeastern United States, Lee et al.[10] observed highly oxidized organic nitrates from monoterpenes especially during nighttime. It has been well demonstrated that highly oxidized molecules (HOM) in the atmosphere are rapidly formed from peroxy radical (RO_2) autoxidation in monoterpene ozonolysis.[23,24,24–26] Recently, Guo et al. reported HOM formation from limonene + NO_3, but the formation pathways and RO_2 autoxidation rate constants were still unknown;[27] Draper et al.[28] suggested that certain nitrooxy RO_2 from 3-carene + NO_3 oxidation autoxidize on the order of 10^{-2} s^{-1} based on quantum chemical calculations. It is, however, unclear whether limonene-derived nitrooxy RO_2 could undergo autoxidation at rate constants fast enough to compete with RO_2 bimolecular reactions during nighttime (i.e., RO_2 reacting with RO_2, HO_2, and NO_3).[21,22,29,30] Moreover, limonene has two double bonds, hence, has the potential to produce multifunctional organic nitrates from sequential oxidation, indicated by the fact that limonene + O_3/NO_3 has increased total organic nitrate concentrations and SOA mass yields corresponding to the oxidation of each double bond.**[22]** However, the detailed molecular-level evidence has been lacking to elucidate the specific oxidation pathways. In this study, we investigated the NO_3/O_3 oxidation of limonene with different time scales and examined plausible nitrooxy RO_2 autoxidation and sequential oxidation mechanisms based on the measured gas- and particle-phase organic nitrate molecular compositions, quantum chemical calculations, and kinetic simulations.

3.2 Materials and Methods

3.2.1 Laboratory experiments

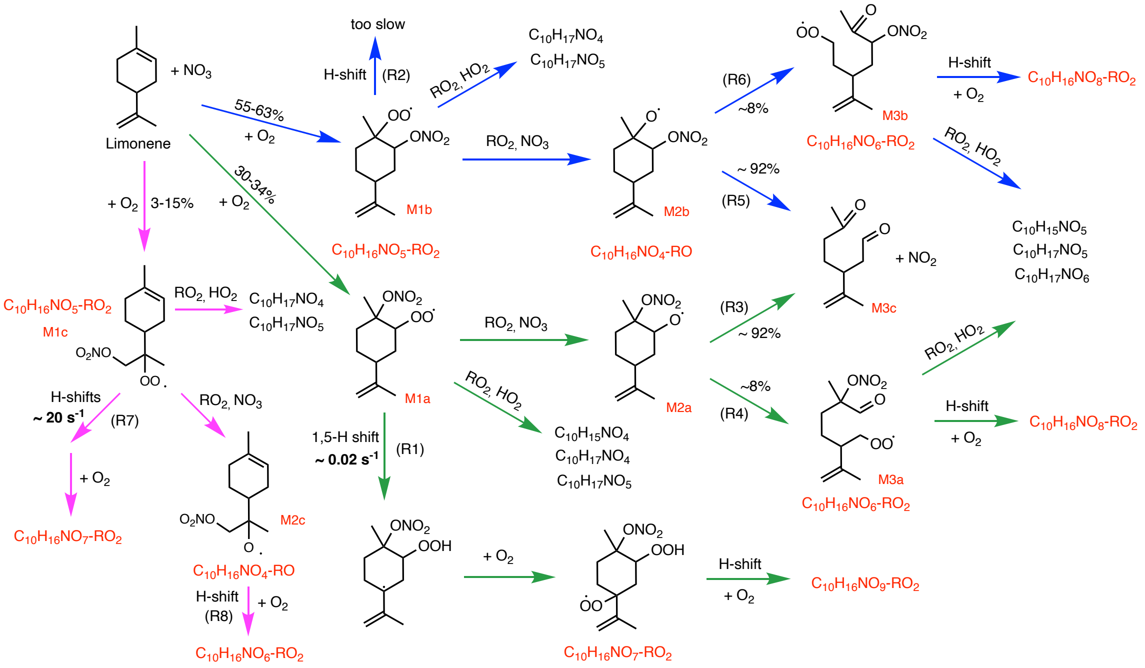

Figure 3.1 Proposed limonene + NO_3 initial gas-phase mechanism.

Limonene (96%, ACROS organics) was oxidized by NO_3/O_3 in a laminar flow tube reactor (FTR, Quartz, volume ~2.1 L) and a continuous flow stirred tank reactor (CFSTR, volume ~250 L, stainless steel enclosure with interior Teflon coating) under 22 °C and relative humidity < 1%.[31,32] The total flow rates in the FTR and CFSTR were 2.1 L min^{-1} and 5 L min^{-1}, respectively; hence the residence times were approximately 1 min in the FTR and 50 min in the CFSTR. The setup for the reactors is illustrated in the Supporting Information (SI) **Figure S3.1**. A clean air generator (Aadco Instruments, Inc.) was used to provide clean dry air for both reactors. Limonene was injected into the reactors in a 1:1000 (v/v) limonene/cyclohexane (99%, ACROS organics) solution using a syringe pump at pre-calculated rates to achieve a limonene injection concentration of 30 ppb. The cyclohexane

(~45 ppm) was used as the OH scavenger. NO_3 was produced by NO_2 + O_3. NO_2 was supplied directly from a gas cylinder of NO_2 through a mass flow controller to reach various concentrations at the entrance of each reactor. O_3 of ~1000 ppb (FTR) and ~300 ppb (CFSTR) was generated by an O_3 generator (Ozone Solution Inc.). The injected NO_2 and O_3 concentrations were designed based on the kinetic model described below, to achieve a range of the fraction of limonene oxidized by NO_3 (f_{NO3}). The concentrations of O_3 and NO_2 (**Table S3.1**) were measured using a 49C O_3 analyzer and a 42C NO_x analyzer (Thermo Environmental Instruments), respectively at the reactor entrances.[33] A scanning electric mobility scanner and a mixing condensation particle counter (Brechtel Inc.) were used to measure the particle size distributions and number concentrations, respectively. No SOA was observed at larger than 5 nm from the FTR, due to the short residence time and low limonene concentration. In contrast, SOA was formed from the CFSTR experiments (**Table S3.1**). For each CFSTR experiment, once SOA mass had stabilized, a Teflon filter (Pall Corporation) was used to collect the SOA at 4 L min^{-1} for 10 h. During the SOA collection, the filter sampler was kept at 0 °C to minimize volatilization and change of composition on filter. Following collection, each filter sample was immediately stored in a freezer at -20 °C until analysis.

3.2.2 Gas- and particle-phase product analysis

The gas-phase oxidation products were analyzed in real time using an iodide-adduct time-of-flight chemical ionization mass spectrometer with a mass resolution ($m/\Delta m$) ~5000 (I-CIMS, Aerodyne Research Inc.).[31,34,35] The I-CIMS is known to be sensitive for multifunctional O-containing and N-containing organic compounds.[10,36–38]

We also utilized an electrospray ionization (ESI) ion-mobility spectrometry time-of-flight mass spectrometer (IMS-TOF) (Tofwerk Inc.) for offline analysis of the particle-phase products.[32,33,35,39–44] To validate the atmospheric relevance of the laboratory-generated limonene SOA, a few 4-h PM_1 aerosol samples collected from Centreville, AL, during the 2013 Southern Oxidant and Aerosol Study (SOAS) field campaign were also analyzed by the IMS-TOF, including one biomass burning sample and five nighttime samples.[2] All the laboratory and field samples were extracted using the same procedure. To each vial containing a filter sample, 20 mL of methanol (HPLC Grade) was added, and the vials were sonicated for 45 min. The filters were then removed from the vials and methanol was evaporated off with a gentle flow of N_2. The sample extracts were immediately dissolved in 100 µL acetonitrile (HPLC Grade) with 0.1 mM NaCl (≥99.5% Sigma-Aldrich). The doped NaCl allows for organic nitrate molecules to form adducts with chloride $[M+Cl]^-$ in the (–)ESI mode, which has been shown to be an effective approach to detect organic nitrates which are otherwise challenging to ionize directly by ESI.[44] Each sample extract was infused into the IMS-TOF using a syringe pump at a rate of 1 $\mu L\ min^{-1}$. The generated ions entered into a drift tube and meet a counterflow of N_2 gas (at 1.2 $L\ min^{-1}$) which serves to separate each ion based on its collisional cross section thereby giving each ion a characteristic drift time.[32,40] The IMS-TOF was operated over a m/Q range of 45–600 Th. The IMS resolution is ($t/\Delta t$) ~100 and the TOF mass resolution is ($m/\Delta m$) ~4000.[32,44]

3.2.3 Quantum chemical calculations and kinetics

To understand the oxidation mechanisms and kinetics in limonene + NO_3 (see **Figure 3.1**), the H-shift of the three primary nitrooxy RO_2 ($C_{10}H_{16}NO_5$-RO_2), the two primary nitrooxy alkoxy radical (RO, $C_{10}H_{16}NO_4$-RO) bond scissions, and the exocyclic $C_{10}H_{16}NO_4$-RO H-shift were calculated by using CCSD(T)-F12a/cc-pVDZ-F12[45,46]//MN15-L/MG3S[47,48] theoretical methods (i.e., pathways R1 – R8 in **Figure 3.1**). Reaction rate constants were calculated by transition state theory[49] with Eckart tunneling.[50] Eckart tunneling is chosen here because our previous investigation[51] has shown that it can agree well with small-curvature tunneling at room temperatures in H-shift processes. Additionally, CCSD(T)-F12a/cc-pVDZ-F12 has been widely used to study H-shift processes in the literature.[52,53] More details are provided in the SI.

3.2.4 MCM-based gas-phase kinetic modeling

To aid the interpretations of the observed products and implement the quantum chemical calculation results, a gas-phase kinetic model was developed based on the Master Chemical Mechanism (MCM, v3.3.1).[54] The model simulates the total reacted limonene concentrations (Δlim) and f_{NO3} in each experiment (**Table S3.1**). Under the experimental conditions, the simulations suggest that the produced OH concentrations were mostly scavenged by cyclohexane and most of limonene was consumed by O_3 and NO_3. The model also provides the bimolecular RO_2 fates under the experimental conditions: the pseudo-first order rates for bimolecular reaction are usually in the range of 0.1 – 0.2 s^{-1} in the experiments, with the RO_2 + RO_2 reactions accounting for > 97% of the RO_2 bimolecular fates (**Table S3.2**). Vapor wall loss was treated the same way as in our previous work.[31] In addition to the original MCM mechanism, we have included new pathways (**Figure 3.1 and Table S3.3**) to reflect the computational results and recent research and examine possible formation mechanisms for organic nitrates. These new pathways include: (1)

Explicitly representing NO_3 addition at three different carbon sites (**Figure 3.1**). Based on previous studies, the lower-estimate of the exocyclic double bond oxidation branching ratio is ~0.03,[22,55] while the higher-estimate of the branching ratio is ~0.15.[30,56] The branching ratios of the two endocyclic $C_{10}H_{16}NO_5$-RO_2 isomers are 0.65:0.35, favoring the formation of more substituted RO_2. Thus, we consider the branching ratios of the three $C_{10}H_{16}NO_5$-RO_2 isomers in the range of 0.63:0.34:0.03 and 0.55:0.30:0.15. (2) H-shift of the three primary $C_{10}H_{16}NO_5$-RO_2 at rate constants estimated by quantum chemical calculations, which produces $C_{10}H_{16}NO_7$-RO_2 in the presence of O_2. (3) Bond scission of the two endocyclic nitrooxy RO ($C_{10}H_{16}NO_4$-RO), which retains the nitrooxy functionality with branching ratios estimated by quantum chemical calculations[28,57] and leads to the formation of a ring-opened nitrooxy RO_2 ($C_{10}H_{16}NO_6$-RO_2) in the presence of O_2.[27,57] (4) H-shift (rate constants by quantum chemical calculations) and fragmentation of the exocyclic $C_{10}H_{16}NO_4$-RO. (5) Bimolecular (i.e., reacting with RO_2, HO_2, and NO_3) and unimolecular (i.e., autoxidation) reactions of the $C_{10}H_{16}NO_6$-RO_2 and $C_{10}H_{16}NO_7$-RO_2 mentioned above. The rate constants for the bimolecular reactions are the same as those used in MCM; the autoxidation rate constants are unknown but are assumed on the same order or 10 times faster than autoxidation of $C_{10}H_{16}NO_5$-RO_2. (6) Sequential O_3 and NO_3 oxidation. In MCM, sequential oxidation is only considered for limonaldehyde ($C_{10}H_{16}O_2$). Here, we include the reactions for all the products that contain double bonds. The rate constants were set to be the same as those used in the original MCM for limonaldehyde.

3.3 Results and Discussion

3.3.1 Overview of the gas- and particle-phase organic nitrate products

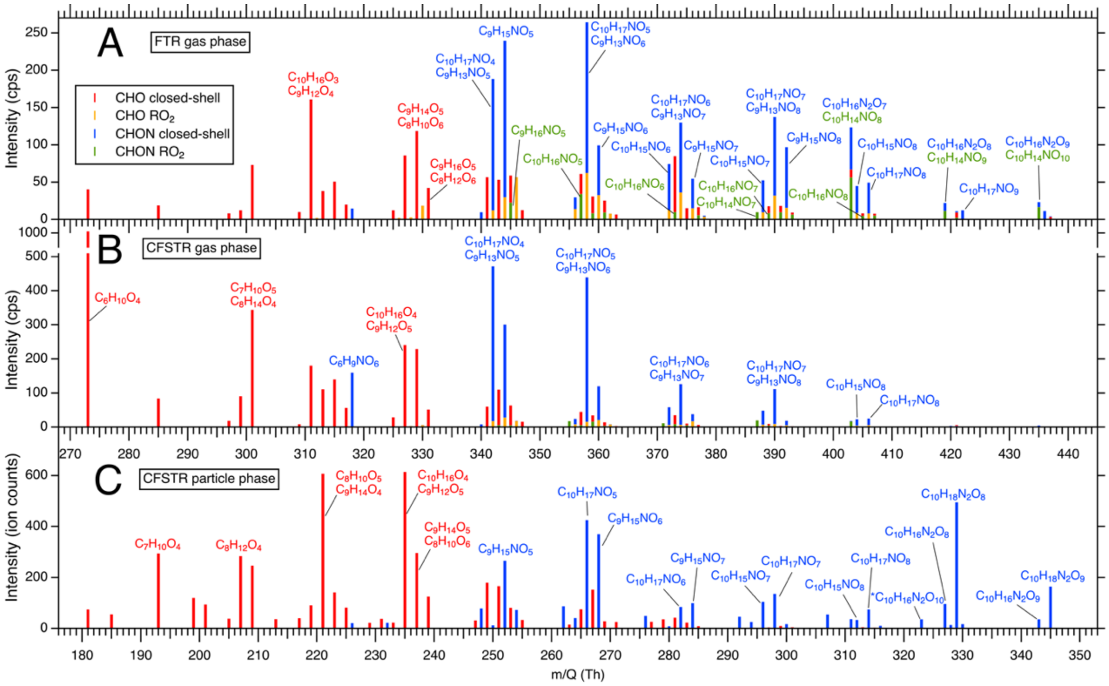

Figure 3.2 Mass spectra plots from a medium f_{NO3} condition (~0.4) are shown for (A) FTR gas-phase I-CIMS measurements, (B) CFSTR gas-phase I-CIMS measurements, and (C) CFSTR particle-phase IMS-TOF measurements. The products are broken down into four categories: non-nitrate (CHO) closed-shell (red), CHO RO_2 (green), organic nitrate (CHON) closed-shell (blue) and CHON RO_2 (orange). Chemical formulas are attached to certain major m/Q. Products in (A) and (B) were identified as $[M+I]^-$ and products in (C) were identified as $[M+Cl]^-$, except that $C_{10}H_{16}N_2O_{10}$ was identified as $[M-H]^-$.

In **Figure 3.2**, mass spectra are shown for f_{NO3} ~0.4 from the FTR gas-phase (**Figure 3.2A**), CFSTR gas-phase (**Figure 3.2B**), and CFSTR particle-phase (**Figure 3.2C**) measurements, with the same product molecular mass lined up vertically. The observed products are broken down into four categories: non-nitrate (CHO) closed-shell products, CHO-RO_2, organic nitrate (CHON) closed-shell products, and nitrooxy RO_2 (CHON-RO_2). With respect to the organic nitrates, we consistently observed significant intensities for the major CHON series including $C_{10}H_{15,17}NO_{4-9}$ and $C_9H_{13,15}NO_{5-8}$, in both reactors and both phases. In addition, CHON-RO_2 species (e.g., $C_{10}H_{16}NO_{5-9}$ and $C_{10}H_{14}NO_{7-10}$) were detected from the FTR, owing to that the FTR was directly interfaced with the I-CIMS inlet. The speciated RO_2 measurement could help probe the RO_2 autoxidation chemistry, as discussed in the following section.[31] There were certain nominal masses which may contain both CHON and CHO-RO_2 or CHO and CHON-RO_2 ions. The high-resolution peak fittings support that the identified species are not due to misassignment of peaks (**Figure S3.2)**. In addition, the CHON and CHON-RO_2 intensities increase with f_{NO3} (**Figure S3.3 and Figure 3.3A**), ruling out interferences from CHO-RO_2 and CHO peaks. As shown in **Figure 3.2**, CHON are rapidly formed in the gas phase (on ~1-min time scale) and those with low enough volatility (highly oxidized) can partition to the particle phase on ~50-min time scale. The gas-particle partitioning may thus account for the much lower concentrations of gas-phase high-molecular-weight products (e.g., m/Q >370 Th) in the CFSTR than in the FTR (**Figure 3.2B**). Interestingly, dinitrates with chemical formulas of $C_{10}H_{16}N_2O_{7-9}$ and $C_{10}H_{18}N_2O_{8-10}$ were observed in both the gas and particle phases. Their intensities account for 1–2% of total product signals in the gas phase but up to nearly 40% in the particle phase. The two nitrate functional groups likely correspond to the two double bonds in limonene being oxidized by NO_3 but could also contain the peroxyacetyl nitrate (PAN) functionality from acyl RO_2 + NO_2, especially for those detected in the FTR. It should also be mentioned that the same C_{10}-dinitrate formulas have been observed during the SOAS field campaign, with diurnal patterns indicating nighttime formation.[58] The comparison between the laboratory-generated dinitrates and field measurements will be discussed later. There are also abundant CHO products, whose formation is most likely from limonene ozonolysis because their total intensities decrease with increased f_{NO3} (**Figures S3.4–S3.5**). In addition, dimer products (i.e., with n_C>10) were also observed in the experiments, but at much lower abundances than the monomers (**Figure S3.6**). The focus of this work is the organic nitrates (i.e., CHON and CHON-RO_2), thus, the CHO compounds and dimers are not discussed in detail.

3.3.2 Constraints of limonene nitrooxy RO_2 autoxidation

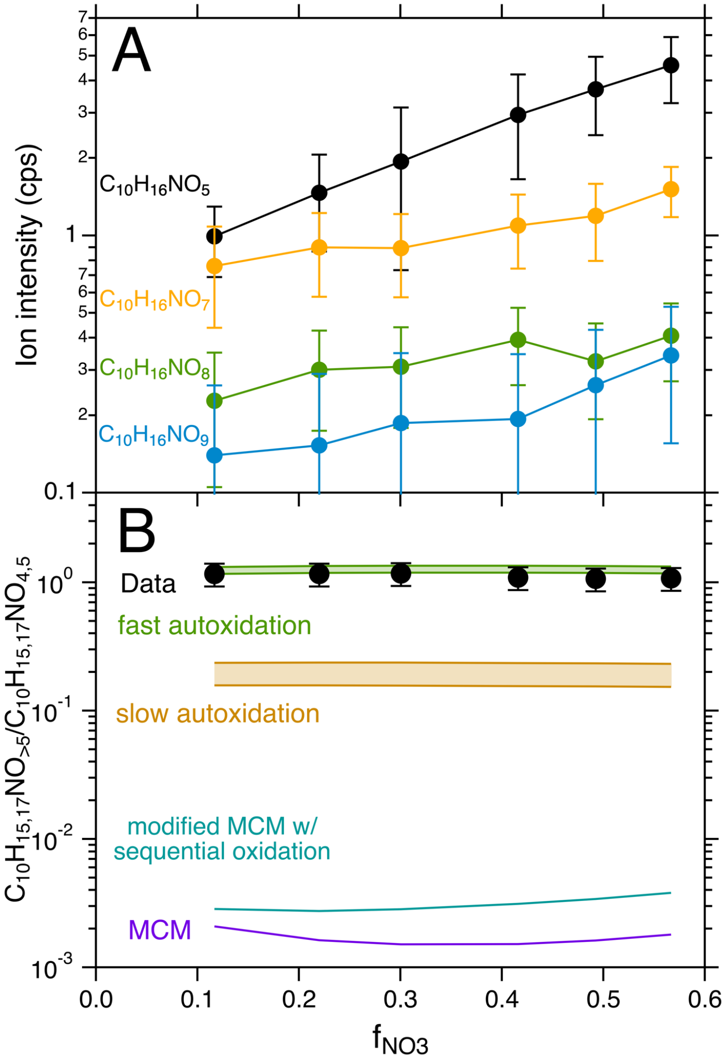

Figure 3.3 (A) The I-CIMS intensities of the major CHON-RO_2 as a function of f_{NO3} in the FTR experiments. (B) The ratios of C_{10} HOM CHON to first-generation CHON from the FTR measurements (black symbols), in comparison to four different kinetic model scenarios: (1) original MCM; (2) modified MCM with sequential oxidation but without CHON-RO_2 autoxidation; (3) with CHON-RO_2 autoxidation at the slower rate (i.e., M1a and M1c undergoing H-shift at 0.02 s^{-1} and 20 s^{-1}, respectively); and (4) with CHON-RO_2 autoxidation at the faster rate (i.e., M1a and M1c undergoing H-shift at 0.2 s^{-1} and 20 s^{-1}, respectively).

Figure 3.3B shows the ratio of the summed C_{10} HOM CHON ($C_{10}H_{15,17}NO_{>5}$) and first-generation CHON ($C_{10}H_{15,17}NO_{4\text{-}5}$) as a function of f_{NO3} in the FTR experiments. The measurements show high CHON ratios of ~1.2 across the studied f_{NO3} range (assuming the same I-CIMS response factor for all the CHON species), indicating that the HOM CHON formation is important. Besides autoxidation illustrated in **Figure 3.1**, the other possible route to form the HOM CHON and CHON-RO_2 is through NO_3 oxidation of oxidized CHO products. For example, the original MCM mechanism includes NO_3 + limonaldehyde to produce $C_{10}H_{16}NO_7$-RO_2. Likewise, the same reactions could occur for the other CHO products (i.e., $C_{10}H_{14,16}O_{2\text{-}4}$) that contain double bonds and lead to the observed CHON-RO_2 formulas (i.e., $C_{10}H_{14,16}NO_{7\text{-}9}$). However, this mechanism turns out to be unlikely because it requires sequential NO_3 oxidation which would take longer than 1 min to produce high enough concentrations of the CHON-RO_2. In support of this, the original MCM model predicts CHON ratios lower by ~ 3 orders of magnitude than the measurements (**Figure 3.3B**). In the modified MCM model, although NO_3 oxidation of all the $C_{10}H_{14,16}O_{2\text{-}4}$ that contain double bonds was included (**Table S3.3**), the model still largely under-predicts the CHON ratios. In addition, the formation of HOM CHON through ozonolysis-initiated autoxidation followed by NO_2 addition for acyl-RO_2 (PAN-like products) can also be ruled out because it is unlikely that acyl-RO_2 are formed at continuous oxygen numbers. These results suggest that autoxidation very likely occurs to explain the high HOM CHON products. Among the observed CHON-RO_2, $C_{10}H_{16}NO_5$-RO_2 are the primary CHON-RO_2 from limonene + NO_3, while the rest may be HOM CHON-RO_2 from autoxidation reactions. The high CHON ratios shown in **Figure 3.3B** suggest that autoxidation under the experimental conditions is competitive against RO_2 bimolecular reactions.

The quantum chemical calculations performed here suggest that the two endocyclic $C_{10}H_{16}NO_5$-RO_2 isomers (M1a and M1b in **Figure 3.1**) have very different enthalpies of activation at 0 K for the H-shifts of methyl group and endocyclic carbon sites to the terminal oxygen of RO_2 in $C_{10}H_{16}NO_5$-RO_2 as described in **Figures S3.7–S3.14**. These calculations reveal that the enthalpies of activation of these H-shift pathways differ largely from ~21 to 44 kcal mol^{-1}. The calculated results show that the $C_{10}H_{16}NO_5$-RO_2 with NO_3 added on the less substituted endocyclic double bond carbon (M1b), which has been considered the major pathway in limonene + NO_3 oxidation (0.55–0.63 branching ratio),[27,57] was found to have at least an enthalpy of activation of 27.6 kcal mol^{-1} at 0 K to perform H-shift (**Figure S3.11**). In contrast, the $C_{10}H_{16}NO_5$-RO_2 with NO_3 added on the more substituted endocyclic double bond carbon (M1a, 0.30–0.34 branching ratio) appears to have a much smaller enthalpy of activation of 21.0 kcal mol^{-1} at 0 K (**Figure 3.4A**) and is estimated to undergo 1,5-H shift at a rate constant on the order of 0.02 s^{-1} at 298 K, as shown in **Table S3.4A**. It should be noted that the calculated enthalpies of activation of H-shift reactions for large molecules like the $C_{10}H_{16}NO_5$-RO_2 may have high uncertainties. According to previous investigations, the present theoretical methods could lead to a factor of ~10 difference for the H-shift rate constant.[52,59] Thus, we suggest that the 1,5-H shift rate constant for M1a could be as high as 0.2 s^{-1}. This range is within one order of magnitude of the RO_2 bimolecular reaction rates in the experiments (**Table S3.2**). In the real atmosphere, this rate is also competitive compared to RO_2 bimolecular reaction rates in most clean and even lightly polluted nighttime environments. For instance, in the southeastern United States, the nighttime RO_2 bimolecular reaction rate is ~0.005 – 0.01 s^{-1}.[2] In addition, we also consider H-shift of the exocyclic $C_{10}H_{16}NO_5$-RO_2 (M1c, 0.03–0.15 branching ratio) as shown in **Figures S3.24–S3.26**. We find a lower reaction pathway by TS1c4-1 with enthalpy of activation of 11.8 kcal mol^{-1} at 0 K in **Figure S3.26** at the MN15-L/MG3S level. This phenomenon is consistent with the literature.[60,61] This lower energy barrier leads to a much faster H-shift than the endocyclic $C_{10}H_{16}NO_5$-RO_2 at ~20 s^{-1} (**Table S3.4B**). The fast H-shift rate constant is highly consistent with prior calculations by Chen et al.[25] The uncertainty of this estimated rate constant is less critical, because with the fast H-shift, all the exocyclic $C_{10}H_{16}NO_5$-RO_2 likely undergo autoxidation and contribute substantially to the HOM CHON formation, despite the low branching ratio of this pathway.[22,55]

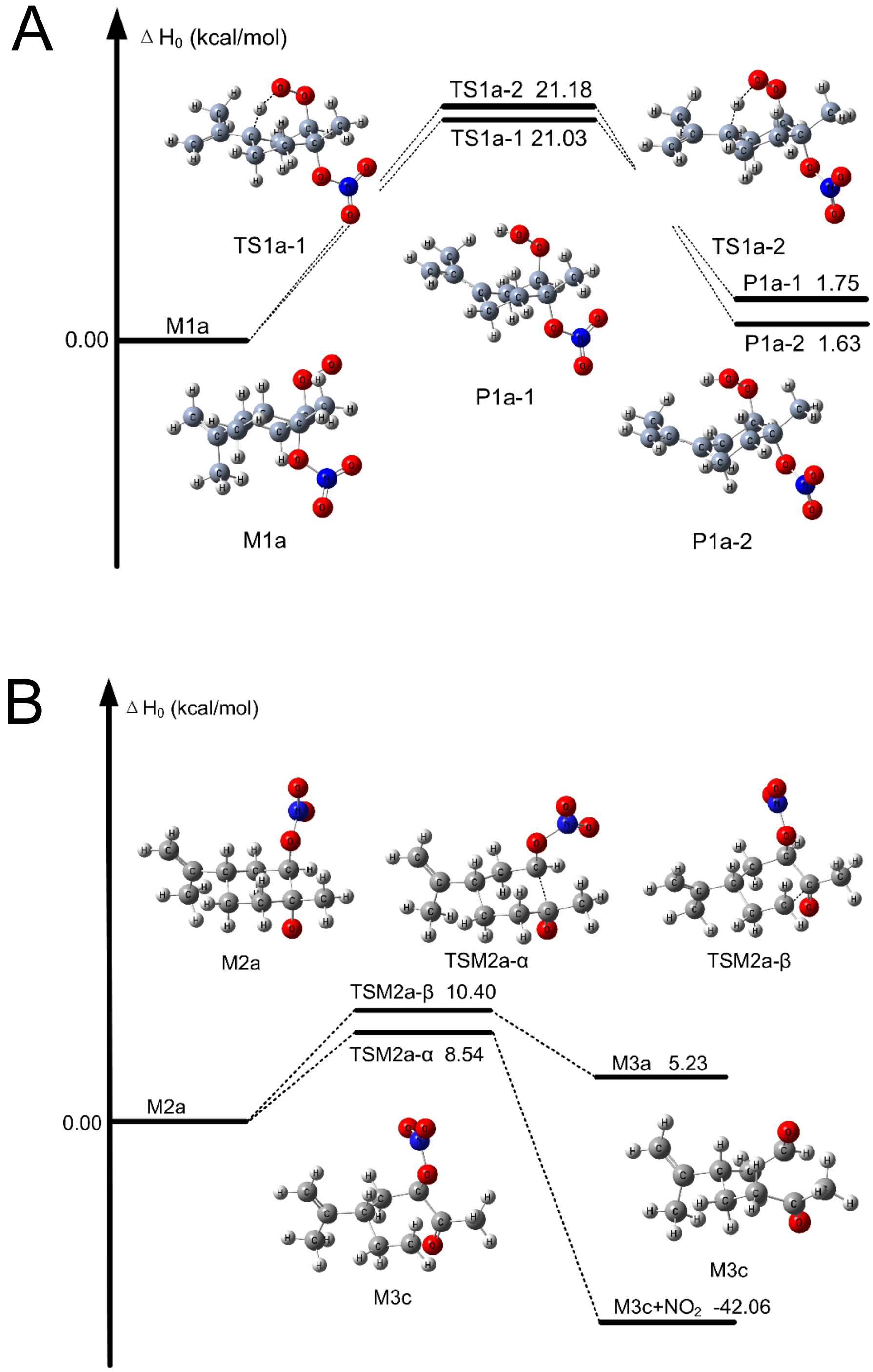

Figure 3.4 Quantum chemical calculation results of (A) $C_{10}H_{16}NO_5$-RO_2 (M1a) H-shift energy barrier, and (B) $C_{10}H_{16}NO_4$-RO (M2a) bond scission energy barrier.

The bond scission pathways of the two endocyclic $C_{10}H_{16}NO_4$-RO isomers (M2a and M2b) were also investigated. The calculated results show that there is a 1.8 – 5.6 kcal mol^{-1} difference between the two scission channels in the enthalpies of activation at 0 K for the two endocyclic $C_{10}H_{16}NO_4$-RO isomers (**Figures S3.15–S3.22**). The calculations suggest that the bond scission of both $C_{10}H_{16}NO_4$-RO isomers favors the formation of limonaldehyde and NO_2 (**Figure 3.4B**), but approximately 8% of the $C_{10}H_{16}NO_4$-RO may retain the nitrooxy functionality and open the six-membered ring to form $C_{10}H_{16}NO_6$-RO_2. This branching ratio is consistent with previous work showing high yields of limonaldehyde in limonene + NO_3 (69–86%).[20,22] Furthermore, we also consider H-shift of the $C_{10}H_{16}NO_4$-RO (M2c) formed from the exocyclic $C_{10}H_{16}NO_5$-RO_2, due to the potential importance of RO's H-shift.[62] As shown in **Figures S3.27–S3.30**, the most favorable pathway has been found by TS2c3-1 with enthalpy of activation of 6.9 kcal mol^{-1} at 0 K by MN15-L/MG3S in **Figure S3.29**. The corresponding unimolecular H-shift rate constant is estimated to be about 1.5×10^6 s^{-1}, fast enough to compete with RO fragmentation (not calculated but assumed to be ~10^6 s^{-1}).[54] Therefore, the present findings show that the RO_2 and RO formed by NO_3 addition to the exocyclic double bond and the more substituted carbon of the endocyclic double bond of limonene can undergo autoxidation.

For the $C_{10}H_{16}NO_5$-RO_2 M1a isomer, a $C_{10}H_{16}NO_7$-RO_2 may be formed following O_2 addition (**Figure 3.1**), which is likely to undergo further 1,5-H shift with the exocyclic double bond to result in a ring-closure $C_{10}H_{16}NO_9$-RO_2. Previous studies suggest that such cyclization reactions may occur rapidly.[25,63] Likewise, the exocyclic $C_{10}H_{16}NO_7$-RO_2 from M1c autoxidation could also undergo rapid H-shift.[25] For the endocyclic $C_{10}H_{16}NO_6$-RO_2

isomers (M3a and M3b), with the six-membered ring open leading to less strained transition states, they are also expected to undergo fast autoxidation and produce $C_{10}H_{16}NO_8$-RO_2 in the presence of O_2. The hydrogens on the tertiary and the aldehydic carbons could both facilitate rapid H-shift. Therefore, it is reasonable to assume that the proposed $C_{10}H_{16}NO_7$-RO_2 and $C_{10}H_{16}NO_6$-RO_2 may autoxidize at least as fast as the $C_{10}H_{16}NO_5$-RO_2 M1a isomer. The bimolecular reaction products of the HOM CHON-RO_2 are hence $C_{10}H_{15,17}NO_{6\text{-}9}$, consistent with the observation in **Figure 3.2A**.

With the quantum chemical calculation results implemented into the kinetic model assuming the lower estimated branching ratio (0.03) for the exocyclic double bond oxidation, autoxidation may explain 24–31% of the HOM CHON with M1a and M1c H-shift at 0.02 s^{-1} and 20 s^{-1}, respectively; while the percentage increases to 123–135% with M1a H-shift rate constant increased to 0.2 s^{-1}, as shown in **Figure 3.3B**. Adjusting the M1c H-shift rate constant within a factor of 10 has little effect on the overall model performance because M1c autoxidation always over-competes bimolecular pathways within this range of rapid H-shift rate constants. With the higher estimated branching ratio (0.15) for the exocyclic double bond oxidation, this pathway with faster H-shift contributes significantly larger to the HOM CHON, leading to 63–31% of the HOM CHON accounted by autoxidation even with M1a undergoing H-shift at 0.02 s^{-1}. Despite the uncertainties existing in both measurements and calculations, the results considering the autoxidation mechanism greatly outperforms the mechanisms without autoxidation, strongly supporting its validity. The CHON-RO_2 autoxidation mechanism demonstrated here, however, could not explain the presence of $C_{10}H_{14}NO_{7\text{-}10}$-$RO_2$ in the FTR, suggesting that unrecognized pathways still exist. Nevertheless, our findings coupling measurements, quantum chemical calculations, and kinetic modeling provide compelling evidence and strong constraints of CHON-RO_2 autoxidation from NO_3-intiated oxidation of limonene at a rate constant fast enough to compete with bimolecular reactions in the laboratory and under atmospheric nighttime conditions. The results also suggests that the often-omitted "minor" pathways in limonene + NO_3 should be carefully considered in future chemical mechanisms.

3.3.3 Role of sequential oxidation in organic nitrate formation.

With the oxidation extended to a longer time scale in the CFSTR, a larger degree of oxidation could occur that has led to SOA formation. The gas- and particle-phase oxidation products shown in **Figure 3.2B** and **3.2C** are featured by the same CHON chemical formulas as in **Figure 3.2A**, but their detailed composition and formation mechanisms can be more complex, as a result of both CHON-RO_2 autoxidation and sequential oxidation. In **Figure 3.5A**, the total CHON intensities observed in the gas and particle phases at each f_{NO3} are displayed with pie charts showing fractions of C_{10}-mononitrates, C_9-mononitrates, C_{10}-dinitrates, and smaller CHON (with n_C<9). The total CHON intensities continue to increase with f_{NO3} in both the gas and particle phases as expected, while the individual categories varied more dynamically (**Figure 3.5B–5D**).

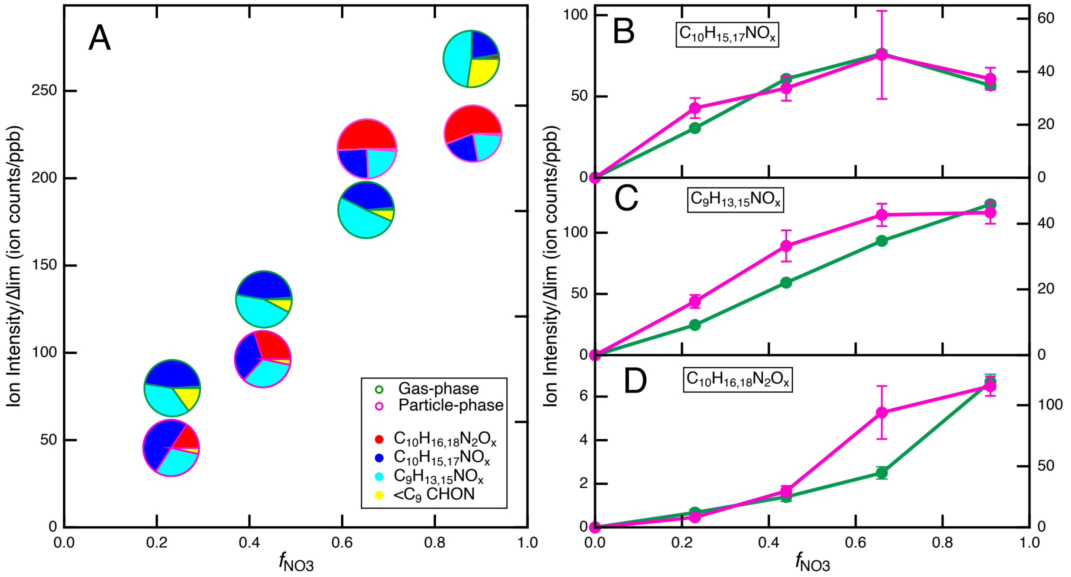

Figure 3.5 (A) Pie charts plotted at relative intensity/Δlim (cps ppb^{-1}) for total CHON intensity in the CFSTR experiments with gas-phase results outlined in green and particle-phase results outlined in pink. Each pie chart in (A) is broken down into fractions of different product types: C_{10}-mononitrates (dark blue), C_9-mononitrates (teal blue), C_{10}-dinitrates (red), and smaller CHON (yellow). The sum of the fractions at each f_{NO3} equals the total intensity/Δlim at each f_{NO3}. The summed intensity evolution of (B) C_{10}-mononitrates, (C) C_9-mononitrates and (D) C_{10}-dinitrates are plotted as a function of f_{NO3}. Trends for the gas-phase results are shown in green and those for the particle-phase results are shown in pink.

First, the enhancement of the $C_{10}H_{15,17}NO_x$ products in both phases slows down at high f_{NO3} (**Figure 3.5B** and **Figure S3.31**), suggesting that their abundance is not solely dependent on NO_3 oxidation. As mentioned above, it is possible that the initial NO_3/O_3 oxidation products of limonene (e.g., $C_{10}H_{14,16}O_{2\text{-}4}$) which still contain a double bond could be sequentially oxidized by NO_3 and form $C_{10}H_{15,17}NO_{6\text{-}9}$. Unlike the FTR conditions, the CFSTR experiments have long enough time to allow for such sequential oxidation. Thus, at high f_{NO3}, the inhibited ozonolysis of limonene leads to the reduced formation of C_{10}-CHO and hence C_{10}-mononitrates from the sequential NO_3 oxidation pathway. This result highlights the importance to consider the synergistic role of both O_3 and NO_3 in nighttime CHON formation. It is also notable that the C_9-mononitrates contribute large fractions of total CHON intensities under all conditions. A straightforward mechanism to explain their formation is through NO_3 oxidation of the endocyclic double bond of limonene followed by ozonolysis of the exocyclic double bond to form C_9-CHON compounds (and the C_1-Criegee intermediate). However, this mechanism is expected to occur only in the CFSTR experiments since it requires sequential oxidation. Further, because this mechanism involves ozonolysis, the C_9-CHON products are expected to have the similar relationship with f_{NO3} as the C_{10}-mononitrates. In contrast, the total C_9-mononitrates increase more linearly with f_{NO3} (**Figure 3.5C**), suggesting that there must be a pathway from limonene + NO_3 that quickly forms C_9-mononitrates via fragmentation (which could also explain their presence in the FTR). The detailed mechanism is unclear but warrants further studies. Other smaller fragmentation products (with $n_C<9$) in the gas phase are also noticeable from the CFSTR experiments, but their contribution to SOA formation is minor.

Finally, it is remarkable that a large fraction of the particle-phase CHON is from C_{10}-dinitrates, up to almost 60% of the total CHON ion intensity (**Figure 3.5A**). Despite the elusive sensitivities of different CHON species in the (–)ESI, one can still expect important contribution of the dinitrates in SOA. In strong contrast, the C_{10}-dinitrates represent $\leq 2\%$ of the total CHON intensity in the gas-phase, consistent with their very low volatility. Their generic formation mechanism through sequential NO_3 oxidation is proposed in **Figure S3.32**. In **Figure 3.5D**, the summed intensities of the six major C_{10}-

dinitrate products ($C_{10}H_{16}N_2O_{7-9}$ and $C_{10}H_{18}N_2O_{8-10}$) exhibit an approximate quadratic relationship with f_{NO3}, especially in the gas phase, consistent with sequential NO_3 oxidation.

3.4 Atmospheric relevance

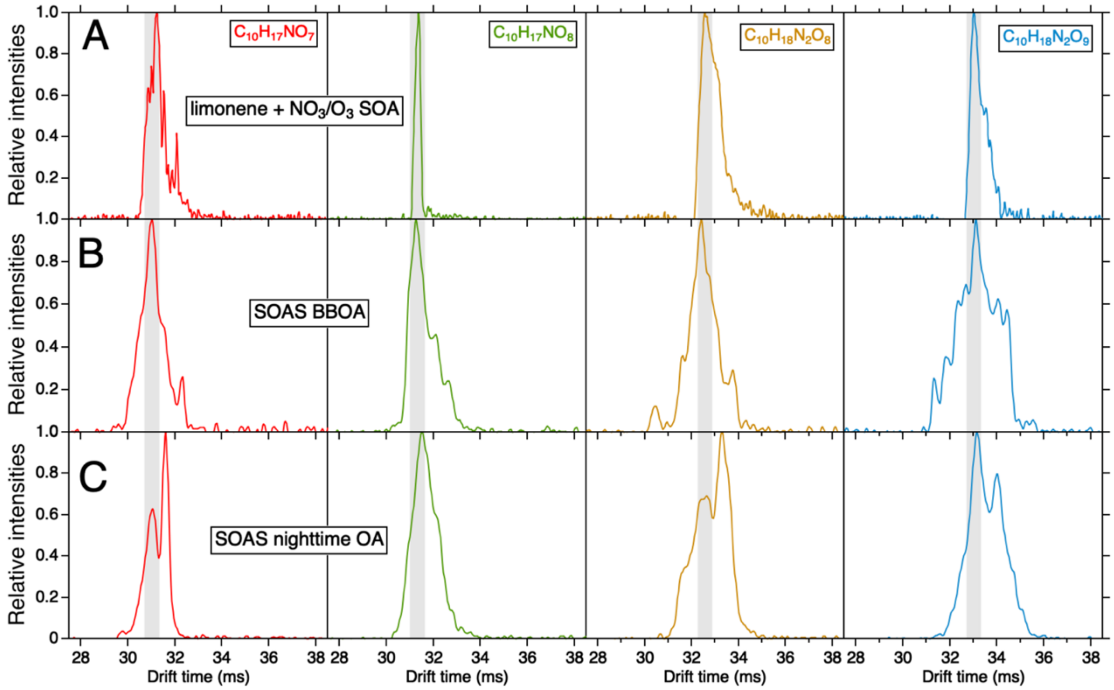

Figure 3.6 IMS-TOF driftgrams for major C_{10}-mononitrates ($C_{10}H_{17}NO_{7-8}$) and C_{10}-dinitrates: ($C_{10}H_{18}N_2O_{8-9}$). Panel (A): SOA from the limonene CFSTR experiments; panel (B): ambient aerosol samples from the 2013 SOAS campaign during a biomass burning event (BBOA); panel (C) SOAS nighttime aerosol samples.

In this work, we report formation of limonene-derived highly oxidized CHON formed from both CHON-RO_2 autoxidation (e.g., the C_{10}-mononitrates) and sequential NO_3 oxidation (e.g., both the C_{10}-mononitrates and C_{10}-dinitrates). During the SOAS field campaign where monoterpenes contribute significantly to SOA,[2] the highly oxidized C_{10}-mononitrates ($C_{10}H_{17}NO_{7-8}$) were reported as the most abundant particle-phase CHON species;[10] the same dinitrate formulas observed in this work ($C_{10}H_{16}N_2O_{7-9}$ and $C_{10}H_{18}N_2O_{8-}$

$_{10}$) have also been measured during SOAS.[22,58] However, which monoterpenes contributed to their formation and how they are formed were unclear. Therefore, we compared the major C_{10}-mononitrates and C_{10}-dinitrates measured in this work with the aerosol samples collected from SOAS. In **Figure 3.6**, we show the isomer-resolved IMS-TOF driftgram comparison of the most abundant C_{10}-mononitrates and C_{10}-dinitrates measured in this study (**Figure 3.6A**) and during SOAS (**Figure 3.6B** for the biomass burning sample and **Figure 3.6C** for the combined nighttime samples). The same CHON chemical formulas were observed in all the six SOAS filter samples. Remarkably, the major driftgram peaks of all these limonene-derived CHON in the laboratory-generated SOA line up well with those observed from the biomass burning and the nighttime aerosol samples, suggesting that the same structured CHON were present in our limonene + NO_3/O_3 experiments and SOAS. Further, although the driftgrams of the SOAS samples are usually broader and more complex due to the various monoterpene sources and pathways, CHON derived from limonene + NO_3/O_3 are often the most abundant isomeric products in the SOAS samples. These findings also demonstrate that the limonene CHON-RO_2 autoxidation and sequential oxidation studied in this work are also key processes in the real atmosphere where limonene emissions are abundant.

3.5 Supporting Information

3.5.1 Quantum Chemical Computational Methods and Strategies

The optimized geometries and frequency calculations for reactants, intermediates, transition states, and products were done by using MN15-L/MG3S[47,48] method because our previous investigations have been shown that MN15-L can obtain reliable results for hydrogen shift process.[51,64,65] Intrinsic reaction coordinate[66] calculations were performed by using MN15-L/MG3S to determine whether the located transition state connects the corresponding reactant and product. Single point energies were calculated by using CCSD(T)-F12a/cc-pVDZ-F12[45,46] theoretical methods. The method was chosen based on computational cost and accuracy. The wavefunction stability was tested to converge the right solution.

Kinetics calculations were estimated by using conventional transition state theory (TST) with Eckart tunneling,[50] where the rate constant (k_{TST}) is obtained for the lower conformer of transition states with the lowest reactant. Often, recrossing effects are quite small in the hydrogen shift; therefore, we ignore the recrossing effects in kinetics calculations. In addition, a scalar factor of 0.977 was used to correct the zero-point vibrational energies.

The electronic structure calculations were done by using Gaussian 16 for density functional calculations, while CCSD(T)-F12a/cc-pVDZ-F12 was calculated by using Molpro 2019.2.3 code. The kinetic calculations were performed by using Polyrate 2017C code and Gaussrate 2017-B. Multistructural generation of each isomer was done by using MSTor code.

3.5.2 Reactions of $C_{10}H_{16}NO_5$-RO_2 Hydrogen shift pathways by NO_3 initiated addition to the double bond in the endocyclic of limonene

For the two $C_{10}H_{16}NO_5$-RO_2 (~65% branching ratio and ~35% branching ratio) produced in limonene + NO_3 oxidation, we consider eight isomers caused by NO_3 and O_2 attacking sites on the cyclic of limonene. We labeled M1aX (~35% branching ratio) to indicate that O_2 attacks the side and NO_3 attacks the methyl carbon middle, but we label it M1bX (~65% branching ratio) to indicate that for NO_3 attacks the side and O_2 attacks the methyl carbon middle.

For each isomer, we considered possible hydrogen shift pathways outside the ring and on the ring, as shown in **Figures S3.7-S3.14**. We have found that the most favorable hydrogen shift pathway is M1a3 pathway with an enthalpy of activation of 21.03 kcal/mol at 0 K in limonene + NO_3 oxidation (~35% branching ratio) (**Figure S3.39**). The M1a3 pathway is 1,5-H shift process on the ring. We do not consider other hydrogen shift pathways due to high enthalpy of activation of ~ 22 – 44 kcal/mol at 0 K in limonene + NO_3 oxidation.

3.5.3 Reactions of $C_{10}H_{16}NO_4$-RO bond scission pathways by NO_3 initated addition to the double bond in the endocyclic of limonene

For $C_{10}H_{16}NO_4$-RO, there have eight isomers considered in current calculations and each of them have two reaction mechanism: one is C-C bond scission directly, other is C-C bond scission with NO_2 removal, as shown in **Figures S3.15-S3.22**. We labeled M2aX to indicate that O_2 lies the side and NO_3 lies the methyl carbon middle, but we label it M2bX to indicate that for NO_3 lies the side and O_2 lies the methyl carbon middle.

Compare the two reaction mechanisms, the C-C bond scission simultaneously with NO_2 removal is more favorable because the enthalpies of activation are 1.82 – 5.56 kcal/mol lower than those of the C-C bond scission directly at 0 K. We estimate approximately 8% for the C-C bond scission directly.

3.5.4 Hydrogen shift reactions of $C_{10}H_{16}NO_5$-RO_2 and $C_{10}H_{16}NO_4$-RO pathways by NO_3 initated addition to the double bond in the exocyclic of limonene

For $C_{10}H_{16}NO_5$-RO_2, we also considered four isomers caused by NO_3 and O_2 attacking site on the exocyclic of limonene and we labeled as M1c1, M1c2, M1c3, and M1c4 (~3% branching ratio). We considered possible hydrogen shift pathways for each isomer, as shown in **Figures S3.23-S3.26** to determine whether these processes can occur. However, it is noted that the contribution of these hydrogen shifts is quite small for the atmospheric oxidation of limonene by NO_3. Therefore, we only did these calculations by using MN15-L/MG3S density functional methods. The calculation results shows that 1, 6-H shift, 1, 6-closed ring, and 1,5-H shift pathways are more favorable pathways with the enthalpy of activation of 11.77 – 14.82 kcal/mol at 0 K (**Figures S3.24-S3.26**). The most favorable pathway is TS1c4-1 with enthalpy of activation of 11.77 kcal/mol at 0 K in M1c4 isomer, which occurs 1, 6-H shift in **Figure S3.26**.

For $C_{10}H_{16}NO_4$-RO, we also considered four isomers labelled as M2c1, M2c2, M2c3, and M2c4 and their possible hydrogen shift pathways, as shown in **Figures S3.27-S3.30**. The calculation results shows that 1,4-H shift is the most favorable pathway in all possible hydrogen shift pathways. These 1,4-H shift has the enthalpies of activation of 6.94 – 16.24 kcal/mol at 0 K in **Figures S3.27-S3.30**. The most favorable pathway is TS2c3-1 with enthalpy of activation of 6.94 kcal/mol at 0 K in M2c3 isomer, which listed in **Figure S3.29**. The present findings show that these peroxy and alkoxy radicals are formed by the exocyclic double bond of limonene initiated by NO_3, which can act as a potential site of autoxidation initiation.

3.5.5 Details of the rate constants

We only consider the rate constant calculations of the more favorable energy pathway in all hydrogen shift pathways, but consider all the rate constant calculations of C-C bond scission pathways. The calculated rate constants at 298 K are provided in **Table S3.4A** and **Table S3.4B**.

We considered the exocyclic double bond of limonene as a potential site of autoxidation initiation and calculated the rate constants at 298 K in **Table S3.4B**. All rate constants are calculated using conventional transition state theory with Eckart tunneling at the MN15-L/MG3S level.

For $C_{10}H_{16}NO_5$-RO_2, the estimated rate constants of 1, 5-H shift from 4.32×10^2 to 7.4×10^3 s^{-1} at 298 K, in which the 1, 5-H shift on the ring close to C=C bond (TS1c4-2) is the most favorable with a rate constant of 7.4×10^3 s^{-1} at 298 K. However, the 1, 6-H shift on the ring close to C=C bond (TS1c4-1) is the fastest reaction pathways with a rate constant 6.01×10^4 s^{-1} at 298 K in all unimolecular reactions, which is faster than the 1, 6-allylic rate constant of 36 s^{-1} at 298 K in the autoxidation of limonene initiated by OH radical at the CCSD(T)-F12a level;[60] This further indicates that the autoxidation rate constant from 1, 6-H shift site on the ring close to C=C bond are more feasible than other any sites in $C_{10}H_{16}NO_5$-RO_2, which is consistent with the unimolecular reactivity of autoxidation of limonene initiated by OH radical.[60,61]

For $C_{10}H_{16}NO_5$-RO, the estimated rate constants of 1, 4-H shift from 2.5×10^1 to 1.0×10^8 s^{-1} at 298 K, in which the 1, 4-H shift on the ring close to C=C bond viaTS2c3-1 is the fastest reaction pathways with a rate constant of 1.0×10^8 s^{-1} at 298 K. The rate constant of 1.0×10^8 s^{-1} at 298 K is faster than the rate coefficient of H-migration in substituted alkoxy radicals at 298 K predicted by previous SAR study.[62] It is noted that the 1, 5-H shift (TS2c1-2) is also fast with a rate constant of 2.82×10^4 s^{-1} at 298 K. Our calculation results show that alkoxy radical ($C_{10}H_{16}NO_5$-RO) hydrogen shift reaction is orders of magnitude faster than peroxy radical ($C_{10}H_{16}NO_5$-RO_2).

Table S3.1 The employed O_3 and NO_2 concentrations are listed along with the modeled f_{NO3} and modeled reacted limonene (Δlim) for the FTR on the left and for the CFSTR in the middle. Peak SOA mass concentrations (μg m^{-3}) (assuming an average SOA density of 1.33 g cm^{-3}) during filter collection experiments in the CFSTR are shown on the right.

	FTR				CFSTR				
Condition	O_3 (ppb)	NO_2 (ppb)	f_{NO3}	Δlim (ppb)	O_3 (ppb)	NO_2 (ppb)	f_{NO3}	Δlim (ppb)	SOA Mass Concentration (ug m^{-3})
1	1000	0	0	7.9	300	0	0	24.6	35
2	1000	23.2	0.11	8.7	300	25	0.23	26.2	37
3	1000	46.4	0.22	9.5	300	40	0.44	27.2	35
4	1000	69.5	0.30	10.2	300	60	0.66	28.3	37
5	1000	115.6	0.42	11.4	300	150	0.91	29.7	60
6	1000	161.5	0.50	12.4					
7	1000	229.9	0.58	13.6					

Table S3.2 MCM-simulated RO_2 bimolecular pseudo-first order rate under the experimental conditions.

FTR						CFSTR					
O_3 (ppb)	NO_2 (ppb)	$k_{RO2+RO2}$ (s^{-1})	$k_{RO2+HO2}$ (s^{-1})	$k_{RO2+NO3}$ (s^{-1})	Total (s^{-1})	O_3 (ppb)	NO_2 (ppb)	$k_{RO2+RO2}$ (s^{-1})	$k_{RO2+HO2}$ (s^{-1})	$k_{RO2+NO3}$ (s^{-1})	Total (s^{-1})
1000	0	0.175	6.16×10^{-3}	0	0.181	300	0	0.068	2.76×10^{-3}	0	0.071
1000	23.2	0.176	3.65×10^{-3}	1.17×10^{-4}	0.180	300	25	0.075	1.64×10^{-3}	5.20×10^{-5}	0.077
1000	46.4	0.185	3.10×10^{-3}	2.34×10^{-4}	0.188	300	40	0.093	1.18×10^{-3}	1.25×10^{-4}	0.094
1000	69.5	0.192	2.73×10^{-3}	3.43×10^{-4}	0.195	300	60	0.138	7.34×10^{-4}	2.61×10^{-4}	0.139
1000	115.6	0.205	2.24×10^{-3}	5.41×10^{-4}	0.208	300	150	0.287	2.95×10^{-4}	9.12×10^{-4}	0.288
1000	161.5	0.215	1.91×10^{-3}	7.13×10^{-4}	0.218						
1000	229.9	0.227	1.58×10^{-3}	9.28×10^{-4}	0.230						

Table S3.3 Modified and new reactions in the MCM limonene + NO$_3$ mechanism.

Reaction[a]	Rate constant[b] (cm^3 mole^{-1} s^{-1} or s^{-1})	Note
LIMONENE + NO3 = 0.65×NLIMO2+0.35×NLIMO2B	1.22×10^{-11}	c
NLIMO2B + HO2 = NLIMOOH	KRO2HO2×0.914	
NLIMO2B + NO = NLIMO + NO2	KRO2NO	
NLIMO2B + NO3 = NLIMO + NO2	KRO2NO3	
NLIMO2B + RO2 = LIMBNO3	$8.8\times10^{-13}\times0.2$	d
NLIMO2B + RO2 = C10H15NO4	$8.8\times10^{-13}\times0.2$	d
NLIMO2B + RO2 = NLIMO	$8.8\times10^{-13}\times0.6$	d
NLIMO = LIMAL + NO2	KDEC×0.92	e
NLIMO2B = C10H16NO7RO2	kautox_M1a	f
NLIMO = C10H16NO6RO2	KDEC×0.08	e
C10H16NO*x*RO2 + HO2 = C10H17NO*x*	KRO2HO2×0.914	g
C10H16NO*x*RO2 + NO = C10H16NO(*x*-1)RO + NO2	KRO2NO	g
C10H16NO*x*RO2 + NO3 = C10H16NO(*x*-1)RO + NO2	KRO2NO3	g
C10H16NO*x*RO2 + RO2 = C10H17NO(*x*-1)	$5\times10^{-13}\times0.25$	g,h
C10H16NO*x*RO2 + RO2 = C10H15NO(*x*-1)	$5\times10^{-13}\times0.10$	g,h
C10H16NO*x*RO2 + RO2 = C10H16NO(*x*-1)RO	$5\times10^{-13}\times0.65$	g,h
C10H16NO*x*RO2 = C10H16NO(*x*+2)RO2	kautox_other	g,i
C10H16NO(*x*-1)RO = fragmentation products	KDEC×(1-fROautox)×0.8	g,j
C10H16NO(*x*-1)RO = C10H15NO(*x*-1) + HO2	KDEC×(1-fROautox)×0.2	g,j
C10H16NO(*x*-1)RO = C10H16NO(*x*+1)RO2	KDEC×fROautox	g,j
C10H16NO(*x*+2)RO2 = C10H15NO(*x*+1) + OH	kself_termination	g,k
LIMALACO + NO3 = C10H14NO8RO2	2.6×10^{-13}	l
LIMALBCO + NO3 = C10H14NO8RO2	2.6×10^{-13}	l
LIMBCO + NO3 = C10H16NO7RO2	2.6×10^{-13}	l
LIMALBOH + NO3 = C10H16NO8RO2	2.6×10^{-13}	l
LIMONONIC + NO3 = C10H16NO8RO2	2.6×10^{-13}	l
LIMALAOH + NO3 = C10H16NO8RO2	2.6×10^{-13}	l
LIMALBOOH + NO3 = C10H16NO9RO2	2.6×10^{-13}	l
LIMALAOOH + NO3 = C10H16NO9RO2	2.6×10^{-13}	l
C923CO3H + NO3 = C10H16NO9RO2	2.6×10^{-13}	l
LIMALACO + O3 = 0.67×LMLKACO + 0.67×HCHO + 0.33×CH2OOF + 0.33×C9RO2	8.3×10^{-18}	m
LIMALBCO + O3 = 0.67×LMLKBCO + 0.67×HCHO + 0.33×CH2OOF + 0.33×C9RO2	8.3×10^{-18}	m

LIMBCO + O3 = 0.67×LMKBCO + 0.67×HCHO + 0.33×CH2OOF + 0.33×C9RO2	8.3×10^{-18}	m
LIMALBOH + O3 = 0.67×LMLKBOH + 0.67×HCHO + 0.33×CH2OOF + 0.33×C9RO2	8.3×10^{-18}	m
LIMONONIC + O3 = 0.67×KLIMONONIC + 0.67×HCHO + 0.33×CH2OOF + 0.33×C9RO2	8.3×10^{-18}	m
LIMALAOH + O3 = 0.67×LMLKAOH + 0.67×HCHO + 0.33×CH2OOF + 0.33×C9RO2	8.3×10^{-18}	m
LIMALBOOH + O3 = 0.67×LMLKBOOH + 0.67×HCHO + 0.33×CH2OOF + 0.33×C9RO2	8.3×10^{-18}	m
LIMALAOOH + O3 = 0.67×LMLKAOOH + 0.67×HCHO + 0.33×CH2OOF + 0.33×C9RO2	8.3×10^{-18}	m
C923CO3H + O3 = 0.67×C817CO3H + 0.67×HCHO + 0.33×CH2OOF + 0.33×C9RO2	8.3×10^{-18}	m

[a]Chemical names are from MCM for most species; new names are given for species not existing in MCM. [b]All rate constants are from MCM except for the H shift rate constants. [c]The minor pathway (35%) to form M1a (NLIMO2B) is included. [d]RO_2 + RO_2 reactions for NLIMO2B; the same product name is used for the alcohol (LIMBNO3) and RO (NLIMO) as for NLIMO2 and a new ketone product (C10H15NO4) is added. [e]The branching ratios are based on quantum calculations. [f]The autoxidation rate constant is based on the quantum calculations. [g]Generic RO_2 and RO chemistry for HOM CHON-RO2 with $x = 6 – 9$. [h]RO_2 + RO_2 reactions for HOM CHON-RO2; the reaction rate constants and branching ratios are averages of values for secondary RO_2 and tertiary RO_2 in MCM. [i]The further autoxidation rate constant for HOM CHON-RO2, which is assumed to be equal to or faster than kautox_M1a. [j]Branching ratio of RO decomposition vs. isomerization for HOM CHON-RO. [k]Self-termination reactions for HOM CHON-RO2 that contain at least one secondary -OOH group. [l]Rate constants follow that for limonaldehyde + NO_3. [m]Rate constants follow that for limonaldehyde + O_3.

Table S3.4A The estimated rate constants *k* (s^{-1}) for the H shift and carbon-carbon bond scission process of limonene + NO_3 oxidation.

Reactions	298 K, *k* (s^{-1})
TS1a3-1[a]	1.70E-02
TSM2a1α	1.88E+06
TSM2a1β	4.81E+03
TSM2a2α	1.60E+06
TSM2a2β	5.15E+02
TSM2a3α	1.61E+06
TSM2a3β	5.49E+02
TSM2a4α	1.57E+13
TSM2a4β	1.35E+09
TSM2b1α	3.71E+06
TSM2b1β	2.85E+05
TSM2b2α	8.96E+05
TSM2b2β	6.49E+04
TSM2b3α	2.66E+06
TSM2b3β	5.73E+03
TSM2b4α	2.39E+07
TSM2b4β	1.41E+04

[a] TS1a3-1 is the transition state of 1,5-H shift on the ring in limonene + NO_3 oxidation.

[b] TSM2a1α and TSM2a1β denote that the formation pathway of limonaldehyde and NO_2 and the C-C bond scission directly, respectively. The other pathways are the same label way.

Table S3.4B The estimated rate constants *k* (s^{-1}) for the H shift reactions of $C_{10}H_{16}NO_5$-RO_2 and $C_{10}H_{16}NO_4$-RO pathways.

Reactions	298 K, *k* (s^{-1})
TS1c2-1	1.46E+03
TS1c3-1	1.76E+03
TS1c3-2	4.32E+02
TS1c3-3	2.68E+00
TS1c4-1	6.01E+04
TS1c4-2	7.40E+03
TS2c1-1	8.30E+05
TS2c1-2	2.82E+04
TS2c1-3	2.50E+01
TS2c2-1	7.78E+02
TS2c2-2	7.69E+01
TS2c3-1	1.00E+08
TS2c3-2	7.88E+00
TS2c4-1	3.78E+07
TS2c4-2	2.40E+02

[a] TS1c2-1, TS1c3-2, and TS1c4-2 are the transition state of 1, 5-H shift on the ring close to C=C bond in the M1c2, M1c3, and M1c4 isomers of $C_{10}H_{16}NO_5$-RO_2, respectively; TS1c3-1 is 1, 6-ring closed on the ring in M1c1 isomer, TS1c3-3 and TS1c4-1 are 1, 6-H shift on the ring close to C=C bond in the M1c3 and M1c4 isomers, respectively.

[b] TS2c1-1, TS2c2-1, TS2c2-2, TS2c3-1, TS2c3-2, TS2c4-1, and TS2c4-2 are the transition state of 1, 4-H shift on the ring in the M2c1, M2c2, M2c3, and M2c4 isomers of $C_{10}H_{16}NO_5$-RO, respectively; TS2c1-2 is the transition state of 1, 5-H shift on the ring in the M2c1 isomers of $C_{10}H_{16}NO_5$-RO.

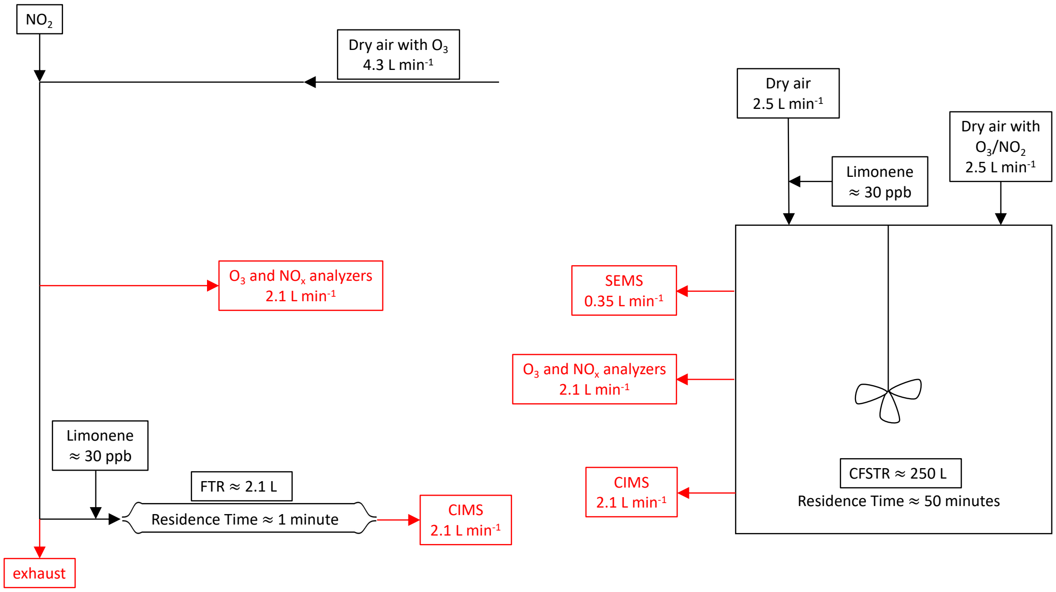

Figure S3.1 Diagrams of the experimental setup for the FTR (left) and CFSTR (right). O_3, NO_2 and limonene injected with dry air are shown in black and outflows to analytical instruments and to exhaust are shown in red.

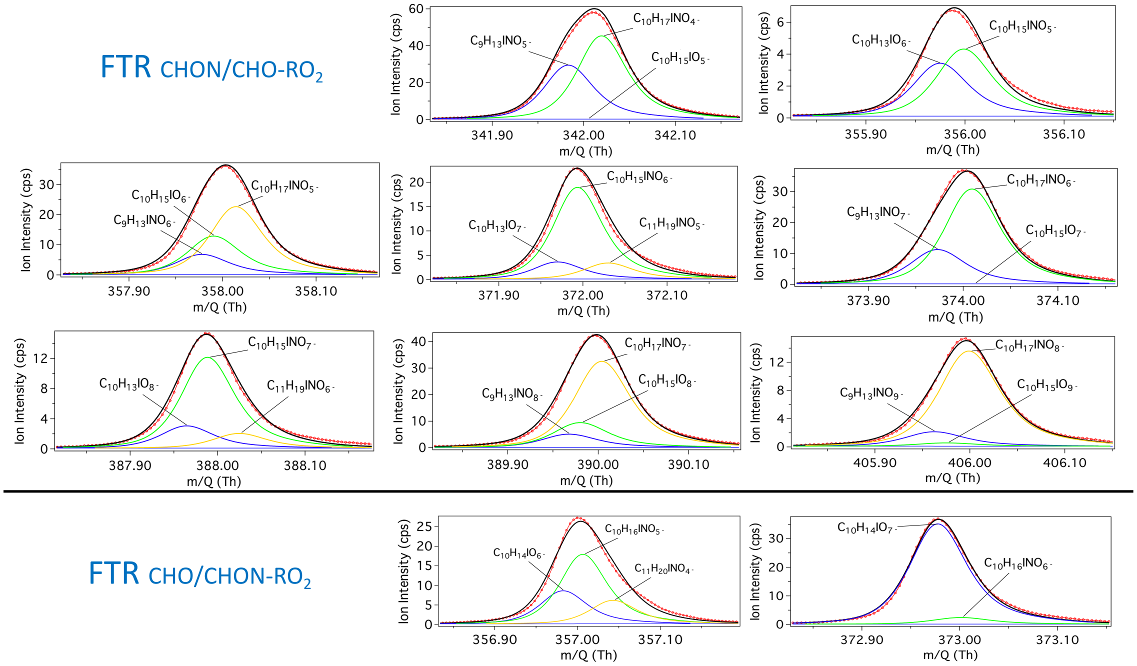

Figure S3.2 The peak fittings from the I-CIMS data for eight major CHON/CHO-RO$_2$ and two major CHO/CHON-RO$_2$ in the FTR. At each m/Q, multiple peaks were identified and shown by chemical formula labels. The red peaks represent the raw peak intensity, the black peaks represent the total summed fitting of all peaks and other colored peaks represent individual formula fittings.

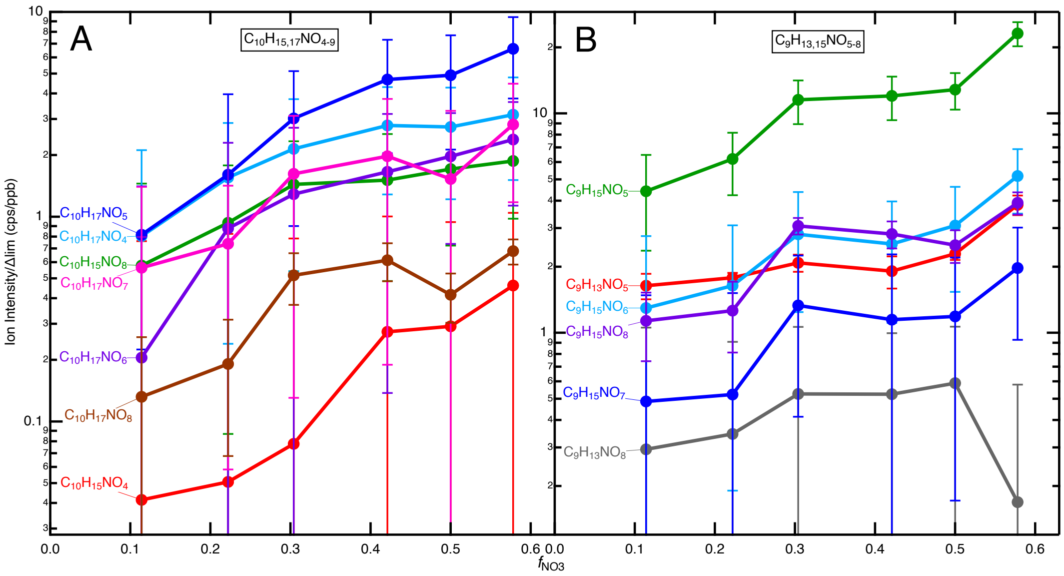

Figure S3.3 The gas-phase ion intensities for: (A) $C_{10}H_{15,17}NO_{4-9}$ and (B) $C_9H_{13,15}NO_{5-8}$ using a log scale vs. f_{NO3} for the FTR experiments. Different colors are used within each panel and corresponding-colored labels are included to distinguish each chemical formula. The error bars represent the standard deviations.

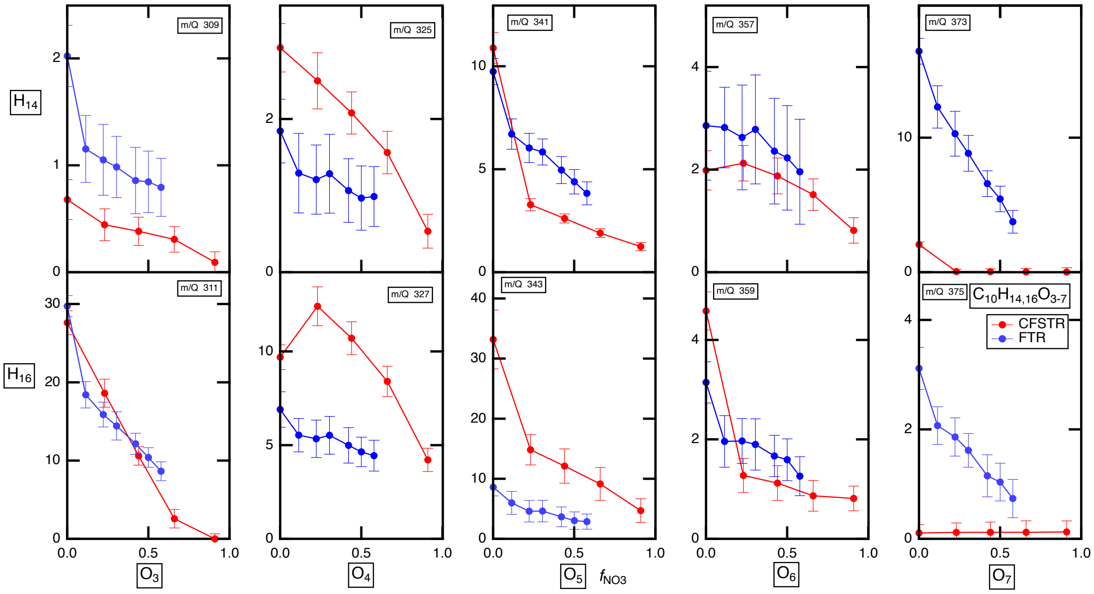

Figure S3.4 The gas-phase ion intensities of all the identified $C_{10}H_{14,16}O_{3\text{-}7}$ as a function of f_{NO3}. The FTR results are shown in blue and the CFSTR results are shown in red.

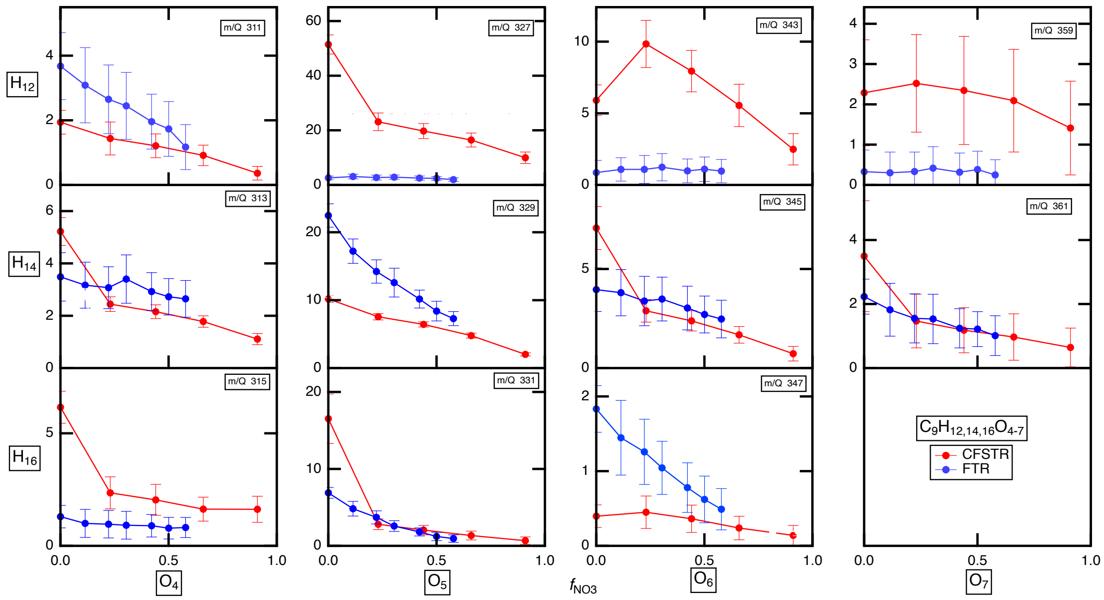

Figure S3.5 The gas-phase ion intensities of all identified $C_9H_{12,14,16}O_{4-7}$ as a function of f_{NO3}. The FTR results are shown in blue and the CFSTR results are shown in red.

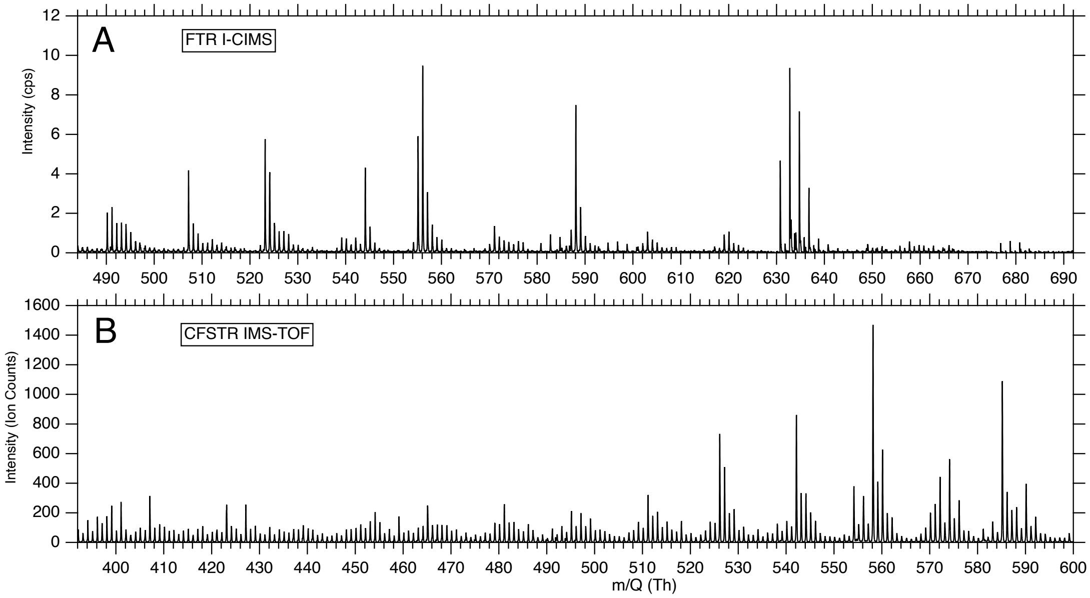

Figure S3.6 Mass spectra of the dimer ranges for (A) gas phase (I-CIMS) in the FTR and (B) particle phase (IMS-TOF) in the CFSTR. The *x*-axes are different to account for different ion-adducts (i.e., iodide-adduct in the I-CIMS and chloride-adduct in the IMS-TOF, that differ by 92 Th). At these dimer ranges, the chemical formulas are challenging to be assigned with high confidence, and hence the dimer products are not discussed in detail.

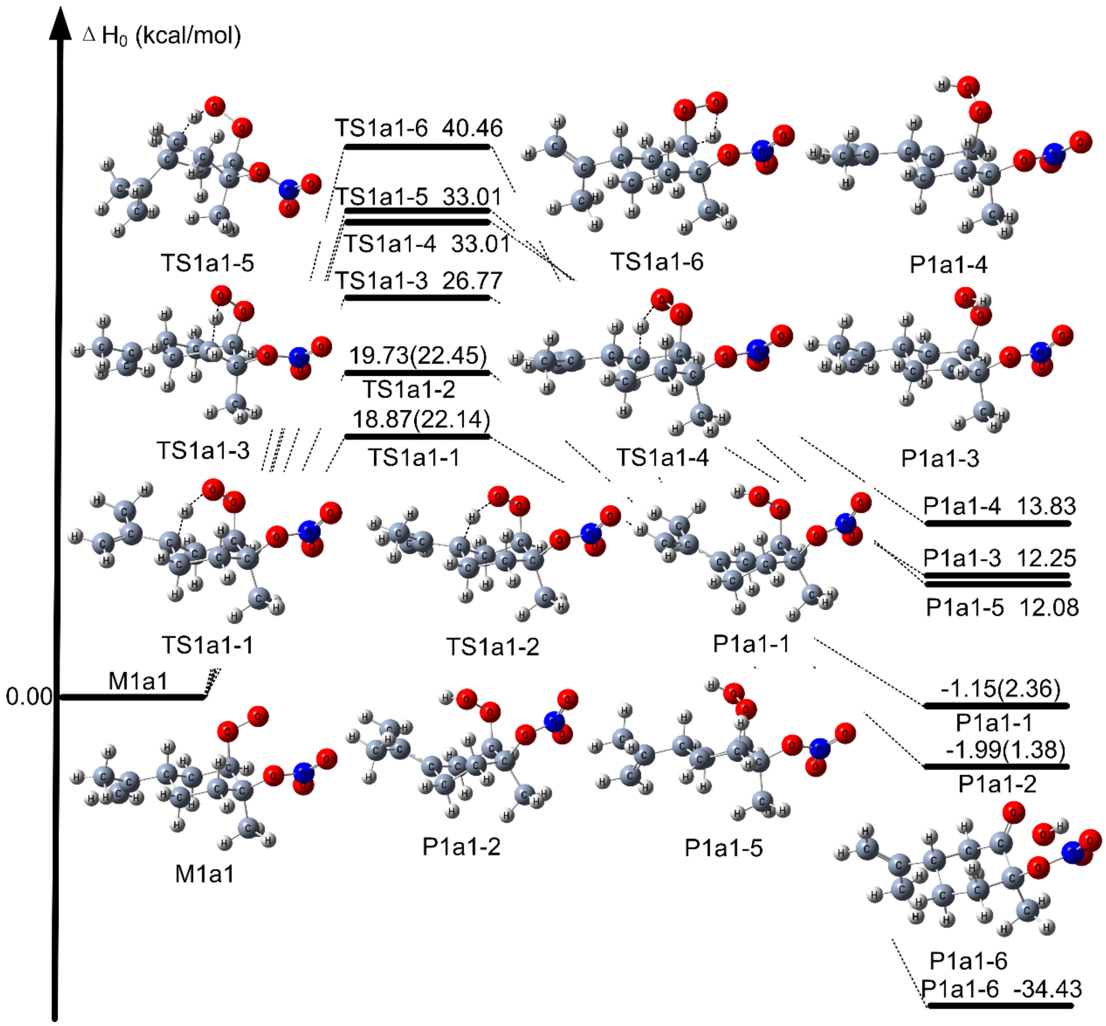

Figure S3.7 The calculated enthalpy profile at 0 K for the M1a1 isomer H-shift reaction at the MN15-L/MG3S (in parentheses at CCSD(T)-F12a/cc-pVDZ-F12//MN15-L/MG3S) level.

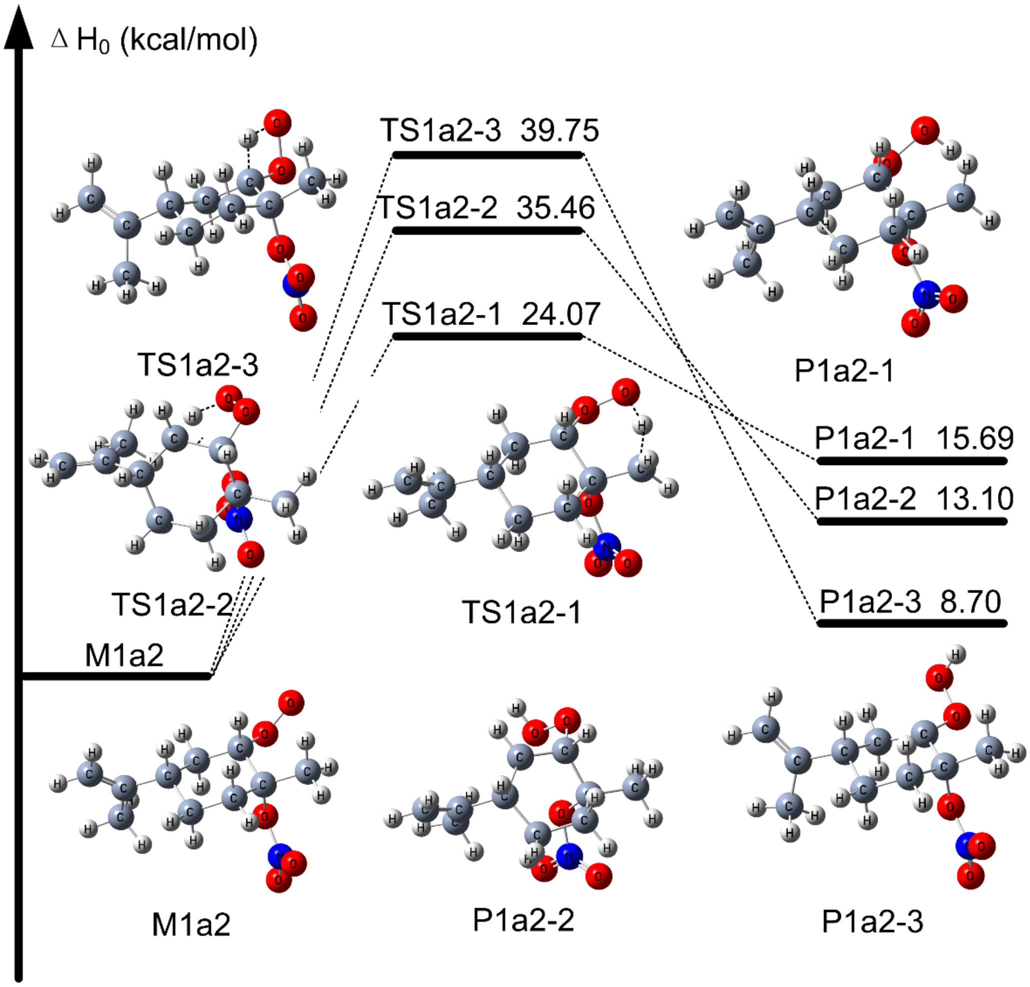

Figure S3.8 The calculated enthalpy profile at 0 K for the M1a2 isomer H-shift reaction at the MN15-L/MG3S level.

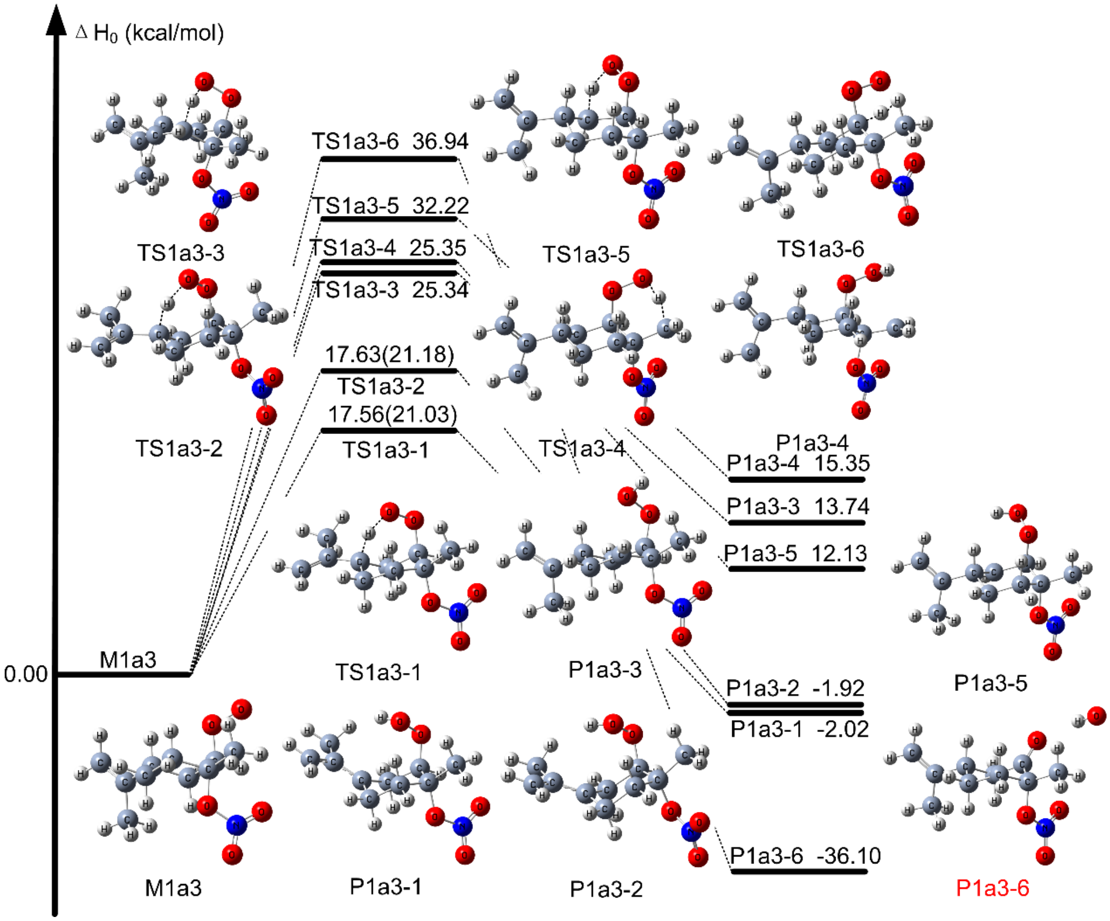

Figure S3.9 The calculated enthalpy profile at 0 K for the M1a3 isomer H-shift reaction at the MN15-L/MG3S (in parentheses at CCSD(T)-F12a/cc-pVDZ-F12//MN15-L/MG3S) level.

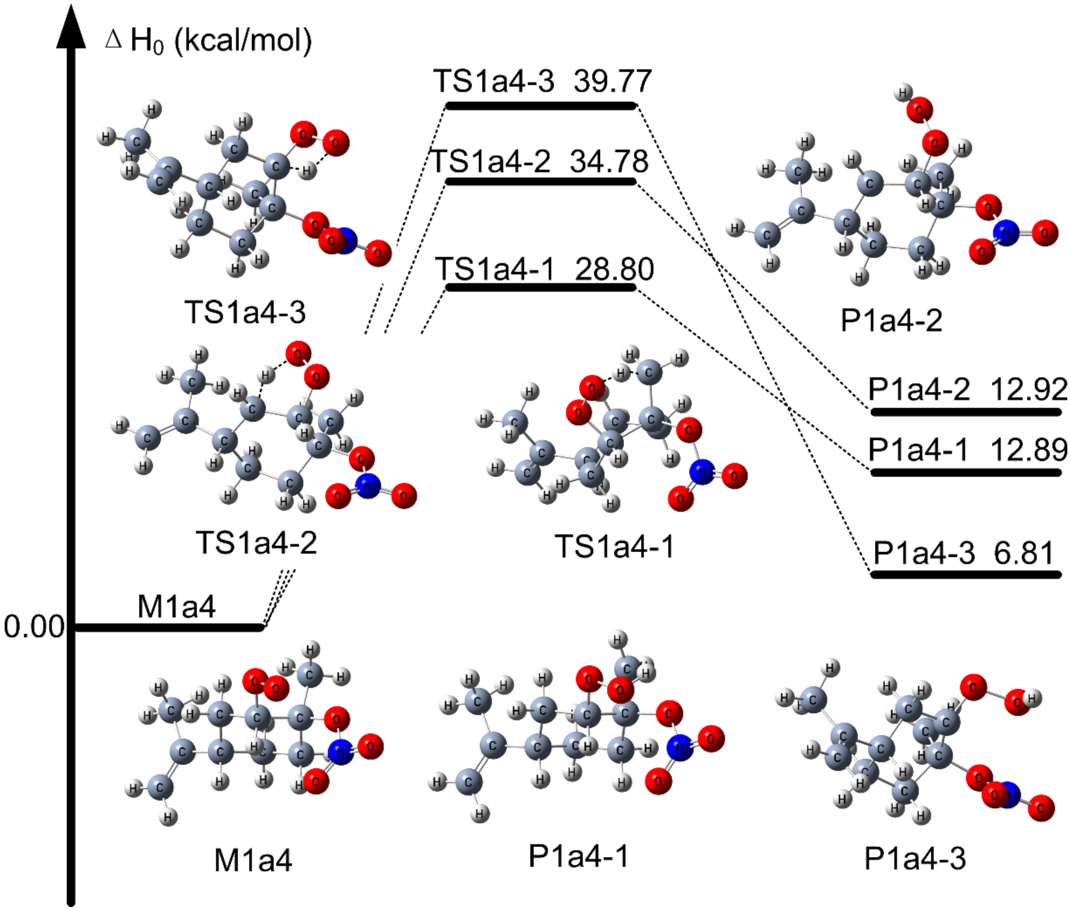

Figure S3.10 The calculated enthalpy profile at 0 K for the M1a4 isomer H-shift reaction at the MN15-L/MG3S level.

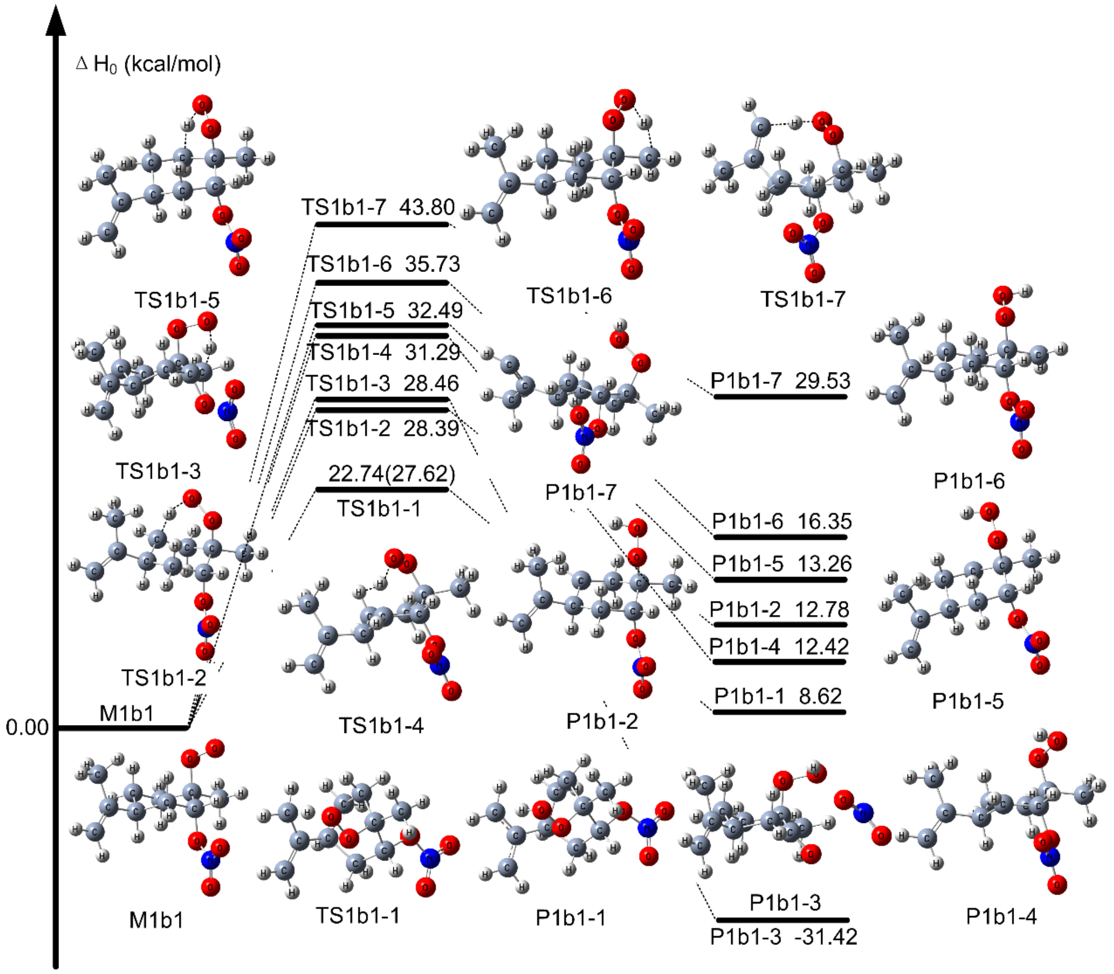

Figure S3.11 The calculated enthalpy profile at 0 K for the M1b1 isomer H-shift reaction at the MN15-L/MG3S (in parentheses at CCSD(T)-F12a/cc-pVDZ-F12//MN15-L/MG3S) level.

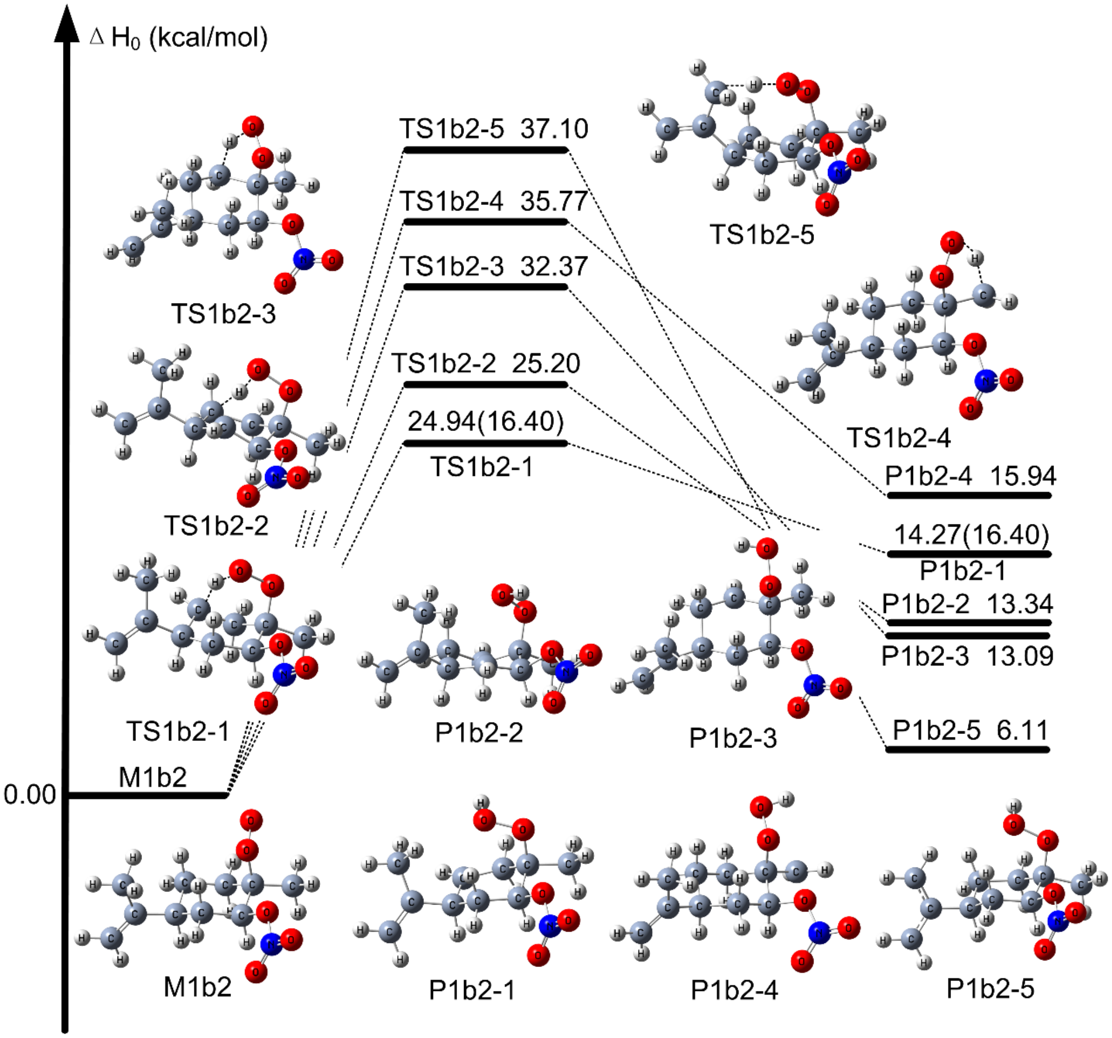

Figure S3.12 The calculated enthalpy profile at 0 K for the M1b2 isomer H-shift reaction at the MN15-L/MG3S (in parentheses at CCSD(T)-F12a/cc-pVDZ-F12//MN15-L/MG3S) level.

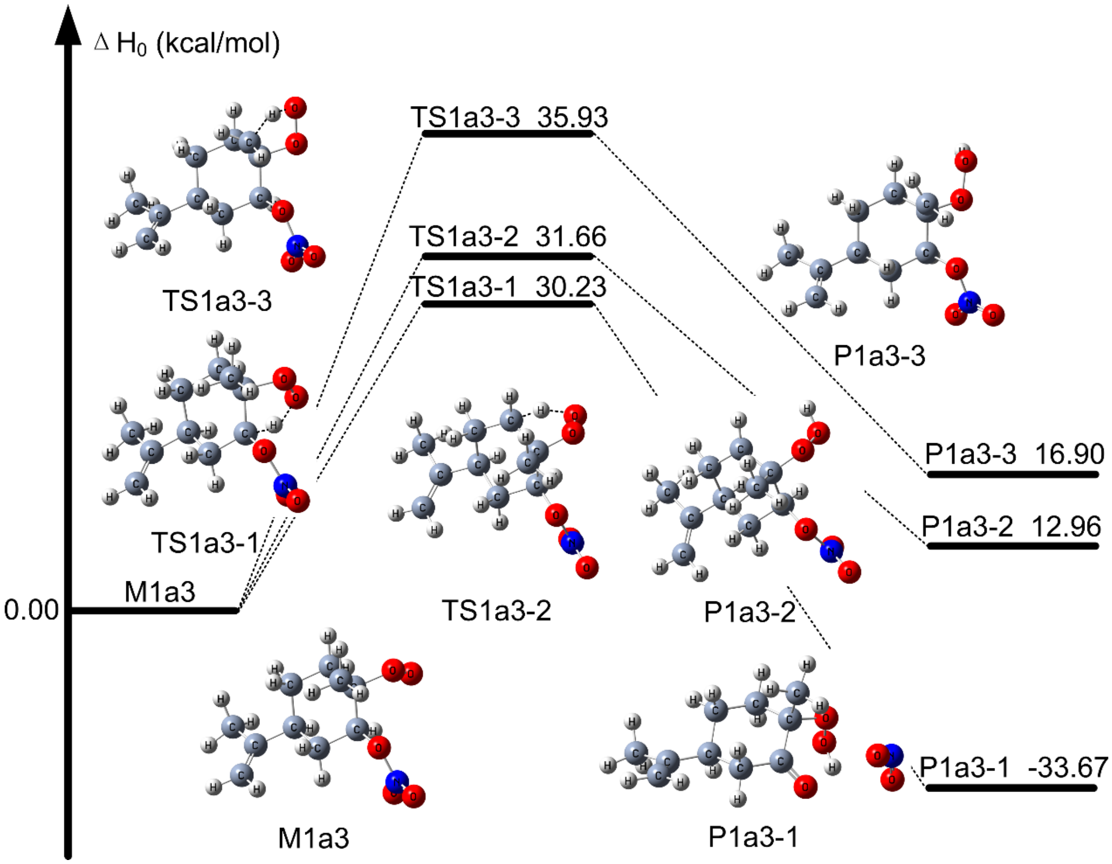

Figure S3.13 The calculated enthalpy profile at 0 K for the M1b3 isomer H-shift reaction at the MN15-L/MG3S level.

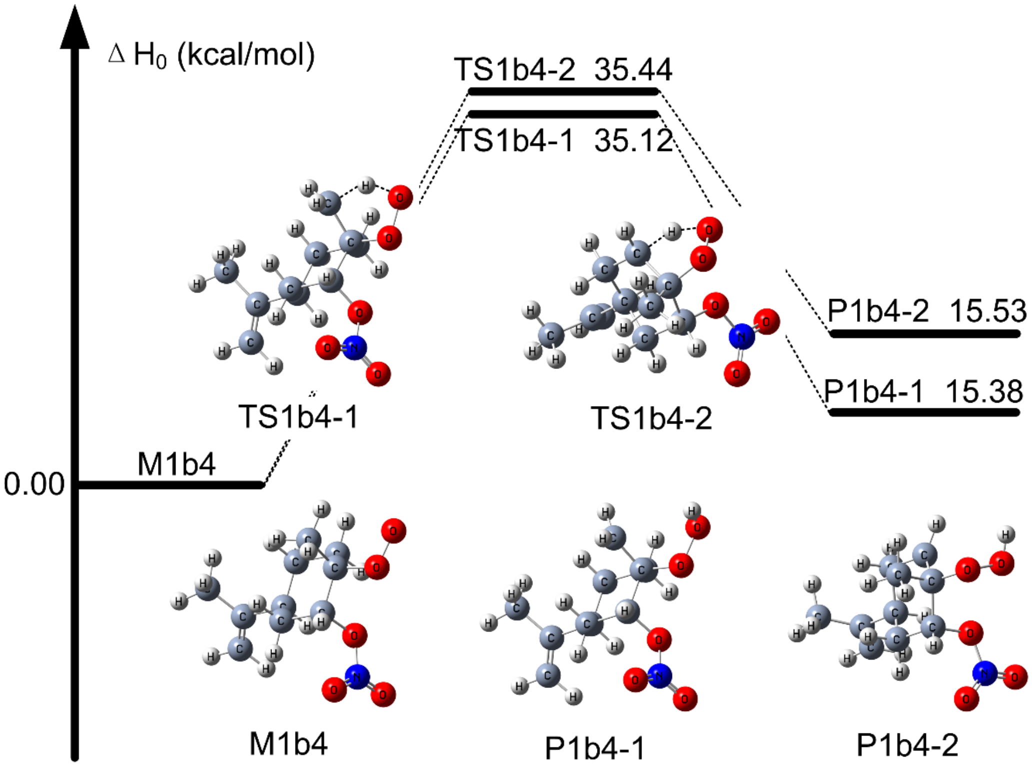

Figure S3.14 The calculated enthalpy profile at 0 K for the M1b4 isomer H-shift reaction at the MN15-L/MG3S level.

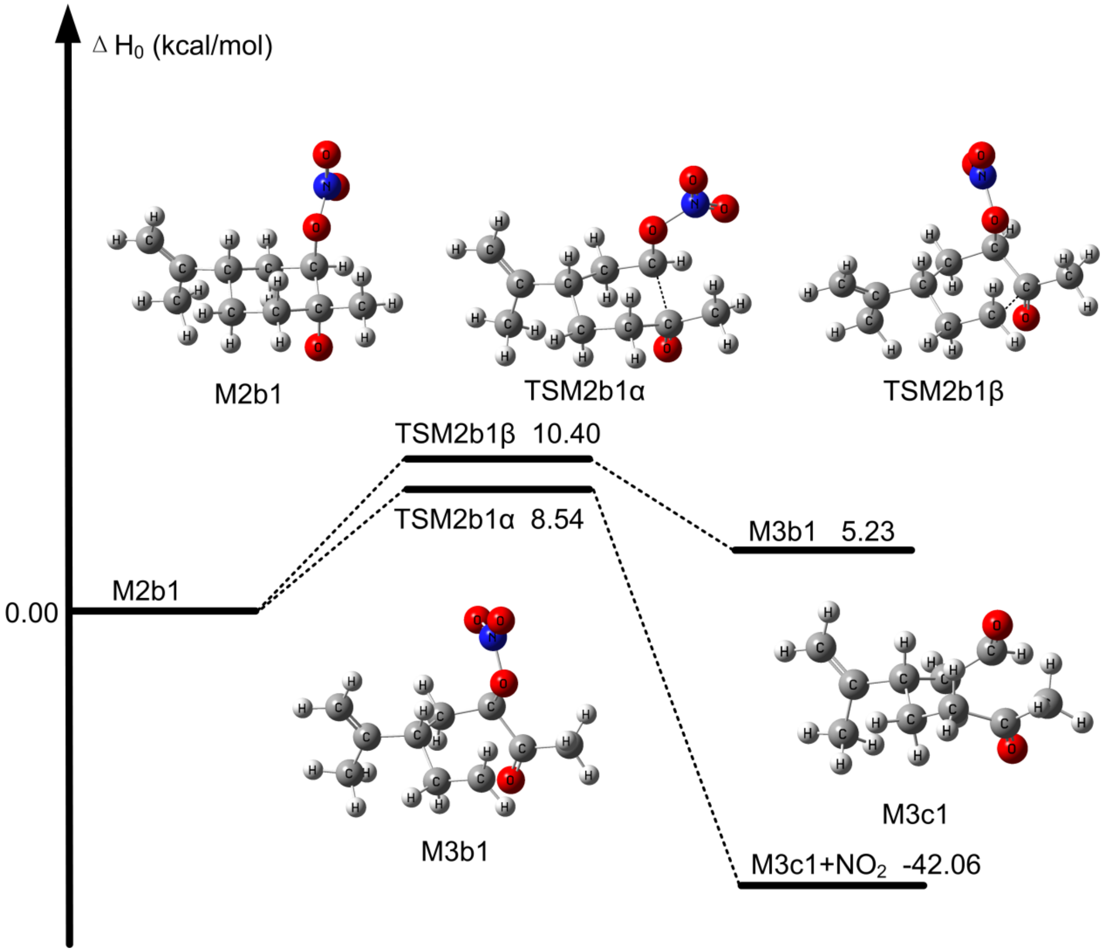

Figure S3.15 The calculated enthalpy profile at 0 K for the M2b1 isomer C-C bond scission and C-C bond scission concerted with NO_2 remove reaction at the CCSD(T)-F12a/cc-pVDZ-F12/MN15-L/MG3S level.

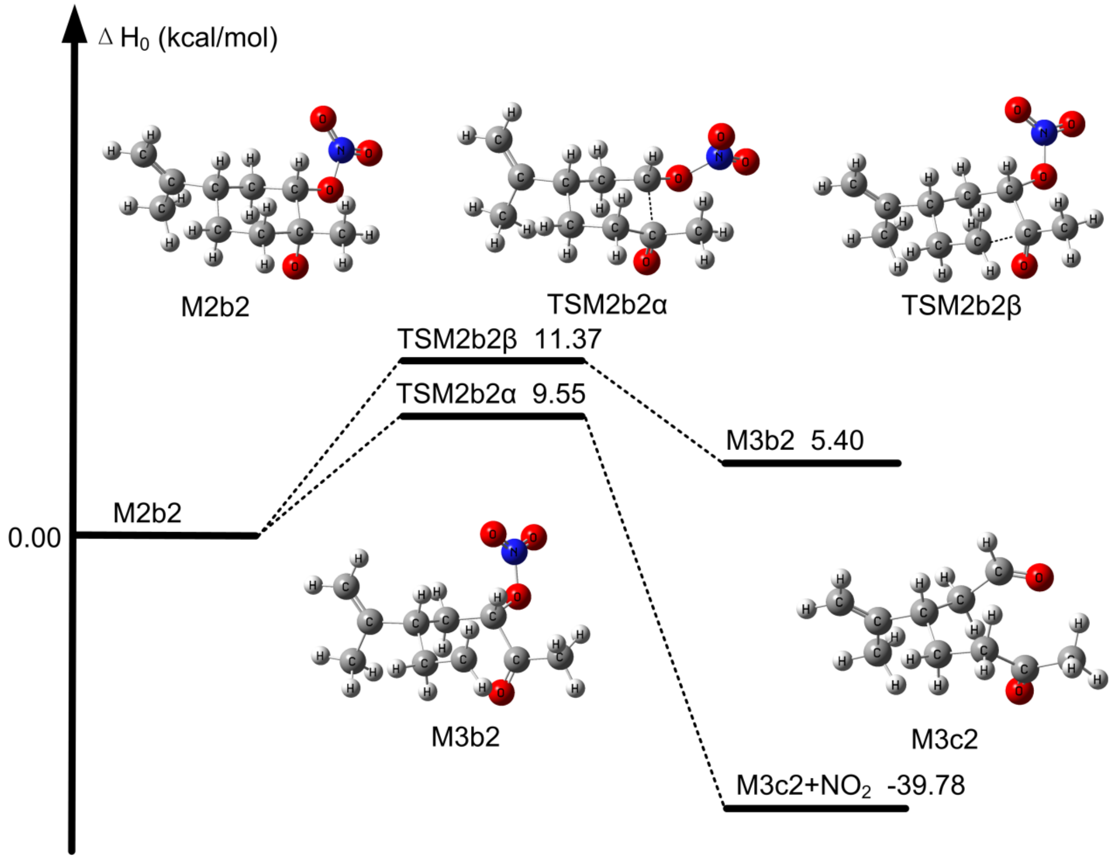

Figure S3.16 The calculated enthalpy profile at 0 K for the M2b2 isomer C-C bond scission and C-C bond scission concerted with NO_2 remove reaction at the CCSD(T)-F12a/cc-pVDZ-F12/MN15-L/MG3S level.

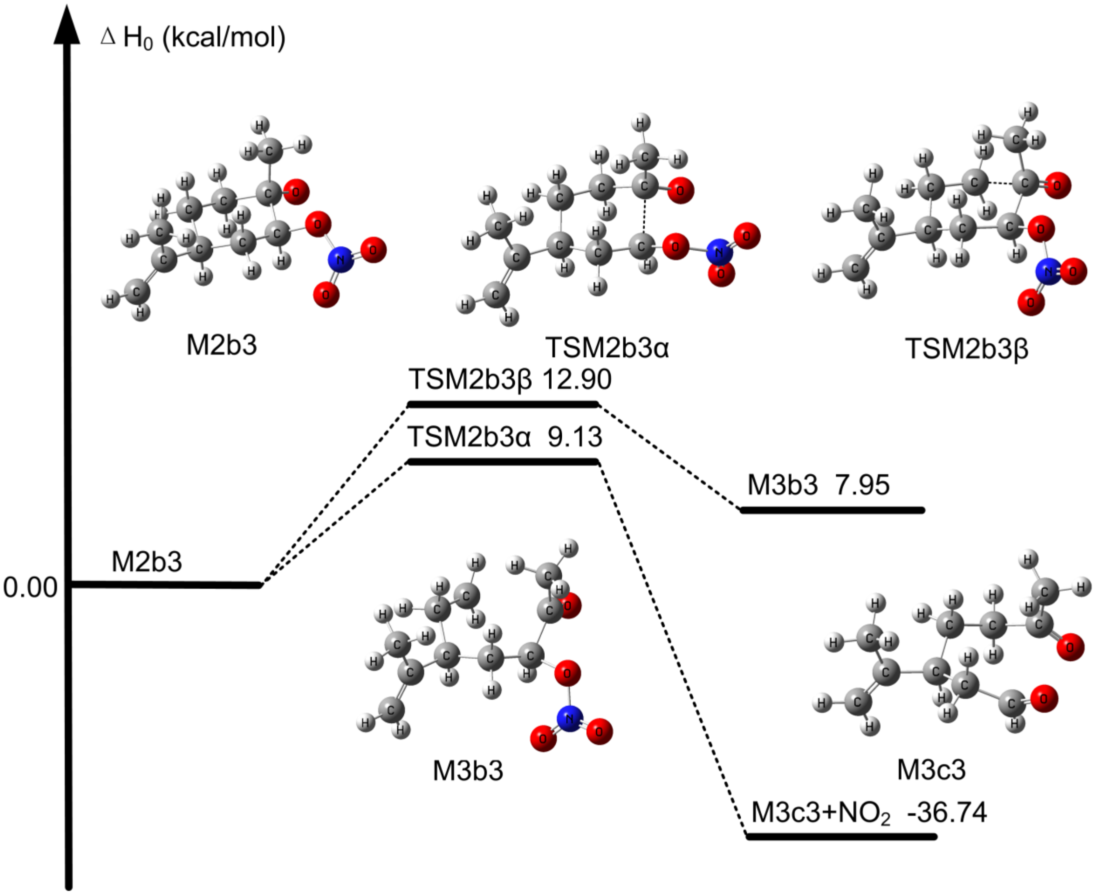

Figure S3.17 The calculated enthalpy profile at 0 K for the M2b3 isomer C-C bond scission and C-C bond scission concerted with NO_2 remove reaction at the CCSD(T)-F12a/cc-pVDZ-F12/MN15-L/MG3S level.

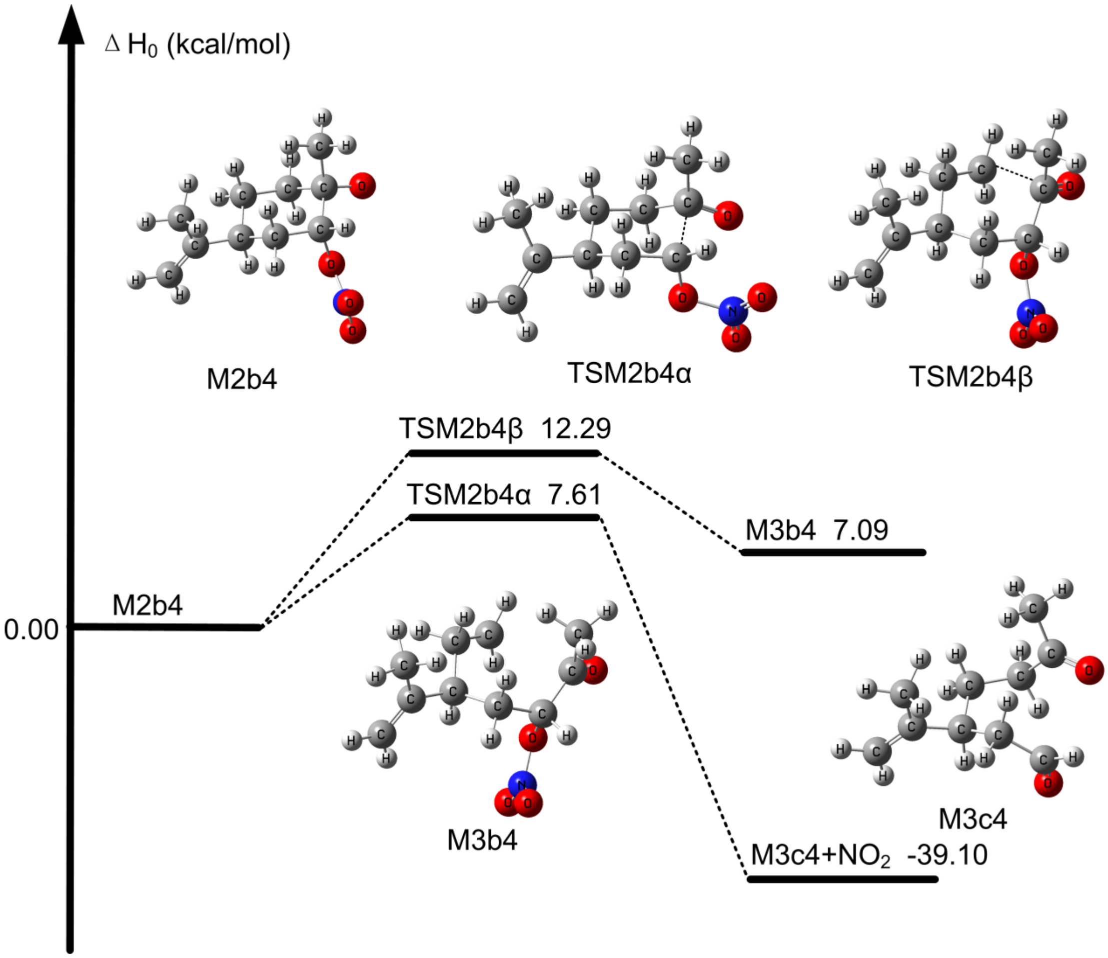

Figure S3.18 The calculated enthalpy profile at 0 K for the M2b4 isomer C-C bond scission and C-C bond scission concerted with NO_2 remove reaction at the CCSD(T)-F12a/cc-pVDZ-F12/MN15-L/MG3S level.

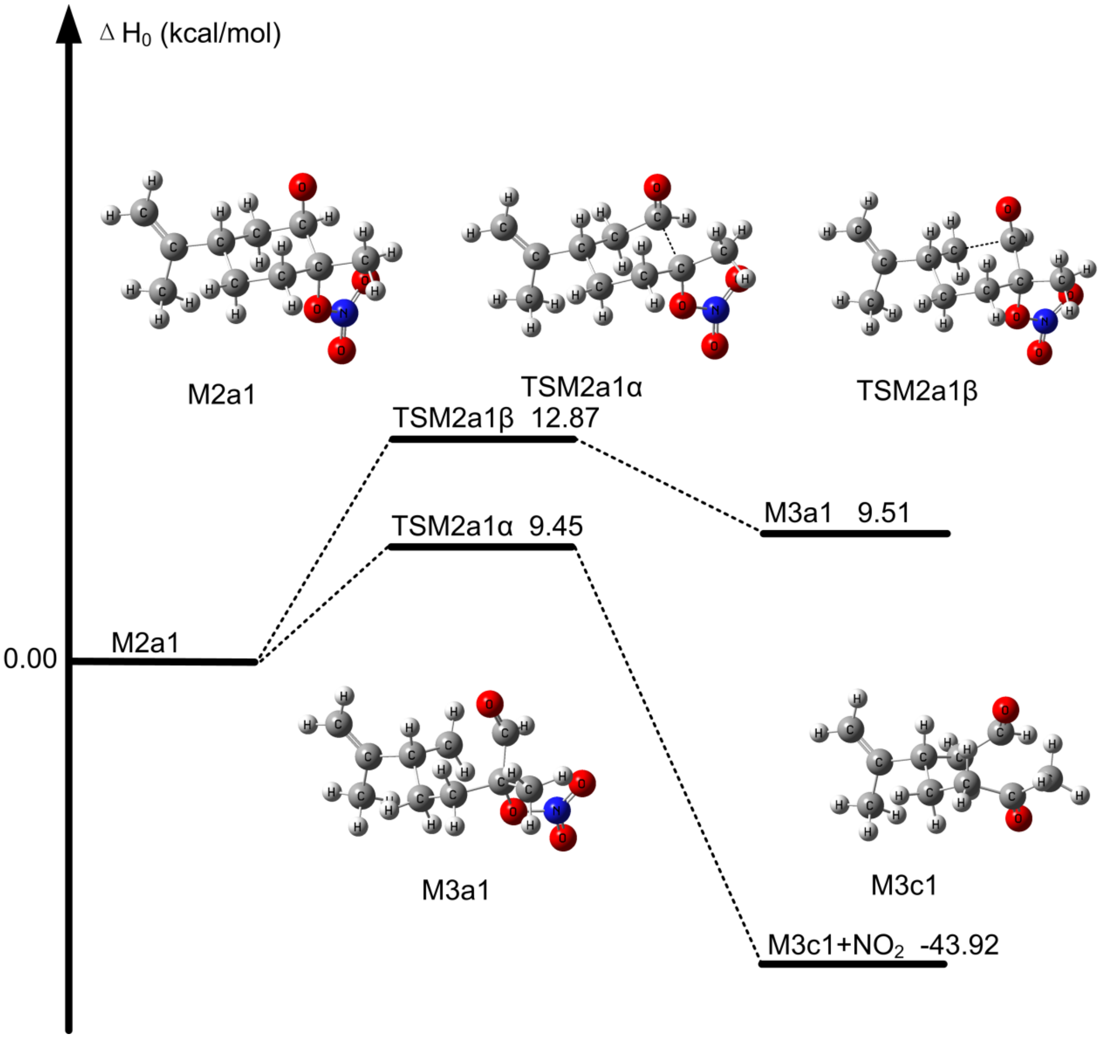

Figure S3.19 The calculated enthalpy profile at 0 K for the M2a1 isomer C-C bond scission and C-C bond scission concerted with NO_2 remove reaction at the CCSD(T)-F12a/cc-pVDZ-F12/MN15-L/MG3S level.

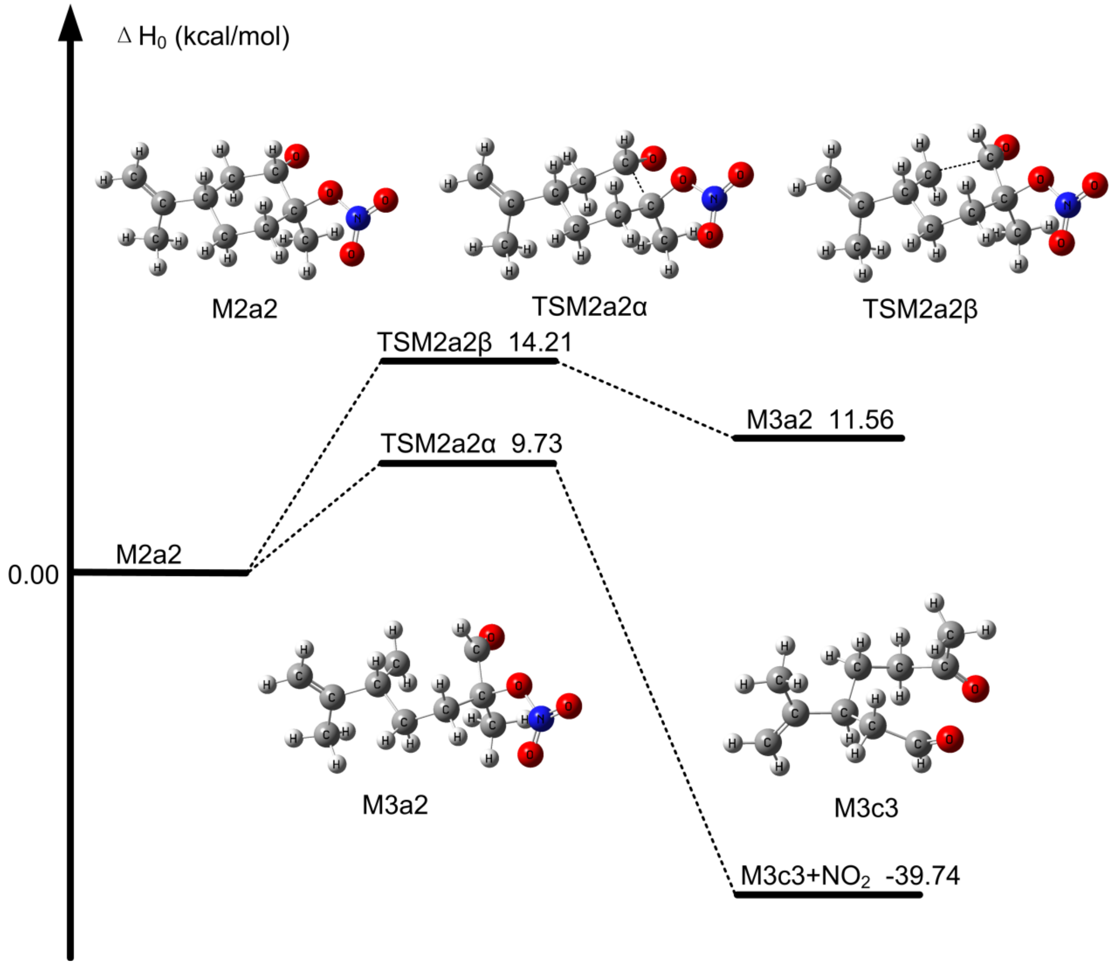

Figure S3.20 The calculated enthalpy profile at 0 K for the M2a2 isomer C-C bond scission and C-C bond scission concerted with NO₂ remove reaction at the CCSD(T)-F12a/cc-pVDZ-F12/MN15-L/MG3S level.

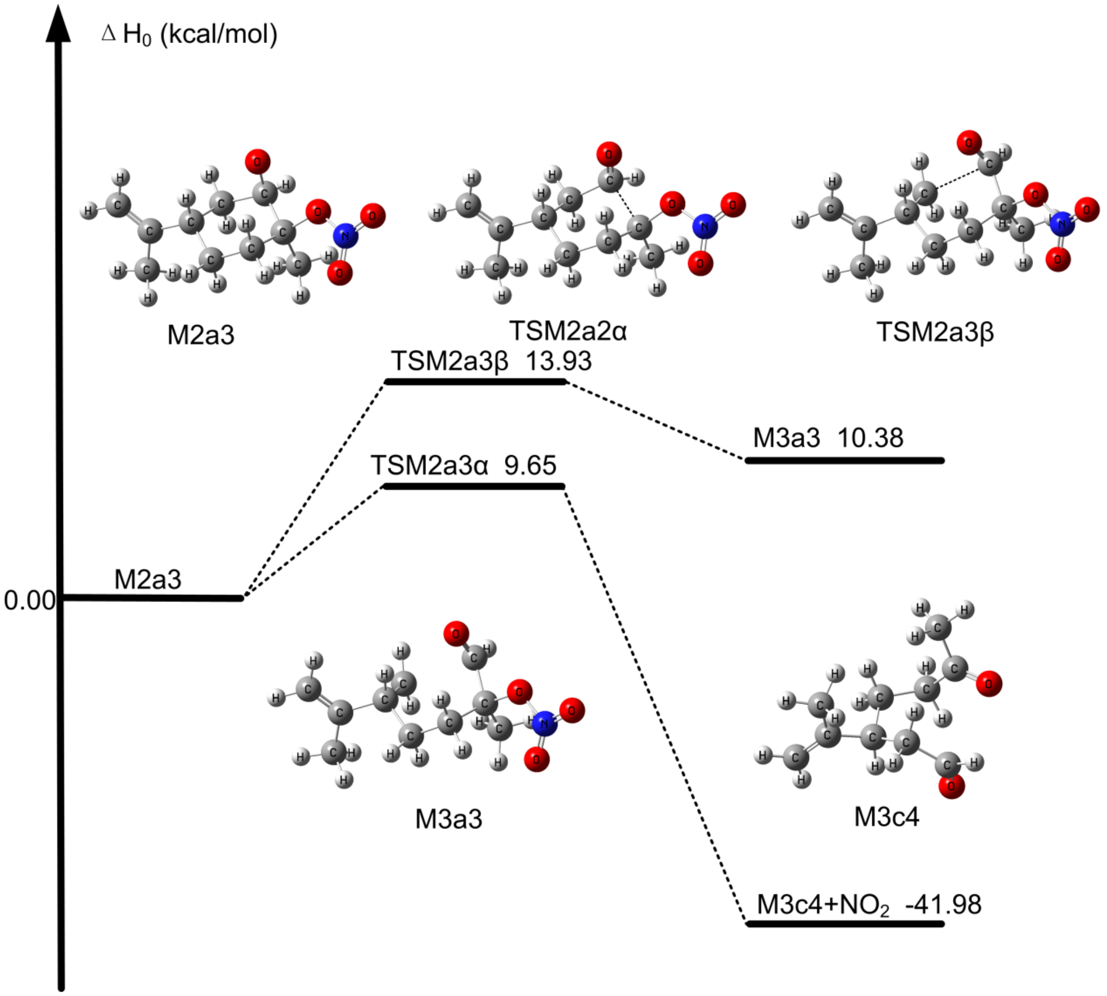

Figure S3.21 The calculated enthalpy profile at 0 K for the M2a3 isomer C-C bond scission and C-C bond scission concerted with NO_2 remove reaction at the CCSD(T)-F12a/cc-pVDZ-F12/MN15-L/MG3S level.

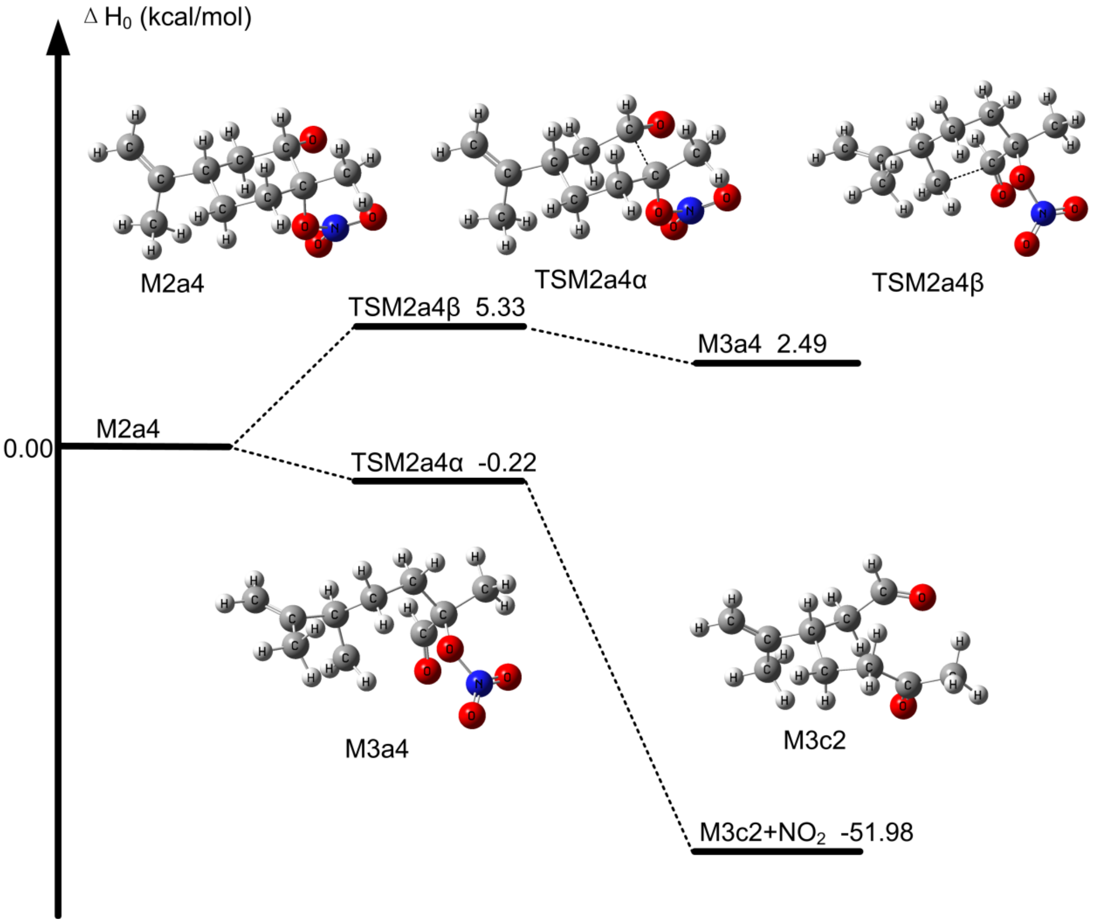

Figure S3.22 The calculated enthalpy profile at 0 K for the M2a4 isomer C-C bond scission and C-C bond scission concerted with NO_2 remove reaction at the CCSD(T)-F12a/cc-pVDZ-F12/MN15-L/MG3S level.

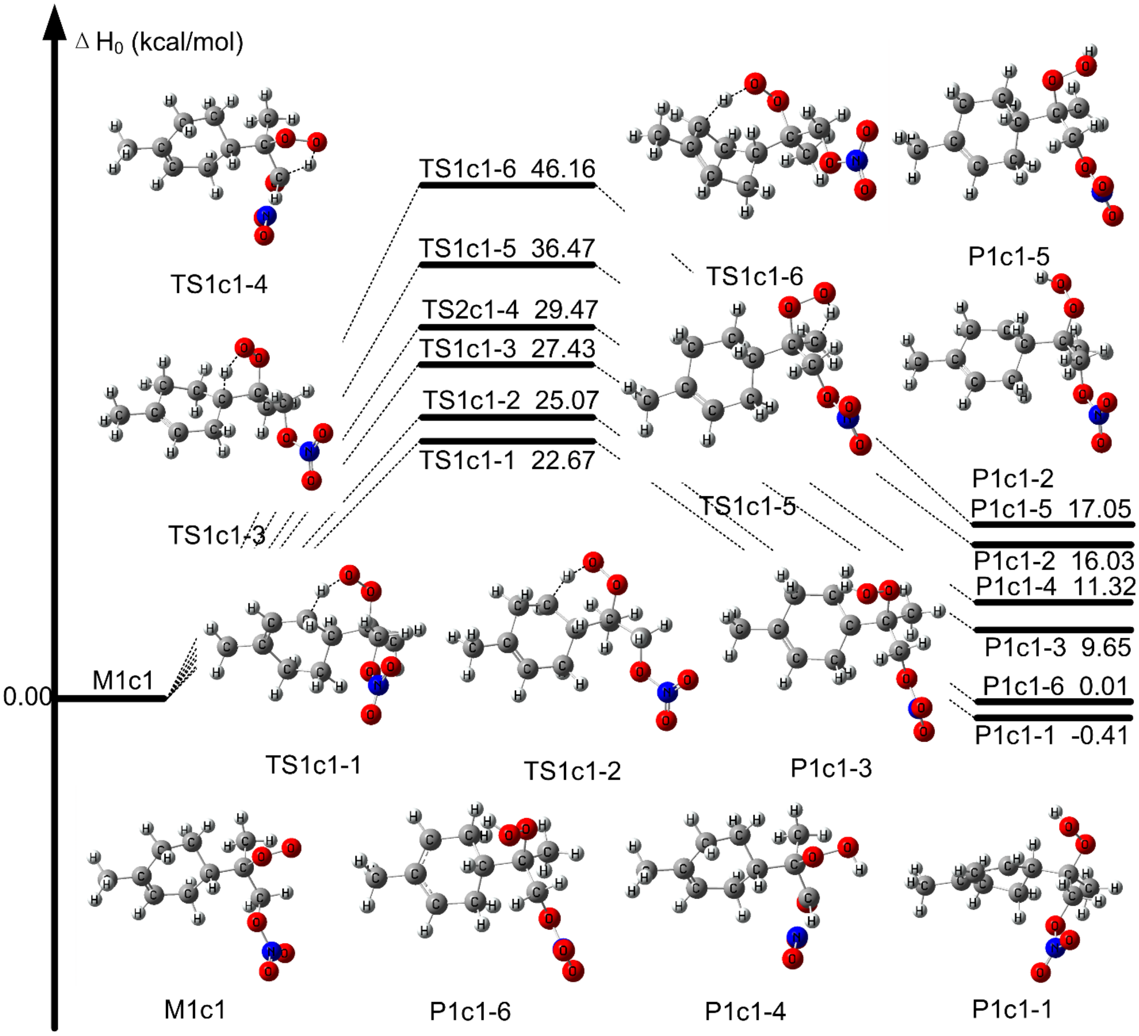

Figure S3.23 The calculated enthalpy profile at 0 K for the M1c1 isomer H-shift reaction at the MN15-L/MG3S level.

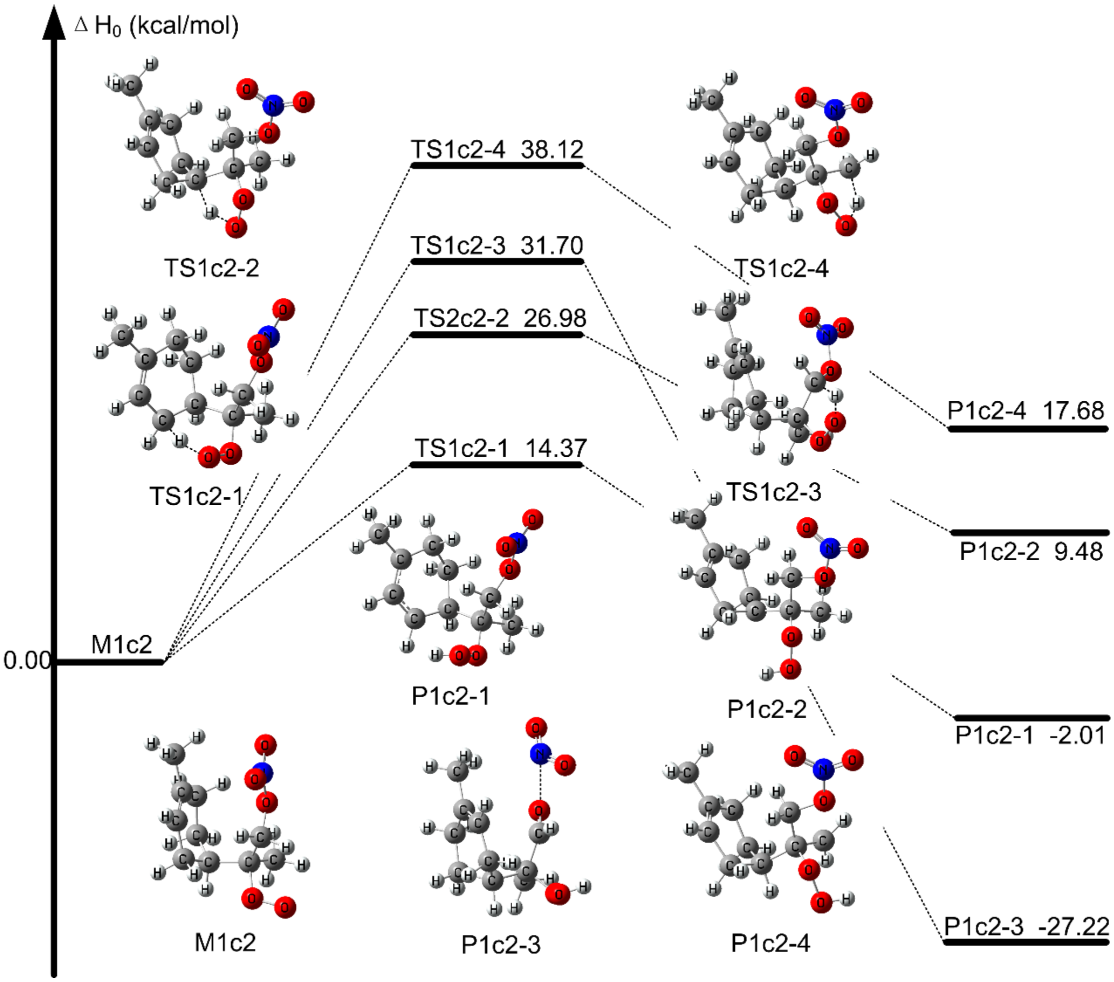

Figure S3.24 The calculated enthalpy profile at 0 K for the M1c2 isomer H-shift reaction at the MN15-L/MG3S level.

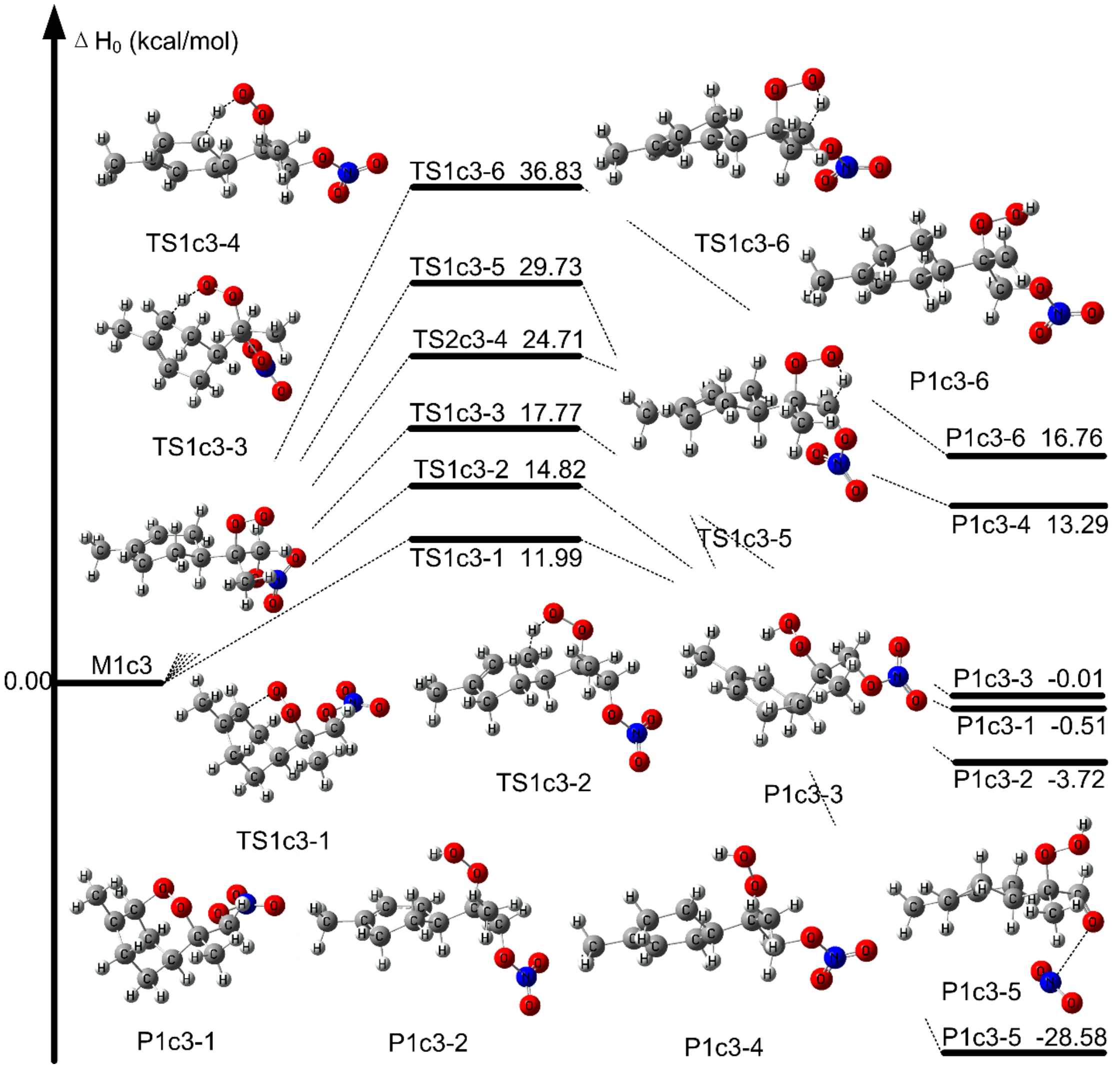

Figure S3.25 The calculated enthalpy profile at 0 K for the M1c3 isomer H-shift reaction at the MN15-L/MG3S level.

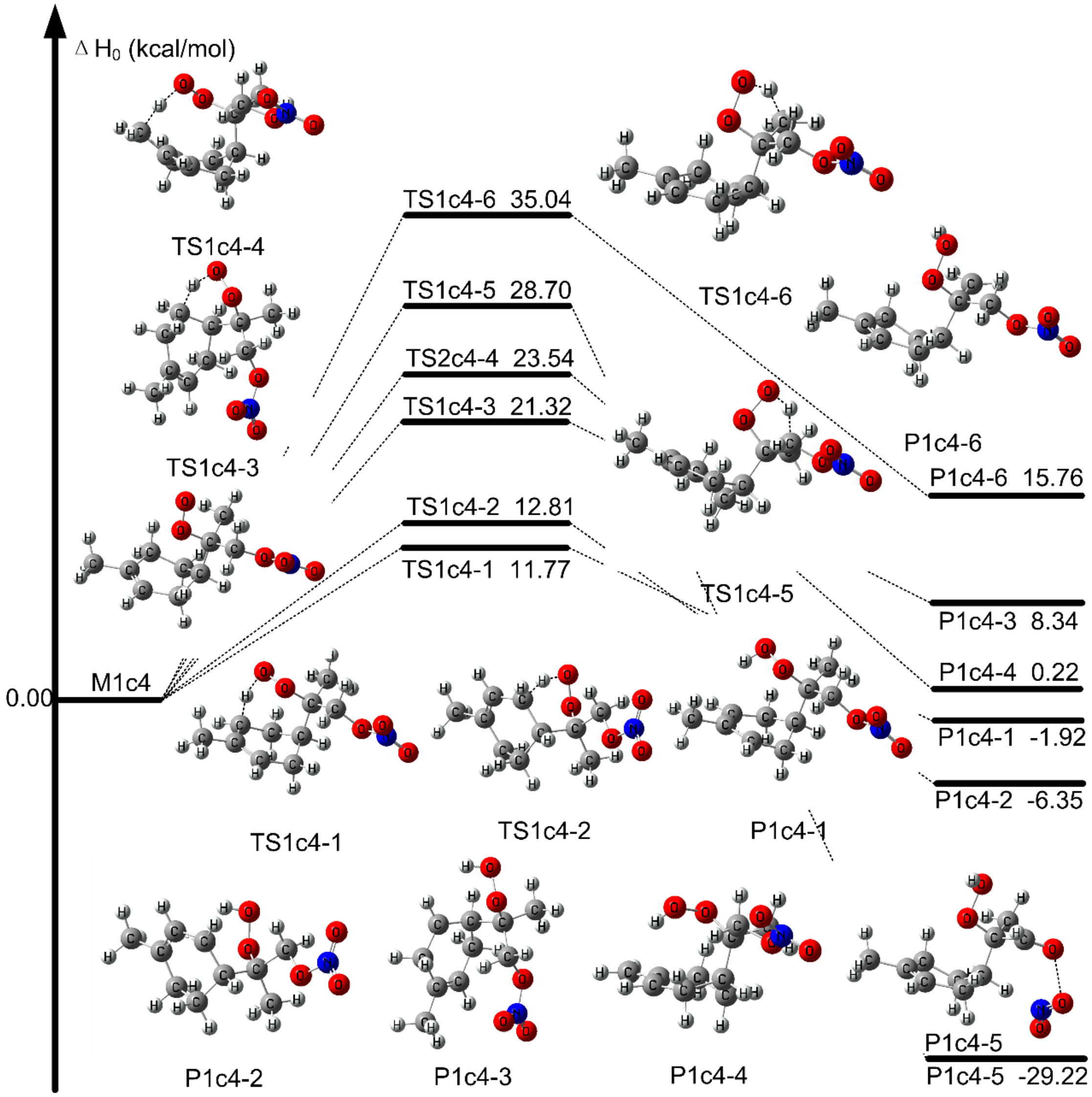

Figure S3.26 The calculated enthalpy profile at 0 K for the M1c4 isomer H-shift reaction at the MN15-L/MG3S level.

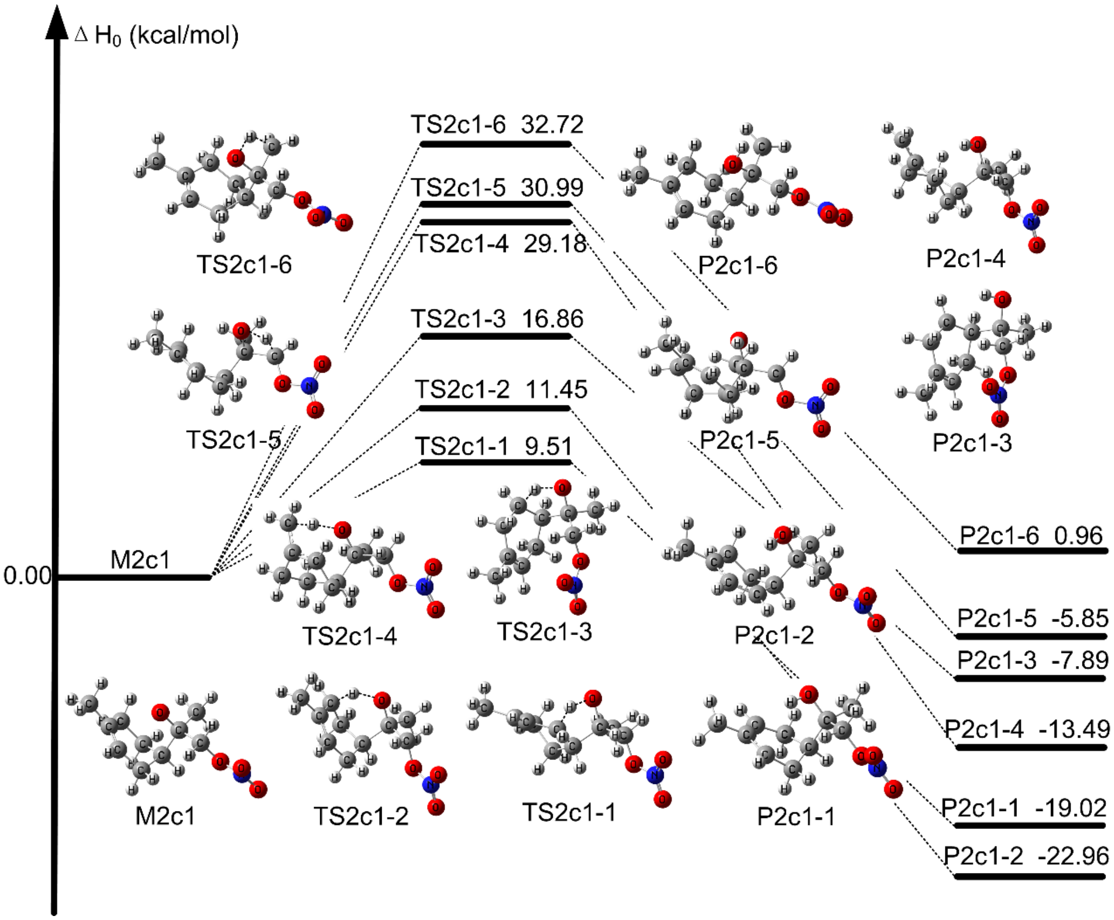

Figure S3.27 The calculated enthalpy profile at 0 K for the M2c1 isomer H-shift reaction at the MN15-L/MG3S level.

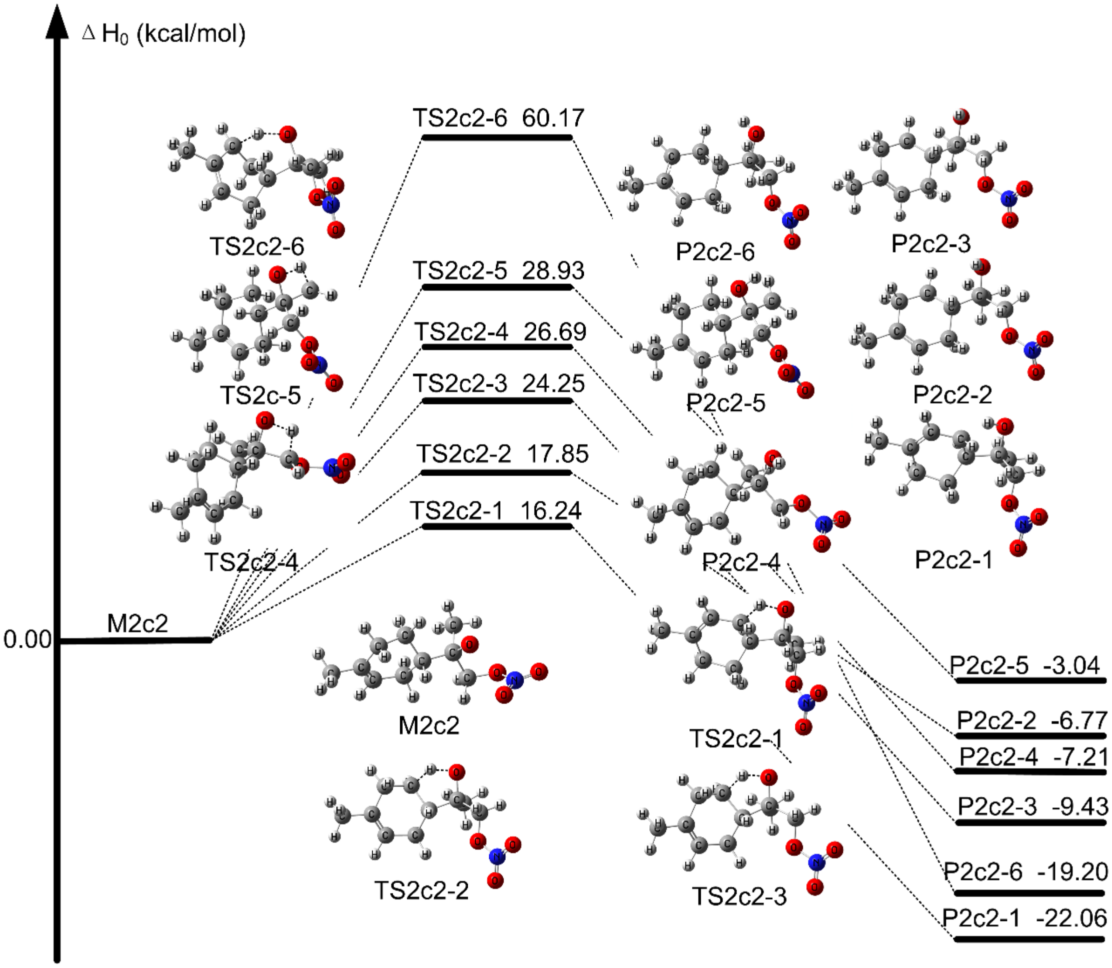

Figure S3.28 The calculated enthalpy profile at 0 K for the M2c2 isomer H-shift reaction at the MN15-L/MG3S level.

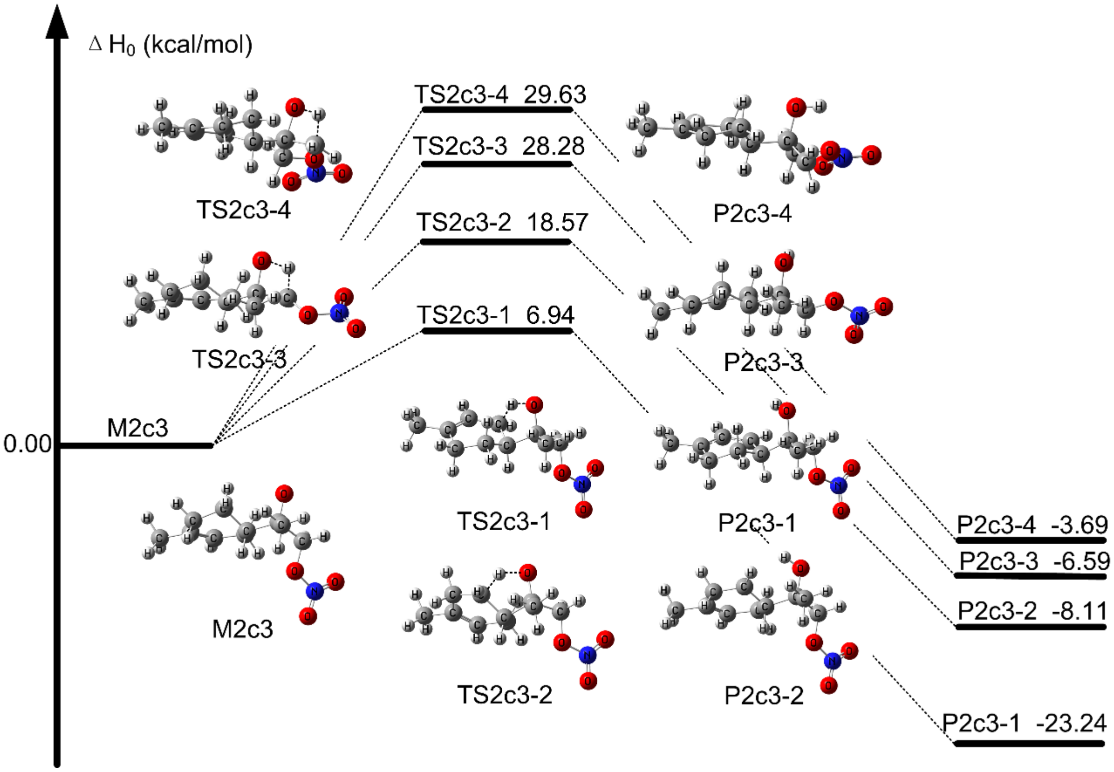

Figure S3.29 The calculated enthalpy profile at 0 K for the M2c3 isomer H-shift reaction at the MN15-L/MG3S level.

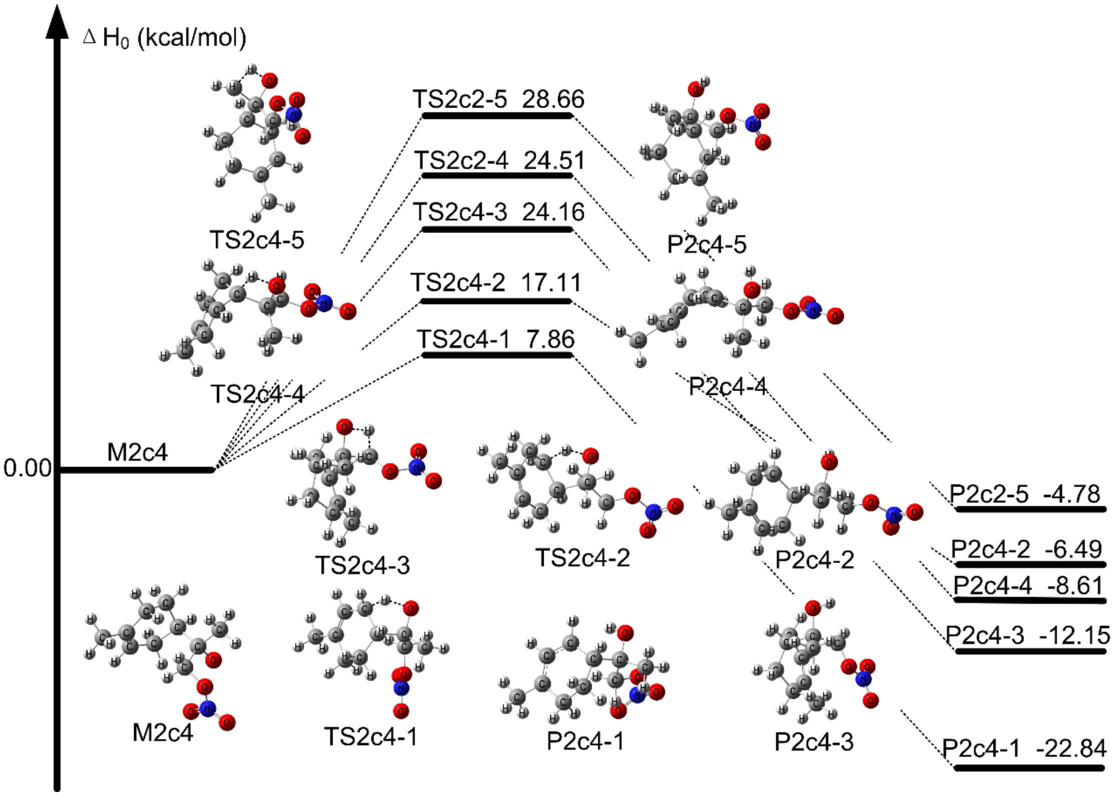

Figure S3.30 The calculated enthalpy profile at 0 K for the M2c4 isomer H-shift reaction at the MN15-L/MG3S level.

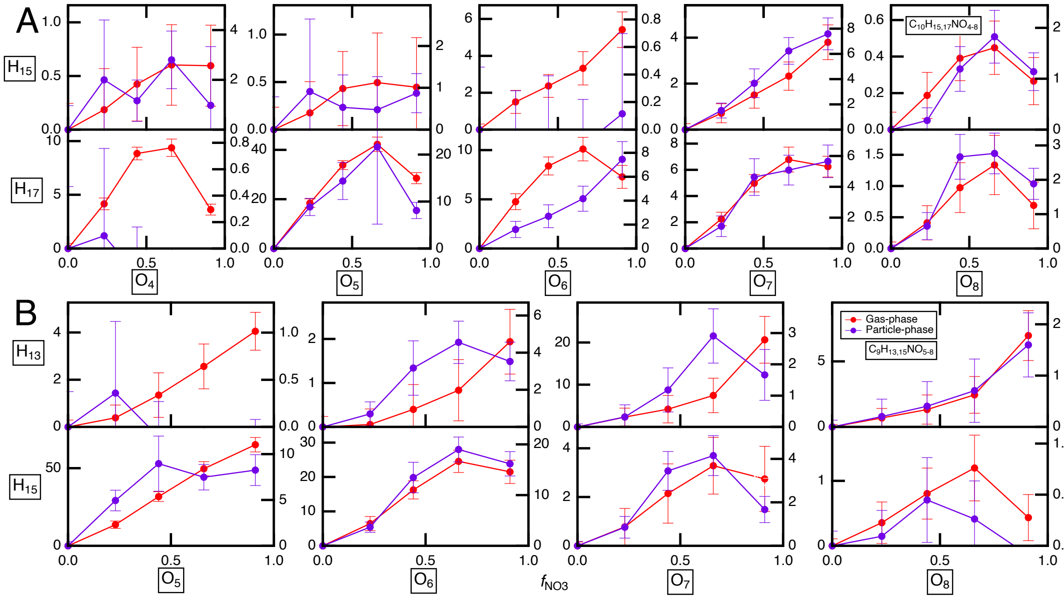

Figure S3.31 The CFSTR ion intensities of all the individual identified (A) $C_{10}H_{15,17}NO_{4-8}$ and (B) $C_9H_{13,15}NO_{5-8}$ as a function of f_{NO3}. The gas-phase data are shown in red and the particle-phase data are shown in purple.

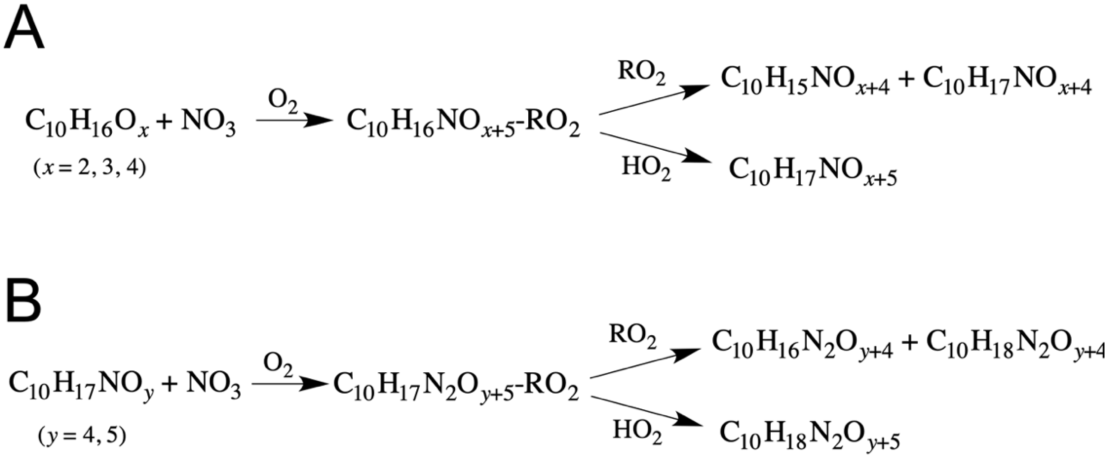

Figure S3.32 Proposed generic sequential NO_3 oxidation mechanisms for (A) formation of highly oxidized C_{10}-mononitrates, and (B) formation of the C_{10}-dinitrates. The reactants are known first-generation oxidation products with a double bond in MCM.

3.6 References

(1) Kanakidou, M.; Seinfeld, J. H.; Pandis, S. N.; Barnes, I.; Dentener, F. J.; Facchini, M. C.; Van Dingenen, R.; Ervens, B.; Nenes, A.; Nielsen, C. J.; Swietlicki, E.; Putaud, J. P.; Balkanski, Y.; Fuzzi, S.; Horth, J.; Moortgat, G. K.; Winterhalter, R.; Myhre, C. E. L.; Tsigaridis, K.; Vignati, E.; Stephanou, E. G.; Wilson, J. Organic Aerosol and Global Climate Modelling: A Review. *Atmos. Chem. Phys.* **2005**, *5* (4), 1053–1123.

(2) Zhang, H.; Yee, L. D.; Lee, B. H.; Curtis, M. P.; Worton, D. R.; Isaacman-VanWertz, G.; Offenberg, J. H.; Lewandowski, M.; Kleindienst, T. E.; Beaver, M. R.; Holder, A. L.; Lonneman, W. A.; Docherty, K. S.; Jaoui, M.; Pye, H. O. T.; Hu, W.; Day, D. A.; Campuzano-Jost, P.; Jimenez, J. L.; Guo, H.; Weber, R. J.; de Gouw, J.; Koss, A. R.; Edgerton, E. S.; Brune, W.; Mohr, C.; Lopez-Hilfiker, F. D.; Lutz, A.; Kreisberg, N. M.; Spielman, S. R.; Hering, S. V.; Wilson, K. R.; Thornton, J. A.; Goldstein, A. H. Monoterpenes Are the Largest Source of Summertime Organic Aerosol in the Southeastern United States. *Proc Natl Acad Sci USA* **2018**, *115* (9), 2038–2043.

(3) Guenther, A. B.; Jiang, X.; Heald, C. L.; Sakulyanontvittaya, T.; Duhl, T.; Emmons, L. K.; Wang, X. The Model of Emissions of Gases and Aerosols from Nature Version 2.1 (MEGAN2.1): An Extended and Updated Framework for Modeling Biogenic Emissions. *Geosci. Model Dev.* **2012**, *5* (6), 1471–1492.

(4) World Health Organization. 1998.

(5) Hatch, L. E.; Luo, W.; Pankow, J. F.; Yokelson, R. J.; Stockwell, C. E.; Barsanti, K. C. Identification and Quantification of Gaseous Organic Compounds Emitted from Biomass Burning Using Two-Dimensional Gas Chromatography–Time-of-Flight Mass Spectrometry. *Atmos. Chem. Phys.* **2015**, *15* (4), 1865–1899.

(6) Khan, M. A. H.; Ashfold, M. J.; Nickless, G.; Martin, D.; Watson, L. A.; Hamer, P. D.; Wayne, R. P.; Canosa-Mas, C. E.; Shallcross, D. E. Night-Time NO_3 and OH Radical Concentrations in the United Kingdom Inferred from Hydrocarbon Measurements. *Atmos. Sci. Lett.* **2008**, *9* (3), 140–146.

(7) Nøjgaard, J. K. Indoor Measurements of the Sum of the Nitrate Radical, NO_3, and Nitrogen Pentoxide, N_2O_5 in Denmark. *Chemosphere* **2010**, *79* (8), 898–904.

(8) Draper, D. C.; Farmer, D. K.; Desyaterik, Y.; Fry, J. L. A Qualitative Comparison of Secondary Organic Aerosol Yields and Composition from Ozonolysis of Monoterpenes at Varying Concentrations of NO_3; *Atmos. Chem. Phys.* **2015**, *15* (21), 12267–12281.

(9) Rollins, A. W.; Browne, E. C.; Min, K.-E.; Pusede, S. E.; Wooldridge, P. J.; Gentner, D. R.; Goldstein, A. H.; Liu, S.; Day, D. A.; Russell, L. M.; Cohen, R. C. Evidence for NO_x Control over Nighttime SOA Formation. *Science* **2012**, *337* (6099), 1210–1212.

(10) Lee, B. H.; Mohr, C.; Lopez-Hilfiker, F. D.; Lutz, A.; Hallquist, M.; Lee, L.; Romer, P.; Cohen, R. C.; Iyer, S.; Kurtén, T.; Hu, W.; Day, D. A.; Campuzano-Jost, P.; Jimenez, J. L.; Xu, L.; Ng, N. L.; Guo, H.; Weber, R. J.; Wild, R. J.; Brown, S. S.; Koss, A.; de Gouw, J.; Olson, K.; Goldstein, A. H.; Seco, R.; Kim, S.; McAvey, K.; Shepson, P. B.; Starn, T.; Baumann, K.; Edgerton, E. S.; Liu, J.; Shilling, J. E.; Miller, D. O.; Brune, W.; Schobesberger, S.; D'Ambro, E. L.; Thornton, J. A. Highly Functionalized Organic Nitrates in the Southeast United States: Contribution to Secondary Organic Aerosol and Reactive Nitrogen Budgets. *Proc Natl Acad Sci USA* **2016**, *113* (6), 1516–1521.

(11) Brown, S. S.; Stutz, J. Nighttime Radical Observations and Chemistry. *Chem. Soc. Rev.* **2012**, *41* (19), 6405.

(12) Perring, A. E.; Pusede, S. E.; Cohen, R. C. An Observational Perspective on the Atmospheric Impacts of Alkyl and Multifunctional Nitrates on Ozone and Secondary Organic Aerosol. *Chem. Rev.* **2013**, *113* (8), 5848–5870.

(13) Kiendler-Scharr, A.; Mensah, A. A.; Friese, E.; Topping, D.; Nemitz, E.; Prevot, A. S. H.; Äijälä, M.; Allan, J.; Canonaco, F.; Canagaratna, M.; Carbone, S.; Crippa, M.; Dall Osto, M.; Day, D. A.; De Carlo, P.; Di Marco, C. F.; Elbern, H.; Eriksson, A.; Freney, E.; Hao, L.; Herrmann, H.; Hildebrandt, L.; Hillamo, R.; Jimenez, J. L.; Laaksonen, A.; McFiggans, G.; Mohr, C.; O'Dowd, C.; Otjes, R.; Ovadnevaite, J.; Pandis, S. N.; Poulain, L.; Schlag, P.; Sellegri, K.; Swietlicki, E.; Tiitta, P.; Vermeulen, A.; Wahner, A.; Worsnop, D.; Wu, H. -C. Ubiquity of Organic Nitrates from Nighttime Chemistry in the European Submicron Aerosol. *Geophys. Res. Lett.* **2016**, *43* (14), 7735–7744.

(14) Ng, N. L.; Brown, S. S.; Archibald, A. T.; Atlas, E.; Cohen, R. C.; Crowley, J. N.; Day, D. A.; Donahue, N. M.; Fry, J. L.; Fuchs, H.; Griffin, R. J.; Guzman, M. I.; Herrmann, H.; Hodzic, A.; Iinuma, Y.; Jimenez, J. L.; Kiendler-Scharr, A.; Lee, B. H.; Luecken, D. J.; Mao, J.; McLaren, R.; Mutzel, A.; Osthoff, H. D.; Ouyang, B.; Picquet-Varrault, B.; Platt, U.; Pye, H. O. T.; Rudich, Y.; Schwantes, R. H.; Shiraiwa, M.; Stutz, J.; Thornton, J. A.; Tilgner, A.; Williams, B. J.; Zaveri, R. A. Nitrate Radicals and Biogenic Volatile Organic Compounds: Oxidation, Mechanisms, and Organic Aerosol. *Atmos. Chem. Phys.* **2017**, *17* (3), 2103–2162.

(15) Fry, J. L.; Draper, D. C.; Barsanti, K. C.; Smith, J. N.; Ortega, J.; Winkler, P. M.; Lawler, M. J.; Brown, S. S.; Edwards, P. M.; Cohen, R. C.; Lee, L. Secondary Organic Aerosol Formation and Organic Nitrate Yield from NO_3 Oxidation of Biogenic Hydrocarbons. *Environ. Sci. Technol.* **2014**, *48* (20), 11944–11953.

(16) Fry, J. L.; Kiendler-Scharr, A.; Rollins, A. W.; Wooldridge, P. J.; Brown, S. S.; Fuchs, H.; Dubé, W.; Mensah, A.; dal Maso, M.; Tillmann, R.; Dorn, H.-P.; Brauers, T.; Cohen, R. C. Organic Nitrate and Secondary Organic Aerosol Yield from NO_3

Oxidation of β-Pinene Evaluated Using a Gas-Phase Kinetics/Aerosol Partitioning Model. *Atmos. Chem. Phys.* **2009**, *9* (4), 1431–1449.

(17) Nah, T.; Sanchez, J.; Boyd, C. M.; Ng, N. L. Photochemical Aging of α-Pinene and β-Pinene Secondary Organic Aerosol Formed from Nitrate Radical Oxidation. *Environ. Sci. Technol.* **2016**, *50* (1), 222–231.

(18) Rollins, A. W.; Fry, J. L.; Hunter, J. F.; Kroll, J. H.; Worsnop, D. R.; Singaram, S. W.; Cohen, R. C. Elemental Analysis of Aerosol Organic Nitrates with Electron Ionization High-Resolution Mass Spectrometry. *Atmos. Meas. Tech.* **2010**, *3* (1), 301–310.

(19) Rollins, A. W.; Pusede, S.; Wooldridge, P.; Min, K.-E.; Gentner, D. R.; Goldstein, A. H.; Liu, S.; Day, D. A.; Russell, L. M.; Rubitschun, C. L.; Surratt, J. D.; Cohen, R. C. Gas/Particle Partitioning of Total Alkyl Nitrates Observed with TD-LIF in Bakersfield: $RONO_2$ Phase Partitioning. *J. Geophys. Res. Atmos.* **2013**, *118* (12), 6651–6662.

(20) Hallquist, M.; Wängberg, I.; Ljungström, E.; Barnes, I.; Becker, K.-H. Aerosol and Product Yields from NO_3 Radical-Initiated Oxidation of Selected Monoterpenes. *Environ. Sci. Technol.* **1999**, *33* (4), 553–559.

(21) Spittler, M.; Barnes, I.; Bejan, I.; Brockmann, K. J.; Benter, Th.; Wirtz, K. Reactions of NO_3 Radicals with Limonene and α-Pinene: Product and SOA Formation. *Atmospheric Environment* **2006**, *40*, 116–127.

(22) Fry, J. L.; Kiendler-Scharr, A.; Rollins, A. W.; Brauers, T.; Brown, S. S.; Dorn, H.-P.; Dubé, W. P.; Fuchs, H.; Mensah, A.; Rohrer, F.; Tillmann, R.; Wahner, A.; Wooldridge, P. J.; Cohen, R. C. SOA from Limonene: Role of NO_3 in Its Generation and Degradation. *Atmos. Chem. Phys.* **2011**, *11* (8), 3879–3894.

(23) Ehn, M.; Thornton, J. A.; Kleist, E.; Sipilä, M.; Junninen, H.; Pullinen, I.; Springer, M.; Rubach, F.; Tillmann, R.; Lee, B.; Lopez-Hilfiker, F.; Andres, S.; Acir, I.-H.; Rissanen, M.; Jokinen, T.; Schobesberger, S.; Kangasluoma, J.; Kontkanen, J.; Nieminen, T.; Kurtén, T.; Nielsen, L. B.; Jørgensen, S.; Kjaergaard, H. G.; Canagaratna, M.; Maso, M. D.; Berndt, T.; Petäjä, T.; Wahner, A.; Kerminen, V.-M.; Kulmala, M.; Worsnop, D. R.; Wildt, J.; Mentel, T. F. A Large Source of Low-Volatility Secondary Organic Aerosol. *Nature* **2014**, *506* (7489), 476–479.

(24) Jokinen, T.; Sipilä, M.; Richters, S.; Kerminen, V.-M.; Paasonen, P.; Stratmann, F.; Worsnop, D.; Kulmala, M.; Ehn, M.; Herrmann, H.; Berndt, T. Rapid Autoxidation Forms Highly Oxidized RO_2 Radicals in the Atmosphere. *Angew. Chem. Int. Ed.* **2014**, *53* (52), 14596–14600.

(25) Chen, J.; Møller, K. H.; Wennberg, P. O.; Kjaergaard, H. G. Unimolecular Reactions Following Indoor and Outdoor Limonene Ozonolysis. *J. Phys. Chem. A* **2021**, *125* (2), 669–680.

(26) Pagonis, D.; Algrim, L. B.; Price, D. J.; Day, D. A.; Handschy, A. V.; Stark, H.; Miller, S. L.; de Gouw, J. A.; Jimenez, J. L.; Ziemann, P. J. Autoxidation of Limonene Emitted in a University Art Museum. *Environ. Sci. Technol. Lett.* **2019**, *6* (9), 520–524.

(27) Guo, Y.; Shen, H.; Pullinen, I.; Luo, H.; Kang, S.; Vereecken, L.; Fuchs, H.; Hallquist, M.; Acir, I.-H.; Tillmann, R.; Rohrer, F.; Wildt, J.; Kiendler-Scharr, A.; Wahner, A.; Zhao, D.; Mentel, T. F. Identification of Highly Oxygenated Organic Molecules and Their Role in Aerosol Formation in the Reaction of Limonene with Nitrate Radical. *Atmos. Chem. Phys.* **2022**, *22*, 11323–11346.

(28) Draper, D. C.; Myllys, N.; Hyttinen, N.; Møller, K. H.; Kjaergaard, H. G.; Fry, J. L.; Smith, J. N.; Kurtén, T. Formation of Highly Oxidized Molecules from NO_3 Radical Initiated Oxidation of Δ-3-Carene: A Mechanistic Study. *ACS Earth Space Chem.* **2019**, *3* (8), 1460–1470.

(29) Ahmad, W.; Coeur, C.; Cuisset, A.; Coddeville, P.; Tomas, A. Effects of Scavengers of Criegee Intermediates and OH Radicals on the Formation of Secondary Organic Aerosol in the Ozonolysis of Limonene. *J. Aerosol Sci.* **2017**, *110*, 70–83.

(30) Leungsakul, S.; Jaoui, M.; Kamens, R. M. Kinetic Mechanism for Predicting Secondary Organic Aerosol Formation from the Reaction of D-Limonene with Ozone. *Environ. Sci. Technol.* **2005**, *39* (24), 9583–9594.

(31) Zhao, Z.; Zhang, W.; Alexander, T.; Zhang, X.; Martin, D. B. C.; Zhang, H. Isolating α-Pinene Ozonolysis Pathways Reveals New Insights into Peroxy Radical Chemistry and Secondary Organic Aerosol Formation. *Environ. Sci. Technol.* **2021**, *55* (10), 6700–6709.

(32) Mayorga, R. J.; Zhao, Z.; Zhang, H. Formation of Secondary Organic Aerosol from Nitrate Radical Oxidation of Phenolic VOCs: Implications for Nitration Mechanisms and Brown Carbon Formation. *Atmos. Environ.* **2021**, *244*, 117910.

(33) Zhao, Z.; Le, C.; Xu, Q.; Peng, W.; Jiang, H.; Lin, Y.-H.; Cocker, D. R.; Zhang, H. Compositional Evolution of Secondary Organic Aerosol as Temperature and Relative Humidity Cycle in Atmospherically Relevant Ranges. *ACS Earth Space Chem.* **2019**, *3* (11), 2549–2558.

(34) Zhang, W.; Zhang, H. Secondary Ion Chemistry Mediated by Ozone and Acidic Organic Molecules in Iodide-Adduct Chemical Ionization Mass Spectrometry. *Anal. Chem.* **2021**, *93* (24), 8595–8602.

(35) Zhao, Z.; Tolentino, R.; Lee, J.; Vuong, A.; Yang, X.; Zhang, H. Interfacial Dimerization by Organic Radical Reactions during Heterogeneous Oxidative Aging of Oxygenated Organic Aerosols. *J. Phys. Chem. A* **2019**, *123* (50), 10782–10792.

(36) Iyer, S.; He, X.; Hyttinen, N.; Kurtén, T.; Rissanen, M. P. Computational and Experimental Investigation of the Detection of HO_2 Radical and the Products of Its Reaction with Cyclohexene Ozonolysis Derived RO_2 Radicals by an Iodide-Based Chemical Ionization Mass Spectrometer. *J. Phys. Chem. A* **2017**, *121* (36), 6778–6789.

(37) Mohr, C.; Lopez-Hilfiker, F. D.; Yli-Juuti, T.; Heitto, A.; Lutz, A.; Hallquist, M.; D'Ambro, E. L.; Rissanen, M. P.; Hao, L.; Schobesberger, S.; Kulmala, M.; Mauldin, R. L.; Makkonen, U.; Sipilä, M.; Petäjä, T.; Thornton, J. A. Ambient Observations of Dimers from Terpene Oxidation in the Gas Phase: Implications for New Particle Formation and Growth: Ambient Observations of Gas-Phase Dimers. *Geophys. Res. Lett.* **2017**, *44* (6), 2958–2966.

(38) Zhang, X.; Lambe, A. T.; Upshur, M. A.; Brooks, W. A.; Gray Bé, A.; Thomson, R. J.; Geiger, F. M.; Surratt, J. D.; Zhang, Z.; Gold, A.; Graf, S.; Cubison, M. J.; Groessl, M.; Jayne, J. T.; Worsnop, D. R.; Canagaratna, M. R. Highly Oxygenated Multifunctional Compounds in α-Pinene Secondary Organic Aerosol. *Environ. Sci. Technol.* **2017**, *51* (11), 5932–5940.

(39) Zhao, Z.; Xu, Q.; Yang, X.; Zhang, H. Heterogeneous Ozonolysis of Endocyclic Unsaturated Organic Aerosol Proxies: Implications for Criegee Intermediate Dynamics and Later-Generation Reactions. *ACS Earth Space Chem.* **2019**, *3* (3), 344–356.

(40) Zhao, Z.; Yang, X.; Lee, J.; Tolentino, R.; Mayorga, R.; Zhang, W.; Zhang, H. Diverse Reactions in Highly Functionalized Organic Aerosols during Thermal Desorption. *ACS Earth Space Chem.* **2020**, *4* (2), 283–296.

(41) Zhao, Z.; Mayorga, R.; Lee, J.; Yang, X.; Tolentino, R.; Zhang, W.; Vuong, A.; Zhang, H. Site-Specific Mechanisms in OH-Initiated Organic Aerosol Heterogeneous Oxidation Revealed by Isomer-Resolved Molecular Characterization. *ACS Earth Space Chem.* **2020**, *4* (5), 783–794.

(42) Krechmer, J. E.; Groessl, M.; Zhang, X.; Junninen, H.; Massoli, P.; Lambe, A. T.; Kimmel, J. R.; Cubison, M. J.; Graf, S.; Lin, Y.-H.; Budisulistiorini, S. H.; Zhang, H.; Surratt, J. D.; Knochenmuss, R.; Jayne, J. T.; Worsnop, D. R.; Jimenez, J.-L.; Canagaratna, M. R. Ion Mobility Spectrometry–Mass Spectrometry (IMS–MS) for on- and Offlineanalysis of Atmospheric Gas and Aerosol Species. *Atmos. Meas. Tech.* **2016**, *9* (7), 3245–3262.

(43) Zhang, X.; Krechmer, J. E.; Groessl, M.; Xu, W.; Graf, S.; Cubison, M.; Jayne, J. T.; Jimenez, J. L.; Worsnop, D. R.; Canagaratna, M. R. A Novel Framework for Molecular Characterization of Atmospherically Relevantorganic Compounds Based on Collision Cross Section and Mass-to-Charge Ratio. *Atmos. Chem. Phys.* **2016**, *16* (20), 12945–12959.

(44) Zhang, X.; Zhang, H.; Xu, W.; Wu, X.; Tyndall, G. S.; Orlando, J. J.; Jayne, J. T.; Worsnop, D. R.; Canagaratna, M. R. Molecular Characterization of Alkyl Nitrates in Atmospheric Aerosols by Ion Mobility Mass Spectrometry. *Atmos. Meas. Tech.* **2019**, *12* (10), 5535–5545.

(45) Adler, T. B.; Knizia, G.; Werner, H.-J. A Simple and Efficient CCSD(T)-F12 Approximation. *J. Chem. Phys.* **2007**, *127* (22), 221106.

(46) Knizia, G.; Adler, T. B.; Werner, H.-J. Simplified CCSD(T)-F12 Methods: Theory and Benchmarks. *J. Chem. Phys.* **2009**, *130* (5), 054104.

(47) Yu, H. S.; He, X.; Truhlar, D. G. MN15-L: A New Local Exchange-Correlation Functional for Kohn–Sham Density Functional Theory with Broad Accuracy for Atoms, Molecules, and Solids. *J. Chem. Theory Comput.* **2016**, *12* (3), 1280–1293.

(48) Lynch, B. J.; Zhao, Y.; Truhlar, D. G. Effectiveness of Diffuse Basis Functions for Calculating Relative Energies by Density Functional Theory. *J. Phys. Chem. A* **2003**, *107* (9), 1384–1388.

(49) Eyring, H. The Activated Complex in Chemical Reactions. *J. Chem. Phys.* **1935**, *3* (2), 107–115.

(50) Eckart, C. The Penetration of a Potential Barrier by Electrons. *Phys. Rev.* **1930**, *35* (11), 1303–1309.

(51) Long, B.; Bao, J. L.; Truhlar, D. G. Atmospheric Chemistry of Criegee Intermediates: Unimolecular Reactions and Reactions with Water. *J. Am. Chem. Soc.* **2016**, *138* (43), 14409–14422.

(52) Praske, E.; Otkjær, R. V.; Crounse, J. D.; Hethcox, J. C.; Stoltz, B. M.; Kjaergaard, H. G.; Wennberg, P. O. Atmospheric Autoxidation Is Increasingly Important in Urban and Suburban North America. *Proc. Natl. Acad. Sci. U.S.A.* **2018**, *115* (1), 64–69.

(53) Møller, K. H.; Bates, K. H.; Kjaergaard, H. G. The Importance of Peroxy Radical Hydrogen-Shift Reactions in Atmospheric Isoprene Oxidation. *J. Phys. Chem. A* **2019**, *123* (4), 920–932.

(54) *Master Chemical Mechanism (MCM, v3.3.1).*

(55) Donahue, N. M.; Tischuk, J. E.; Marquis, B. J.; Huff Hartz, K. E. Secondary Organic Aerosol from Limona Ketone: Insights into Terpene Ozonolysis via Synthesis of Key Intermediates. *Phys. Chem. Chem. Phys.* **2007**, *9* (23), 2991–2998.

(56) Wang, L.; Wang, L. The Oxidation Mechanism of Gas-Phase Ozonolysis of Limonene in the Atmosphere. *Phys. Chem. Chem. Phys.* **2021**, *23* (15), 9294–9303.

(57) Kurtén, T.; Møller, K. H.; Nguyen, T. B.; Schwantes, R. H.; Misztal, P. K.; Su, L.; Wennberg, P. O.; Fry, J. L.; Kjaergaard, H. G. Alkoxy Radical Bond Scissions Explain the Anomalously Low Secondary Organic Aerosol and Organonitrate Yields From α-Pinene + NO_3. *J. Phys. Chem. Lett.* **2017**, *8* (13), 2826–2834.

(58) Massoli, P.; Stark, H.; Canagaratna, M. R.; Krechmer, J. E.; Xu, L.; Ng, N. L.; Mauldin, R. L.; Yan, C.; Kimmel, J.; Misztal, P. K.; Jimenez, J. L.; Jayne, J. T.; Worsnop, D. R. Ambient Measurements of Highly Oxidized Gas-Phase Molecules during the Southern Oxidant and Aerosol Study (SOAS) 2013. *ACS Earth Space Chem.* **2018**, *2* (7), 653–672.

(59) Vereecken, L.; Nozière, B. H Migration in Peroxy Radicals under Atmospheric Conditions. *Atmos. Chem. Phys.* **2020**, *20* (12), 7429–7458.

(60) Møller, K. H.; Otkjær, R. V.; Chen, J.; Kjaergaard, H. G. Double Bonds Are Key to Fast Unimolecular Reactivity in First-Generation Monoterpene Hydroxy Peroxy Radicals. *J. Phys. Chem. A* **2020**, *124* (14), 2885–2896.

(61) Piletic, I. R.; Kleindienst, T. E. Rates and Yields of Unimolecular Reactions Producing Highly Oxidized Peroxy Radicals in the OH-Induced Autoxidation of α-Pinene, β-Pinene, and Limonene. *J. Phys. Chem. A* **2022**, *126* (1), 88–100.

(62) Vereecken, L.; Peeters, J. A Structure–Activity Relationship for the Rate Coefficient of H-Migration in Substituted Alkoxy Radicals. *Phys. Chem. Chem. Phys.* **2010**, *12* (39), 12608.

(63) Vereecken, L.; Vu, G.; Wahner, A.; Kiendler-Scharr, A.; Nguyen, H. M. T. A Structure Activity Relationship for Ring Closure Reactions in Unsaturated Alkylperoxy Radicals. *Phys. Chem. Chem. Phys.* **2021**, *23* (31), 16564–16576.

(64) Long, B.; Bao, J. L.; Truhlar, D. G. Unimolecular Reaction of Acetone Oxide and Its Reaction with Water in the Atmosphere. *Proc. Natl. Acad. Sci. U.S.A.* **2018**, *115* (24), 6135–6140.

(65) Long, B.; Bao, J. L.; Truhlar, D. G. Rapid Unimolecular Reaction of Stabilized Criegee Intermediates and Implications for Atmospheric Chemistry. *Nat Commun* **2019**, *10* (1), 2003.

(66) Gonzalez, Carlos.; Schlegel, H. Bernhard. Reaction Path Following in Mass-Weighted Internal Coordinates. *J. Phys. Chem.* **1990**, *94* (14), 5523–5527.

CHAPTER 4: Chemical structure regulates the formation of secondary organic aerosol and brown carbon in nitrate radical oxidation of pyrrole and methylpyrroles

4.1 Introduction

In recent years, wildfires have shown a global increase in occurrence and severity.[1,2] Biomass burning events release volatile organic compounds (VOCs) and particulate matter into the atmosphere which impact the Earth's radiative budget, air quality and human health.[3,4] Nitrogen-containing heterocyclic VOCs such as pyrrole and its methyl derivatives could represent an important portion of wildfire emissions. From fuels native to North America, pyrrole has emission factors ranging from 0.014 – 0.11 g kg^{-1}, 1-methylpyrrole (1-MP) from 0.0023 – 0.023 g kg^{-1} and 2-methylpyrrole (2-MP) from 0.0023 – 0.015 g kg^{-1}.[5,6] In comparison, another class of well-studied wildfire emissions, phenolic VOCs, have total emission factors ranging from 0.10 – 0.64 g kg^{-1} from similar fuels.[7–9] During biomass burning events, increased levels of NO_x (= NO + NO_2) can quickly react with ozone (O_3) to produce nitrate radicals (NO_3), which may act as the primary oxidant for some VOCs during nighttime,[10–12] and even during daytime.[13] The NO_3 oxidation of pyrrole and methylpyrroles has been understudied but may represent a significant pathway towards the formation of secondary organic aerosol (SOA).[14] These SOA are often found to be light absorbing (i.e., forming brown carbon, BrC), which further enhance their climate impacts.[15–17] Therefore, it is of vital importance to understand the NO_3 oxidation chemistry of pyrrole and methylpyrroles and incorporate it into the current air quality and climate models.

Several prior studies have investigated NO_3 oxidation of heterocyclic VOCs such as furan and methylfurans,[18–20] but there have been very few studies of pyrrole and methylpyrroles.[14,21] The primary nighttime oxidant, NO_3, has been shown to react very quickly with pyrrole in the gas phase with a rate constant of 4.9×10^{-11} cm^3 $molecules^{-1}$ s^{-1}.[22,23] The low-volatile products from NO_3 oxidation of pyrrole can partition into the particle phase with significant SOA yields and exhibit strong light-absorbing properties.[14] Pyrrole has been reported to have 109 ± 29% SOA yield from NO_3 oxidation and an average mass absorption coefficient (<MAC>) of 0.34 ± 0.07 m^2 g^{-1} from 290 – 700 nm encompassing the UV and visible light.[14] However, the composition and formation mechanism of SOA and BrC from NO_3 oxidation of pyrrole and methylpyrroles remain poorly understood. Pyrrole and methylpyrroles contain double bonds which might undergo NO_3 addition following mechanisms like those established for many alkenes to form organic nitrates;[24–29] they are also aromatic compounds, thus it is conceivable that they could also undergo reactions involving H-abstraction by NO_3 like those reported for phenolic VOCs and form nitroaromatics in the presence of NO_2.[30–35] In the NO_3 oxidation of phenolic VOCs, nitroaromatic products generally constituted a significant portion of SOA mass and may contribute to the strong light absorption.[30,32,33,36–39] In this study, we investigate the SOA formation from NO_3 oxidation of pyrrole, 1-MP and 2-MP using a comprehensive suite of analytical instrumentation. We identify the major SOA products from NO_3 oxidation of the three N-containing heterocyclic VOCs, measure the optical properties of their SOA, and discuss how the chemical structure regulates the oxidation mechanisms that lead to the distinct formation of light-absorbing chromophores.

4.2 Materials and Methods

4.2.1 Chemicals and reagents

The chemicals and reagents used in this study and their purities and suppliers are as follows: pyrrole (TCI America, >99%), 1-methylpyrrole (TCI America, >99%), 2-methylpyrrole (aa blocks, 98%), sodium chloride (99.5%, Sigma Aldrich), methanol (HPLC Grade Fischer Chemical), and acetonitrile (HPLC Grade Fischer Chemical). All chemicals were used without further purification.

4.2.2 Laboratory experiments

All the experiments (see **Table 4.1**) were performed in a 10 m^3 Teflon FEP smog chamber under dark conditions, low relative humidity (RH < 20%), at room temperature (20 – 25°C) and pressure (730 Torr). A duplicate experiment was performed for each of the five conditions listed in **Table 4.1** to verify reproducibility. NO_3 radicals were generated through the reaction of O_3 and NO_2 in the chamber. O_3 was introduced into the chamber using an O_3 generator (A2Z Ozone 3GLAB) and the initial concentration of O_3 for each experiment was ~ 1400 – 1700 ppb. Directly following this, NO_2 (Airgas) was injected into the chamber to achieve an NO_2 concentration of ~ 150 ppb or 450 ppb. Thus, the initial NO_2/O_3 ratio in the chamber was approximately 0.1 or 0.3, which is similar to that measured in relatively fresh wildfire plumes.[40] The O_3 and NO_x concentrations in the chamber were measured in real-time by an O_3 analyzer (Advanced Pollution Instrumentation, Inc.) and a NO_x analyzer (Teledyne Instruments), respectively. O_3 and NO_2 were allowed to react for ~ 1 h in the chamber before injection of pyrrole, 1-MP, or

2-MP at approximately 200 ppb by passing 15 L min^{-1} of N_2 gas through a heated jar containing the liquid VOC to initiate the NO_3 oxidation experiment. A scanning electrical mobility scanner and a mixing condensation particle counter (SEMS and MCPC, Brechtel Manufacturing Inc.) were used to measure size distribution and number concentrations of the SOA from 10 – 800 nm with 140 size bins. After the formed SOA mass concentrations reached a plateau, SOA samples were collected on PTFE membrane filters (Tisch Scientific) at 16.7 L min^{-1} for 1 h, allowing for a total collected SOA mass of 149 – 422 μg, estimated based on the measured aerosol effective densities described below. The collected SOA samples were stored at -20°C until analysis. Before all the aerosol measurements, the particles from the chamber passed through a 30 cm-long diffusion dryer filled with silica gel (Sigma-Aldrich) and Purafil (Thermo Scientific).

In addition to the chamber experiments, we also performed kinetic experiments in a continuous flow stirred tank reactor (CFSTR) to constrain the oxidation rate constants of 1-MP and 2-MP in reactions with O_3 and NO_3 radicals.[35,41] The decays of the methylpyrroles relative to pyrrole upon oxidation by O_3 and NO_3 radicals were measured by a proton-transfer reaction mass spectrometer (PTR-MS). Details are described in the **Supplemental Information (SI)**.

4.2.3 SOA Chemical Characterization

The collected SOA filter samples were extracted for offline chemical analysis. Specifically, 20 mL of methanol was added to each vial containing a filter sample followed by 45-min sonication. The filters were then removed from the vials and methanol was evaporated off with a gentle flow of N_2. Immediately after filter extraction, the extracts were dissolved in 100 μL acetonitrile with 0.1 mM NaCl for analysis using an electrospray ionization (ESI) ion mobility spectrometry time-of-flight mass spectrometer (IMS-TOF, Tofwerk Inc.) in the negative ion mode. The doped NaCl allows for molecules to form adducts with chloride $[M+Cl]^-$ in (–)ESI, which has been shown to be an effective approach to detect non-acidic organic nitrates which are otherwise challenging to ionize directly by ESI.[42] Each sample extract was injected into the IMS-TOF using a syringe pump at a rate of 1 $\mu L\ min^{-1}$. After the (–)ESI, the generated ions enter into a drift tube and are met with a counterflow of N_2 gas (at 1.2 $L\ min^{-1}$) which serves to separate different ions based on their collisional cross sections thereby giving each ion a characteristic drift time.[35,43] Upon exiting the drift tube, the ions were focused through a pressure-vacuum interface which contains two segmented quadrupoles operated at ~ 2 mbar and 5×10^{-3} mbar, respectively. By varying the voltages between the two segmented quadrupoles, collision-induced dissociation (CID) of parent ions is achieved. The IMS-TOF was operated over an m/Q range of 45 – 600 Th. The IMS resolution is $(t/\Delta t) \sim 100$ and the TOF mass resolution is $(m/\Delta m) \sim 4000$, determined by various standard ions with m/Q between 100 – 200 Th.[35,42] All the IMS-TOF data processing were performed using Tofware (version 3.2.0, Tofwerk Inc.) running with Igor Pro (Wavemetrics Inc.).[35,44]

In addition, size-resolved mass distributions and particle chemical composition were measured in real-time by a mini aerosol mass spectrometer (mAMS) coupled with a compact time-of-flight mass spectrometer (Aerodyne Research, Inc.).[45] The size-resolved aerosol mass distribution was compared with the concurrent SEMS-derived aerosol volume distribution to determine the effective aerosol density (ρ_{eff}).[45–47] The calculation of ρ_{eff} is described in the **SI, Text S2**. The calculated ρ_{eff} was then used to estimate the SOA mass concentrations shown in **Table 4.1**. The mass accuracy of the mAMS is ~ 20 ppm and the resolving power is ~ 1200 – 1300. Size selected ammonium nitrate particles or dry polystyrene latex spheres were regularly used to calibrate the sensitivity and sizing capability of the mAMS. High resolution analysis of the raw mass spectra was conducted from *m/Q* 20 – 115 Th to calculate the mass concentrations of all species.[48] Besides, supportive gas-phase chemical analysis was performed for selected experiments (pyrrole and 1-MP) with a chemical ionization mass spectrometer using iodide (I^-) as the reagent ion (I-CIMS, Aerodyne Research Inc.). The I^- forms adducts ($[M + I]^-$) with functionalized molecules containing oxygens and nitrogens. Further details about this instrument can be found in our previous publication.[14]

4.2.4 SOA Optical Property Characterization

Online analysis of the SOA optical properties was performed using a Photoacoustic Extinctiometer (PAX, Droplet Measurement Technology, Boulder, CO). The PAX allows for measurements of absorption and scattering coefficients at 375 nm ($\beta_{abs,375}$ and $\beta_{scat,375}$) at 1 Hz, which were averaged to the SEMS scan time interval (140 s).[14] Online <MAC> at 375 nm (<MAC>$_{\text{online},375}$) was estimated by:

$$MAC_{online,375} = \frac{\beta_{abs,375}}{C_{SOA}}$$

where C_{SOA} is the estimated SOA mass concentration. The calculation of C_{SOA} is described in the **SI**. The single scattering albedo (SSA) at 375 nm was calculated by:

$$SSA_{375} = \frac{\beta_{scat,375}}{\beta_{scat,375} + \beta_{abs,375}}$$

The calculated SSA is size dependent and is calculated as a function of size parameter (α). α was determined with the following equation using d_m and the wavelength of radiation used in PAX (λ = 375 nm):[46]

$$\alpha_{375} = \frac{\pi d_m}{\lambda}$$

Offline <MAC> profiles were obtained using measurements from a UV-Vis spectrophotometer (Beckman DU-640). All the UV-Vis spectroscopy measurements were operated under 293 K and 1 atm.[14] The SOA filter samples were extracted using acetonitrile as the solvent, following the same extraction procedure as described above. The data from these measurements were used to calculate the <*MAC*> in $m^2\ g^{-1}$ for each sample:

$$< MAC >_{offline} = \frac{A(\lambda) \times \ln(10)}{b \times C_m}$$

where $A(\lambda)$ is the absorbance at the wavelength of interest, b is path length of cuvette (0.01 m) and C_m is the concentration of SOA in g m^{-3}.[14] Additionally, the absorption Angström exponent (*AAE*) was calculated for each <MAC> profile from this data:

$$AAE_{\frac{\lambda_1}{\lambda_2}} = \frac{-\ln \frac{< MAC > (\lambda_1)}{< MAC > (\lambda_2)}}{\ln (\frac{\lambda_1}{\lambda_2})}$$

where λ_1 and λ_2 are two selected wavelengths. $AAE_{290/400}$ and $AAE_{400/600}$ were calculated, which will improve our understanding of the wavelength dependence of light absorption in the UV (290 – 400 nm) and visible (400 – 600 nm) regions.[14]

In addition, offline analysis of chemical composition and light absorption was also carried out using liquid chromatography coupled (LC) with a diode array detector (DAD) and (–)ESI high resolution time of flight mass spectrometer ((–)ESI-HR-TOFMS, Agilent 6545 series).[14]

4.2.5 Kinetic simulations for NO_3 concentrations and TD-DFT calculations

In this work, since direct NO_3 measurement was unavailable, a kinetic model was used to estimate the concentrations of NO_3 before VOC injection for each experiment based on the measured initial O_3 and NO_2 concentrations.[49] The gas-phase loss of NO_3 and N_2O_5 to the Teflon wall are incorporated into the simulations using rates reported in previous research.[50] The model suggests that NO_3 concentrations stabilized at ~8.0 ppb and ~22.0 ppb for NO_x/O_3 ratios of 0.1 and 0.3, respectively before VOC injections. The kinetic model was also used to estimate the fractions of VOCs oxidized by NO_3 vs. O_3 using reaction rates reported in previous literature (for pyrrole)[22] and constrained in the CFSTR experiments in this work (for the methylpyrroles). As described in the **SI**, 1-MP reacts with O_3 faster than pyrrole by a factor of ~ 3.3 and with NO_3 slower than pyrrole by a factor of ~ 1.9. In contrast, 2-MP reacts faster with both O_3 and NO_3 than pyrrole by a factor of ~ 10.3 and ~ 9.8, respectively. Despite the variations in their reactivities, over 92% of all three VOCs was oxidized by NO_3 under the chamber conditions based on the kinetic model, suggesting the dominance of NO_3 oxidation chemistry in the SOA formation.

In addition, time-dependent density functional theory (TD-DFT) computational chemistry approaches were also used in this study to predict the UV-Vis spectra for several BrC chromophores of interest.[51] The calculations for the predicted UV-Vis spectra were performed with the Gaussian 16 program and the spectra were visualized using GaussView 06 software. All calculations were computed with acetonitrile as the solvent to be consistent with the offline UV-Vis measurements. To optimize the geometry PBE0 functional method with the 6-311+G(d,p) basis set was used, along with acetonitrile as the solvent. Likewise, the same functional method and basis set were used for the TD-DFT calculations, with 20 excited states. The cartesian coordinates for optimized geometries used for the simulated UV-Vis spectra are listed in **Tables S4.1-S4.2**.

4.3 Results and Discussion

4.3.1 Chemical Composition of the SOA

Figure 4.1 presents the (–)ESI-IMS-TOF mass spectra for SOA from NO_3 oxidation of pyrrole, 2-MP and 1-MP in the experiments with initial $NO_2/O_3 = 0.3$, with chemical formulas highlighted for the major product ions. Similar mass spectra from the initial $NO_2/O_3 = 0.1$ experiments are shown in the **SI, Figure S4.1**. All the identified major ions contain at least two nitrogen atoms and have $[M-H]^-$ chemical formulas, despite the usage of NaCl as the dopant. This deprotonation ionization scheme was previously reported for nitroaromatics and nitrophenols using the same instrument.[35,42,52] In contrast, non-acidic organic nitrates were found to mainly form $[M+Cl]^-$ adducts with doped Cl^-.[42] Alternatively, organic nitrates containing acidic groups may also exhibit $[M-H]^-$. The acidic groups could be carboxylic acids or alcohols on heterocyclic rings.[53] To distinguish between nitroaromatics and acidic organic nitrates (which may also deprotonate by the acidic groups in (–)ESI), we introduce a term for the three studied VOC systems, "NO_x index":

$$I_{NOx} = \frac{n_O}{n_N - 1}$$

where n_O and n_N are the numbers of oxygens and nitrogens per formula, respectively; $n_N - 1$ represents the number of additional nitrogens to the initial pyrrole or methylpyrroles. Thus, for products which only contain nitro groups (–NO_2), I_{NOx} = 2. To form organic nitrates (–ONO_2) through NO_3 addition to a double bond, another O-containing functional group must be added via peroxy radical chemistry. Therefore, for organic nitrate products, $I_{NOx} \geq 4$. I_{NOx} between 2 and 4 likely suggests multifunctional species that contain both –NO_2 and –ONO_2.

Table 4.1 Summary of Experimental Conditions

VOC	$[O_3]_{eq}$ (ppb)[b]	$[NO_x]_{eq}$ (ppb)[b]	Peak SOA mass conc. ($\mu g\ m^{-3}$)[c]	$<MAC>_{offline}$ ($m^2\ g^{-1}$) (375 nm and 290-700 nm average)[d]	$AAE_{290/400}$ and $AAE_{400/600}$	SSA_{375}[e]
Pyrrole	1332	265	298	0.35/0.21	4.98/6.23	0.80 ± 0.01
1-MP	1308	262	250	0.13/0.07	5.14/8.00	0.97 ± 0.00
2-MP	1392	177	422	0.69/0.35	4.72/8.83	0.76 ± 0.01
Pyrrole	908	88	149	0.23/0.13	4.46/5.18	0.80 ± 0.02
1-MP	898	76	175	0.16/0.08	5.27/6.81	0.97 ± 0.00

[a] A duplicate experiment was performed for each of the five conditions and the values reported in the table are averages of duplicates which usually vary within 10%; [b] Steady-state O_3 and NO_x concentrations measured before 200 ppb of VOC injection. Here, NO_2, NO_3, and N_2O_5 could be detected as NO_x; [c] Peak SOA mass was calculated using calculated effective SOA density for each experiment; [d] The 290 – 700 nm results for <MAC> are averaged values within the specific wavelength ranges; [e] The average SSA_{375} throughout the experiments when the size parameter was greater than 1.

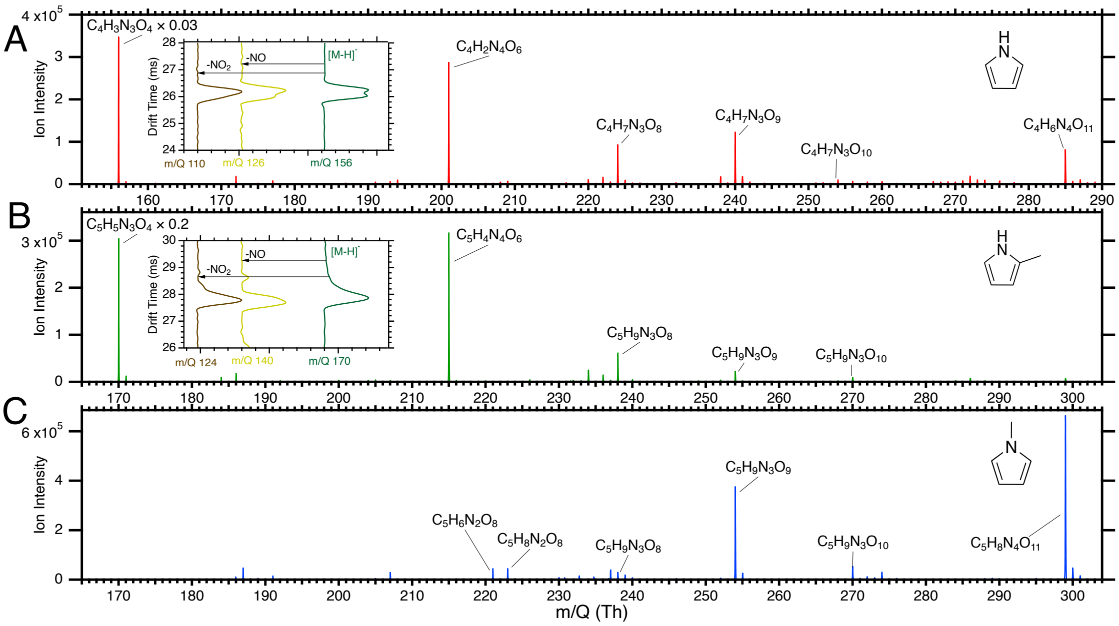

Figure 4.1 (–)ESI-IMS-TOF mass spectra with major products highlighted for (A) pyrrole + NO3 SOA, (B) 2-MP + NO3 SOA, and (C) 1-MP + NO3 SOA. For simplicity, the molecular formulas are labeled. The intensities of significant products, C4H3N3O4 for pyrrole and C5H5N3O4 for 2-MP, are multiplied by factors of 0.03 and 0.2 respectively to make the additional key products visible. The inserted plots in (A) and (B) show characteristic fragment ions ([M-H-NO]– and [M-H-NO2]–) for C4H3N3O4 in pyrrole SOA and C5H5N3O4 in 2-MP SOA using IMS drift time vs. intensity data obtained at high CID voltage (20 V). The x-axes are shifted by +14 in (B) and (C) in comparison to (A), to account for the difference by –CH2 in the VOC precursors, so that the oxidation products can be more easily compared.

From the NO_3 oxidation of pyrrole (**Figure 4.1A**) and 2-MP (**Figure 4.1B**), the most significant products identified in the SOA are $C_4H_3N_3O_4$ (*m/Q* 156 Th) and $C_5H_5N_3O_4$ (*m/Q* 170 Th), respectively. These formulas both have two additional nitrogens with I_{NOx} = 2, corresponding to dinitropyrrole and 2-methyl-dinitropyrrole, respectively. Following methods described in previous literature for identifying nitroaromatics in the IMS-TOF, we looked for the fragments of $[M\text{-}H\text{-}NO]^-$ and $[M\text{-}H\text{-}NO_2]^-$ at high CID voltage for these species which is indicative of the presence of $-NO_2$ functionality.[42] We found evidence of such fragments by identifying identical drift times between $[M\text{-}H]^-$, $[M\text{-}H\text{-}NO]^-$ and [M-

H-NO_2]$^-$ for $C_4H_3N_3O_4$ in the pyrrole SOA and $C_5H_5N_3O_4$ in the 2-MP SOA (inserted plots in **Figure 4.1A** and **Figure 4.1B**), thereby confirming that they are dinitropyrrole and 2-methyl-dinitropyrrole, respectively. It should be mentioned that their ion intensities are 5 – 30 times higher than the second largest product ions and thus are the most important products in these oxidation systems. Similarly, the second largest products in the pyrrole and 2-methylpyrrole SOA are $C_4H_2N_4O_6$ (*m/Q* 201 Th) and $C_5H_4N_4O_6$ (*m/Q* 215 Th), which have three additional nitrogens with I_{NOx} = 2, corresponding to trinitropyrrole and 2-methyl-trinitropyrrole, respectively. Although authentic standards are unavailable for quantification, prior work has shown that the relative sensitivities for SOA constituents in ESI-MS may vary by 1 – 2 orders of magnitude, and species with similar chemical structures and functional groups appear to have smaller variation.[54] Considering these factors, the dinitro- and trinitro-products are still major constituents in the SOA from pyrrole and 2-MP, clearly suggesting that these two heterocyclic VOCs exhibit a strong aromatic character during NO_3 oxidation and mainly form nitroaromatic products.

Strikingly, the SOA from 1-MP + NO_3 do not show the same behavior, despite the very similar chemical structure as pyrrole and 2-MP (**Figure 4.1C**). In fact, the same dinitro- and trinitro-products were not observed at all in 1-MP SOA. Instead, the main products in 1-MP SOA are $C_5H_9N_3O_{8-10}$ and $C_5H_8N_4O_{11}$. These products have I_{NOx} from 3.7 to 5, suggesting that they contain at least one –NO_3 with non-nitrogen-containing functional groups. Interestingly, similar high-I_{NOx} products were also observed in the SOA from pyrrole and 2-MP (**Figure 4.1A** and **4.1B**), but at much smaller intensities. These results strongly suggest that unlike pyrrole and 2-MP, 1-MP exhibits stronger alkene character which preferentially undergoes NO_3 addition. The molecular-level findings from the (–)ESI-IMS-TOF results were well supported by the complementary measurements using the LC-DAD-ESI-HR-TOFMS (**Figure S4.2**), where dinitropyrrole and 2-methyl-dinitropyrrole were found to be the most dominant products in the SOA from pyrrole and 2-MP, but no nitro-products were observed in the 1-MP SOA. In the measurements made by the mAMS, although the high vaporization temperature and ionization energy fragmented the molecular species into small ions and made product interpretation challenging, several characteristic fragment ions could still provide key evidence for the oxidation chemistry (**Figure S4.3**). Specifically, both NO^+ (m/Q 30 Th) and NO_2^+ (m/Q 46 Th) are abundant in the mAMS mass spectra, suggesting that nitro- or nitrate-containing products are major SOA constituents in all three systems. Yet, distinct organic products and patterns are clearly shown. For example, when comparing the SOA from 2-MP and 1-MP (which have the same VOC formulas), the 2-MP SOA contain more fragment ions without oxygen (e.g., $C_3H_{2\text{-}3}^+$ and $C_{2\text{-}3}H_{0\text{-}3}N^+$), while the 1-MP SOA have more fragment ions with oxygen (e.g., $C_2H_{2\text{-}4}NO^+$ and $CHNO_2^+$). Consistent with the individual fragment ions, the 2-MP SOA have a higher fraction of the $C_xH_y^+$ family and the 1-MP SOA have higher fractions of the $C_xH_yO_z^+$ and $C_xH_yO_zN^+$ families. These results imply that the 1-MP SOA are likely comprised of more oxygen-containing functional groups with oxygens bonded directly with carbons (e.g., –OH and $–ONO_2$) than the 2-MP SOA, agreeing with the molecular composition results.

4.3.2 Optical properties of SOA

To examine how the distinct functionalities in the SOA compositions between pyrrole, 1-MP, and 2-MP discussed above may affect the SOA optical properties, we report the light absorption and scattering properties by combing several online and offline measurements. The results for online and offline optical properties from pyrrole, 1-MP and 2-MP SOA are tabulated in **Table 4.1**. In **Figure 4.2A**, the $<MAC>_{offline}$ is plotted as a function of wavelength for SOA from NO_3 oxidation of pyrrole, 1-MP, and 2-MP. Here, the 2-MP SOA showed to be the most absorbing with the highest $<MAC>_{offline}$, followed by the pyrrole SOA. In contrast, the 1-MP SOA exhibited the least light absorbance with the lowest $<MAC>_{offline}$. These $<MAC>_{offline}$ profiles suggest that the SOA from pyrrole and 2-MP are greatly light absorbing in the near UV-range showing a peak of absorbance around 330 nm. The online optical measurements performed with the PAX show strong agreement with the offline measurements. In **Figure 4.2B**, the $<MAC>_{online,375nm}$ is plotted vs. experiment time, showing significant light absorption for the 2-MP SOA and the pyrrole SOA and much lower light absorption for the 1-MP SOA. 2-MP shows an average $<MAC>_{online,375}$ of $0.89 \pm 0.03\ m^2\ g^{-1}$, followed by pyrrole ($0.54 \pm 0.01\ m^2\ g^{-1}$) and 1-MP ($0.06 \pm 0.01\ m^2\ g^{-1}$). In **Figure 4.2C**, the SSA_{375} is plotted vs. size parameter, where the 2-MP SOA shows the lowest average SSA_{375} of 0.76 ± 0.01, followed by pyrrole (0.80 ± 0.01) and 1-MP (0.97 ± 0.00). The SSA_{375} of the pyrrole SOA from NO_3 oxidation agrees with previously reported results from similar experiments.[14] Therefore, we suggest that the SOA from NO_3 oxidation of 2-MP and pyrrole are strong BrC and show significant light-absorbing capabilities while those from 1-MP show little light-absorbing property and are mostly light scattering. Our calculations of AAE show minimal difference in wavelength dependence in the UV-range (290 – 400 nm) between pyrrole, 1-MP, and 2-MP SOA. However, in the visible range (400 – 600 nm), the SOA derived from the methylpyrroles exhibited stronger wavelength dependence than the pyrrole SOA.

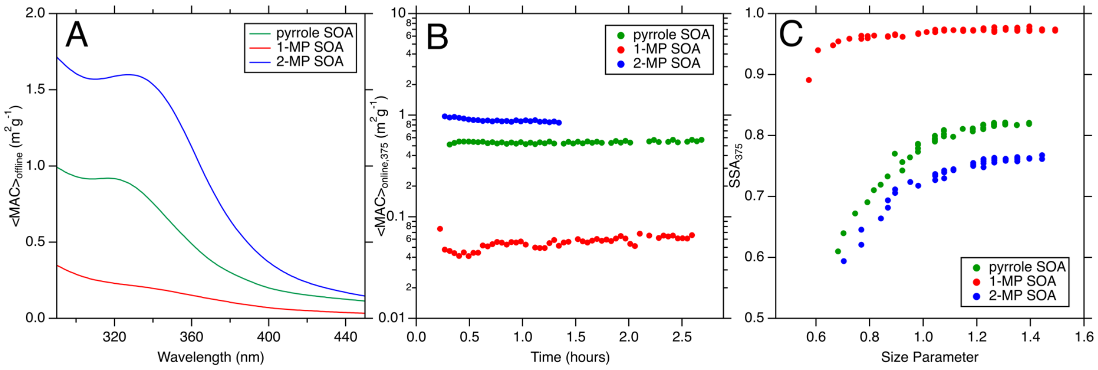

Figure 4.2 (A): $<\mathrm{MAC}>_{\mathrm{offline}}$ vs. wavelength (290-450 nm) calculated from UV-Vis and SEMS data of SOA from NO_3 oxidation (with the high-NO_2 condition) of pyrrole (green), 1-MP (red) and 2-MP (blue). (B): $<\mathrm{MAC}>_{\mathrm{online,375}}$ timeseries and (C): SSA_{375} calculated from the online PAX measurements.

By considering the SOA molecular compositions and optical properties synergistically for all three studied nitrogen-containing heterocyclic VOCs, it is conceivable that their SOA light absorption could be positively related to the abundance of the nitroaromatic products in the SOA. This is consistent with the fact that nitroaromatics have been shown to be strongly light absorbing. In previous studies of NO_3 oxidation of aromatic VOCs, nitroaromatic products generally constituted a significant portion of SOA mass and may have contributed to increased light absorption.[30,32,33,36–39] Although prior work also suggested that organic nitrates could contribute to BrC,[55] their light absorbing ability is likely much weaker. Further, we show that the $<\mathrm{MAC}>_{\mathrm{online,375nm}}$ measurements from all the NO_3 oxidation experiments (including the duplicate experiments) exhibit clear positive correlations with the ratio of NO^+ and NO_2^+ fragments to total organic ions obtained by the mAMS, which indicate that nitro and nitrate species are likely major contributors to BrC in the SOA (**Figure 4.3**). Interestingly, the $\langle MAC \rangle_{online,375nm}$ exhibits a negative correlation with the $CHO_{>1}N^+$ family (**Figure S4.4**). Assuming that oxygenated organic nitrates ($RONO_2$), as are expected to have formed in the 1-MP system, are more likely to form fragment ions in the $CHO_{>1}N^+$ family (because of the higher oxygen content) than nitroaromatics (RNO_2), this contrast implies that it is the nitroaromatics, rather than organic nitrates, that contribute to the BrC in these systems. In support of this, the LC-DAD-ESI-HR-TOFMS results exhibit strong light absorption at wavelength 320 – 340 nm for dinitropyrrole and 2-methyl-dinitropyrrole (**Figure S4.2**), consistent with the UV-Vis results. In addition, the TD-DFT calculations show that the predicted UV-Vis spectra of dinitropyrroles (the dominant SOA constituents from pyrrole + NO_3) peak at approximately the same observed UV-Vis peak of the total pyrrole SOA, while organic nitrates show very different spectral shapes with much lower absorbance (by more than two orders of magnitude) under the TD-DFT calculations (**Figure S4.5**). These pieces of evidence collectively suggest that nitroaromatics are clearly the dominant, if not the only, BrC chromophores in the SOA formed from NO_3 oxidation of pyrrole and 2-MP.

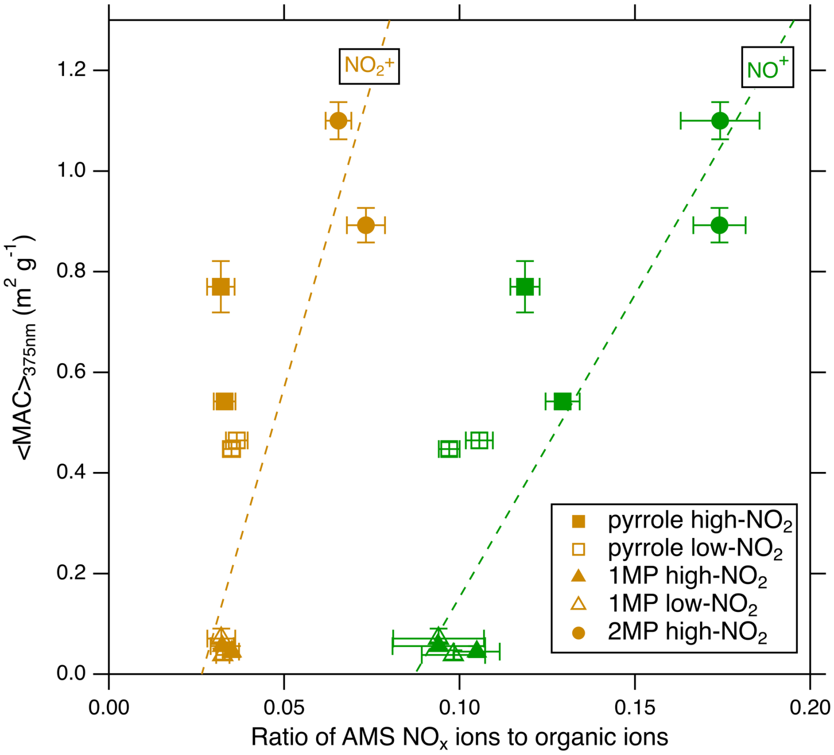

Figure 4.3 The correlations between <MAC>$_{online,375nm}$ and AMS ion ratios of NO$^+$ (green) and NO$_2^+$ (brown) to total organic ions for all the performed experiments. The dashed lines represent the error-weighted Pearson correlation fittings (R = 0.78 for NO$_2^+$ and 0.81 for NO$^+$).

4.3.3 Proposed mechanisms for formation of nitroaromatics from NO$_3$ oxidation of pyrrole and methylpyrroles

After demonstrating that nitroaromatics in the SOA from pyrrole and 2-MP are the dominant constituents and contributors to BrC, it is critical to elucidate their formation mechanisms in the pyrrole and 2-MP systems and explain why nitroaromatics are not largely formed in the 1-MP system. Apparently, a key difference is that both pyrrole and 2-MP are secondary amines with N–H bonds, while 1-MP is a tertiary amine without an N–H bond. Therefore, we propose that the N–H bonds play an important role in the NO$_3$ oxidation of pyrrole and 2-MP that led to the substantial formation of nitroaromatics. In

Figure 4.4, a mechanism is proposed for the addition of 1, 2, and 3 $–NO_2$ groups to the backbone of pyrrole through NO_3 oxidation. In this mechanism, we propose H-abstraction by NO_3 for pyrrole on the 1-position (H in the N–H bond), followed by a pyrrolyl radical-shift. NO_2 then adds to this radical and a subsequent H-shift would occur to move the hydrogen back to the 1-position and form a nitropyrrole. This initial step is somewhat similar to that proposed for H-abstraction of phenolic species in which nitrophenols are observed.[30–34] The nitropyrroles were not observed in the pyrrole + NO_3 SOA by the IMS-TOF measurements, likely because they are too volatile to partition to the particle phase. But they were indeed dominant gas-phase products, confirmed by the I-CIMS results (**Figure S4.6**), supporting our proposed mechanism. From here, the mechanism repeats itself beginning with the same H-abstraction on the 1-position by NO_3 for the additions of the second and third $–NO_2$ groups. Through this process, the original aromaticity is retained, facilitating sequential $–NO_2$ addition. For simplicity, the formation of only one dinitropyrrole isomer and one trinitropyrrole isomer are explicitly shown in **Figure 4.4**, but there could be up to 4 positional dinitropyrrole isomers and 2 trinitropyrrole isomers, depending on how the pyrrolyl radicals shift. In agreement with this, we observe 4 isomers for dinitropyrrole from the extracted ion chromatogram in the LC-DAD-ESI-HR-TOFMS (**Figure S4.2**). The proposed mechanism is also consistent with the results that higher NO_2 concentrations led to stronger light absorption in the two pyrrole experiments (**Table 4.1** and **Figure 4.3**), as higher NO_2 concentrations could enhance formation of dinitro- and trinitro-pyrroles. In the real atmosphere affected by wildfire, NO_2 concentrations have been reported to be as high as ~ 60 ppb, somewhat lower than the experimental conditions in this work.[56] With lower NO_2 concentrations, it is possible that oxygen addition on the pyrrolyl radicals (producing peroxy radicals) could become more competitive in comparison to NO_2 addition (producing nitropyrroles). However, the likely gas-phase products from peroxy radical chemistry are found to be lower than the nitropyrroles by ~ 3 orders of magnitude with ~ 90 ppb of NO_2 (**Figure S4.7**), suggesting that the NO_2 addition is the dominant pathway for the pyrrolyl radicals even with ambient-level NO_2 concentrations. These results are highly consistent with prior work on phenoxy radicals from phenol oxidation[57] and *o*-semiquinone radicals from catechol oxidation,[30] both of which suggested dominant NO_2 addition in comparison to oxygen addition.

The mechanism for addition of NO_2 to 2-MP would be analogous to that of pyrrole except that there is a methyl group in the 2-position which might interfere the pyrrolyl radical shift and hence the number of possible positional isomers in comparison to pyrrole. In fact, the results shown in **Figure S4.2** suggest that there are two major 2-methyl-dinitropyrrole isomers in the 2-MP SOA. It should be noted that there has not been direct measurement-based evidence for the proposed radical or hydrogen shift in the (methyl)pyrrole or the phenolic NO_3 oxidation systems, suggesting that other unrecognized mechanisms cannot be fully ruled out. However, combining all the pieces of evidence discussed above and in the literature,[30–34] this mechanism appears to be a highly likely one.

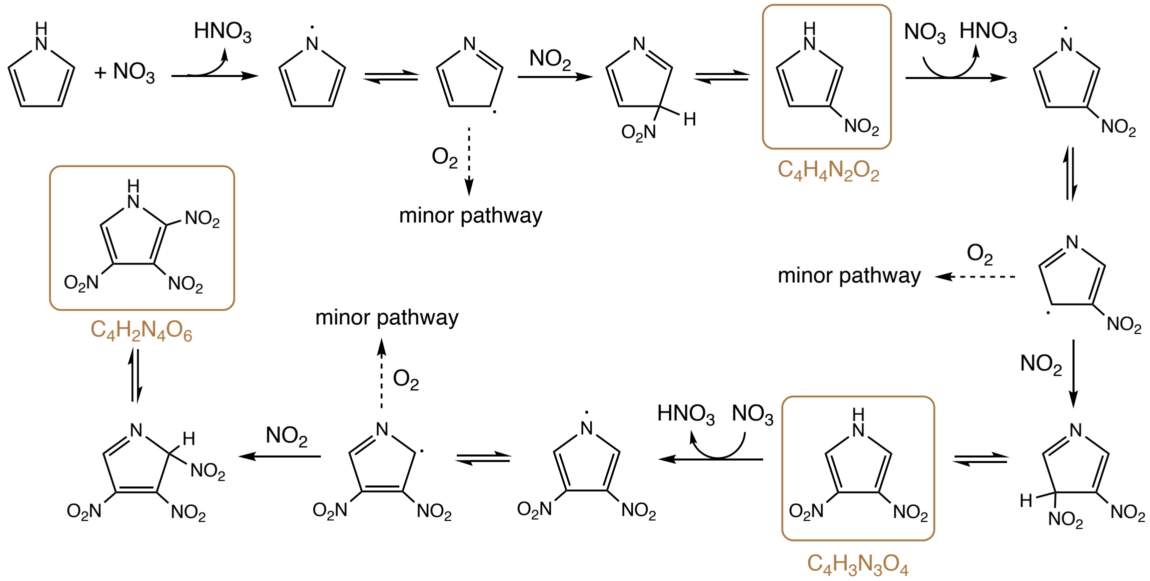

Figure 4.4 Proposed chemical mechanism for the addition of 1, 2 and 3 NO_2 groups to pyrrole. Only one isomer for each of $C_4H_4N_2O_2$, $C_4H_3N_3O_4$, $C_4H_2N_4O_6$ is shown, but multiple isomers are possibly formed, depending on how the pyrrolyl radicals undergo shift.

In comparison to this mechanism, 1-MP is a tertiary amine and does not contain a N–H bond like pyrrole and 2-MP. Thus, the mechanism shown in **Figure 4.4** does not work for 1-MP, explaining the absence of dinitro- and trinitro-products in the 1-MP SOA. Based on the measurements discussed above, we also suggest the hydrogen in the N–H bond must be more susceptible to abstraction by NO_3 than other hydrogens on the ring. Instead, in the NO_3 oxidation of 1-MP, we rather observed products with $–NO_3$ and additional oxygen-containing functionality (e.g., –OH). The lack of the secondary amine structure in the backbone of 1-MP may require other mechanisms to occur for 1-MP such as NO_3 addition to the double bond. A tentative mechanism is proposed in **Figure S4.8**, which may explain some of the observed 1-MP gas-phase and SOA constituents. Particularly, the dominant gas-phase product, $C_5H_7NO_2$ (**Figure S4.6**) is likely formed through nitrooxy alkoxy radical bond scission and NO_2 removal.[58] The analogous product in the pyrrole system ($C_4H_5NO_2$) appears to be much smaller (**Figure S4.6**), again supporting that NO_3 oxidation of pyrrole is mainly through H-abstraction. For 1-MP, the breaking of aromaticity through the addition of $–NO_3$ and –OH functional groups ultimately lead to decreased light absorption in the SOA. Conversely, the retention of aromaticity and the addition of a strong electron-withdrawing group, $–NO_2$, increases the strong light absorption of the pyrrole and 2-MP SOA. The proposed mechanisms highlight the importance of secondary amines as key structures in pyrrole and methylpyrroles to form BrC chromophores.

4.4 Atmospheric Implications

In this study, we have demonstrated that small differences in the structures of pyrrole and its methyl derivatives have significant implications for the optical properties of their SOA from NO_3 oxidation. The NO_3 oxidation of 2-MP and pyrrole led to SOA compositions which were almost entirely caused by products resulting from the addition of two or three $–NO_2$ groups. These nitroaromatic products resulted in the strong light absorption of the SOA from 2-MP and pyrrole. To understand the significance of the pyrrole and methylpyrroles on SOA mass concentration and BrC light absorption from atmospheric biomass burning of different fuels, we estimate the SOA formation potential (SOA_{pot}, g of SOA potentially formed per kg of fuel) and absorption cross-section emission factor (EF_{abs}, m^2 of absorption per kg of fuel) for pyrrole, 2-MP, and several other relevant VOC oxidation systems (i.e., phenolic VOC + NO_3 and toluene + OH/NO_x).[14] The estimations are based on emission factors (EF) from typical biomass burning fuels reported in previous work,[5,8,9] SOA yields from previous laboratory oxidation studies,[35,59] and the reported <MAC> results for the corresponding SOA in literature:[35,60]

$$SOA_{pot,i} = EF_i \times Y_{SOA,i}$$

$$EF_{abs,i} = SOA_{pot,i} \times < MAC >_i$$

where $Y_{SOA,i}$ is the estimated SOA yield for a VOC species, i. The details are shown in **Tables S4.3– S4.5**. For the VOCs whose SOA yields or <MAC> values are unknown, we use results from a similar VOC in the same category as a reasonable approximate. From these calculations, we compare the SOA_{pot} and EF_{abs} between the summed SOA from NO_3 oxidation of pyrrole and 2-MP with total phenolic + NO_3 SOA and toluene photooxidation SOA. In a recent study, Palm et al. reported that phenolic SOA may contribute to 29 ± 15% of biomass burning BrC during daytime and underscored the importance to study nighttime processes of biomass burning emissions.[61] Kodros et al. also pointed out that nighttime oxidation of biomass burning emissions may be an overlooked source of oxidized organic aerosols.[62] Here, we estimate that the total SOA_{pot} from NO_3 oxidation of pyrrole and 2-MP may be 119 – 189% of that from NO_3 oxidation of phenolic VOCs and 52 – 277% of that from toluene photooxidation. In addition, the total EF_{abs} of pyrrole and 2-MP SOA is 25 – 49% of that for the phenolic + NO_3 SOA and 36 – 170% of that for toluene photooxidation SOA. The large variations in these comparisons are due to strong fuel dependence of the VOC emission factors. Although SOA yields and <MAC> results were obtained from different studies under different experimental conditions, and thus some uncertainties are expected, these findings clearly demonstrate that the SOA from nighttime oxidation of pyrrole and 2-MP will significantly contribute to SOA mass concentration and light absorption in biomass burning derived aerosols. Therefore, their oxidation chemistry and contribution to SOA and BrC need to be implemented in air quality and climate models. The SOA and BrC formation from nighttime oxidation of nitrogen-containing heterocyclic VOCs have been understudied. This study filled the knowledge gap and demonstrated that small differences in chemical structure for these nitrogen-containing heterocyclic VOCs have significant impacts on the chemical composition and light-absorption of SOA.

4.5 Supporting Information

4.5.1 CFSTR kinetic experiments.

To validate that 1-methylpyrrole (1-MP) and 2-methylpyrrole (2-MP) both primarily react with NO_3 under the studied conditions, we performed four experiments using the relative rate method referencing known reaction rates of pyrrole with O_3 and NO_3 to estimate the reaction rates of 1-MP and 2-MP with O_3 and with NO_3.[22] The experiments were performed in a continuous flow stirred tank reactor (CFSTR, volume ~250 L, stainless steel enclosure with interior coating by Teflon PFA) under 20°C and relative humidity < 5%.[35,41] The total flow rate in the CFSTR was 2.8 L min^{-1} providing a residence time of approximately 89 minutes. A clean air generator (Aadco Instruments, Inc.) was used to provide clean dry air for the experiments. For each experiment, approximately 2 μL of one of the methylpyrroles and 2 μL of pyrrole were injected into the reactor using a syringe to achieve ~2.2 ppm of each VOC in the reactor. Before injection of oxidants, the first-order rate of dilution and wall loss of the VOCs was measured with a highly sensitive proton-transfer reaction mass spectrometer (PTR-MS, Ionicon Analytik GmbH). Pyrrole is measured at *m/Q* 68 Th ($C_4H_6N^+$) and the methylpyrroles are measured at *m/Q* 82 Th ($C_5H_8N^+$). For the O_3 oxidation experiments, ~ 100 ppb O_3 was injected by passing O_2 through an O_3 generator (Ozone Solution Inc.). For NO_3 decay experiments, ~ 150 ppb NO_2 (20 ppm in N_2, Airgas Inc.) was injected followed by ~ 100 ppb O_3. Upon reaction with O_3 or with NO_3, we could measure VOC decay due to O_3 or NO_3 with the PTR-MS. For NO_3 oxidation experiments, we waited until O_3 concentration had decreased to < 10 ppb to ensure that the VOCs were primarily oxidized by NO_3. The concentrations of O_3

and NO_2 were measured using a 49C O_3 analyzer and a 42C NO_x analyzer (Thermo Environmental Instruments). The oxidation reactions can be expressed in the following ordinary differential equation:

$$\frac{d[VOC]}{dt} = -k[VOC][oxidant]$$

where k represents the rate constant in cm^3 $molecule^{-1}$ s^{-1}, $[VOC]$ represents the concentration of pyrrole, 1-MP or 2-MP and $[oxidant]$ represents the concentration of O_3 or NO_3. Solving the equation gives:

$$\frac{[VOC]}{[VOC]_0} = e^{(-k[oxidant] \times t)}$$

where t represents the time in seconds and $[VOC]_0$ represents the VOC concentration at the beginning of the decay period. Then, a lognormal fit of the VOC concentration during the decay period yields:

$$ln\left(\frac{[VOC]}{[VOC]_0}\right) = -k't$$

Using a linear fit, we can find the slope, k', which is equal to $k[oxidant]$. Finally, using the relative rate method, the rate of 1-MP or 2-MP with O_3 or NO_3 is calculated using:

$$\frac{(k'_{oxidant} - k'_{dilution})_{methylpyrrole}}{(k'_{oxidant} - k'_{dilution})_{pyrrole}} = \frac{k_{methylpyrrole}}{k_{pyrrole}}$$

where $k'_{oxidant}$ and $k'_{dilution}$ are the lognormal slopes from this equation during the oxidant decay period and the VOC dilution period respectively. Using known reaction rates of pyrrole with O_3 and NO_3 and solving this equation for $k_{methylpyrrole}$ provides an estimation of the reaction rate of the oxidant with the methylpyrroles.[22] Using this approach, we estimate the reaction rates of 1-MP and 2-MP with O_3 to be 5.28×10^{-17} cm^3 $molecule^{-1}$ s^-

^{1} and 1.64 × 10^{-16} cm^3 molecule^{-1} s^{-1} respectively. We estimate the reaction rates of 1-MP and 2-MP with NO_3 to be 2.55 × 10^{-11} cm^3 molecule^{-1} s^{-1} and 4.80 × 10^{-10} cm^3 molecule^{-1} s^{-1}, respectively.

4.5.2 Calculations of MF_{OA}, ϱ_{eff}, and C_{SOA}.

Ratios of NO^+/NO_2^+ from the experiments were used along with the corresponding value during ammonium nitrate calibrations to estimate the contribution of organonitrate/nitroorganics to the total measured nitrate (i.e., the organic fraction of nitrate, $f_{NO3,org}$)[63]:

$$f_{NO3,org} = \frac{\left(R_{exp} - R_{AN}\right)(1 + R_{lit})}{(R_{lit} - R_{AN})(1 + R_{exp})}$$

where R refers to the ratio of NO^+/NO_2^+ in the experiments (R_{exp}), during ammonium nitrate calibrations (R_{AN}), and the expected value for organonitrate/nitroorganics (R_{lit}, 3.58-3.89) calculated following the "ratio-of-ratio" procedure outlined in Day et al.[64] The organic mass fraction of the aerosols (MF_{OA}) was estimated using:

$$MF_{OA} = \frac{OA + NO_3^- \times f_{NO3,org}}{Total\ AMS\ Mass}$$

where OA and NO_3^- are the mass concentrations of organic and nitrate aerosols, respectively, and the denominator is the sum of all the species measured by the mAMS.

Total mAMS species mass distributions in the vacuum aerodynamic space were averaged onto 10-minute time intervals and compared with mobility-based volume distributions in the same time interval. Log-normal fits to the distributions were obtained and the geometric mean diameters of each distribution, d_{va} and d_m, respectively, were calculated. The aerosol effective density (ρ_{eff}) during each time interval was calculated as[47]:

$$\rho_{eff} = \rho_0 \times \frac{d_{va}}{d_m}$$

where ρ_0 is unit density. Next, a time-dependent fit to the calculated effective densities was obtained to determine the effective density values corresponding to the finer time scales of mAMS mass distributions averaged onto the SEMS measurement frequency (140 s). The total mass concentration of organic aerosols (C_{SOA}) was calculated using:

$$C_{SOA} = V_{aerosol} \times \rho_{eff} \times MF_{OA}$$

where $V_{aerosol}$ is the total volume concentration of particles based on the volume distributions determined by SEMS.

Table S4.1 Cartesian coordinates of optimized geometries of 2,5-dinitropyrrole and 3,4-dinitropyrrole obtained from DFT calculations.

2,5-dinitropyrrole: PBE0 (acetonitrile)				3,4-dinitropyrrole: PBE0 (acetonitrile)			
C	0.25368	0.00003	1.08498	C	-1.61481	0.00033	1.11375
C	1.58391	0.00001	0.69988	C	-0.29627	0.00007	0.71908
C	1.58391	0.00001	-0.69988	C	-0.29627	0.00007	-0.71908
C	0.25368	0.00003	-1.08498	C	-1.61481	0.00033	-1.11375
N	-0.55187	0.00004	0.00000	N	-2.37909	0.00100	0.00000
H	-1.56437	0.00007	0.00000	H	-3.38926	0.00166	0.00000
H	2.43455	-0.00001	1.36260	H	-2.03063	0.00042	2.10749
H	2.43455	-0.00001	-1.36260	H	-2.03063	0.00042	-2.10749
N	-0.31077	0.00004	2.39135	N	0.74422	-0.00033	1.70714
O	-1.52906	-0.00003	2.47406	O	1.90605	0.00155	1.35814
O	0.45769	-0.00006	3.33459	O	0.38257	-0.00215	2.87598
N	-0.31077	0.00004	-2.39135	N	0.74422	-0.00033	-1.70714
O	-1.52906	-0.00003	-2.47406	O	1.90605	0.00155	-1.35814
O	0.45769	-0.00006	-3.33459	O	0.38257	-0.00215	-2.87598

Table S4.2 Cartesian coordinates of optimized geometries of 2,5-dihydroxy-3,4-dinitratepyrrole and 3,4-dihydroxy-2,5-dinitratepyrrole obtained from DFT calculations.

2,5-dihydroxy-3,4-dinitratepyrrole: PBE0 (acetonitrile)				3,4-dihydroxy-2,5-dinitratepyrrole: PBE0 (acetonitrile)			
C	0.09814	-1.98381	0.20727	C	1.17833	0.4903	0.99063
C	0.34982	-0.47644	0.40441	C	0.73228	1.50975	-0.09393
C	-1.04033	0.11535	0.10502	C	-0.82355	1.60647	0.07567
C	-1.73507	-0.88251	-0.85698	C	-1.17809	0.43913	1.02299
N	-0.81383	-1.99094	-0.89164	N	0.01258	0.23539	1.7357
H	-1.21981	-2.88411	-1.13785	H	0.04174	-0.35559	2.55308
H	0.71822	-0.2315	1.3945	H	2.01088	0.81944	1.60301
H	-1.86277	-0.44498	-1.84939	H	1.19614	2.47223	0.10817
H	1.01075	-2.53055	-0.03389	H	-2.03483	0.60724	1.66485
H	-1.61213	0.16437	1.02797	H	-1.07034	2.52712	0.60565
O	-0.49162	-2.53112	1.39475	O	1.60245	-0.79959	0.36547
H	0.21239	-2.78246	2.00781	O	-1.47578	-0.79152	0.21823
O	-3.01438	-1.2721	-0.3621	O	-1.5075	1.59992	-1.14667
H	-3.69764	-0.80626	-0.85944	H	-0.89304	1.23648	-1.80625
O	-1.0398	1.40234	-0.53319	O	1.05293	1.06739	-1.40043
O	1.25393	0.04773	-0.59415	H	1.56694	1.74655	-1.85147
N	2.62517	-0.07501	-0.27648	N	-2.80489	-0.9701	-0.15235
O	2.92526	-0.6137	0.7604	O	-2.96794	-1.91664	-0.88584
O	3.33514	0.39592	-1.12485	O	-3.64203	-0.21507	0.28799
N	-0.76408	2.4939	0.32385	N	2.90658	-0.83264	-0.10987
O	-0.53484	2.25723	1.48431	O	3.60494	0.14564	0.04243
O	-0.7981	3.54923	-0.24994	O	3.19904	-1.88461	-0.62662

Table S4.3 SOA yields and average <MAC> from the NO_3 oxidation of pyrrole, 1-MP and 2-MP, several phenolic VOCs and from the photooxidation of toluene from literature.

VOC + oxidant	SOA yield	Reference for SOA Yield	$\langle MAC \rangle_{offline,290-700}$	Reference for $\langle MAC \rangle_{offline,290-700}$
pyrrole + NO_3	0.54	this study	0.21	this study
1-MP + NO_3	0.38	this study	0.07	this study
2-MP + NO_3	0.64	this study	0.35	this study
phenol + NO_3	0.05	Mayorga et al.[35]	0.90	Mayorga et al.[35]
2-methylphenol + NO_3	0.12	Ramasamy et al.[65]	0.90[b]	Mayorga et al.[35]
3+4-methylphenol	0.01	Iinuma et al.[66]	0.90[b]	Mayorga et al.[35]
2,6-dimethylphenol	0.12[a]	Ramasamy et al.[65]	0.90[b]	Mayorga et al.[35]
2,5-dimethylphenol	0.12[a]	Ramasamy et al.[65]	0.90[b]	Mayorga et al.[35]
catechol + NO_3	0.18	Mayorga et al.[35]	1.39	Mayorga et al.[35]
catechol + NO_3	1.50	Finewax et al.[30]		
4-methylcatechol + NO_3	0.09	Mayorga et al.[35]	1.30	Mayorga et al.[35]
guaiacol + NO_3	0.12	Mayorga et al.[35]	0.30	Mayorga et al.[35]
guaiacol + NO_3	0.13	Meng et al.[67]		
toluene + high NO_x	0.11	Jiang et al.[59]	0.30	Liu et al.[60]

[a]SOA yield and [b]$\langle MAC \rangle_{offline,290-700}$ could not be found in literature, so values from 2-methylphenol + NO_3 and phenol + NO_3 were used.[35,65]

Table S4.4 Potential SOA formation (SOA_{pot}, g kg^{-1}) from the NO_3 oxidation of pyrrole, 1-MP, 2-MP, several phenolic VOCs, and from the photooxidation of toluene under high NO_x released from six different fuels. In the last two rows of the table, the ratios of summed SOA_{pot} for pyrrole + 2MP to phenolic SOA and pyrrole + 2MP to toluene SOA are shown for each fuel type.

VOC + oxidant	Black Spruce	Ponderosa Pine	Giant Cutgrass	Wire Grass	Rice Straw	Indonesian Peat
pyrrole + NO_3	0.0227	0.0600	0.0124	0.0074	0.0271	0.0300
1-MP + NO_3	0.0040	0.0080	0.0009	0.0015	0.0022	0.0118
2-MP + NO_3	0.0031	0.0098	0.0014	--	0.0043	0.0115
phenol + NO_3	0.0064	0.0246	0.0075	0.0029	0.0130	0.0239
2-methylphenol + NO_3	0.0025	0.0059	0.0017	0.0013	0.0051	0.0112
3+4-methylphenol	0.0002	0.0004	0.0001	0.0001	0.0003	--
2,6-dimethylphenol	--	--	--	--	0.0004	--
2,5-dimethylphenol	--	0.0013	--	--	0.0009	--
catechol + NO_3	0.0112	0.0021	--	--	--	--
4-methylcatechol + NO_3	--	0.0001	--	--	--	--
guaiacol + NO_3	0.0016	0.0068	--	0.0025	0.0013	0.0097
toluene + high NO_x[a]	0.0470	0.0551	0.01125	0.0032	0.0161	0.1033
Ratio pyrrole + 2-MP SOA to phenolic SOA	1.36	1.89	1.57	1.31	1.59	1.19
Ratio pyrrole + 2-MP SOA to toluene SOA	0.63	1.41	1.31	2.77	2.09	0.52

[a] The SOA yield of toluene under high NO_x were used from a study by Jiang et al.[59]

Table S4.5 Absorption cross-section emission factor (EF_{abs}, $m^2\ kg^{-1}$) of SOA from the NO_3 oxidation of pyrrole, 1-MP, 2-MP, several phenolic VOCs, and from the photooxidation of toluene under high NO_x released from six different fuels. In the last two rows of the table, the ratios of summed EF_{abs} for pyrrole + 2MP to phenolic SOA and pyrrole + 2MP to toluene SOA are shown for each fuel type.

VOC + oxidant	Black Spruce	Ponderosa Pine	Giant Cutgrass	Wire Grass	Rice Straw	Indonesian Peat
pyrrole + NO_3	0.0048	0.0126	0.0026	0.0015	0.0057	0.0063
1-MP + NO_3	0.0003	0.0006	0.0001	0.0001	0.0002	0.0008
2-MP + NO_3	0.0011	0.0034	0.0005	--	0.0015	0.0040
phenol + NO_3	0.0057	0.0221	0.0067	0.0026	0.0117	0.0214
2-methylphenol + NO_3	0.0022	0.0053	0.0015	0.0011	0.0045	0.0100
3+4-methylphenol	0.0002	0.0004	0.0001	0.0001	0.0002	--
2,6-dimethylphenol	--	--	--	--	0.0004	--
2,5-dimethylphenol	--	0.0012	--	--	0.0008	--
catechol + NO_3	0.0156	0.0029	--	--	--	--
4-methylcatechol + NO_3	--	0.0001	--	--	--	--
guaiacol + NO_3	0.0005	0.0021	--	0.0008	0.0004	0.0030
toluene + high NO_x[a]	0.0142	0.0166	0.0034	0.0010	0.0048	0.0312
Ratio pyrrole + 2-MP SOA to phenolic SOA	0.25	0.49	0.38	0.36	0.41	0.32
Ratio pyrrole + 2-MP SOA to toluene SOA	0.43	1.00	0.93	1.70	1.52	0.36

[a] The <MAC> of toluene SOA under high NO_x were used from a study by Liu et al.[60] over the range of 300-700 nm while other values shown in this table were calculated using <MAC> over the range of 290-700 nm.

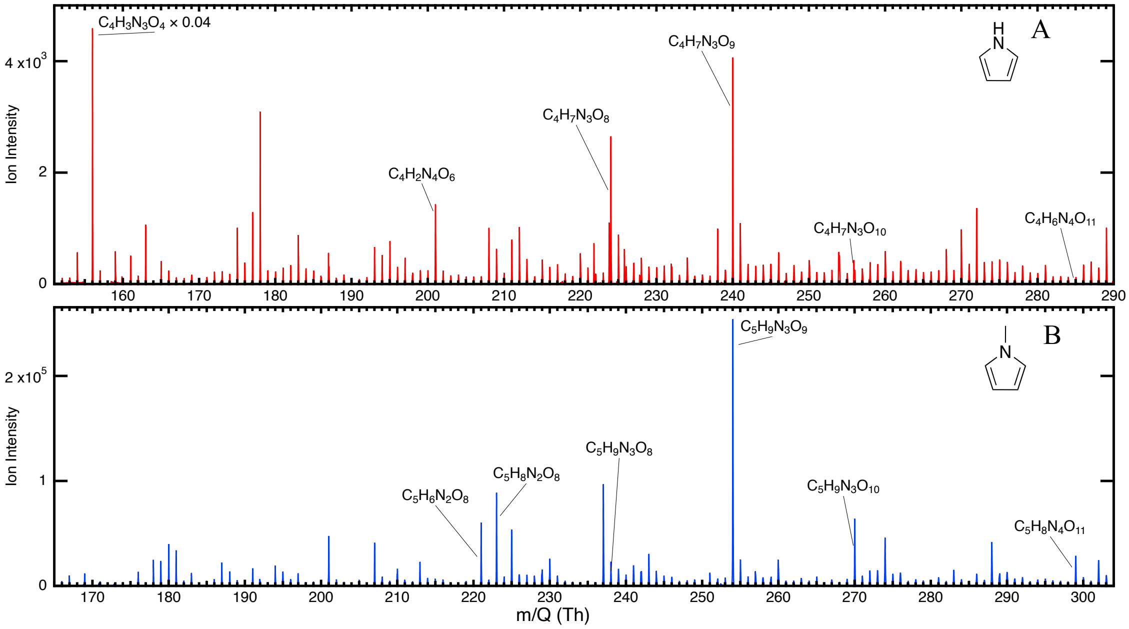

Figure S4.1 (–)ESI-IMS-TOF mass spectra with major products labeled for (A) pyrrole SOA, and (B) 1-MP SOA from experiments with a NO_x/O_3 ratio of 0.1. The intensities of a significant product, $C_4H_3N_3O_4$ for pyrrole, is multiplied by a factor of 0.04 to make the additional key products visible. The *x*-axis is shifted by +14 in (B) in comparison to (A), to account for the difference by –CH_2 in the VOC precursors, so that the oxidation products can be more easily compared.

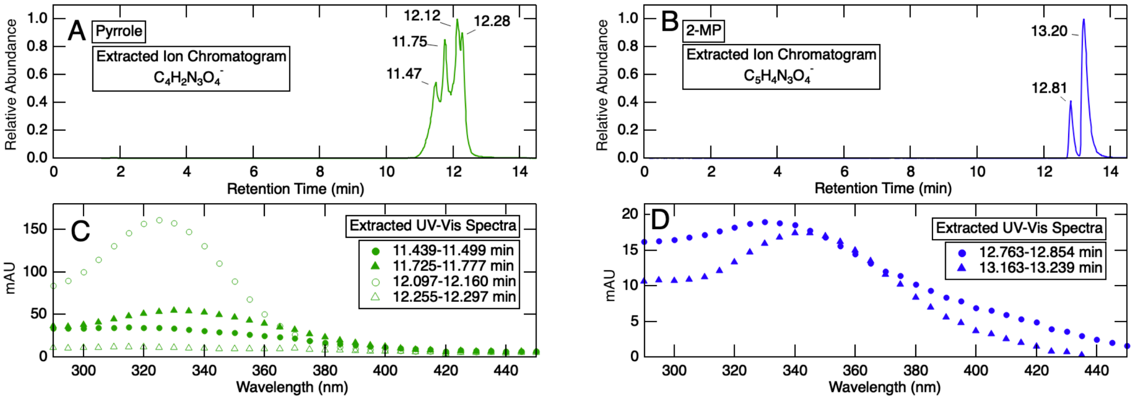

Figure S4.2 Extracted ion chromatograms for (A) dinitropyrrole in pyrrole SOA and (B) 2-methyl-dinitropyrrole in 2-MP SOA. Extracted UV-Vis spectra (mAU, milli absorbance units) of (C) pyrrole SOA for retention times: 11.439-11.499 min, 11.725-11.777 min, 12.097-12.160 min, 12.255-12.297 min and (D) 2-MP SOA for retention times: 12.763-12.854 min and 13.163-13.239 min.

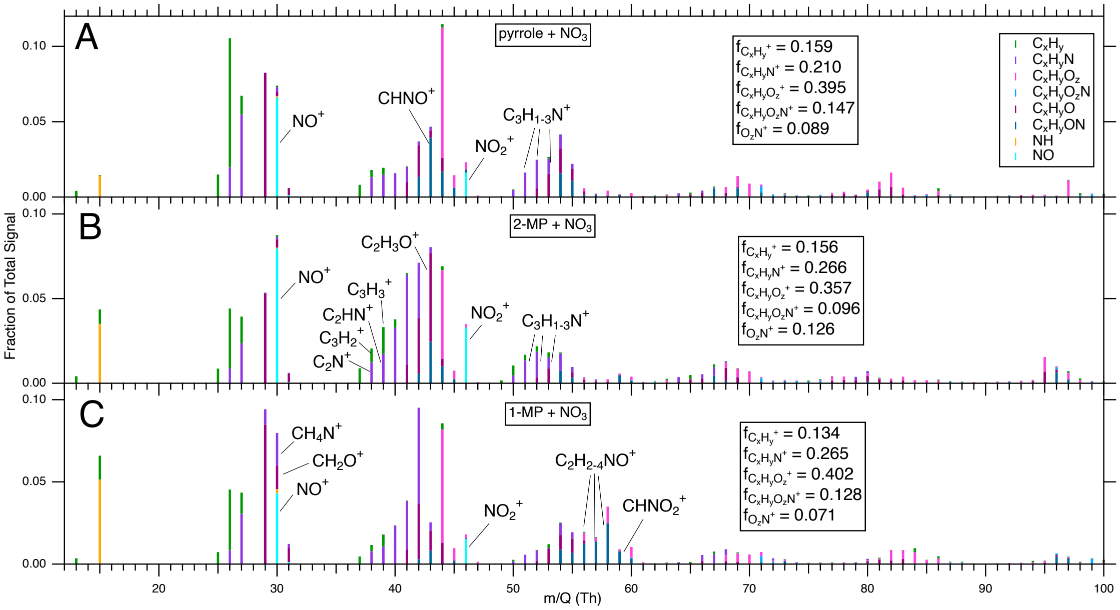

Figure S4.3 Mass spectra from the mAMS for (A) pyrrole SOA, (B) 2-MP SOA, and (C) 1-MP SOA.

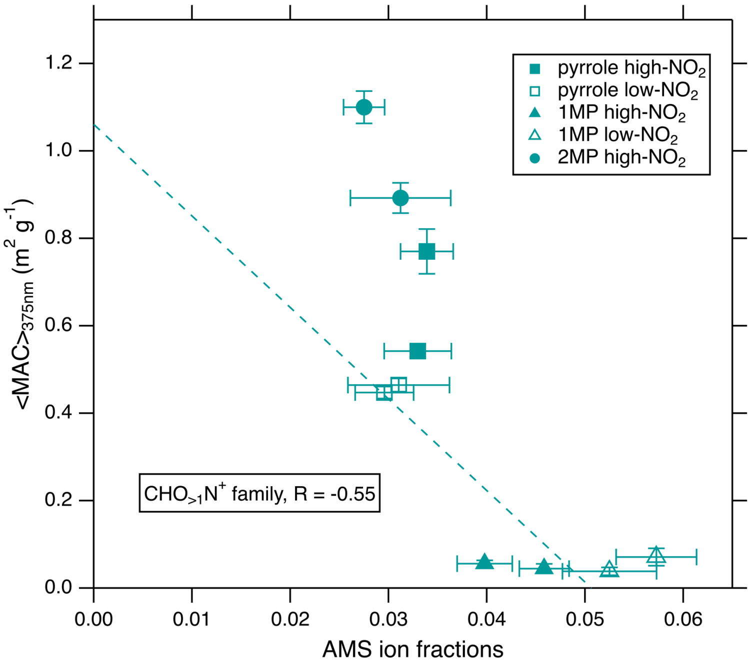

Figure S4.4 The correlations between <MAC>$_{online,375nm}$ and AMS ion fractions of CHO$_{>1}$N$^+$ fragments for all five experiments. The dashed lines represent the error-weighted linear fittings with the Pearson correlation coefficients (R) shown.

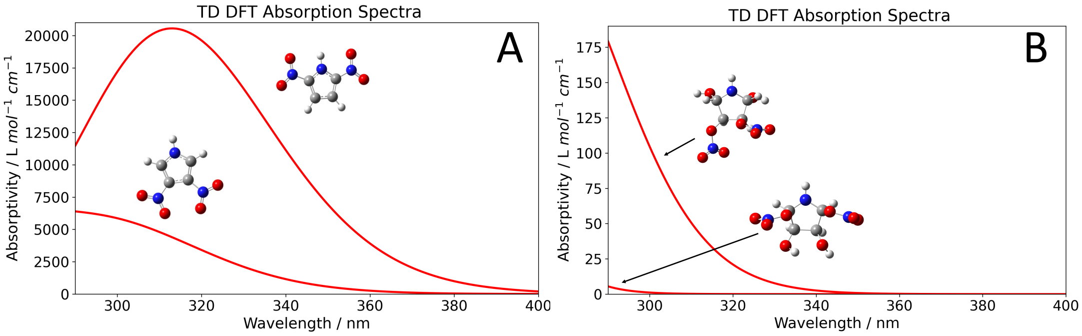

Figure S4.5 TD-DFT absorption spectra for (A) 2,5-dinitropyrrole and 3,4-dinitropyrrole and (B) 2,5-dihydroxy-3,4-dinitratepyrrole and 3,4-dihydroxy-2,5-dinitratepyrrole calculated with acetonitrile as the solvent. The spectra are labeled with their corresponding chemical structure.

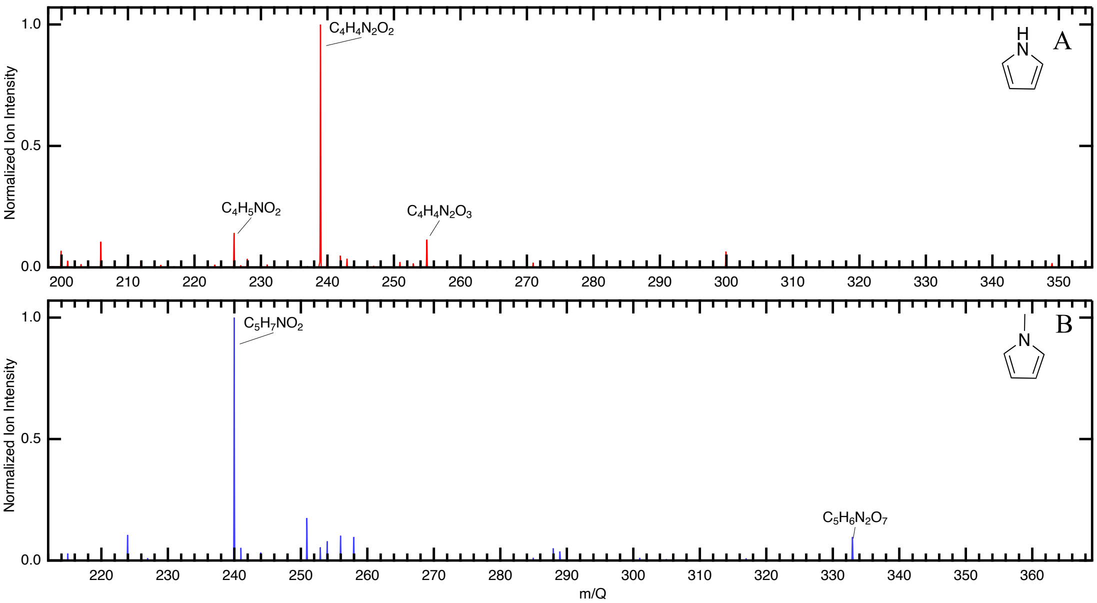

Figure S4.6 CIMS mass spectra with major gas-phase products highlighted for (A) pyrrole, and (B) 1-MP from experiments with a NO_x/O_3 ratio of 0.1. The ion intensity on the y-axis is normalized to the intensity of the largest product shown. The *x*-axis is shifted by +14 in (B) in comparison to (A), to account for the difference by $–CH_2$ in the VOC precursors, so that the oxidation products can be more easily compared.

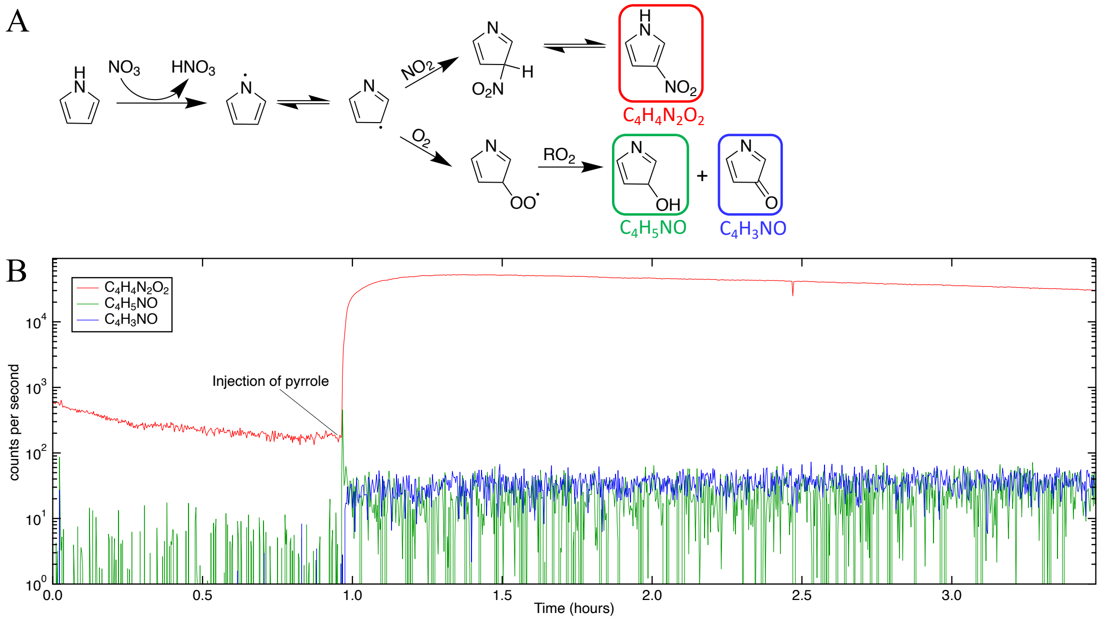

Figure S4.7 (A) A mechanism to explain the pyrrolyl radical's fates through O_2 addition and NO_2 addition. (B) The I-CIMS timeseries of the pyrrole + NO_3 experiment with the products shown in (A).

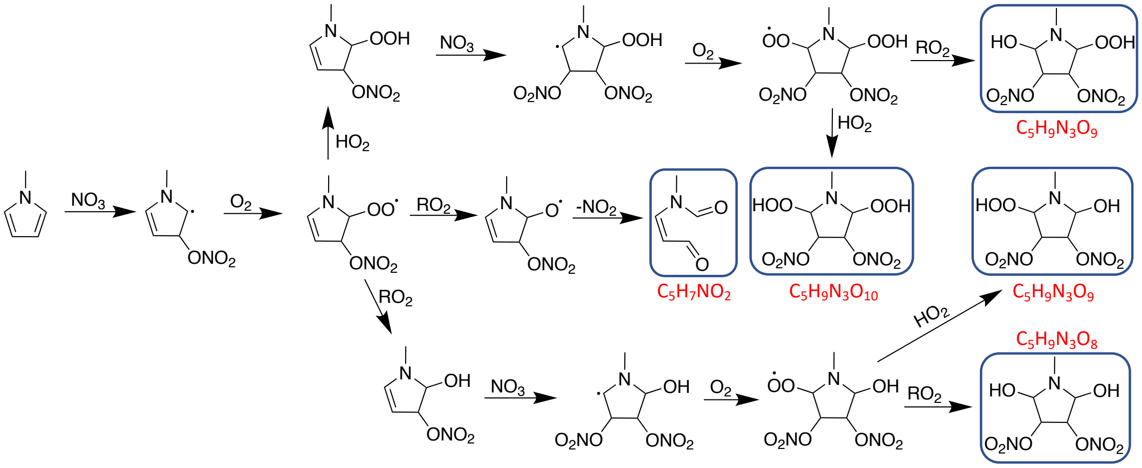

Figure S4.8. Proposed mechanism showing the formation of $C_5H_7NO_2$ and $C_5H_9N_3O_{8-10}$ from the NO_3 oxidation of 1-MP.

4.6 References

(1) Di Virgilio, G.; Evans, J. P.; Blake, S. A. P.; Armstrong, M.; Dowdy, A. J.; Sharples, J.; McRae, R. Climate Change Increases the Potential for Extreme Wildfires. *Geophysical Research Letters* **2019**, *46* (14), 8517–8526.

(2) Dennison, P. E.; Brewer, S. C.; Arnold, J. D.; Moritz, M. A. Large Wildfire Trends in the Western United States, 1984-2011. *Geophys. Res. Lett.* **2014**, *41* (8), 2928–2933.

(3) Crutzen, P. J.; Andreae, M. O. Biomass Burning in the Tropics: Impact on Atmospheric Chemistry and Biogeochemical Cycles. *Science* **1990**, *250* (4988), 1669–1678.

(4) Pope, C. A.; Dockery, D. W. Health Effects of Fine Particulate Air Pollution: Lines That Connect. *Journal of the Air & Waste Management Association* **2006**, *56* (6), 709–742.

(5) Hatch, L. E.; Luo, W.; Pankow, J. F.; Yokelson, R. J.; Stockwell, C. E.; Barsanti, K. C. Identification and Quantification of Gaseous Organic Compounds Emitted from Biomass Burning Using Two-Dimensional Gas Chromatography–Time-of-Flight Mass Spectrometry. *Atmos. Chem. Phys.* **2015**, *15* (4), 1865–1899.

(6) Koss, A. R.; Sekimoto, K.; Gilman, J. B.; Selimovic, V.; Coggon, M. M.; Zarzana, K. J.; Yuan, B.; Lerner, B. M.; Brown, S. S.; Jimenez, J. L.; Krechmer, J.; Roberts, J. M.; Warneke, C.; Yokelson, R. J.; de Gouw, J. Non-Methane Organic Gas Emissions from Biomass Burning: Identification, Quantification, and Emission Factors from PTR-ToF during the FIREX 2016 Laboratory Experiment. *Atmos. Chem. Phys.* **2018**, *18* (5), 3299–3319.

(7) Hatch, L. E.; Yokelson, R. J.; Stockwell, C. E.; Veres, P. R.; Simpson, I. J.; Blake, D. R.; Orlando, J. J.; Barsanti, K. C. Multi-Instrument Comparison and Compilation of Non-Methane Organic Gas Emissions from Biomass Burning and Implications for Smoke-Derived Secondary Organic Aerosol Precursors. *Atmos. Chem. Phys.* **2017**, *17* (2), 1471–1489.

(8) Oros, D. R.; Simoneit, B. R. T. Identification and Emission Factors of Molecular Tracers in Organic Aerosols from Biomass Burning Part 1. Temperate Climate Conifers. *Applied Geochemistry* **2001**, *16* (13), 1513–1544.

(9) Fine, P. M.; Cass, G. R.; Simoneit, B. R. T. Chemical Characterization of Fine Particle Emissions from the Fireplace Combustion of Wood Types Grown in the Midwestern and Western United States. *Environmental Engineering Science* **2004**, *21* (3), 387–409.

(10) Brown, S. S.; Stutz, J. Nighttime Radical Observations and Chemistry. *Chem. Soc. Rev.* **2012**, *41* (19), 6405.

(11) Stockwell, C. E.; Yokelson, R. J.; Kreidenweis, S. M.; Robinson, A. L.; DeMott, P. J.; Sullivan, R. C.; Reardon, J.; Ryan, K. C.; Griffith, D. W. T.; Stevens, L. Trace Gas Emissions from Combustion of Peat, Crop Residue, Domestic Biofuels, Grasses, and Other Fuels: Configuration and Fourier Transform Infrared (FTIR) Component of the Fourth Fire Lab at Missoula Experiment (FLAME-4). *Atmos. Chem. Phys.* **2014**, *14* (18), 9727–9754.

(12) Bluvshtein, N.; Lin, P.; Flores, J. M.; Segev, L.; Mazar, Y.; Tas, E.; Snider, G.; Weagle, C.; Brown, S. S.; Laskin, A.; Rudich, Y. Broadband Optical Properties of Biomass-Burning Aerosol and Identification of Brown Carbon Chromophores: OPTICAL AND CHEMICAL PROPERTIES OF BROWN CARBON AEROSOLS. *J. Geophys. Res. Atmos.* **2017**, *122* (10), 5441–5456.

(13) Decker, Z. C. J.; Robinson, M. A.; Barsanti, K. C.; Bourgeois, I.; Coggon, M. M.; DiGangi, J. P.; Diskin, G. S.; Flocke, F. M.; Franchin, A.; Fredrickson, C. D.; Gkatzelis, G. I.; Hall, S. R.; Halliday, H.; Holmes, C. D.; Huey, L. G.; Lee, Y. R.; Lindaas, J.; Middlebrook, A. M.; Montzka, D. D.; Moore, R.; Neuman, J. A.; Nowak, J. B.; Palm, B. B.; Peischl, J.; Piel, F.; Rickly, P. S.; Rollins, A. W.; Ryerson, T. B.; Schwantes, R. H.; Sekimoto, K.; Thornhill, L.; Thornton, J. A.; Tyndall, G. S.; Ullmann, K.; Van Rooy, P.; Veres, P. R.; Warneke, C.; Washenfelder, R. A.; Weinheimer, A. J.; Wiggins, E.; Winstead, E.; Wisthaler, A.; Womack, C.; Brown, S. S. Nighttime and Daytime Dark Oxidation Chemistry in Wildfire Plumes: An Observation and Model Analysis of FIREX-AQ Aircraft Data. *Atmos. Chem. Phys.* **2021**, *21* (21), 16293–16317.

(14) Jiang, H.; Frie, A. L.; Lavi, A.; Chen, J. Y.; Zhang, H.; Bahreini, R.; Lin, Y.-H. Brown Carbon Formation from Nighttime Chemistry of Unsaturated Heterocyclic Volatile Organic Compounds. *Environ. Sci. Technol. Lett.* **2019**, *6* (3), 184–190.

(15) Lin, P.; Fleming, L. T.; Nizkorodov, S. A.; Laskin, J.; Laskin, A. Comprehensive Molecular Characterization of Atmospheric Brown Carbon by High Resolution Mass Spectrometry with Electrospray and Atmospheric Pressure Photoionization. *Anal. Chem.* **2018**, *90* (21), 12493–12502.

(16) Lin, P.; Bluvshtein, N.; Rudich, Y.; Nizkorodov, S. A.; Laskin, J.; Laskin, A. Molecular Chemistry of Atmospheric Brown Carbon Inferred from a Nationwide Biomass Burning Event. *Environ. Sci. Technol.* **2017**, *51* (20), 11561–11570.

(17) Lin, P.; Liu, J.; Shilling, J. E.; Kathmann, S. M.; Laskin, J.; Laskin, A. Molecular Characterization of Brown Carbon (BrC) Chromophores in Secondary Organic Aerosol Generated from Photo-Oxidation of Toluene. *Phys. Chem. Chem. Phys.* **2015**, *17* (36), 23312–23325.

(18) Joo, T.; Rivera-Rios, J. C.; Takeuchi, M.; Alvarado, M. J.; Ng, N. L. Secondary Organic Aerosol Formation from Reaction of 3-Methylfuran with Nitrate Radicals. *ACS Earth Space Chem.* **2019**, *3* (6), 922–934.

(19) Jiang, J.; Carter, W. P. L.; Cocker, D. R.; Barsanti, K. C. Development and Evaluation of a Detailed Mechanism for Gas-Phase Atmospheric Reactions of Furans. *ACS Earth Space Chem.* **2020**, *4* (8), 1254–1268.

(20) Li, M.; Liu, Y.; Wang, L. Gas-Phase Ozonolysis of Furans, Methylfurans, and Dimethylfurans in the Atmosphere. *Phys. Chem. Chem. Phys.* **2018**, *20* (38), 24735–24743.

(21) Tekle-Röttering, A.; Lim, S.; Reisz, E.; Lutze, H. V.; Abdighahroudi, M. S.; Willach, S.; Schmidt, W.; Tentscher, P. R.; Rentsch, D.; McArdell, C. S.; Schmidt, T. C.; von Gunten, U. Reactions of Pyrrole, Imidazole, and Pyrazole with Ozone: Kinetics and Mechanisms. *Environ. Sci.: Water Res. Technol.* **2020**, *6* (4), 976–992.

(22) Atkinson, Roger.; Aschmann, S. M.; Winer, A. M.; Carter, W. P. L. Rate Constants for the Gas-Phase Reactions of Nitrate Radicals with Furan, Thiophene, and Pyrrole at 295 +/- 1 K and Atmospheric Pressure. *Environ. Sci. Technol.* **1985**, *19* (1), 87–90.

(23) Cabañas, B.; Baeza, M. T.; Salgado, S.; Martín, P.; Taccone, R.; Martínez, E. Oxidation of Heterocycles in the Atmosphere: Kinetic Study of Their Reactions with NO_3 Radical. *J. Phys. Chem. A* **2004**, *108* (49), 10818–10823.

(24) Fry, J. L.; Draper, D. C.; Barsanti, K. C.; Smith, J. N.; Ortega, J.; Winkler, P. M.; Lawler, M. J.; Brown, S. S.; Edwards, P. M.; Cohen, R. C.; Lee, L. Secondary Organic Aerosol Formation and Organic Nitrate Yield from NO_3 Oxidation of Biogenic Hydrocarbons. *Environ. Sci. Technol.* **2014**, *48* (20), 11944–11953.

(25) Fry, J. L.; Kiendler-Scharr, A.; Rollins, A. W.; Brauers, T.; Brown, S. S.; Dorn, H.-P.; Dubé, W. P.; Fuchs, H.; Mensah, A.; Rohrer, F.; Tillmann, R.; Wahner, A.; Wooldridge, P. J.; Cohen, R. C. SOA from Limonene: Role of NO_3 in Its Generation and Degradation. *Atmos. Chem. Phys.* **2011**, *11* (8), 3879–3894.

(26) Fry, J. L.; Kiendler-Scharr, A.; Rollins, A. W.; Wooldridge, P. J.; Brown, S. S.; Fuchs, H.; Dubé, W.; Mensah, A.; dal Maso, M.; Tillmann, R.; Dorn, H.-P.; Brauers, T.; Cohen, R. C. Organic Nitrate and Secondary Organic Aerosol Yield from NO_3 Oxidation of β-Pinene Evaluated Using a Gas-Phase Kinetics/Aerosol Partitioning Model. *Atmos. Chem. Phys.* **2009**, *9* (4), 1431–1449.

(27) Rollins, A. W.; Fry, J. L.; Hunter, J. F.; Kroll, J. H.; Worsnop, D. R.; Singaram, S. W.; Cohen, R. C. Elemental Analysis of Aerosol Organic Nitrates with Electron Ionization High-Resolution Mass Spectrometry. *Atmos. Meas. Tech.* **2010**, *3* (1), 301–310.

(28) Rollins, A. W.; Pusede, S.; Wooldridge, P.; Min, K.-E.; Gentner, D. R.; Goldstein, A. H.; Liu, S.; Day, D. A.; Russell, L. M.; Rubitschun, C. L.; Surratt, J. D.; Cohen, R. C. Gas/Particle Partitioning of Total Alkyl Nitrates Observed with TD-LIF in Bakersfield: $RONO_2$ Phase Partitioning. *J. Geophys. Res. Atmos.* **2013**, *118* (12), 6651–6662.

(29) Nah, T.; Sanchez, J.; Boyd, C. M.; Ng, N. L. Photochemical Aging of α-Pinene and β-Pinene Secondary Organic Aerosol Formed from Nitrate Radical Oxidation. *Environ. Sci. Technol.* **2016**, *50* (1), 222–231.

(30) Finewax, Z.; de Gouw, J. A.; Ziemann, P. J. Identification and Quantification of 4-Nitrocatechol Formed from OH and NO3 Radical-Initiated Reactions of Catechol in Air in the Presence of NO_x: Implications for Secondary Organic Aerosol Formation from Biomass Burning. *Environ. Sci. Technol.* **2018**, *52* (4), 1981–1989.

(31) Finewax, Z.; de Gouw, J. A.; Ziemann, P. J. Products and Secondary Organic Aerosol Yields from the OH and NO_3 Radical-Initiated Oxidation of Resorcinol. *ACS Earth Space Chem.* **2019**, *3* (7), 1248–1259.

(32) Vidović, K.; Lašič Jurković, D.; Šala, M.; Kroflič, A.; Grgić, I. Nighttime Aqueous-Phase Formation of Nitrocatechols in the Atmospheric Condensed Phase. *Environ. Sci. Technol.* **2018**, *52* (17), 9722–9730.

(33) Bolzacchini, E.; Bruschi, M.; Hjorth, J.; Meinardi, S.; Orlandi, M.; Rindone, B.; Rosenbohm, E. Gas-Phase Reaction of Phenol with NO_3. *Environ. Sci. Technol.* **2001**, *35* (9), 1791–1797.

(34) Kroflič, A.; Grilc, M.; Grgić, I. Unraveling Pathways of Guaiacol Nitration in Atmospheric Waters: Nitrite, A Source of Reactive Nitronium Ion in the Atmosphere. *Environ. Sci. Technol.* **2015**, *49* (15), 9150–9158.

(35) Mayorga, R. J.; Zhao, Z.; Zhang, H. Formation of Secondary Organic Aerosol from Nitrate Radical Oxidation of Phenolic VOCs: Implications for Nitration Mechanisms and Brown Carbon Formation. *Atmos. Environ.* **2021**, *244*, 117910.

(36) Frka, S.; Šala, M.; Kroflič, A.; Huš, M.; Čusak, A.; Grgić, I. Quantum Chemical Calculations Resolved Identification of Methylnitrocatechols in Atmospheric Aerosols. *Environ. Sci. Technol.* **2016**, *50* (11), 5526–5535.

(37) Kitanovski, Z.; Čusak, A.; Grgić, I.; Claeys, M. Chemical Characterization of the Main Products Formed through Aqueous-Phase Photonitration of Guaiacol. *Atmos. Meas. Tech.* **2014**, *7* (8), 2457–2470.

(38) Vidović, K.; Kroflič, A.; Šala, M.; Grgić, I. Aqueous-Phase Brown Carbon Formation from Aromatic Precursors under Sunlight Conditions. *Atmosphere* **2020**, *11* (2), 131.

(39) Yuan, B.; Liggio, J.; Wentzell, J.; Li, S.-M.; Stark, H.; Roberts, J. M.; Gilman, J.; Lerner, B.; Warneke, C.; Li, R.; Leithead, A.; Osthoff, H. D.; Wild, R.; Brown, S. S.; de Gouw, J. A. Secondary Formation of Nitrated Phenols: Insights from Observations during the Uintah Basin Winter Ozone Study (UBWOS) 2014. *Atmos. Chem. Phys.* **2016**, *16* (4), 2139–2153.

(40) Singh, H. B.; Anderson, B. E.; Brune, W. H.; Cai, C.; Cohen, R. C.; Crawford, J. H.; Cubison, M. J.; Czech, E. P.; Emmons, L.; Fuelberg, H. E. Pollution Influences on Atmospheric Composition and Chemistry at High Northern Latitudes: Boreal and California Forest Fire Emissions. *Atmospheric Environment* **2010**, *44* (36), 4553–4564.

(41) Zhao, Z.; Zhang, W.; Alexander, T.; Zhang, X.; Martin, D. B. C.; Zhang, H. Isolating α-Pinene Ozonolysis Pathways Reveals New Insights into Peroxy Radical Chemistry and Secondary Organic Aerosol Formation. *Environ. Sci. Technol.* **2021**, *55* (10), 6700–6709.

(42) Zhang, X.; Zhang, H.; Xu, W.; Wu, X.; Tyndall, G. S.; Orlando, J. J.; Jayne, J. T.; Worsnop, D. R.; Canagaratna, M. R. Molecular Characterization of Alkyl Nitrates in Atmospheric Aerosols by Ion Mobility Mass Spectrometry. *Atmos. Meas. Tech.* **2019**, *12* (10), 5535–5545.

(43) Zhao, Z.; Yang, X.; Lee, J.; Tolentino, R.; Mayorga, R.; Zhang, W.; Zhang, H. Diverse Reactions in Highly Functionalized Organic Aerosols during Thermal Desorption. *ACS Earth Space Chem.* **2020**, *4* (2), 283–296.

(44) Zhao, Z.; Le, C.; Xu, Q.; Peng, W.; Jiang, H.; Lin, Y.-H.; Cocker, D. R.; Zhang, H. Compositional Evolution of Secondary Organic Aerosol as Temperature and Relative Humidity Cycle in Atmospherically Relevant Ranges. *ACS Earth Space Chem.* **2019**, *3* (11), 2549–2558.

(45) Bahreini, R.; Keywood, M. D.; Ng, N. L.; Varutbangkul, V.; Gao, S.; Flagan, R. C.; Seinfeld, J. H.; Worsnop, D. R.; Jimenez, J. L. Measurements of Secondary Organic Aerosol from Oxidation of Cycloalkenes, Terpenes, and m-Xylene Using an Aerodyne Aerosol Mass Spectrometer. *Environ. Sci. Technol.* **2005**, *39* (15), 5674–5688.

(46) Cui, Y.; Frie, A. L.; Dingle, J. H.; Zimmerman, S.; Frausto-Vicencio, I.; Hopkins, F.; Bahreini, R. Influence of Ammonia and Relative Humidity on the Formation and Composition of Secondary Brown Carbon from Oxidation of 1-Methylnaphthalene and Longifolene. *ACS Earth Space Chem.* **2021**, *5* (4), 858–869.

(47) DeCarlo, P. F.; Slowik, J. G.; Worsnop, D. R.; Davidovits, P.; Jimenez, J. L. Particle Morphology and Density Characterization by Combined Mobility and Aerodynamic

Diameter Measurements. Part 1: Theory. *Aerosol Science and Technology* **2004**, *38* (12), 1185–1205.

(48) Bahreini, R.; Middlebrook, A. M.; Brock, C. A.; de Gouw, J. A.; McKeen, S. A.; Williams, L. R.; Daumit, K. E.; Lambe, A. T.; Massoli, P.; Canagaratna, M. R.; Ahmadov, R.; Carrasquillo, A. J.; Cross, E. S.; Ervens, B.; Holloway, J. S.; Hunter, J. F.; Onasch, T. B.; Pollack, I. B.; Roberts, J. M.; Ryerson, T. B.; Warneke, C.; Davidovits, P.; Worsnop, D. R.; Kroll, J. H. Mass Spectral Analysis of Organic Aerosol Formed Downwind of the Deepwater Horizon Oil Spill: Field Studies and Laboratory Confirmations. *Environ. Sci. Technol.* **2012**, *46* (15), 8025–8034.

(49) Bloss, C.; Wagner, V.; Jenkin, M. E.; Volkamer, R.; Bloss, W. J.; Lee, J. D.; Heard, D. E.; Wirtz, K.; Martin-Reviejo, M.; Rea, G.; Wenger, J. C.; Pilling, M. J. Development of a Detailed Chemical Mechanism (MCMv3.1) for the Atmospheric Oxidation of Aromatic Hydrocarbons. *Atmos. Chem. Phys.* **2005**, *5* (3), 641–664.

(50) Fry, J. L.; Draper, D. C.; Barsanti, K. C.; Smith, J. N.; Ortega, J.; Winkler, P. M.; Lawler, M. J.; Brown, S. S.; Edwards, P. M.; Cohen, R. C.; Lee, L. Secondary Organic Aerosol Formation and Organic Nitrate Yield from NO_3 Oxidation of Biogenic Hydrocarbons. *Environ. Sci. Technol.* **2014**, *48* (20), 11944–11953.

(51) Chen, J. Y.; Rodriguez, E.; Jiang, H.; Chen, K.; Frie, A.; Zhang, H.; Bahreini, R.; Lin, Y.-H. Time-Dependent Density Functional Theory Investigation of the UV–Vis Spectra of Organonitrogen Chromophores in Brown Carbon. *ACS Earth Space Chem.* **2020**, *4* (2), 311–320.

(52) Zhang, X.; Krechmer, J. E.; Groessl, M.; Xu, W.; Graf, S.; Cubison, M.; Jayne, J. T.; Jimenez, J. L.; Worsnop, D. R.; Canagaratna, M. R. A Novel Framework for Molecular Characterization of Atmospherically Relevantorganic Compounds Based on Collision Cross Section and Mass-to-Charge Ratio. *Atmos. Chem. Phys.* **2016**, *16* (20), 12945–12959.

(53) De Haan, D. O.; Jansen, K.; Rynaski, A. D.; Sueme, W. R. P.; Torkelson, A. K.; Czer, E. T.; Kim, A. K.; Rafla, M. A.; De Haan, A. C.; Tolbert, M. A. Brown Carbon Production by Aqueous-Phase Interactions of Glyoxal and SO_2. *Environ. Sci. Technol.* **2020**, *54* (8), 4781–4789.

(54) Lopez-Hilfiker, F. D.; Pospisilova, V.; Huang, W.; Kalberer, M.; Mohr, C.; Stefenelli, G.; Thornton, J. A.; Baltensperger, U.; Prevot, A. S. H.; Slowik, J. G. An Extractive Electrospray Ionization Time-of-Flight Mass Spectrometer (EESI-TOF) for Online Measurement of Atmospheric Aerosol Particles. *Atmos. Meas. Tech.* **2019**, *12* (9), 4867–4886.

(55) Liu, S.; Shilling, J. E.; Song, C.; Hiranuma, N.; Zaveri, R. A.; Russell, L. M. Hydrolysis of Organonitrate Functional Groups in Aerosol Particles. *Aerosol Science and Technology* **2012**, *46* (12), 1359–1369.

(56) Bourgeois, I.; Peischl, J.; Neuman, J. A.; Brown, S. S.; Allen, H. M.; Campuzano-Jost, P.; Coggon, M. M.; DiGangi, J. P.; Diskin, G. S.; Gilman, J. B.; Gkatzelis, G. I.; Guo, H.; Halliday, H.; Hanisco, T. F.; Holmes, C. D.; Huey, L. G.; Jimenez, J. L.; Lamplugh, A. D.; Lee, Y. R.; Lindaas, J.; Moore, R. H.; Nowak, J. B.; Pagonis, D.; Rickly, P. S.; Robinson, M. A.; Rollins, A. W.; Selimovic, V.; St. Clair, J. M.; Tanner, D.; Vasquez, K. T.; Veres, P. R.; Warneke, C.; Wennberg, P. O.; Washenfelder, R. A.; Wiggins, E. B.; Womack, C. C.; Xu, L.; Zarzana, K. J.; Ryerson, T. B. *Comparison of Airborne Measurements of NO, NO_2;, HONO, NO_y; and CO during FIREX-AQ*, https://doi.org/10.5194/amt-2021-432; preprint; Gases/In Situ Measurement/Instruments and Platforms, 2022.

(57) Platz, J.; Nielsen, O. J.; Wallington, T. J.; Ball, J. C.; Hurley, M. D.; Straccia, A. M.; Schneider, W. F.; Sehested, J. Atmospheric Chemistry of the Phenoxy Radical, C6H5O(•): UV Spectrum and Kinetics of Its Reaction with NO, NO_2 , and O_2. *J. Phys. Chem. A* **1998**, *102* (41), 7964–7974.

(58) Kurtén, T.; Møller, K. H.; Nguyen, T. B.; Schwantes, R. H.; Misztal, P. K.; Su, L.; Wennberg, P. O.; Fry, J. L.; Kjaergaard, H. G. Alkoxy Radical Bond Scissions Explain the Anomalously Low Secondary Organic Aerosol and Organonitrate Yields From α-Pinene + NO_3. *J. Phys. Chem. Lett.* **2017**, *8* (13), 2826–2834.

(59) Jiang, H.; Jang, M.; Yu, Z. Dithiothreitol Activity by Particulate Oxidizers of SOA Produced from Photooxidation of Hydrocarbons under Varied NO_x Levels. *Atmos. Chem. Phys.* **2017**, *17* (16), 9965–9977.

(60) Liu, J.; Lin, P.; Laskin, A.; Laskin, J.; Kathmann, S. M.; Wise, M.; Caylor, R.; Imholt, F.; Selimovic, V.; Shilling, J. E. Optical Properties and Aging of Light-Absorbing Secondary Organic Aerosol. *Atmos. Chem. Phys.* **2016**, *16* (19), 12815–12827.

(61) Palm, B. B.; Peng, Q.; Fredrickson, C. D.; Lee, B. H.; Garofalo, L. A.; Pothier, M. A.; Kreidenweis, S. M.; Farmer, D. K.; Pokhrel, R. P.; Shen, Y.; Murphy, S. M.; Permar, W.; Hu, L.; Campos, T. L.; Hall, S. R.; Ullmann, K.; Zhang, X.; Flocke, F.; Fischer, E. V.; Thornton, J. A. Quantification of Organic Aerosol and Brown Carbon Evolution in Fresh Wildfire Plumes. *Proc. Natl. Acad. Sci. U.S.A.* **2020**, *117* (47), 29469–29477.

(62) Kodros, J. K.; Papanastasiou, D. K.; Paglione, M.; Masiol, M.; Squizzato, S.; Florou, K.; Skyllakou, K.; Kaltsonoudis, C.; Nenes, A.; Pandis, S. N. Rapid Dark Aging of Biomass Burning as an Overlooked Source of Oxidized Organic Aerosol. *Proc. Natl. Acad. Sci. U.S.A.* **2020**, *117* (52), 33028–33033.

(63) Farmer, D. K.; Matsunaga, A.; Docherty, K. S.; Surratt, J. D.; Seinfeld, J. H.; Ziemann, P. J.; Jimenez, J. L. Response of an Aerosol Mass Spectrometer to Organonitrates and Organosulfates and Implications for Atmospheric Chemistry. *Proc. Natl. Acad. Sci. U.S.A.* **2010**, *107* (15), 6670–6675.

(64) Day, D. A.; Campuzano-Jost, P.; Nault, B. A.; Palm, B. B.; Hu, W.; Guo, H.; Wooldridge, P. J.; Cohen, R. C.; Docherty, K. S.; Huffman, J. A.; de Sá, S. S.; Martin, S. T.; Jimenez, J. L. A Systematic Re-Evaluation of Methods for Quantification of Bulk Particle-Phase Organic Nitrates Using Real-Time Aerosol Mass Spectrometry. *Atmos. Meas. Tech.* **2022**, *15* (2), 459–483.

(65) Ramasamy, S.; Nakayama, T.; Imamura, T.; Morino, Y.; Kajii, Y.; Sato, K. Investigation of Dark Condition Nitrate Radical- and Ozone-Initiated Aging of Toluene Secondary Organic Aerosol: Importance of Nitrate Radical Reactions with Phenolic Products. *Atmospheric Environment* **2019**, *219*, 117049.

(66) Iinuma, Y.; Böge, O.; Gräfe, R.; Herrmann, H. Methyl-Nitrocatechols: Atmospheric Tracer Compounds for Biomass Burning Secondary Organic Aerosols. *Environ. Sci. Technol.* **2010**, *44* (22), 8453–8459.

(67) Meng, L.; Coeur, C.; Fayad, L.; Houzel, N.; Genevray, P.; Bouzidi, H.; Tomas, A.; Chen, W. Secondary Organic Aerosol Formation from the Gas-Phase Reaction of Guaiacol (2-Methoxyphenol) with NO_3 Radicals. *Atmospheric Environment* **2020**, *240*, 117740.

CHAPTER 5: Conclusions and Future Work

5.1 Summary of Dissertation Work

The body of work presented in this dissertation represents significant advancements to the field of atmospheric chemistry including 1) improvements to the mechanistic understanding of the NO_3 oxidation of major types of wildfire-emitted VOCs leading to the formation of BrC and 2) elucidation of autoxidation as a potential mechanism leading to the formation of highly oxidized organic nitrates in the NO_3 oxidation of limonene.

In Chapter 2, we reported the identification of many products which were previously undiscovered from the NO_3 oxidation of a variety phenolic VOCs. With our IMS-TOF, we were able to gain structural information for some of these products. We proposed mechanisms for the formation of diphenyl ether dimers forming from the NO_3 oxidation of phenol and suggested that these dimers may contribute significantly to SOA mass due to their low volatility. Finally, we also found the SOA from NO_3 oxidation of phenolic VOCs to be highly light absorbing. From this, we were able to add to the growing body of evidence that nitroaromatic compounds formed from NO_3 oxidation of wildfire-emitted VOCs contribute strongly to the light absorption of BrC.

In Chapter 3, we identified highly oxidized organic nitrates forming on a short timescale from the NO_3 oxidation of limonene and proposed two autoxidation pathways through which they could form. We also identified several highly oxidized dinitrates forming from the NO_3 oxidation of limonene. With our IMS-TOF, we compared the data from our experiments to ambient samples and found that certain mono- and dinitrate products observed in our experiments were also identified during ambient wildfire and nighttime samples from the Southeastern United States. This demonstrates that autoxidation and sequential oxidation from limonene are key processes occurring in the real atmosphere quickly leading to highly oxidized organic nitrates.

In Chapter 4, we found a direct correlation between wildfire-emitted VOC precursor structure and light absorption of BrC revealing the impact of an easily abstractable hydrogen in the initial attack of the nitrate radical. In the presence of an easily abstractable hydrogen, pyrrole and 2-MP were more susceptible to H-abstraction by NO_3 followed by radical shift and NO_2 addition. In the absence of an easily abstractable hydrogen, in the case of 1-MP, the initial NO_3 oxidation is more likely to proceed through addition to the double bond leading to the formation of organonitrates. The nighttime oxidation of pyrrole, 1-MP and 2-MP were largely understudied, and we provided key insights into SOA chemical composition from each of these VOCs. Furthermore, we proposed a novel mechanism for the addition of 1, 2, and 3 nitro groups to the backbone of pyrrole in the gas-phase.

5.2 Future Work

5.2.1 Daytime and Nighttime Aging of SOA

Following the characterization of SOA and BrC from the NO_3 oxidation of these studied wildfire-emitted VOCs, it is critical to investigate how these SOA evolve during atmospheric aging (e.g. further nighttime and daytime atmospheric processing). Due to limitations in experimental design as well as analytical instruments, most studies have focused on either daytime or nighttime oxidation of VOCs. These investigations are crucial in broadening our understanding of specific reaction pathways and gas-particle partitioning from these processes, but they are not able to elucidate the combined effects of daytime and nighttime processing on reaction pathways. Despite the need for this type of study, developing an experimental setup to study the multiphase daytime and nighttime processing of these VOCs has remained a challenge. We plan to investigate the compositional variation that photooxidation plays along with nighttime oxidation in the multiphase SOA aging of these VOCs, which remains widely unknown.

The lifetime of SOA particles in the atmosphere can be as long as several days up to a week, underlining the importance of exploring the daytime and nighttime atmospheric aging of BrC.[1–3] During the daytime, reactions of OH and photolysis drive aging of SOA and BrC.[4–6] Previous studies have investigated the photochemical aging of BrC from biomass burning precursors and some have observed photo-bleaching of BrC while others have observed photo-enhancement in early aging followed by photo-bleaching in later aging.[5,7–9] Investigations of the nighttime aging of BrC have shown photo-enhancement of BrC due to the formation of new chromophores.[4,10,11] Nitroaromatics are well-known chromophores contributing significantly to BrC from aromatic precursors.[12–18] Additionally, N-containing carbonyl chromophores have been recently shown to contribute up to 40% of light absorption in pyrrole BrC.[19] These proposed studies to investigate the multiphase daytime and nighttime aging of SOA and BrC will enhance the detailed mechanistic understanding of multiphase aging processes and provide experimental results that are more relevant to timescales of the real atmosphere.

5.3 References

(1) Decker, Z. C. J.; Zarzana, K. J.; Coggon, M.; Min, K.-E.; Pollack, I.; Ryerson, T. B.; Peischl, J.; Edwards, P.; Dubé, W. P.; Markovic, M. Z.; Roberts, J. M.; Veres, P. R.; Graus, M.; Warneke, C.; de Gouw, J.; Hatch, L. E.; Barsanti, K. C.; Brown, S. S. Nighttime Chemical Transformation in Biomass Burning Plumes: A Box Model Analysis Initialized with Aircraft Observations. *Environ. Sci. Technol.* **2019**, *53* (5), 2529–2538.

(2) Bluvshtein, N.; Flores, J. M.; He, Q.; Segre, E.; Segev, L.; Hong, N.; Donohue, A.; Hilfiker, J. N.; Rudich, Y. Calibration of a Multi-Pass Photoacoustic Spectrometer Cell Using Light-Absorbing Aerosols. *Atmos. Meas. Tech.* **2017**, *10* (3), 1203–1213.

(3) Selimovic, V.; Yokelson, R. J.; McMeeking, G. R.; Coefield, S. In Situ Measurements of Trace Gases, PM, and Aerosol Optical Properties during the 2017 NW US Wildfire Smoke Event. *Atmos. Chem. Phys.* **2019**, *19* (6), 3905–3926.

(4) Li, C.; He, Q.; Hettiyadura, A. P. S.; Käfer, U.; Shmul, G.; Meidan, D.; Zimmermann, R.; Brown, S. S.; George, C.; Laskin, A.; Rudich, Y. Formation of Secondary Brown Carbon in Biomass Burning Aerosol Proxies through NO_3 Radical Reactions. *Environ. Sci. Technol.* **2020**, *54* (3), 1395–1405.

(5) Sumlin, B. J.; Pandey, A.; Walker, M. J.; Pattison, R. S.; Williams, B. J.; Chakrabarty, R. K. Atmospheric Photooxidation Diminishes Light Absorption by Primary Brown Carbon Aerosol from Biomass Burning. *Environ. Sci. Technol. Lett.* **2017**, *4* (12), 540–545.

(6) Zhao, R.; Lee, A. K. Y.; Huang, L.; Li, X.; Yang, F.; Abbatt, J. P. D. Photochemical Processing of Aqueous Atmospheric Brown Carbon. *Atmos. Chem. Phys.* **2015**, *15* (11), 6087–6100.

(7) Forrister, H.; Liu, J.; Scheuer, E.; Dibb, J.; Ziemba, L.; Thornhill, K. L.; Anderson, B.; Diskin, G.; Perring, A. E.; Schwarz, J. P.; Campuzano-Jost, P.; Day, D. A.; Palm, B. B.; Jimenez, J. L.; Nenes, A.; Weber, R. J. Evolution of Brown Carbon in Wildfire Plumes. *Geophysical Research Letters* **2015**, *42* (11), 4623–4630.

(8) Li, C.; He, Q.; Schade, J.; Passig, J.; Zimmermann, R.; Meidan, D.; Laskin, A.; Rudich, Y. Dynamic Changes in Optical and Chemical Properties of Tar Ball Aerosols by Atmospheric Photochemical Aging. *Atmos. Chem. Phys.* **2019**, *19* (1), 139–163.

(9) Schnitzler, E. G.; Liu, T.; Hems, R. F.; Abbatt, J. P. D. Emerging Investigator Series: Heterogeneous OH Oxidation of Primary Brown Carbon Aerosol: Effects of Relative Humidity and Volatility. *Environ. Sci.: Processes Impacts* **2020**, 10.1039.D0EM00311E.

(10) Bluvshtein, N.; Lin, P.; Flores, J. M.; Segev, L.; Mazar, Y.; Tas, E.; Snider, G.; Weagle, C.; Brown, S. S.; Laskin, A.; Rudich, Y. Broadband Optical Properties of Biomass-Burning Aerosol and Identification of Brown Carbon Chromophores: OPTICAL AND CHEMICAL PROPERTIES OF BROWN CARBON AEROSOLS. *J. Geophys. Res. Atmos.* **2017**, *122* (10), 5441–5456.

(11) Lin, P.; Bluvshtein, N.; Rudich, Y.; Nizkorodov, S. A.; Laskin, J.; Laskin, A. Molecular Chemistry of Atmospheric Brown Carbon Inferred from a Nationwide Biomass Burning Event. *Environ. Sci. Technol.* **2017**, *51* (20), 11561–11570.

(12) Finewax, Z.; de Gouw, J. A.; Ziemann, P. J. Identification and Quantification of 4-Nitrocatechol Formed from OH and NO3 Radical-Initiated Reactions of Catechol in Air in the Presence of NO_x: Implications for Secondary Organic Aerosol Formation from Biomass Burning. *Environ. Sci. Technol.* **2018**, *52* (4), 1981–1989.

(13) Vidović, K.; Lašič Jurković, D.; Šala, M.; Kroflič, A.; Grgić, I. Nighttime Aqueous-Phase Formation of Nitrocatechols in the Atmospheric Condensed Phase. *Environ. Sci. Technol.* **2018**, *52* (17), 9722–9730.

(14) Bolzacchini, E.; Bruschi, M.; Hjorth, J.; Meinardi, S.; Orlandi, M.; Rindone, B.; Rosenbohm, E. Gas-Phase Reaction of Phenol with NO_3. *Environ. Sci. Technol.* **2001**, *35* (9), 1791–1797.

(15) Frka, S.; Šala, M.; Kroflič, A.; Huš, M.; Čusak, A.; Grgić, I. Quantum Chemical Calculations Resolved Identification of Methylnitrocatechols in Atmospheric Aerosols. *Environ. Sci. Technol.* **2016**, *50* (11), 5526–5535.

(16) Kitanovski, Z.; Čusak, A.; Grgić, I.; Claeys, M. Chemical Characterization of the Main Products Formed through Aqueous-Phase Photonitration of Guaiacol. *Atmos. Meas. Tech.* **2014**, *7* (8), 2457–2470.

(17) Vidović, K.; Kroflič, A.; Šala, M.; Grgić, I. Aqueous-Phase Brown Carbon Formation from Aromatic Precursors under Sunlight Conditions. *Atmosphere* **2020**, *11* (2), 131.

(18) Yuan, B.; Liggio, J.; Wentzell, J.; Li, S.-M.; Stark, H.; Roberts, J. M.; Gilman, J.; Lerner, B.; Warneke, C.; Li, R.; Leithead, A.; Osthoff, H. D.; Wild, R.; Brown, S. S.; de Gouw, J. A. Secondary Formation of Nitrated Phenols: Insights from Observations during the Uintah Basin Winter Ozone Study (UBWOS) 2014. *Atmos. Chem. Phys.* **2016**, *16* (4), 2139–2153.

(19) Chen, K.; Mayorga, R.; Hamilton, C.; Bahreini, R.; Zhang, H.; Lin, Y.-H. Contribution of Carbonyl Chromophores in Secondary Brown Carbon from Nighttime Oxidation of Unsaturated Heterocyclic Volatile Organic Compounds. *Environ. Sci. Technol.* **2023**, *57* (48), 20085–20096.